# The Application of Ru(II) Polypyridyl Complexes to Cellular Imaging and Sensing

A thesis submitted to Dublin City University for the award of PhD

By

Aisling Byrne B.Sc. (Hons)

School of Chemical Sciences,

Dublin City University,

Glasnevin,

Dublin 9.

August 2016

Supervisor:

Professor. Tia E. Keyes

# *Declaration*

I hereby certify that this material, which I now submit for assessment on the programme of study leading to the award of PhD. is entirely my own work, that I have exercised reasonable care to ensure that the work is original, and does not to the best of my knowledge breach any law of copyright, and has not been taken from the work of others save and to the extent that such work has been cited and acknowledged within the text of my work.

Signed: _____

ID No.: _____

Date: _____

## *Acknowledgements*

Firstly, I would like to thank my supervisor, Prof. Tia Keyes, for giving me this great opportunity, for all your help and guidance over the past few years, and all your motivation over the last few months. I am forever greatful for everything.

A massive thank you to my research group, I'm very lucky to have worked with you all! Kellie, Ciaran, Elaine, Hazel, Andrea, Samantha, Kerileng, Bincy, Sean, Mohammad and Aaron. Thanks for all your help along the way and for the great nights at the Christmas partys over the years. Thanks to Dr. Roisin Moriarty for training me at the beginning, and to Dr. Una Prendergast for training me and for always being there when I had a question.

I especially want to thank Chris, Colm, Aurelian, Eimear, Claire and Creina for all the coffees, lunches, the rants and the bants. I definitely would not have survived without you guys being there. You made my time in DCU so much fun, with all the nights out and trips that I will never forget. And to Chris, for all your help teaching me chemistry over the last few months, no matter how simple or trivial my questions were, you always gave me your time and patience, so thanks for it all. You guys were always there, and I have definitely made some great life-long friends.

Eadaoin, hon, the past year would not have been same without you! I'm so lucky that you were put in the lab with me, you helped make the past year the best I have had in DCU so far, couldn't imagine the place without you!

Daz, my number one hun, thanks for all your encouragement over the past few months, without which I definietly would not have gotten through to the end, especially not without your jar of motivation! I will never, ever forget all you did for me.

Suzanne, there are not enough words to even begin to say thank you! I am so lucky to have gone through undergrad and now postgrad with you, I'd say we look mad different now….. You helped me in ways you'll never know, and the memories we have from the past 4 years alone are some of the best! (Are you coming on the boat?)

Finally, the biggest thanks is to my family. Mam, dad, Kev, and granny, for everything! Your support, words of encouragement, love and patience got me to where I am today, this is for you!

# Table of Contents

**Chapter 3: Ru (II) Polypyridyl complex conjugated to a Mitochondrial Penetrating Peptide (MPP) sequence as an Oxygen Sensor**



**Chapter 4: Dual-emission Ruthenium-BODIPY ratiometric complex for Oxygen Sensing**

**List of Abbreviations**

ACN - Acetonitrile

Anti A – Antimycin A

Arg - Arginine

ATP – Adenine Triphosphatase

Bpy - 2,2'-bipyridine

BODIPY - Boron dipyrromethane

CHO – Chinese Hamster Ovary

CLSM – Confocal laser scanning microscopy

CPP – Cell-penetrating peptide

CTAB - Cetrimonium bromide

DMSO – Di-methyl Sulfoxide

DNA – Deoxyribonucleic acid

Dppz - dipyridophenazine

ER – Endoplasmic reticulum

FCCP - Carbonylcyanide-4-(trifluoromethoxy)-phenylhydrazone

FD-FLIM – Frequency domain – fluorescent lifetime imaging microscopy

FLIM - fluorescent lifetime imaging microscopy

FRET – Fluorescence Resonance Energy Transfer

GFP – Green fluorescent protein

GLUT – Glucose transporters

HBSS – Hank's balanced salt solution

HeLa – Human cervical cancer cell

Hep2 – Human cervical cell line

HIV - human immunodeficiency virus

HTP – High throughput

$IC_{50}$ - Concentration at which exhibits 50% cell population death

$icO_2$ – Intracellular oxygen

ICS – Inter-system crossing

Ir – Iridium

MC – Metal centred

MCF-7 – Breast cancer cell line

MEF – Mouse embryonic fibroblast cells

MLCT – Metal-to-ligand charge transfer

MPP – Mitochondria penetrating peptide

mtDNA – Mitochondrial deoxyribonucleic acid

MTT – Cell viability assay

NA – Numerical aperture

NAD - Nicotinamide adenine dinucleotide

NIR – Near infra red

NLS – Nuclear localising sequence

NPC – Nuclear pore complex

Os - Osmium

Pd – Palladium

PDL – Photo diode laser

PDT – Photo-dynamic therapy

PEBBLE - Photonic explorer for bioanalysis with biologically localized embedding

PEG – Poly-ethylene glycol

Phen - 1,10-phenanthroline

Pic - 4-Carboxylphenyl)imidazo[4,5-f][1,10]phenanthroline)

PLIM – Phosphorescent lifetime imaging microscopy

PMT – Photomultiplier tube

Pt - Platinum

PTM – Post-translational modifications

Re - Rhenium

RGB – Red green blue

ROS – Reactive oxygen species

Ru – Ruthenium

SD – Standard deviation

SP2 – Mouse myeloma cell

STED – Stimulated emission depletion

TAT – Transactivator of transcription

TCSPC – Time correlated single photon counting

TCSPC-FLIM - Time correlated single photon counting – fluorescent lifetime imaging microscopy

TD-FLIM – Time-domain fluorescent lifetime imaging microscopy

TOM – Translocase outer membrane

UV – Ultra violet

UV/Vis – Ultra-violet/Visible

**List of Amino Acids**

**A -** Alanine (Ala)

**C -** Cysteine (Cys)

**D -** Aspartic Acid (Asp)

**E -** Glutamic Acid (Glu)

**F -** Phenylalanine (Phe)

**G -** Glycine (Gly)

**H -** Histidine (His)

**I -** Isoleucine (Ile)

**K -** Lysine (Lys)

**L -** Leucine (Leu)

**M -** Methionine (Met)

**N -** Asparagine (Asn)

**P -** Proline (Pro)

**Q -** Glutamine (Gln)

**R -** Arginine (Arg)

**S -** Serine (Ser)

**T -** Threonine (Thr)

**V -** Valine (Val)

**W -** Tryptophan (Trp)

**Y -** Tyrosine (Tyr)

# Abstract


## The Application of Ru(II) Polypyridyl Complexes to Cellular Imaging and Sensing

### Aisling Byrne

Fluorescent microscopy is the key bio-imaging tool that is used to study live cells. Luminescent transition metal complex have been explored extensively for many years across a range of applications from solar energy to molecular therapeutics, but it is only over the last decade that they have been seriously considered as cellular imaging probes. Their unique photophysical properties including large Stokes shift, red emission wavelengths, good photostability, and sensitivity to molecular oxygen mean they are more than just contrast agents, making them invaluable in diagnostics and theranostics. A key aim of this thesis was to drive forward the demonstrated applications of luminescent Ru(II) and Os(II) probes conjugated to cell penetrating peptides in cellular imaging and sensing using confocal microscopy, and the relatively new phenomenon of super resolution microscopy, specifically, STimulated Emission Depletion (STED) microscopy.

Chapter 1 overviews the general photophysical and optical of ruthenium and osmium polypyridyl complexes, examining the current status of their application in live cellular imaging and sensing. Microscopy techniques such as confocal laser scanning microscopy, stimulated emission depletion (STED) microscopy and fluorescence lifetime imaging microscopy (FLIM) are discussed and how they are used alongside luminescent probes for cellular sensing.

Despite its NIR emission and high photostability Os(II) complexes have not been reported as general imaging probes before this report. Chapter 2 describes a novel Os(II) complex conjugated to the octa-arginine ($R_8$) cell-penetrating peptide sequence as a cellular imaging probe, and compares it to its Ru(II) analogue. The photophysical properties of $[Os(bpy)_2(pic\text{-}arg_8)]^{10+}$ and $[Ru(bpy)_2(pic\text{-}arg_8)]^{10+}$ are examined and compared, as well as its ability to be taken up by live CHO and Sp2 cells, examined by confocal microscopy.

Chapter 3 outlines a novel Ru(II) oxygen sensing probe, conjugated to the mitochondrial localising peptide sequence FrFkFrFk, in order to direct the complex to the mitochondria of live HeLa cells using confocal microscopy to confirm location. Fluorescent lifetime imaging microscopy (FLIM) allowed $[(Ru(bpy)_2phen\text{-}Ar)_2\text{-}FrFKFrFK]^{7+}$ to measure oxygen concentrations and reactive oxygen species (ROS) from within the mitochondria of live HeLa cells.

Chapter 4 focuses on ratiometric oxygen sensing in live cells. Here, two probes are examined – a ratiometric molecule and a ratiometric core-shell nanoparticle. In both cases, the oxygen-sensitive probe consists of a Ru(II) complex, while the oxygen-insensitive reference probe is a BODIPY complex.

Finally, Chapter 5 describes the application of Ru(II) probes to STimulated Emission Depletion (STED) microscopy. Here, signal peptides conjugated to two novel Ru(II) probes directs them to the endoplasmic reticulum (ER) and nucleus of HeLa cells. The probes performance under confocal microscopy and STED is compared in the improved image resolution achieved as well as their photostability under the intense STED

depletion laser. High resolution images of the ER and nuclear DNA during the stages of mitosis are captured using STED microscopy.

# Chapter 1 - Introduction

Fluorescent probes are a crucial part of a biologists imaging toolbox which allows biologists to visualise subcellular components in vivo, both structurally and functionally. The observation of many biological processes relies on the ability to identify and locate subcellular contrasted against complex environments. The recent dramatic evolution of microscopy, in particular the development of super-resolution microscopes means that the demands for new imaging probes, with improved features such as photostability and sensitivity to the environment for multi-modal imaging has grown dramatically. Traditionally, all probes used for imaging and theranostic purposes haven been based on organic dyes. Organic fluorophores have short-lived excited state lifetimes, <10 ns, and susceptible to photobleaching when used under laser scanning microscopy. Their short-lived lifetime's means they are unable to monitor long lived bimolecular processes such as oxygen sensing, limiting their uses as cell imaging probes. Still today all but a few of the commercial probes available are based on organic molecules.

Luminescent transition metal complexes such as those of Ru, Os and Ir are potentially of great interest to the area of bio photonics and theranostics, but are only starting to be seen as real alternatives to the organic probes. Transition metal complexes possess unique photophysical properties which can be exploited in the design of diagnostic and imaging probes.[1] They have versatile chemistries which permit their optical tuning so that they emit in the red, away from the biological window. Their large Stokes shifts avoids self-quenching, and allows for such probes to be used in a variety of sensing techniques, such as resonance Raman, to which organic probes are unsuited. Their long luminescent lifetimes makes them ideal for environmental sensing in cells, such as measuring oxygen concentration, making them more than just contrast agents. They can be highly photostable, which is an important factor for imaging in order to avoid photobleaching. The transition metals that have been extensively applied as luminescent cellular imaging probes include Ru(II), Ir(III), and less commonly Re(I). Surprisingly, until this report, Os(II) complexes had not been explored as general imaging probes, only as anti-cancer agents. The long lifetimes and environmental sensitivity of these complexes makes them very attractive in combining therapeutics with detection methods in regards to cell imaging techniques. The focus of this thesis will be to examine the application of novel luminescent complexes in sensing and imaging in live cells.

## 1.1 Principles of Photophysics

When a molecule absorbs a photon of light, it becomes excited, typically from its ground state ($S_0$) to a higher energy state. The excited molecule is generally unstable and will seek to relax back to its ground state through a range of deactivation pathways. Figure 1.1 shows the Jablonski diagram which illustrates the photophysical deactivation processes through which the molecule can lose its excess energy when returning back to its ground state. Luminescence is a radiative form of emission, and occurs as either fluorescence or phosphorescence, depending on the excited molecule.

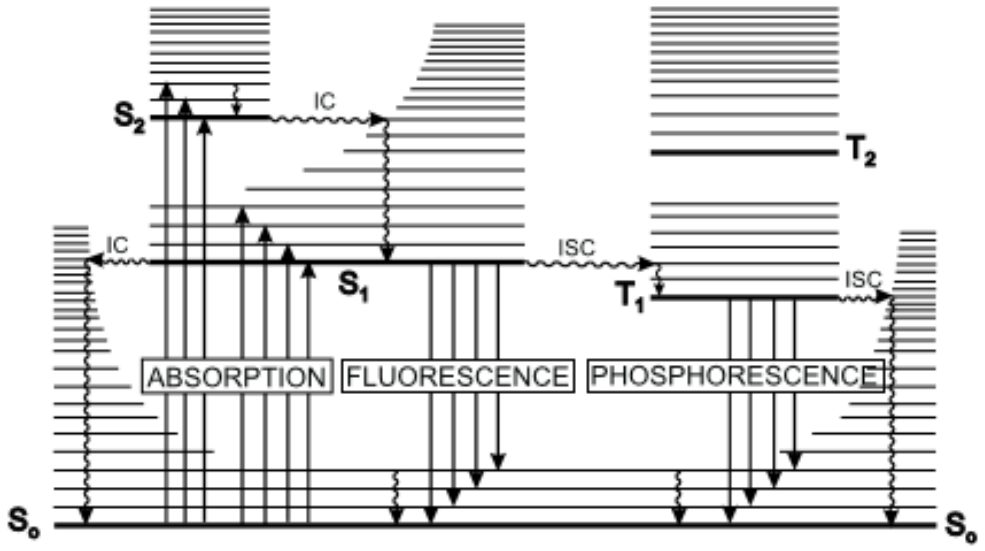


**Figure 1.1** Jablonski diagram illustrating the absorption and deactivation processes following excitation by a photon of light.[2]

Fluorescence is observed when the excited photon emits from the lowest vibrational state of the first excited state to ground state of the same multiplicity. From Figure 1.1 its shows the situation for most organic fluorophores wherein fluorescence occurs as the molecule deactivates from the first singlet excited state to the ground state, $S_1 \rightarrow S_0$. The fluorescent lifetime of this emission is very short, of the order of $10^{-9}$ s.

Phosphorescence is observed when the excited molecule emits a photon emits as it deactivates between energy states of different multiplicities, typically from a triplet state $T_1$, back to ground state, $S_0$. When absorption occurs, the molecule becomes excited, $S_0 \rightarrow S_1$. The molecule undergoes intersystem crossing (ISC), i.e. from a singlet excited state to a triplet excited state, $S_1 \rightarrow T_1$. The deactivation process $T_1 \rightarrow S_0$ is called phosphorescence. Crossing between different multiplicities like this is, in principle, forbidden and typically phosphorescence can only be observed in organic fluorophores under conditions of very low temperature, if at all. However, spin-orbit coupling within molecules that contain heavy atoms can lead to lifting of the selection rule allowing phosphorescence to be observed at room temperature. This forbidden nature of the phosphorescence transition leads to slow emission decay rates, and as a result the molecule has a long phosphorescent lifetime, of the order of $10^{-3} – 10^{-1}$ s. This is a typical deactivation process of transition metal complexes who possess heavy atoms.

### 1.1.1 Luminescent Lifetime (τ) and Quantum Yield (φ)

The luminescent lifetime and quantum yield are two key characteristics that reflect the intensity of emission from a luminophore as they quantitatively assess the emission efficiency. Both can be affected by external factors such as the solvent, oxygen, pH and temperature.

The quantum yield (φ) describes the number of photons emitted compared to the number of photons absorbed. Luminophores with the highest quantum yields display the brightest emission. The quantum yield can be determined by the emissive rate of the luminophore (Γ) and its rate of non-radiative decay to ground state ($k_{nr}$). Equation 1.1 reflects the fraction of luminophores that decay through emission:

$$\Phi_f = \frac{k_{nr}}{k_r + k_{nr}} \quad \text{..... Equation 1.1}$$

Where $k_r$ is the rate of luminescence. The lifetime of the excited state of a molecule (τ) is defined as the average time the molecule spends in the excited state prior to relaxation to the ground state. It is defined as the average time taken for the luminescence intensity

to decay following excitation to $1/e^{th}$ of its initial intensity. Equation 1.2 shows the luminescent lifetime of a molecule:

$$\tau = \frac{1}{k_r + k_{nr}} \quad \text{.....Equation 1.2}$$

Few molecules emit their photons at precisely $t = \tau_n$. The luminescent lifetime of a luminophore in the absence of non-radiative processes is called the natural lifetime, $\tau_n$, which is shown in Equation 1.3:

$$\tau_n = \frac{1}{\Gamma} \quad \text{..... Equation 1.3}$$

Where $\Gamma$ is the emissive decay rate of the luminophore. $\tau_n$ can also be calculated using the quantum yield, shown in Equation 1.4:

$$\tau_n = \frac{\tau}{\Phi} \quad \text{..... Equation 1.4}$$

Where the natural lifetime is a function of the measure lifetime $\tau$ and the quantum yield $\Phi$.

### 1.1.2 Properties for Ideal Imaging Probes

Luminescent metal complexes are increasingly being used as multi-modal imaging probes. To date, polypyridyl complexes of transition-metals such as Ruthenium, Iridium, and to a lesser extent Rhenium and Osmium have been exploited for cell imaging applications. Their advantages include a large Stokes shift, which helps avoid self-quenching occurring. Synthetically tuneable emission which easily enables red emission in the near IR region exploiting the optical window. As they are in a triplet state ($^3$MLCT) they possess long phosphorescent lifetimes. This is useful as it means their

emission can be differentiated easily from sample auto-fluorescence on the basis of lifetime. Auto-fluorescence occurs from naturally fluorescent molecules in the cell, found in the cell medium and tissues such as nicotinamide adenine dinucleotide (NAD), melanin, riboflavin, and aromatic residues in proteins.[3] Their emission occurs in the blue end of the visible spectrum, and lifetimes for such emissions, as they originate from fluorescence, are typically in the range of less than 10 ns. For this reason, luminescent complexes that possess a red to NIR emission with long lifetimes are preferable as biological probes.

The photostability of a metal complex is important when they are being considered as an imaging probe as all fluorophores undergo photo-bleaching upon illumination, but extending the period for which it can be irradiated before bleaching or decomposition is the key. A longer emissive lifetime makes the complex more sensitive to its surrounding environment as it has more time for interactions to occur, such as with molecular oxygen, producing singlet $O_2$, to measure $O_2$ levels, pH, and for diffusion of analytes during the excited lifetime. Good cell permeabilisation is also an important feature. In recent years metal complexes have been made cell permeable, and have also been directed to specific targeted cellular locations by use of peptide, without which they could not cross the cell membrane, which will be discussed *in section 1.5*. A successful metal complex for cell imaging should also be bio-compatible. It should be non-toxic, quantitative, remain stable over long periods of time in vivo and not interfere with normal cell function.[4]

## 1.2 Photophysical properties of Ruthenium (II) Polypyridyl Complexes

Ruthenium is a rare transition metal and, as with all $d^8$ transition metals, Ruthenium can exist in a number of oxidative states, of which only it's oxidation state (II) forms luminescent complexes, making it a $d^6$ transition metal. The photophysical properties of $[Ru(bpy)_3]^{2+}$, the first such luminescent complex reported, has been detailed extensively.[5-7] Figure 1.2 shows an energy level diagram of the excited state of $[Ru(bpy)_3]^{2+}$ (A) and its photophysical properties (B). The multiplicity of the excited states may be singlet or triplet. Upon excitation, the metal centre undergoes absorption, leading to population of the first singlet $^1$MLCT state. Because of the heavy metal, spin orbit couple enables intersystem crossing (ISC) to occur co resulting in the formation of

a triplet $^3$MLCT excited state in Ru(II) complexes from where the complex emits through phosphorescence, and thus, recovery of the ground state of the molecule.

The absorbance spectrum of $[Ru(bpy)_3]^{2+}$ shows a metal-to-ligand (d-π*) transition at 451 nm. A strong absorbance at 286 nm attributed to the π-π* transitions within the bpy ligands, and when excited into the MLCT at 451 nm, $[Ru(bpy)_3]^{2+}$ has an emission maxima centered around 611 nm. In aerated aqueous solution it has a quantum yield of 0.028 and exhibits a long luminescent lifetime of 650 ns.[8]

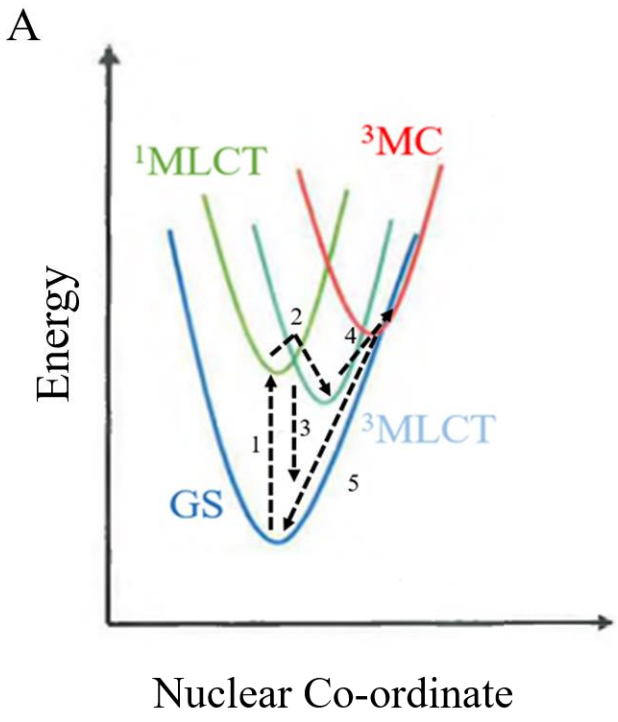

B

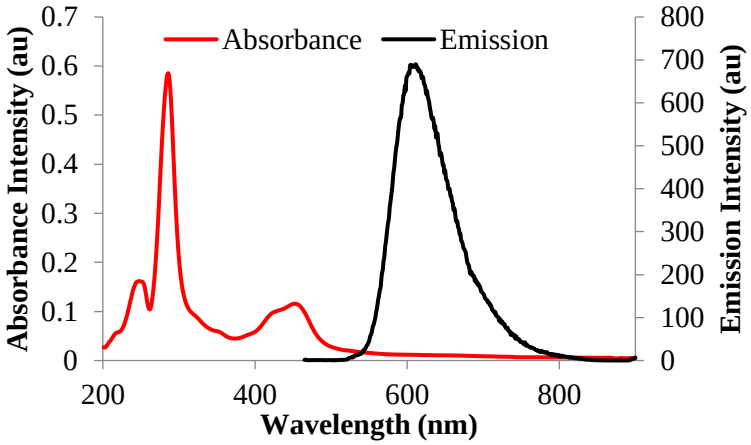


**Figure 1.2** (A) Energy level diagram for a $d^6$ transition metal-ligand complex. Excited state processes: 1) absorption of light with excitation from ground state (GS) to the $^1$MLCT state, 2) ISC to the $^3$MLCT, 3) relaxation to GS from $^3$MLCT, 4) Thermal population of the $^3$MC state, 5) deactivation of the $^3$MC state to the ground state.[5] (B) Typical spectroscopy of $[Ru(bpy)_3]^{2+}$ at 50 μM in PBS solution showing the absorbance and emission profile.

Ru(II) polypyridyl complexes have been extensively examined as sensing and bio-imaging tools in recent years due to their unique and desirable photo-physical properties. Its large Stokes shift avoids self-quenching, and its long phosphorescent lifetimes, in the 100s of ns to microseconds, makes Ru(II) complexes sensitive to local environment, particularly to molecular oxygen. These properties can be tuned with the manipulation of the coordinating ligands. Figure 1.3 shows the more widely used polypyridyl ligands, such as 2,2'-bipyridine (bpy), 1,10-phenanthroline (phen), dipyridophenazine (dppz), and 2-(4-Carboxylphenyl)imidazo[4,5-f][1,10]phenanthroline) (pic). Typically, Ru(II) complexes follow the configuration $[Ru(L\text{-}L)_2(A\text{-}A)]^{2+}$ where LL is a polypyridyl bpy or phen derivative, and AA is a heteroligand. Alterations of the ligands near the luminescent core can selectively tune the photophysical properties. For example, to allow absorption over a wider range of the visible spectrum or introduce pH sensitivity to the photophysics.

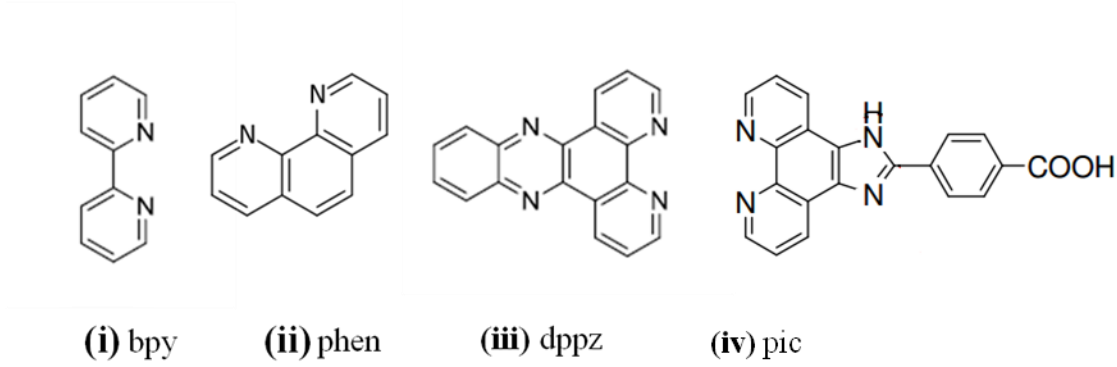


**Figure 1.3** Polypyridyl ligands used in designing novel metal-ligand complexes

Modification of ligands coordinated to the Ru(II) centre not only alters the photophysical properties of the complex, but can render the complex more selective towards a specific target. [9] For example, the $[Ru(bpy)_2(dppz)]^{2+}$ complex exhibits strong affinity for DNA. Crucially, it has been shown to be a 'light-switch for DNA', displaying virtually no luminescence in aqueous solution but exhibiting moderately intense, long lived luminescence upon intercalation between the base pairs of the duplex. The effect is attributed to the protection of the phenazine nitrogen on the dppz ligand from hydrogen bonding once the planar aromatic ligand is incorporated into the π-stack of the DNA helix. The group of *Barton et al* have done extensive work demonstrating the light-switch effect.[10-12] The most studied of the molecular light switches is $[Ru(phen)_2(dppz)]^{2+}$. As for the bpy analogue, in aqueous solution it shows no emission, but luminesces brightly when intercalated with DNA. This complex has been the focus of the work by *Turro et al*, where they have looked at the quenching of $[Ru(phen)_2(dppz)]^{2+}$ when bound to DNA,[13] and have used resonance Raman to show that DNA intercalates with the dppz ligand of the complex.[14]

Ionizable ligands can also be introduced into metal complexes to induce pH sensitivity. For example Ru(II) complexes have been combined with ionisable ligands such as 2-(4-Carboxylphenyl)imidazo[4,5-f][1,10]phenanthroline) (pic) ligand, where $[Ru(L\text{-}L)_2(pic)]$.The ligand has 2 ionisable protons located on the imidazole ring, rendering it pH sensitive. [15]

However, even with the many alternative choices of ligands, most Ru(II) and related metal complexes do not readily cross the cell membrane. This has meant that in spite of their photophysical advantages, they had not until recently been explored widely in cell

imaging. Various methods have been examined for improving the uptake of metal complexes in cells, such as the use of PEGylation, liposomes, nanoparticles, and conjugation of cell penetrating peptides, which will be discussed in detail in *section 1.4*. Many have forgone attempting to make the complex permeable and have used solvents or detergents to permeablize the membrane. This is far from ideal as such complexes cannot be said to be permeable and permeabilization can irreversibly change the cell membrane. This thesis will focus on the application of cell-penetrating peptides as vectors to carry the complex across the membrane and also to target it to cellular organelles.

## 1.3 Osmium (II) complexes

Until recently, Ru(II), Ir(III), and to a less extent Re(I), have been the main focus as bio imaging luminescent complexes. However, as described in this thesis, osmium (II) complexes are a possible alternative, although until this report they had not been explored for cell imaging. Os(II) polypyridyl complexes have many of the same photo physical properties of the above mentioned transition metals, with some notable differences due to the atomic mass of the Osmium . Figure 1.4 describes the excited state of $[Os(bpy)_3]^{2+}$.[16]

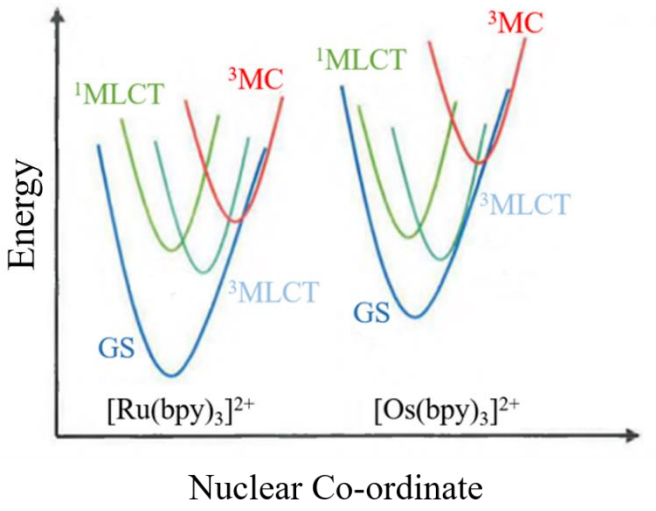


**Figure 1.4** Excited state of $[Os(bpy)_3]^{2+}$ showing the singlet ($^1$MLCT) and triplet ($^3$MLCT) transitions at a higher energy level than $[Ru(bpy)_3]^{2+}$.[16]

Because of its large nuclear mass, Os (II) has a stronger spin-orbit coupling than Ru(II). When excited into the $^{1}$MLCT between 400 and 500 nm it emits from a triplet state ($^{3}$MLCT). Unlike ruthenium, Os(II) can be excited directly into its triplet $^{3}$MLCT through an absorbance at around 550 nm. However, its excited state is not generally as long lived as ruthenium. The main advantage of using Os(II) is that its emission maxima is red shifted compared to analogous Ru(II) complexes and its emission can be more readily tuned to the NIR region using coordinating ligands. For example, $[Os(bpy)_3]^{2+}$ has an emission centred around 710 nm, which is well outside the auto-fluorescent window. A significant advantage osmium has over ruthenium is that osmium has outstanding photostability, as there is no possibility for thermal cross over from its triplet excited state to the destructive metal centred state that is much lower lying in energy for analogous Ruthenium complexes. Figure 1.4 compares the energy level diagrams of $[Ru(bpy)_3]^{2+}$ and $[Os(bpy)_3]^{2+}$. In ruthenium, thermally activated crossover to a metal centred state ($^{3}$MC) leads to the destruction of the M-L bond and to a sharp decrease in the luminescent lifetime with increasing temperature. The $^{3}$MC state of Osmium, on the other hand, cannot be thermally populated as it is far better separated from the $^{3}$MLCT state of the complex well above $k_T$ higher energy, shown in Figure 1.4, making osmium more photostable than ruthenium.[17] This ensures there are no changes in emission intensity or lifetime and no photo-bleaching during cell imaging at 37°C.[18] Until now, there have been no reports of Os(II) complexes applied as imaging probes. Although Os(II) arene complexes have be explored as anti-cancer agents. The group of *Sadler et al* have extensively studied Os(II) arene complexes.[19-22] Their most recent report focuses on the Os(II) arene complex $[Os(\eta^6\text{-p-cym})(NMe2\text{-azpy})I]PF_6$, shown in Figure 1.5, that can induce ROS production in cells.[23] This highly toxic, highly active complex exhibits higher anti-proliferative activity compared to cisplatin in ovarian cancer cells, with an average $GI_{50}$ of 0.75 μM compared to 36.7 μM for cisplatin, where $GI_{50}$ is the concentration of complex which inhibits the growth of 50 % of cells.

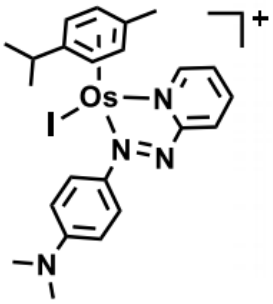


**Figure 1.5** Chemical **s**tructure of the osmium arene complex [Os($\eta^6$-p-cym)(NMe2-azpy)I]$PF_6$.[23]

Chapter 2 examines a novel Os(II) complex and compares its properties and cell compatibility to that of an equivalent Ru(II) complex, to assess if Os(II) can be used as an alternative imaging probe to the much explored ruthenium.

## 1.4 Transport across the cell membrane

Transition metal complexes such as the polypyridyl complexes of Ruthenium and Osmium cannot pass freely across the lipid bilayer of live cells due to their polarity and charge. The inclusion of low concentrations (e.g. 1 to 5 % V/V) of organic solvent such as DMSO or detergents like Triton X in the dye incubation medium have been used to increase the uptake of transition metal complexes by permeablising the membrane. However, the solvent or detergent affects the packing of the cell membrane, making the lipid bilayer more permeable. Electroporation is also method can also be used to get complexes to cross the cell membrane. However, none of these methods are ideal as not only do they damage the cell, the complexes cannot be said to be cell permeable, and they are therefore not extendible to tissue samples.[24] In an attempt to render metal complexes cell permeable, cell-penetrating peptide (CPP) sequences have been used to exploit their cargo carrying ability,[25-27] or polymers such as poly(ethylene glycol) (PEG),[28,29] as well as structurally altering the complex using hydrophobic ligands such as 1, 10-phenanthroline,[30] or lipophilic pendants such as estradiol.[31] A balance of lipophilicity, charge and solubility is key to designing a successful imaging probe that is capable to cross the cell membrane.

Quantitative Structure Activity Relations (QSARs) modelling is used to try and predict the influences of probe chemistry on cell uptake and localisation. [31] QSARs analysis looks at the relevant physiochemical properties of a probe that can be modelled using parameters such as log P or the overall charge of the probe, and what influences such properties have on the cell. There are many physiochemical properties that can influence a probe to be taken up by the cell, such as its charge, and where it will localise, such as the log P value, structural ligands used in the probes design, and the use of CPPs and sugars to promote uptake. For example, lipophilic probes tend to localise in the mitochondria while cationic probes migrate towards the nuclei of live cells. [32,33] QSAR models were initially developed by observing a series of dyes and their interactions with live cells. Properties such as amphiphilicity index (AI), electric charge (Z), width and length (W & L), and head group size and hydrophilicity (HGH & HGS) of the dyes were examined in order to establish a modelling system. [34] These modelling systems were then used to predict the uptake and accumulating patterns of the dyes. The benefits of such models allows for a more critical understanding of current fluorescent probes, and to help in the design of novel probes and assess their behaviour with live cells. These methods will be discussed in this section. [35]

### 1.4.1 Mechanisms of Membrane Translocation

In order to design new fluorescent imaging probes and direct them across the cell membrane, the mechanisms in which the cell allows foreign structures to cross its membrane must be understood. Entry into the cell can be energy-dependent uptake such as active transport or endocytosis, or energy-independent uptake which includes passive and facilitated active diffusion.[36] The mechanism can direct localization of the complex, and can differ between varying cell lines.

Figure 1.6 illustrates the key methods of transport across the cell membrane. Passive and facilitated diffusion are both energy-independent methods. Passive diffusion occurs due to concentration gradients which transport molecules across the lipid bilayer. Passive diffusion is the ideal method of uptake as it has the broadest range of applications and is non-selective. The pharmaceutical industry tries to exploit such mechanisms in drug delivery. For example, animal cell membranes have a potential of -50 to -70 mV.[37] Therefore the uptake of a complex with a positive charge can be driven by membrane potential, provided that the molecule is sufficiently lipophilic to enable it to migrate

across the hydrophobic core of the membrane. This has been explored by Barton and group. They demonstrate the importance of complex charge and lipophilicity to cellular uptake. Here they incubated HeLa cells with $[Ru(DIP)_2(dppz)]^{2+}$ in either HBSS with valinomycin to hyperpolarize the cells, or with K+-HBSS to depolarize the cells. Following incubation the uptake was examined using flow cytometry, and it was found that hyperpolarization promoted uptake of $[Ru(DIP)_2(dppz)]^{2+}$ while depolarization decreased the uptake.[38] Facilitated diffusion involves the transport of the molecule of interest via membrane-bound ion channels or pores, and membrane transport proteins. Glucose, potassium and sodium ions all pass freely using these methods. [39]

Active transport and endocytosis are energy-dependent processes. Active transport involves the participation of proteins such as ATPases which act to bring the molecule into the cell. In order for this to occur, ATPases break down ATP to ADP, releasing a phosphate ion. This reaction releases energy, and this energy is used to bring molecules in and out of the cell, as well as for other cellular functions. Therefore, the cell uses energy in the form of ATP to transport molecules from the cell surface across the membrane upon recognition.

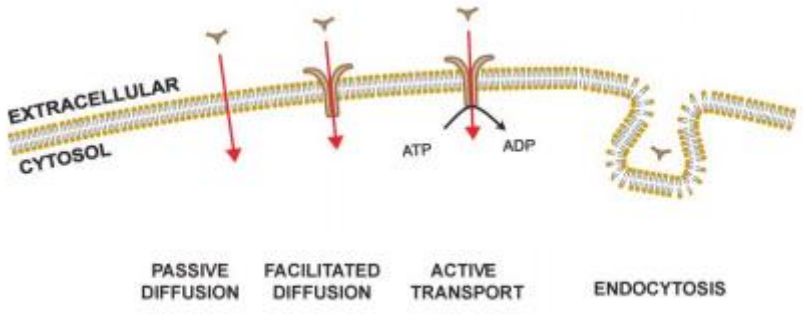


**Figure 1.6** Mechanisms of transport across the cell membrane. Molecules can via passive diffusion, or facilitated diffusion using cell surface carrier proteins. The process of active transport uses energy in the form of ATP to direct the molecules into the cell. Endocytosis brings molecules across by forming vesicles around the molecule to carry it across the membrane.[39]

Endocytosis is a process by which the cell ingests the molecule to bring it into the cell. The plasma membrane is thought to engulf the molecule, forming a vesicle which is carried across the cell membrane and is released once inside the cell. Molecules must reside near the membrane, or directly interact with membrane proteins to enable

endocytosis to occur. Endocytosis is a method of uptake that CPPs can typically exploit by selectively targeting specific cell surface receptors so that molecules will only enter a cell of interest. This is highly advantageous in the design of therapeutic agents for targeting specific diseased states such as apoptosis, cell-proliferation and diabetes.[40,41] For example, the folate receptor on cancer cells is a useful target for tumor specific drug delivery.[42] Human cancer cells show an up-regulation of folate receptors on the cell surface and these increased over the stages in malignancy. Therefore, conjugating macromolecules to folic acid enhances the delivery of the drug to folate-receptor expressing cancer cells rather than normal healthy cells, and enters the cells via receptor-mediated endocytosis.

Studying the temperature dependence of uptake can yield insight into the mechanism of uptake, as it reflects if uptake is energy dependent or independent. At 4 °C all metabolic pathways in the cell are switched off. Therefore all active endocytosis is inhibited and the cell cannot take up the molecule if it is transported actively.

### 1.4.2 Lipophilicity

Lipophilicity is a key physiochemical property that is related to the permeability to biological membranes. It determines absorption, distribution, and toxicity of a complex within a cell.[43,44] The lipophilicity is determined as partition coefficients (log P), which describes the partition equilibrium of an un-ionized solute between water and an immiscible organic solvent. The larger the log P value the greater the lipophilicity. There have been many reports on the importance of lipophilicity in transition metal uptake in live cells and their toxicity.[29,45-47] *Lv et al* reported on a series of Ru(II)-N-hetercyclic carbenes with different alkyl side groups, shown in Figure 1.7, 1-5. The lipophilicity of the 5 compounds were measured, and increased in the following order 2<1<3<4<5. They found that when introduced to live cells that the cytotoxicity of the compounds increased with increasing lipophilicity.[46]

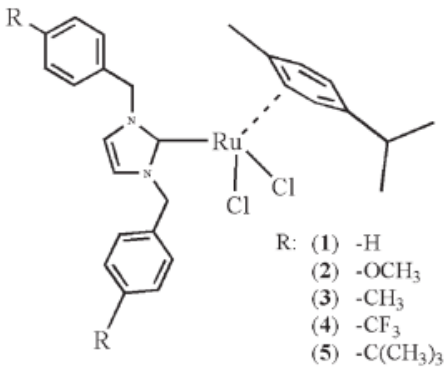


**Figure 1.7** Structure of a series of Ru(II)-N-hetercyclic carbenes and the different side alkyl groups 1-5.[46]

However, it could be argued that in changing the side groups the complex is becoming more toxic rather than the toxicity being a result of the lipophilicity. An example of this can be seen in a report from *Lo et al*. Here they looked at a series of Ir(III) cyclometalated complexes who differed in their ligands. In this case, the lipophilicity and toxicity were not linearly related shown in Figure 1.8. As the lipophilicity increased, the $IC_{50}$ values did not change accordingly as may have been expected, suggesting that, in this case, it is in fact the ligands that are inducing the toxicity and not the lipophilicity.[45]

| **Complex** | **Log *P*** | **$IC_{50}$** |
|---|---|---|
| **2b** | 1.40 | 1.80 ± 0.18 |
| **2a** | 1.46 | >230 |
| **1b** | 2.30 | 5.87 ± 1.81 |
| **4b** | 2.37 | 7.06 ± 1.09 |
| **1a** | 2.44 | 1.40 ± 0.07 |
| **4a** | 2.48 | 29.6 ± 6.94 |
| **3b** | 2.53 | 12.0 ± 1.30c |
| **3a** | 2.56 | 4.00 ± 0.60c |
| **1c** | 2.59 | 0.10 ± 0.02 |

**Figure 1.8** Log P values and the corresponding $IC_{50}$ values of a series of Ir(III) cyclometalated complexes.

### 1.4.3 Charge

Healthy cells have an internal negative charge i.e. are anionic, as a result of there being more potassium ions inside the cell compared to sodium ions present outside the cell. Therefore imaging probes can be taken up via passive diffusion if they are cationic. Using peptide sequences rich in arginine (R) and lysine (K) give a complex an overall positive charge, making it more attractive for uptake. The overall final charge has been shown to affect where the complex localises. For example, lipophilic cations typically localize to the mitochondria. However, an excess of the molecular charge can hinder the complex from accessing the mitochondria to the due to the hydrophobicity of the organelle.[48,49] The charge of the complex has also been shown to alter the toxicity and localisation of a compound within the cell as demonstrated by *Dickerson et al*.[50,51] Uptake studies in A549 human cells showed that Compound 1, with a charge of +2, entered the lysosome and mitochondria whereas compound 2, with a charge of -4 remained in the cytosol. Viability studies shown in Figure 1.9 demonstrated that Compound 1, with a log P value of 1.8 ± 0.02 μM was highly toxic towards the cells inducing toxicity after 72 h exposure in the dark. In contrast, Compound 2 with a log P value of -2.2 ± 0.12 induced no toxic effects on the cells, shown in Figure 1.9.

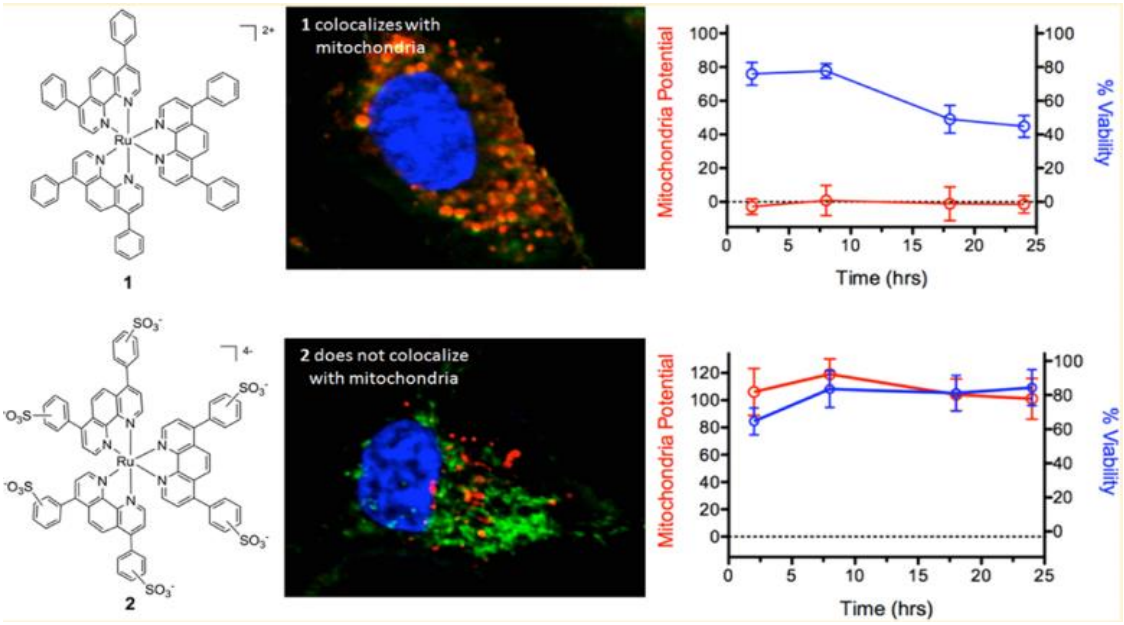


**Figure 1.9** Uptake and viability studies of two analogous ruthenium complexes with differing charge and log P values in A549 human cells. Confocal microscopy showed Compound 1 entered the mitochondria and lysosomes, and was highly toxic towards the cells (top), while Compound 2 remained in the cytosol having no toxic effects on the cells (bottom).[50]

Gupta and co-workers have reported on a series of cyclometalated iridium (III) complexes for cellular imaging where they demonstrated that the cationic nature and hydrogen bonding interactions of Ir (III) contributed to the specific localisation and emission intensity in the endoplasmic reticulum (ER) of MCF7 breast cancer cells, shown in Figure 1.10. [52] Using confocal microscopy they demonstrated that cells treated with complex 1 and 3, which contained –OH groups in position 4' and at 2' and 3' of the appended phenolic ring, localised within the cytoplasm and low fluorescence in the nuclei. In contrast, complex 2, with an –OH group at position 2 of the phenolic ring, showed intense fluorescence in the ER. Under irradiation with 405 nm laser the complex caused extensive photo induced cell death, whereas no toxicity towards cells were observed in the dark. Although highly phototoxic towards cells, they are a useful example of directing imaging probes to specific organelles by means of probe design.

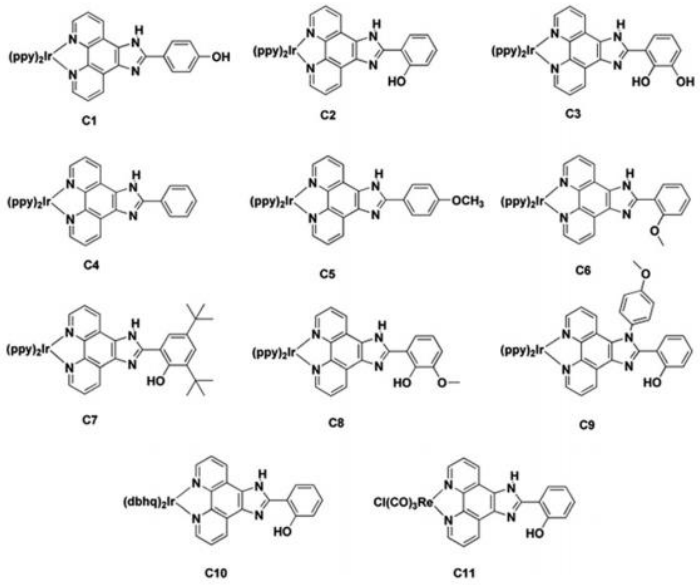


**Figure 1.10** Molecular structures of C1–C11 showing the cyclometalated core and the ancillary ligands. C1–C9 have $[Ir(ppy)_2]^+$ as the cyclometalated core whereas C11 contains $[Re(CO)_3Cl]$ as the metal core.[53]

### 1.4.4 PEGylation

Poly(ethylene glycol) (PEG) is a polymer chain that can be both covalent attached to transition metal complexes to increase their hydrophobicity and improving their solubility. PEG linkers are an attractive means of cell targeting as they have low toxicity towards cells. The reduced toxicity is attributed to the reduced non-selective interaction with DNA, proteins, and organelles.[27] PEG has been both covalently and non-covalently linked to transition metal complexes to increase their hydrophilicity and improving their solubility, water solubility and cell permeability.[54-56] *Lo et al* have done extensive work with PEGylated metal complexes and have examined their effects on cell uptake and imaging.[55,56] Recently they presented a water soluble cyclometaled Ir(III) PEG complex.[57] Uptake studies using confocal microscopy showed the complexes successfully entered HeLa cells and localised in the mitochondrial region of the cell. The complex showed no toxicity towards the cells in the dark but interestingly, exhibited high phototoxicity towards the cells, indicating significant potential as a therapeutic photosensitizer.

### 1.4.5 Sugar Conjugates

Carbohydrate-modified complexes are increasingly being used in cell imaging due to their good biocompatibility, and can serve as new imaging reagents as well as glucose-uptake indicators in live cells. A series of rhenium (I) polypyridine complexes bearing an α-D-glucose have been reported by *Lo et al,* shown in Figure 1.11.[58] Upon incubation with HeLa cells, complex 3 accumulates in the mitochondria. The complexes also exhibited lower toxicity towards the cells than the unconjugated analogues. It is thought that glucose transporters (GLUTs) play an important role in the cellular uptake of these complexes.

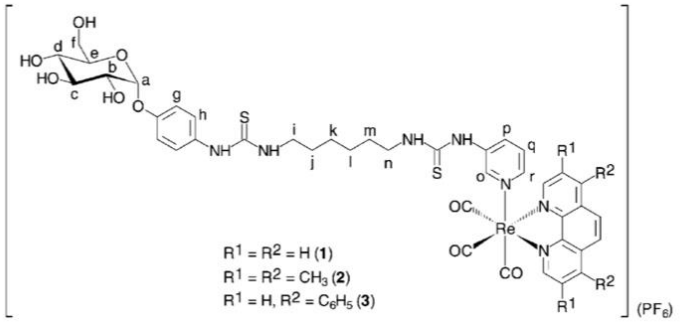


**Figure 1.11** Structure of Re(I) polypyridyl series conjugated to α-D-glucose.[58]

In another report from *Lo et al* they recently demonstrated the effects of lipophilicity on cell uptake and toxicity of a series of phosphorescent iridium (III) complexes.[45] Here they use D-glucose and D-galactose sugar residues to promote cell uptake, where the log P values of the complexes range from 1.4 – 2.59. Complexes 1a-1c, 3a and 3b, and 4a and 4b have significantly higher log P values compared to complexes 2a and 2b, the difference being an extra hydrophobic phenyl ring in the cyclometalating ligands, shown in Figure 1.12. It is noted that the polar sugar entity slightly reduces the log P values compared to the sugar-free complexes. They also demonstrate a difference in cell uptake between the two sugar residues. Focusing on complex 1a, which has a log P value of 2.44, they demonstrate its localisation within the mitochondria of HeLa cells which is a result of its cationic and lipophilic nature. Based on the knowledge that cancerous cells catabolise glucose at a higher rate, these complexes pose as potential cancer imaging agents.

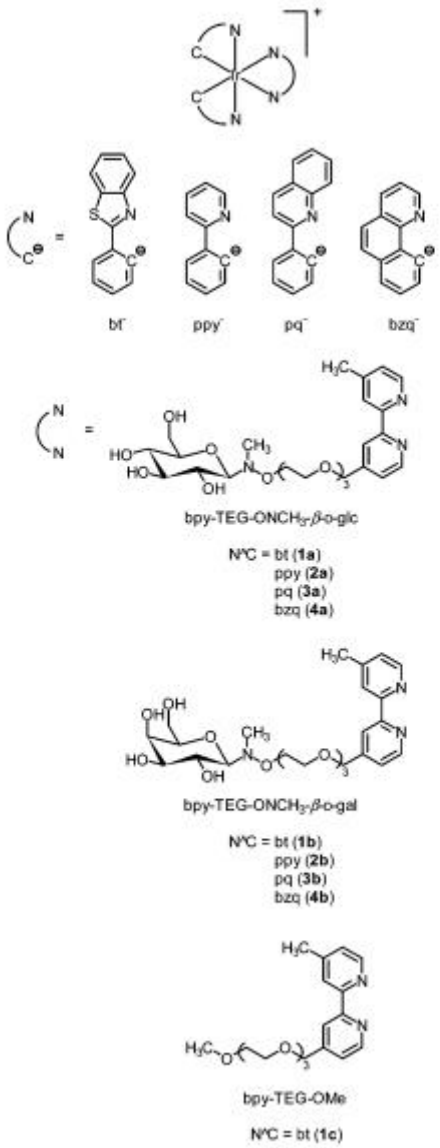


**Figure 1.12** Molecular structure of a series of Ir(III) complexes with D-glucose (1a-4a) and D-galactose sugar residues (1b-4b).[45]

## 1.5 Cell-Penetrating Peptides

Cell-penetrating peptides (CPPs) are short peptide sequences, less than 40 amino acids in length. They function to promote and facilitate cellular uptake of molecules, and can do so at low concentrations. Their primary applications to date has been to transport therapeutic agents across the cell membrane in clinical applications as well as for imaging probes.[41,59]

CPPs are positively charged, with sequences usually containing high loadings of lysine (K) and arginine (R) residues.[35] The first and most widely studied CPP is that of the

human immunodeficiency virus type-1 (HIV-1) TAT peptide. Its high lysine/arginine content renders it successful in permeablizing the cell membrane, and it is this that many CPPs are based on.[60] To date, there has not been many reports using CPPs to direct metal complexes. However within the few reports, CPPs have successfully been shown to be directed and accumulate within the mitochondria[61-63] and nucleus.[64,65] which will be discussed in more detail later on in *section 1.6.*

Polyarginines are CPPs that are useful carriers of membrane impermeable molecules. Positively charged arginine sequences, $Arg_n$, where n ranges from 5-11 residues in length have been examined.[66,67] The polyarginine sequence binds strongly to the phosphate groups on the phospholipid bilayer of the cell membrane. This interaction forms a pore in the membrane which allows the peptide to cross the cell membrane. Once they enter the cell they exhibit non-specific binding, and have been shown to enter the lysosomes and endosomes.[68] Octa-arginine ($Arg_8$) peptide sequences have been found to have optimum penetration abilities whereas sequences below $Arg_6$ are relatively ineffective.[67,69] For example, *Neugebauer et al* compared uptake of two novel polyarginine complexes Ru-Ahx-$R_5$ and Ru-Ahx-$R_8$ to assess if the number of arginine residues would affect cell uptake. Figure 1.13 describes the structure of the $[Ru(bpy)_2pic\text{-}Arg_n]^{2+}$ complex, where n=5 or 8 arginine residues.

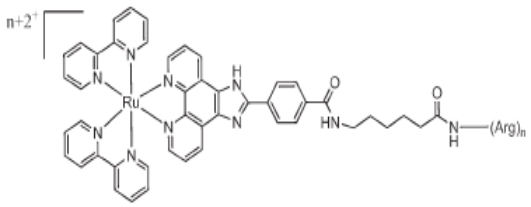


**Figure 1.13** Structure of Ru-Ahx complex with $Arg_n$ = to 5 or 8

Using confocal microscopy, no luminescence was seen from the platelets incubated with Ru-Ahx-$R_5$ (Figure 1.14b). However a strong luminescence was seen from the cells incubated with Ru-Ahx-$R_8$ (Figure 1.14d). Thus, it was concluded that $Arg_5$ has poor cell penetrating abilities, and that it is a chain-length dependent process.

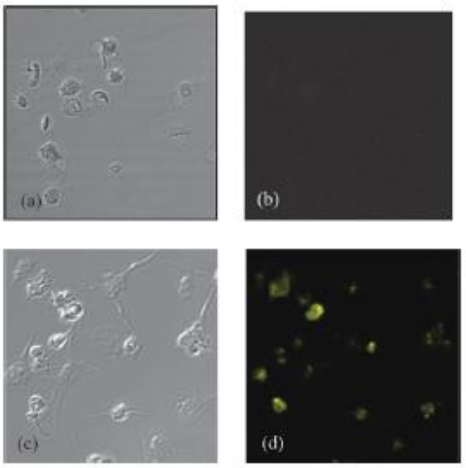


**Figure 1.14** Confocal imaging of the complex in platelet cells. Uptake of Ru-Ahx-$R_5$ (a and b) and Ru-Ahx-$R_8$ (c and d) by human platelet cells[67]

From this work it is evident that polyarginine CPPs, in particular $Arg_8$ chains, are useful in directing metal complexes across a cell membrane. This thesis will use the $Arg_8$ sequence to direct transition metal complexes across the cell membrane. For more precise focusing to target a cell region, a range of peptide sequences have been successful.

## 1.6 Signal peptides

As described, CPPs are used to carry complexes across the cell membrane. Targeting specific cell organelles is challenging but potentially very important in sensing, for example monitoring mitochondrial function. It is has been demonstrated that signal peptides can be exploited for more precise targeting. Signal peptides are based on sequences found in proteins in organelle membranes, for example transcription factors such as NF-κβ. Their recognition within the cells and consequent targeting makes it possible to study and monitor sub-cellular events, and to deliver therapeutics to specific sites. To date, signal peptides have successfully been shown to be directed and accumulate within the mitochondria[62,70] and nucleus.[64,65]

### 1.6.1 Nuclear Localising Signal (NLS) peptides

Many metal complexes are targeted to DNA, for example, [Ru(dppz)$_3$] and related analogues have been widely explored as DNA binders for cell therapy. Therefore gaining entry through the highly restricted nuclear envelope must be achieved for in-cel application of these materials. Nuclear localising signal (NLS) peptides are typically derived from transcription factors and are less than 12 residues in length. They have the ability to cross the cell membrane and enter the nuclear envelope. To date, NLS sequences that have been successfully derived from transcription factors include NF-κB, TCF1-α, TFIIC-β, TFIIE-β, Oct-6 and SV40[71,72], of which NF-κB and SV40 have shown to enter the nucleus selectively.[64,65]

The group of *Ragin et al* have investigated a series of NLS sequence peptides in their abilities to be directed across the cell membrane to the nucleus.[71] Here they examined fluorescently labelled sequences which were derived from various transcription factors. Live uptake studies in MCF-7 breast carcinoma cells showed uptake of all NLS sequences. Confocal microscopy demonstrated that NF-κB peptide sequence localized in the cytoplasm and nuclear regions of the cells (Figure 1.15).

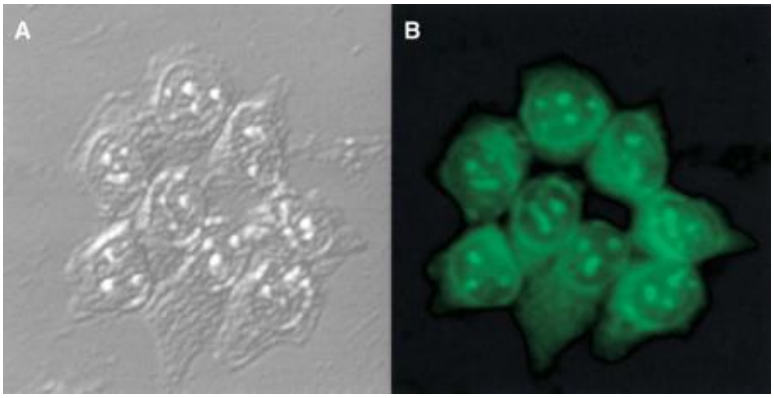


**Figure 1.15** Confocal microscopy of fluorescently labeled NF-κβ in MCF-7 cells showing (A) transmitted light image, and (B) fluorescent light image [71]

However, it was found that TFIIE-β and Oct-6 localized in the cytoplasm only, possibly due to their highly positive charge, showing similar results to that of an $Arg_8$ peptide sequence. This highlights the importance of sequence charge in directing the complex once inside the cell. The mechanism of uptake was evaluated by examining the impact of temperature on uptake. At 4°C, the uptake of NLS sequences NF-κB, TFIIE-β and

HATF-3 were greatly reduced, whereas Oct-6, TCFI-α, SV40 and *C.elegans* SDC3 were unaffected. This demonstrates that the choice of peptide sequence can have significant effects on how a complex crosses the cell membrane as discussed previously.

Of all the NLS sequences investigated by *Ragin et al*, NF-κB was the most effective in promoting transport across nuclear envelope to the nucleus and nucleoli. Following from this result, our group has also successfully demonstrated directing ruthenium complexes conjugated to NF-κβ sequence to the nucleus of CHO cells.[64] It was found that by increasing the lipophilicity of the metal complex by replacing bipyridyl counter ligands with lipophilic diphenylphenanthroline ligands, the complex could be directed to the nucleolus. These results are significant in demonstrating the power of using NLS peptides in directing metal complexes not only through the cell membrane, but through the nuclear envelope too. They open the way to focusing ruthenium complexes directly to nuclear DNA for imaging and therapy, as discussed in Chapter 5.

### 1.6.2 Mitochondria Penetrating Peptides (MPPs)

Mitochondrial penetrating peptides (MPPs) typically consist of 4-8 positively-charged hydrophobic residues.[73] Targeting the mitochondria is of huge importance in imaging and pharmaceutical research, as mitochondria are the engine of the cell. The mitochondria are responsible for the cells energy via ATP synthesis, supplying oxygen to the cell, and regulating apoptosis. Many disease states have been found to involve mitochondrial dysfunction. Therefore, mitochondria targeting peptide sequences are being examined as a means of carrying drugs directly to dysfunctional mitochondria. They are also being conjugated to fluorescent imaging probes in order to monitor and further understand how the mitochondria work in a given disease state.[74] For example, measuring oxygen levels via oxygen probes[75] and ROS production, as discussed in *section 1.8.*[76] To date there has been success in localising molecules within the mitochondria using MPPs.[62,74,77-80] For example, *Horton et al* have looked at various MPP sequences to evaluate the optimal sequence for mitochondria localization.[62] They demonstrated that a sequence of 8-amino acids was most successful in localising in the mitochondria compared to chain lengths with fewer residues. Their optimal sequence also included d-arginine residues (r) to promote cellular stability; FrFKFrFK.

Chapter 3 will focus on the MPP sequence FrFKFrFK in directing a Ru(II) oxygen measuring probe to the mitochondria in order to assess oxygen levels there.

## 1.7 BODIPY-based Fluorescent dyes

The main focus of this work is the $d^6$ transition polypyridyl luminophores. However, in Chapter 4 we exploit BODIPYs as a reference probe. Boron dipyrromethane (BODIPY) compounds are highly fluorescent dyes that are exploited in cell imaging in their own right. The BODIPY dyes comprise of the 4,4-dyfluoro-4-bora-3a,4a-diaza-s-indacene core structure, seen in Figure 1.16. The BODIPY core is the prototype luminophore, from this it exhibits good thermal, chemical and photostability. BODIPY absorbs and emits in the visible region with a narrow absorbance band, shown in Figure 1.17. The advantage of using BODIPY though is their high quantum yield, usually around $\Phi$ = 0.60, but can be as high as 0.90. They have relatively short fluorescent lifetimes, ranging from 0.8-3.5 ns. The disadvantage is that the small Stokes shift and high quantum yield makes the complex prone to self-quenching.

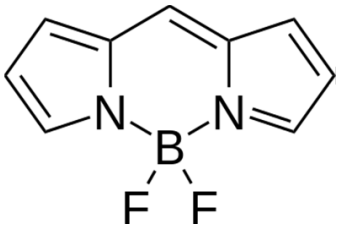


**Figure 1.16** Structure of the BODIPY core.[81]

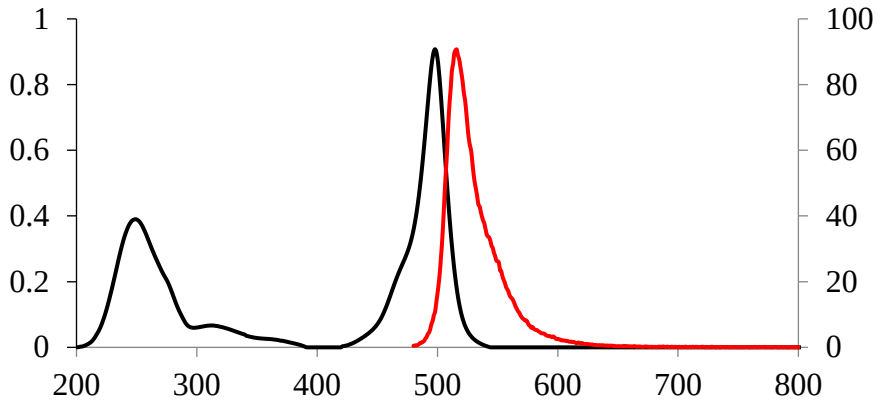


**Figure 1.17** Absorbance and emission spectra of BODIPY parent complex at 15μM in methanol solution, demonstrating the small Stokes shift between the excitation and emission maxima. Slit width = 5 nm.

The spectroscopic properties of BODIPYs can be altered by changing the substituents around the BODIPY core to shift the $\lambda_{max}$ or introduce charge transfer to absorbance, though this can reduce the quantum yield. Emission ranges of 480-700nm have been reported.[81] *Vicente et al* reported on a group of long wavelength red fluorescent 3, 5-diiodo-BODIPY complexes.[82] Their emission maxima's ranged from 576 to 686 nm, with the largest Stokes shift measured to be 23 nm. Uptake and co-localisation studies found that the complexes successfully entered Hep2 cells and located within the endoplasmic reticulum (ER). Our group have successfully developed a mega-Stokes shift BODIPY complex, with a shift of 185 nm and emission maximum of 740 nm.[83] These properties made these BODIPY compounds potentially very attractive as imaging dyes. As described, BODIPYs are widely used as fluorescent labels in bio imaging as their high lipophilicity facilitates them to accumulate in subcellular compartments.[84,85]

BODIPY derivatives have been applied as intracellular sensors. Intracellular pH is an important factor in many physiological processes.[86,87] BODIPY-based dyes have been shown to be useful pH indicators, activating in response to protonation.[88-90] The acidic pH sensitivity is achieved by incorporating a p-(N,N-dialkyl)aniline moiety at the meso-position of the core structure.[91] Here, fluorescence is quenched at a neutral or basic pH, and upon protonation, fluorescence increases significantly. For example, the group of *Kobayashi et al* have demonstrated a pH sensitive BODIPY imaging probe in Her2 positive cells.[88,91] Using confocal microscopy they showed that no fluorescence was seen in the plasma membrane, which is at pH 7.4. Following further incubation with the complex, it localised in the lysosomes. The complex emission intensity had increased significantly in the lysosomes as they have an acidic pH of ~ pH 3.8. Co-localisation studies with LysoTracker dyes confirmed that the BODIPY complex was in the lysosomes (Figure 1.18).

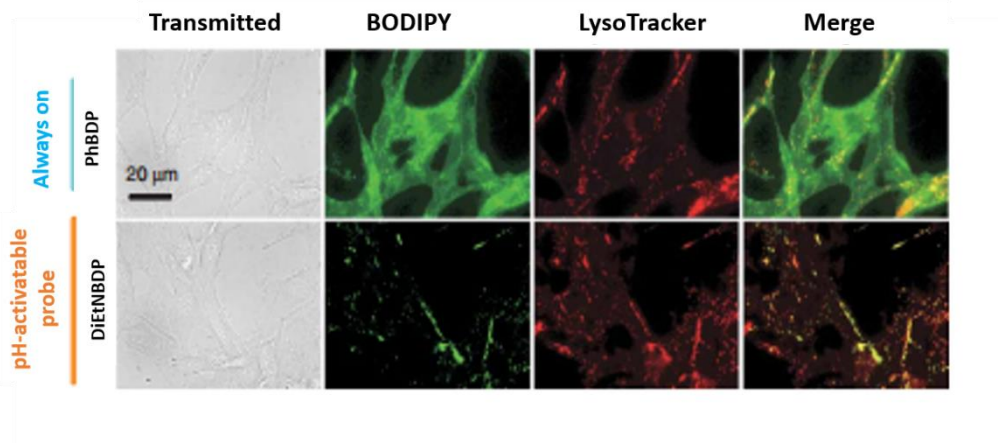


**Figure 1.18** pH-activation of a BODIPY-based imaging probe in Her2 positive cells. The first row shows control cells where the BODIPY is not sensitive to pH, where a solution of Ph-BDP–conjugated trastuzumab (green) was added to the cells. The second row demonstrates the activation of the BODIPY fluorescence once it has entered the lysosomes (pH 4.5), where a solution of DiEtN-BDP–trastuzumab (green) was added to the cells. After incubation for 24 h, localisation was confirmed using LysoTracker red DND-99 (red) co-localizing dye.[88]

The results in Figure 1.17 showed the pH-activation of a BODIPY fluorescent probe at acidic pH in Her2 positive cells, which can be used as a clinical tool for cancer detection and real-time monitoring of therapy. BODIPY complexes have also been applied to measuring viscosity. For example, the group of *Suhling et al* employed a group of BODIPY fluorophores to measure the viscosity of live SK-OV-3 cells using FLIM imaging. They were able to determine the local microviscosity of the cellular environment based on fluorescent lifetime.[92]

In addition, BODIPY chromophores have been coupled to polypyridyl complexes such as ruthenium to be used as a reference dye as they can be quite insensitive to the environment due to their short fluorescent lifetimes.[93] For example, ruthenium shows excellent sensitivity to oxygen. However, BODIPY have much shorter lifetimes, and are less likely to interact with oxygen. By coupling the two complexes, oxygen can be measured using the $O_2$ independent BODIPY as a reference. BODIPY has also been applied as a detector probe to detect ROS as it is quenched when it comes into contact with ROS radicals.[94] *Yamada et al* reported on a BODIPY complex (Figure 1.19) capable of detecting ROS. They incubated their complex with HeLa cells, and introduced hydrogen peroxide, $H_2O_2$, to the cells. $H_2O_2$ is a non-radical ROS. As a result,

the BODIPY fluorescence was quenched, increasing the fluorescence emission intensity in the HeLa cells.[95]

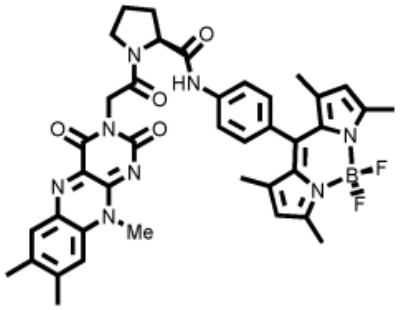


**Figure 1.19** Structure of a ROS sensing BODIPY complex.[95]

## 1.8 Oxygen Sensing Probes

In recent years, there has been significant progress made in the sensing and imaging of intracellular oxygen of live cells and tissue. Intracellular dioxygen ($icO_2$) is central to cellular functions such as respiration and energy production. It has been shown to be a critical marker of cell viability, and can be used to indicate disease, for example cancer cells are known to be of a hypoxic nature.[96] The ability to measure oxygen concentration in the cell, and more specifically in the various sub-cellular locations, is critical in understanding diseased states and the molecular mechanisms of redox-driven cellular activity. One of the valuable characteristics of metal polypyridyl complexes such as Ru(II) and Ir(III) is their long luminescent triplet excited state. This can be exploited to measure lifetime or emission intensity changes in a cell in response to the oxygen environment. In an oxygenated environment, excited states of metal complexes such as Ru(II) are quenched by oxygen which exists is a triplet, ground state, deactivating the complex triplet excited state through energy transfer. This in turn generates singlet oxygen itself, an active ROS species.[97] As a result, the luminescent lifetime and emission intensity decreases. Lifetime-based sensing relies on the photo luminescent quenching

of metal complexes, and is valuable as it is independent of probe concentration, making it a useful quantitative method.

Fluorescence quenching quantitatively diminishes both fluorophore emission intensity and lifetime. Typical quenching reactions include photo-induced electron transfer, or energy transfer. Collisional quenching occurs when the excited fluorophore comes in to contact through mutual diffusion of the fluorophore and the quencher. The quencher must have the appropriate thermodynamic properties to react with the excited state molecule. Quenching competes with fluorescence from the fluorophore, returning to its ground state, or a new state that does not emit a photon. For a diffusion quencher like oxygen, the linear dependence of intensity on oxygen concentration $[O_2]$ can be described using the Stern-Volmer equation (1.5).

$$\frac{I_0}{I} = \frac{\tau_0}{\tau} = 1 + K_{sv} \cdot [O_2] \quad \text{…. Equation 1.5}$$

Where $\tau_0$ and $\tau$ are the luminescence decay times in the presence and absence of oxygen and $I_0$ and I are the respective intensities. $[O_2]$ is the oxygen concentration and $K_{SV}$ is the Stern Volmer constant that quantifies the quenching efficiency of the probe where:

$$K_{SV} = kq \cdot \tau_0 \quad \text{…. Equation 1.6}$$

Where kq is the rate of quenching and $\tau_0$ is the luminescent lifetime in the absence of oxygen.

Measuring the effects of oxygen concentrations in cells may give a better understanding of the role of hypoxia in tumor cells. Luminescent $O_2$ probes are ideal as they are non-invasive. Techniques such as Confocal Microscopy can measure changes in fluorescence intensity, and Fluorescence Lifetime Imaging Microscopy (FLIM) for fluorescent lifetime. Until recently, the only way oxygen was measured in living cells or organelles was invasively using electrodes, such as Clark-type electrodes. Fluorescent lifetime is the optimal method of choice as it is independent of probe concentration, which will affect intensity.

One of the earliest examples of oxygen sensing using metal complexes by means of fluorescence lifetime imaging microscopy (FLIM) was reported by *Mycek et al* who demonstrated the oxygen dependent response of tris(2,2 -bipyridyl)dichloro-ruthenium(II) hexahydrate in human bronchial epithelial cell lines.[98] The complex was taken up by the cells after 4 to 6 hours incubation. The oxygen concentration was modulated in the cytoplasm by bubbling nitrogen into the contacting medium, and was imaged by measuring the changes in the Ru complex luminescent decay time. Although they showed that the luminescent lifetime changed with changing oxygen concentrations in solution, they did not report on a calibration curve, meaning no quantitative data could be retrieved from the FLIM data of the cells. Interestingly, our group have carried extensive uptake studies on $Ru[bpy_3]^{2+}$ in numerous cell lines including CHO, Sp2, and HeLa cells and have not seen any uptake of this complex without the use of DMSO or conjugating cell-penetrating peptides.

Another popular oxygen sensing agent are the phosphorescent porphyrins which are based on platinum(II) and palladium(II) transitions metals. Pt(II)- and Pd(II)-porphyrins possess long lived phosphorescent states in the range of 4-100 μs for Pt(II) and 400-1000 μs for Pd(II) probes rendering them suitable for oxygen quenching.[99] Pt(II)-porphyrin complexes possess ~2-3 times higher emission quantum yields than the Pd(II) derivatives.[100] The group of *Papkovsky et al* have carried out extensive work on Pt(II)- and Pd(II)-porphyrins.[101-105] Recently they reported on a group of phosphorescent tetracarbocylic Pt(II)-coproporphyrin dyes (PtCP) for intracellular oxygen sensing.[106] The complexes were taken up slowly by mouse embryonic fibroblast (MEF) cells via endocytosis, and localised in the cytoplasm. To monitor $ic O_2$ in dPC12 cells, the cells were stimulated with the mitochondrial uncoupler FCCP to alter the concentration of oxygen in the cell. Using luminescent lifetime and emission calibration plot they were able to determine that the $ic O_2$ decreased dramatically to 4 μM after 20 minutes exposure to FCCP. Free metallo-porphyrins tended to aggregate in aqueous solutions as a result of their hydrophobic nature. Therefore, the dyes are normally conjugated to polypeptides or synthetic polymers. *Lebedev et al* reported on a group of Pd-porphyrins encapsulated into poly(arylglycine) dendrimers in order to protect the chromophore from biological activities that may interfere with the oxygen sensing.[107] They introduced the probes to a mouse brain and were able to measure intravascular $pO_2$ using wide-field microscopy. A change in phosphorescence intensity was observed in response to changing oxygen levels.

## 1.9 Reactive Oxygen Species (ROS)

Reactive oxygen species (ROS) are chemically reactive oxygen metabolites. They are highly reactive as they have one or more unpaired electrons in their outer shells. They can be produced by exogenous factors such as UV or heat exposure, or can be generated endogenously in the body in the mitochondria.[108] ROS has been shown to play a role in diseases such as Parkinson's disease and Huntington's disease, as well as neurodegenerative diseases like multiple sclerosis.[109] Polymorphisms in mitochondrial DNA (mtDNA) has also been shown to lead to cancers such as breast and prostate cancers as a result of the overproduction of ROS.[110,111] Cells have developed methods of protecting themselves from ROS by producing antioxidants and degradation pathways.[112] However, increased ROS production in the cell can cause irreversible damage to DNA, cellular functions, and can contribute to disease progression.[113,114] The types of ROS include singlet oxygen ($^1O_2$), superoxide anion, and hydroxyl radical. Collectively, ROS is known as oxidative stress. [115]

Oxidative stress is caused by an imbalance in the cell where the production of ROS is greater than the cell's ability to remove it and repair the damage. The main ROS produced by the mitochondria is singlet oxygen, $^1O_2$. Oxygen has a triplet ground state. If $O_2$ reduction in the cell is incomplete, it forms an activated form of $O_2$, $^1O_2$, and is a highly reactive species. It can induce mitochondria permeability and can promote cell death.[116] When $^1O_2$ is generated, it can either lose its energy in the form of heat, or it can react with a substrate causing oxidative damage. If $^1O_2$ reacts with an organic molecule, peroxides can form. The O-O bond is cleaved, generating further $O_2$ radicals such as hydroperoxide.OH ($O_2.^-$).[97,117]As oxidative stress has been shown to play a role in many cellular dysfunctions,[118-120] further understanding of the underlying mechanisms involved in the process is essential. Fluorescent probes are highly sensitive and selective, which makes them ideal as sensors for ROS.[108,113,121] ROS is very difficult to measure as a result of its high reactivity and short lived lifetimes. There are very few reports regarding transition metal complexes for ROS sensing. One example is that if an Ir(III) phosphorescent ROS sensor.[122] *Zhao et al* found that the emission of their probe was greatly enhanced when it came in contact with hyperchlorite, $ClO^-$, a reactive oxygen species. Hypochlorite plays an important role in the immune system as a signal molecule and it is mainly produced by active phagocytes. All of the studies by Zhao et al were carried out in vitro and were not examined in live cells. Currently, most of the ROS

sensors that are reported are based on organic probes.[123] For example, the group of *Nagano et al* reported on a ROS sensor which was based on rhodamine.[124] They successfully targeted the complex to the mitochondria of HeLa cells. They stimulated ROS production by adding $H_2O_2$ to the cells, and recorded an enhancement in confocal fluorescence intensity as a result of ROS production.

Dihydroanalogues of fluorescent dyes are commonly used probes for ROS production. Examples of which include 2',7'-dichlorofluorescin (DCFH), dihydrorhodamine 123, and Amplex Red. Commercially available imaging probes to allow ROS to be detected using confocal microscopy include Amplex Red and MitoSOX Red.

For example, MitoSOX Red is a fluoro-probe that detects superoxide in mitochondria of live cells.[125] Figure 1.20 shows the generation of superoxide using the mitochondrial uncoupler Antimycin A in myocytes, and detected using MitoSOX Red. Antimycin A is an inhibitor of electron transfer at complex III in mitochondria. It blocks the mitochondria from consuming oxygen in the cell. Therefore, there is a build up of oxygen in the cell, altering the natural concentration.[126] The change in the cellular environment causes the cell to undergo oxidative stress, producing ROS.[127]

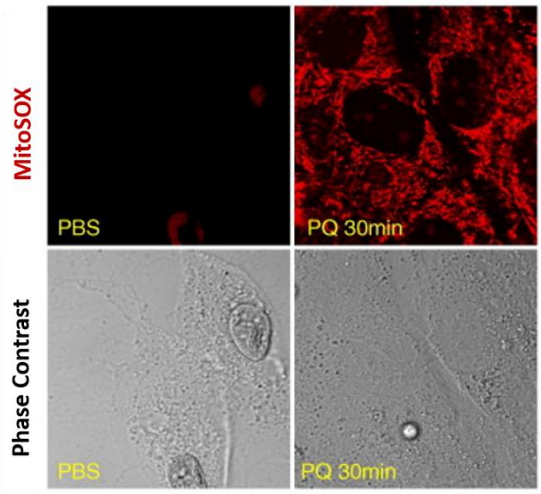


**Figure 1.20** Confocal microscopy detecting the production of superoxide in live myocytes using MitoSOX Red.[125]

By comparing the control cells in PBS to those treated with Antimycin A, it is evident that MitoSOX Red is a highly fluorescent and selective probe for the detection of ROS production in mitochondria.

## 1.10 Ratiometric Oxygen Sensing

As discussed in section 1.8, luminescent lifetime is the most reliable approach to sensing intracellular oxygen concentrations as it is independent of probe concentration. However, lifetime imaging microscopy is a relatively unconventional method and not widely available. On the other hand, emission intensity-based sensing using fluorescence microscopy is possible on more conventional instruments. As emission intensity is influenced by probe concentration, a ratiometric approach is required for oxygen sensing.

Ratiometric sensing has emerged in recent years as another method to measure oxygen *in vivo.* However, it is not an established method, and there are still many issues to be addressed. Ratiometric oxygen sensing allows for oxygen to be measured using optical methods such as confocal microscopy, which can allow for rapid real-time cell imaging of intracellular oxygen.[128] Ratiometric oxygen probes are typically made up of a dual-emitting system that consists of an oxygen-insensitive fluorescent reference, and an oxygen-quenchable phosphorescent sensor.[129] Therefore, the intensity or decay lifetime ratio of fluorescence and phosphorescence can be used to quantify oxygen concentration. Ideally, both the sensor and reference of the dual probe need to be co-excited at a single wavelength while possessing different emission maxima's to avoid any cross talk. Figure 1.21 shows an example of the emission spectra of a ruthenium-coumarin ratiometric probe.[130] In this case, when excited at 405 nm, coumarin exhibits an emission maximum at 467 nm, and Ru(II) at 611 nm. The coumarin emission remains constant while the Ru(II) emission changes over a range of oxygen concentrations, increasing with decreasing oxygen.

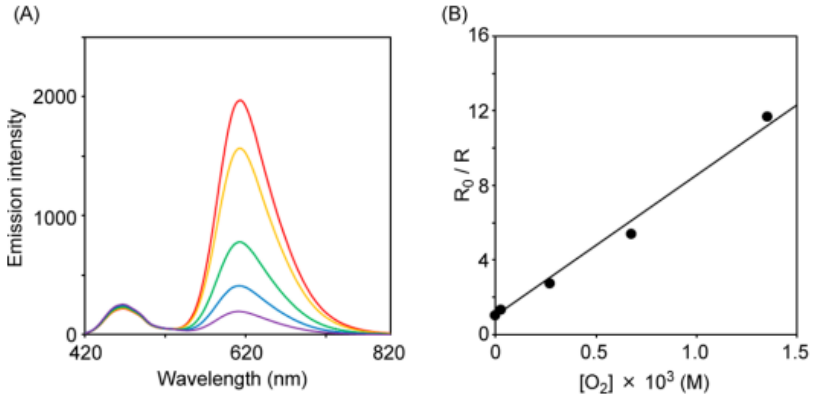


**Figure 1.21** Emission spectra of Ruthenium-coumarin ratiometric oxygen probe (20 μM) in Dulbecco's phosphate buffered saline (DPBS) under different oxygen concentrations (0% $O_2$: red line, 2% $O_2$: orange line, 20% $O_2$: green line, 50% $O_2$: blue line, 100% $O_2$: purple line) (A) and the corresponding Stern-volmer plot of phosphorescence to fluorescence. The spectra were measured with excitation at 405 nm.[130]

From Figure 1.21, the probe shows excellent linearity in response to oxygen. From the slope of the plot it was determined that the Ruthenium-coumarin probe has a KSV value of 7.531 x $10^3$ $M^{-1}$, which is a relatively slow quenching rate. However, more measurements over the range of oxygen concentrations could have been included for a more accurate calibration curve. Single molecule system for self-referenced sensing are difficult to make, because it is difficult to avoid cross-talk between the two probes, such as self-quenching. Therefore most reports of ratiometric probes are particle based. Ratiometric oxygen sensors are most commonly prepared by mixing different dyes to create a dual-emissive particle.[130,131] Recently, ratiometric probes have been encapsulated in nanoparticles,[132-134] PEBBLEs,[135,136] and dendrimers.[137] Their encapsulation helps avoid quenching and interference from biological materials other than oxygen in live cells.[138]

PEBBLEs (Probes Encapsulated By Biologically Localized Embedding) are optical sensors which are designed for minimal invasive monitoring in live cells. PEBBLEs are typically based on hydrogel matrices such as polyacrylamide hydrogel, sol gel silica, and cross-linked decyl methacrylate, and can be between 20 and 100 nm in size.[139] *Wang et al* reported on a RGB PEBBLE for intracellular oxygen sensing.[140] Their ratiometric probe consisted of a Pt(II) oxygen sensor and the fluorophore N-(5-carboxypentyl)-4-piperidino-1,8-naphthalimide butyl ester as the reference dye. Both dyes were encapsulated in hydrophobic polystyrene beads which protected the probes from direct

contact with cellular components. The porosity of the hydrogel materials allow for oxygen to diffuse and come in contact with the oxygen sensitive dye. Figure 1.22 shows the PEBBLEs in NRK cells. At oxygen saturation, the RGB PEBBLEs display a green fluorescence from the reference probe (A). Upon uptake by the cells, the PEBBLEs turn from green to red as a result of the limited oxygen supply in the cells (B-D).

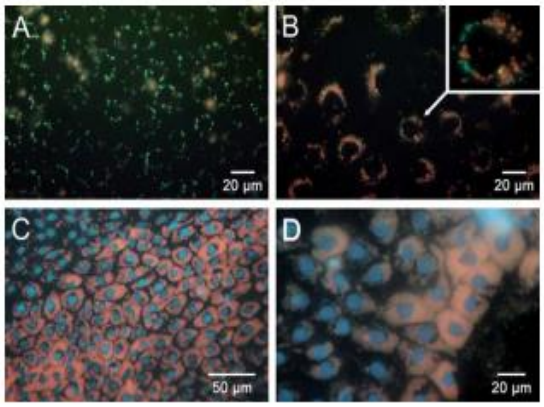


**Figure 1.22** Imaging intracellular oxygen in NRK cells. (A) In the oxygen saturated cell culture medium, RGB PEBBLEs display green fluorescence. (B) After endocytosis (24 h), the colour of RGB PEBBLEs turns from green to red due to the limited oxygen supply in intracellular compartments. The inset shows an enlarged section of a single cell. (C) After 48 h, large amounts of the RGB PEBBLEs have been internalised by the cells. (D) Partial membrane rupture by 2% Triton X-100 releases some RGB PEBBLEs into the cell culture medium where their colour turns from red to green.[140]

The group of *Tobita et al* reported on an Ir(III)-coumarin ratiometric oxygen probe.[141] This is one of the few examples to date of a molecular system where the small-molecule probe was not encapsulated. It showed excellent ratiometric properties in solution, where the emission intensity was shown to have a linear response to oxygen quenching, which resulted in a linear Stern-Volmer plot indicating dynamic quenching. The complex was introduced to HeLa and they were incubated at 20 % oxygen and 2.5 % oxygen to induce hypoxic conditions. Figure 1.23 shows that under saturated oxygen condition's (20 %), the coumarin displays intense emission from with the cells while there is no contribution from the phosphorescent Ir(III) component. However, under hypoxic conditions (2.5 %), the Ir(III) luminescent emission switches on. Although these results demonstrate good ratiometric properties for the mapping of intracellular oxygen, the group did not

quantitatively measure oxygen in the cell, nor did they measure luminescence over a range of oxygen concentrations from within the cell, and therefore did not explore the full potential of this probe.

A

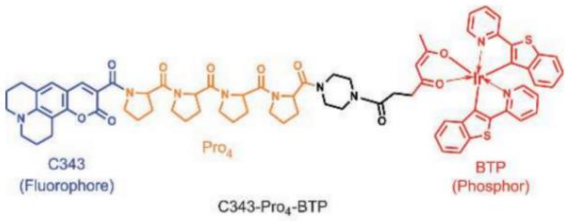


B

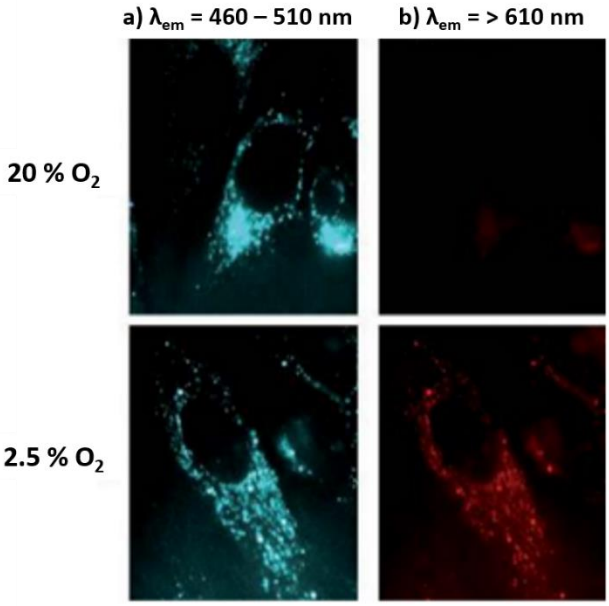


**Figure 1.23** Structure of Ir(III)-coumarin ratiometric oxygen probe (A). Luminescence images ($\lambda_{exc}$=400–410 nm) of Ir(III)-coumarin ratiometric oxygen probe in HeLa cells incubated under 20% and 2.5% $O_2$ conditions (B) observed at emission wavelengths of a) 460–510 nm and b) above 610 nm.[141]

## 1.11 Confocal Laser Scanning Microscopy

Cell imaging using fluorescence microscopy has become an essential tool in biology and life sciences. It provides an insight into how cells function and cell signalling at a subcellular level which has been achieved by labelling the samples with luminophores and using confocal microscopy to acquire an image. Before the development of confocal microscopy, there was wide field microscopy. Here, the sample is illuminated using an

arc or filament lamp, and the entire sample is uniformly exposed to the light source as shown in Figure 1.24a. However, very little detail of cellular structures can be observed this way without labelling. On the other hand, confocal microscopy uses lasers to excite fluorescently labelled samples, where only a specific, focused area of the sample is scanned by the light source (Figure 1.24b). This greatly improves image quality and resolution, as well as resulting in more detailed images.

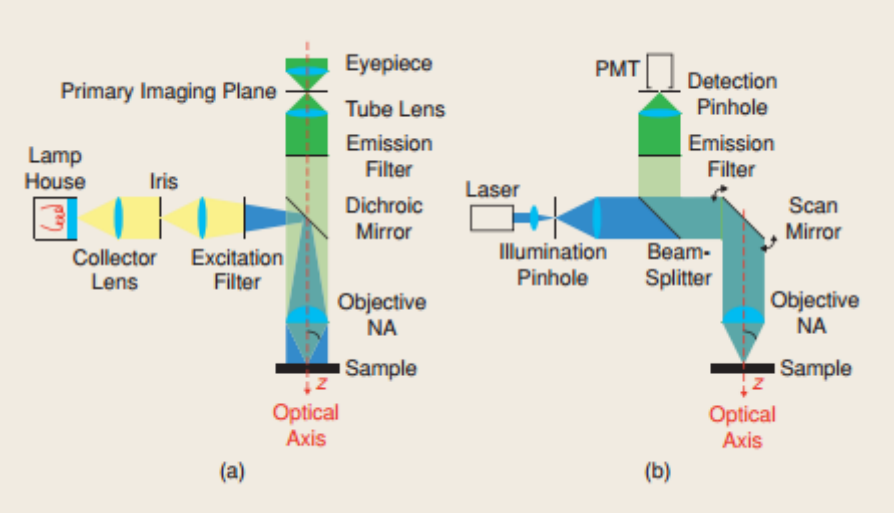


**Figure 1.24** Schematics of (a) widefield and (b) confocal fluorescence microscopes, showing their main components. The illumination path is shown in yellow and/or blue (excitation at 395 nm) and the image-forming path in green (emission at 509 nm). [142]

Confocal laser scanning microscopy (CLSM) is a non-invasive technique used to obtain high-resolution 3D images with little background interference. It has the power to resolve and detect structures at a sub-cellular level, which has led to the requirement of much improved multi-modal imaging probes. The drawbacks of continued laser scanning include photo-bleaching, and general damage to the cell membrane through thermal activation by continuous exposure to the laser. To overcome over-exposure to high-intensity laser beams, other confocal microscopy techniques are available. For example, Spinning Disk Confocal Laser Microscopy (SDCLM). Here, an expanded laser beam scans over an array of micro lenses which are arranged on disk. These micro lenses align with a second disk which contains the pinholes for each micro lens. To acquire an image, the disks are rotated at speeds between 1800-5000 rpm. An array of focused laser beams scan the specimen, unlike the single laser beam of CLSM. [143,144] As multiple pinholes scan the area in parallel, less energy is required to excite the sample. Therefore, there is a reduction in fluorescence bleaching and less damage to the sample. During the

high-speed spinning, stable focus is maintained using an auto-focus system, allowing for rapid, long-term imaging of live cells. [145,146] The imaging technique in which this thesis uses, however, is CLSM. In order to overcome the disadvantages of the high-laser intensities used, new imaging complexes can be designed to ensure these problems are limited.

### 1.11.1 Principle of Confocal Microscopy

The principle distinction between wide-field microscopy and CLSM is the use of pinholes which work to reject light outside of the focal plane for much improved focus and resolution.[142] By passing the exciting and detected light through pinholes, only light directly focused on the pinhole passes through and out of focus light is eliminated. There are 2 pinholes – one before the sample at the excitation line, and one for after the sample for the detection. The fluorescence from the sample is collected at a photomultiplier tube (PMT). To collect an image, the sample is scanned by the laser in the X-Y plane to build up the image on a per-pixel basis. CLSM is much preferred over the conventional wide-field fluorescence microscope as it allows for a much more detailed three dimensional observation in cell imaging. The principle of a confocal microscope is illustrated in Figure 1.25.

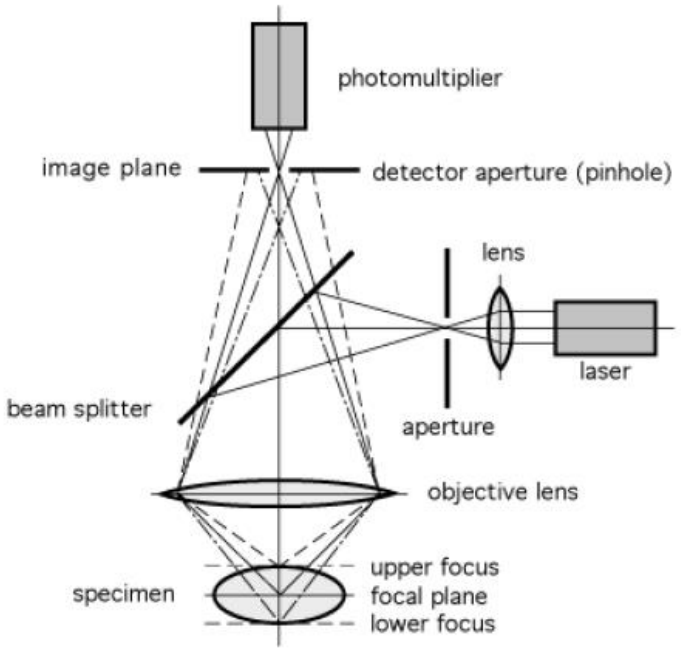


**Figure 1.25** Diagram demonstrating the optical set up of a confocal microscope [147]

The smaller the pinhole, the higher the resolution achieved as there is less out of plane light and noise being let in to the PMTs. However, the disadvantages of restricting the region of observation using a pinhole hole is that the entire field of view is not visible, and there is a decrease in the luminescent intensity. The high-spatial resolution of confocal microscopy has provided power to investigate and detect at a sub-cellular level. CLSM has several other advantages over wide field microscopy; the depth of field can be controlled, background interferences can be eliminated from the focus, and images can be be acquired from different z positions or slices through a sample.[148] A huge advantage of using CLSM is its high z-resolution. Scanning in the z direction allows for a Z-stack to be collected to achieve a 3D image of a sample. In order to do this the sample is moved on a motorised stage to collect images at different depths through the sample.

To overcome the disadvantages associated with CLSM, new imaging probes can be designed to ensure these problems are limited. With the advancements made in CLSM imaging techniques in the past 10 years, there is a requirement for much improved imaging probes to keep up with the ever changing technology. Imaging probes have been designed and developed to coincide with the needs of CLSM. For example, choosing a complex that has a large Stokes shift will avoid self-quenching, while a long lived excited state avoids photo bleaching. Commercial probes for cell staining such as Atto and AlexFluors are widely available, but typical of organic probes, show limited sensitivity to the environment. However, new multimodal imaging probes that can be used to measure oxygen and pH are being designed so that they can be easily monitored in cells using CLSM.

Transition metal complexes have all the necessary characteristics to overcome many of the present issues with organic probes such as photostability and self-quenching. Ru(II) [67,149,150], Ir(III)[151-153], and Re(I)[52,154,155] have been widely explored as general imaging probes in live cell imaging. Their large Stokes shift avoids self-quenching, while their long lived excited state helps to eliminate the short-lived auto fluorescence found in biological samples. They are highly photo stable which allows for continuous monitoring of biological samples. Ru(II) complexes will be the focus of this thesis for CLSM.

## 1.12 STimulated Emission Depletion (STED) microscopy

As discussed in section 1.11, confocal microscopy is currently the key bio imaging tool used to study live cells, tissues, and other biological structures. However, the spatial resolution that can be achieved in conventional optical methods is restricted by the light diffraction limit. The resolution limit of a microscope is defined by Abbe's principle. This states that light with wavelength λ, travelling in a medium with a refractive index *n*, that converges with the angle θ will make a spot the size of *d*. This relationship is described by Equation 1.5:

$$d = \frac{\lambda}{2n\sin\theta} = \frac{\lambda}{2NA} \quad \text{..... Equation 1.7}$$

Where NA is numerical aperture ($\sin\theta n$). Thus a microscope cannot resolve two features that lie located closer to each other than /2NA.

However, the development of a number of significant advances in microscopy in recent years has allowed the diffraction limit to be effectively bypassed. The first of the super resolution techniques to emerge was stimulated emission depletion microscopy, STED.[156] This improvement in resolution of fluorescent microscopy led to the award of the Nobel Prize in chemistry for the creators Stefan W. Hell, William E. Moerner, and Eric Betzig in 2014.

In 2006, a new type of super resolution technique emerged known as single-molecule super resolution imaging, which includes Stochastic Optical Reconstruction Microscopy (STORM) and Photo-Activated Localisation Microscopy (PALM). [157] The principle behind these techniques is that they use photo-switchable fluorophores to obtain high resolution images. The laser activates some of the fluorophores, while other fluorophores remain in a non-emissive, dark state. The difference between STORM and PALM is that STORM uses switchable organic fluorophores in specific reducing buffers, while PALM uses fluorescent proteins. [158] In both cases, however, sufficient photons need to be switched on so that its precise localisation can be determined before the fluorophore switches off. The images of the emitted photons are captured using low-power readout lasers until they reach a dark state or photo-bleach. This process is

repeated to build up an image of the precise location of the single molecule photons in a sample. [158] High number of photons need to be collected compared to the background in order to achieve the highest resolution possible. Background signal can come from auto-fluorescence of the sample or from residual fluorescence from non-activated probes. Dyes such as Cy3 and Cy5 have been used for STORM to reduce background as they produce high photon counts for imaging, where resolutions of 20 nm have been achieved. [159,160] However the focus of this thesis is the application of inorganic probes for STED microscopy.

Figure 1.26 illustrates the principle of STED excitation. The improved resolution is achieved through double excitation of the fluorophore. A focused laser pulse excites the fluorophore, and immediately after the excitation, a red-shifted high-intensity donut-shaped STED beam is applied which overlaps with the excited region. It depletes the fluorescence of the excited fluorophore on the periphery of the excitation spot by stimulated emission, effectively switching the fluorophore to a temporary dark state, for example S1-S0.[161]

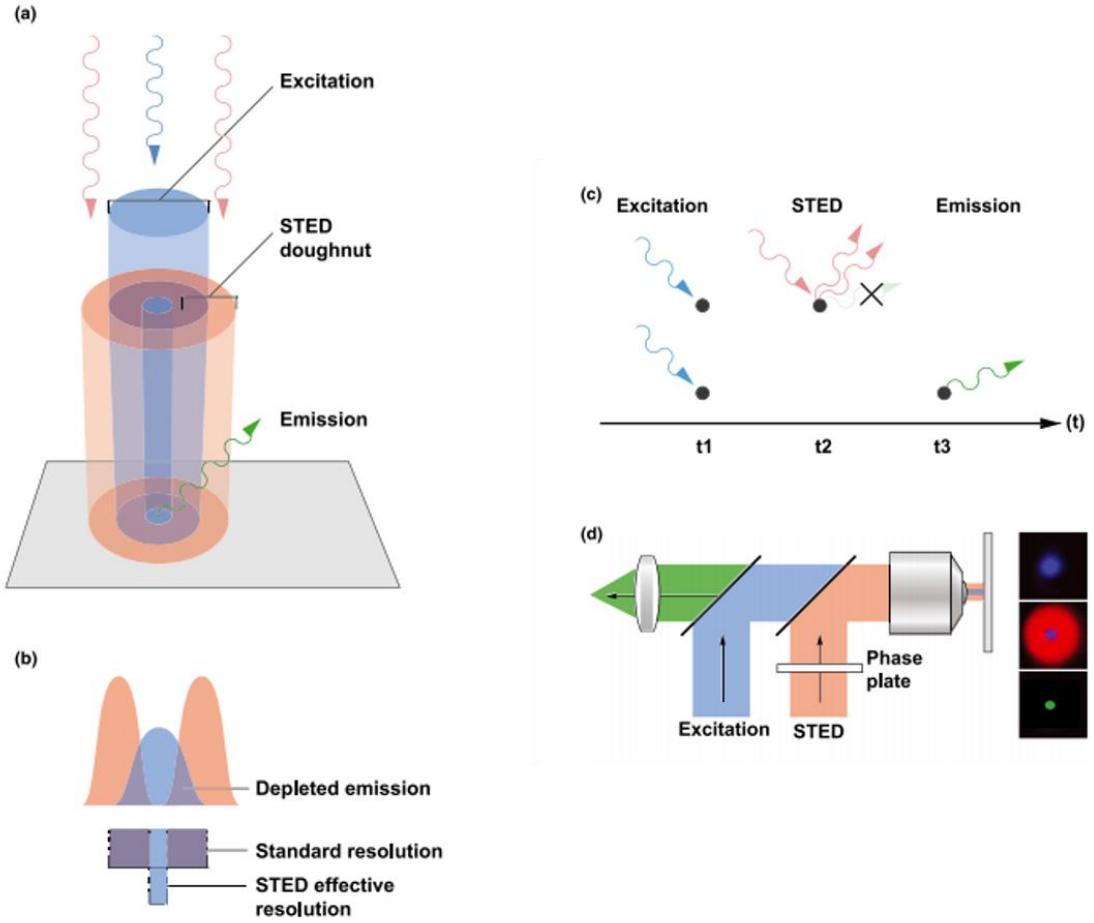


**Figure 1.26** The principles of STED. (a) A laser light is used to excite (blue) fluorescence emission (green) in the area of focus. The STED laser (red) is used to selectively turn off emission in the outer periphery, allowing for better separation of fluorescent entities. (b) Increased depletion power (red) reduces the common area of emission, generating a sharper effective focus with nanoscale resolution power. (c) Following absorption of excitation light (blue photon), fluorescent molecule (black) spontaneously emits fluorescence (green photon) after a short time 't' to return to its ground state. The addition of STED light (red photon) can rapidly stimulate the excited molecule to emit the absorbed energy (additional red photon) and return to the ground state, thus turning off fluorescence (green). (d) Schematic diagram of an optical STED microscope with a phase plate sculpturing the depletion beam (red) into a 'doughnut-shape' in the focal plane, overlapped with the excitation beam (blue), and the resulting effective detected fluorescence emission (green).[162]

STED de-excitation is stimulated using  which coincides with the red tail of the emission of the fluorophore so as to avoid re-excitation of the fluorophore. This reduces the spot size of the incident laser to below the diffraction limit. The improved optical resolution obtained using STED is defined by Equation 1.8

$$d = \frac{\lambda}{2NA\sqrt{1+ I_{max}/I_{sat}}} \quad \text{..... Equation 1.8}$$

Where λ is the emission wavelength, NA is the numerical aperture of the objective lens, $I_{max}$ is the peak intensity of the STED laser within the depletion zone, and $I_{sat}$ is the applied STED laser threshold intensity, in other words the intensity that depletes 50 % of the probes emission intensity.[163] Equation 1.8 indicates that the more efficient the depletion process, the greater the achievable resolution. [164] Since the more intense the STED laser, the greater the depletion. However, the huge intensities required for STED makes significanr demands on the probe regarding stability. In order to achieve STED, a depletion laser is typically between 0.1 – 1 GW $cm^{-2}$, meaning the fluorophore must be highly photostable with the maintenance of a high fluorescent quantum yield. Therefore, the choice of fluorescent probes is important in STED microscopy.

### 1.12.1 Choosing the correct STED probe

Most luminescent probes applied in microscopy are organic dye complexes. The commercially available complexes that are recommended for STED imaging such as Alexa Fluor,[165,166] Atto,[161,166,167] and Chromeo[163,167] are exclusively organic but are used because of their high photostability. However, a key drawback is that organic probes have small Stokes shifts. This makes it harder to apply a STED depletion laser without causing re-excitation of the probe as the laser line may overlap with its absorption spectrum. Thus STED depletes wavelengths at the far red edge of the emission. Choosing the correct dye complex for STED is crucial to achieving optimum resolution.

1) An ideal STED probe should have a large Stokes shift which has many benefits to the imaging process such as avoiding re-excitation by the depletion laser. Re-excitation leads to a prolonged dark state which results in photo bleaching.[168] A large Stokes shift also allows for multi-labelling. Multicolour imaging is fast becoming a method of interest in order to image two or more complexes at the one time.[167] The spectral separation of different labels into two or more excitation/detection channels is required,

and therefore fluorophores with large Stokes shifts enable the number of detection channels required to be reduced and avoid cross talk between the probes.

2) Photostability is essential in STED microscopy as the probe will be exposed to high laser intensities during the depletion process.

3) The emission profile of the probe must be well matched to the chosen STED depletion laser as the greater the overlap with the emission, the greater the extent of stimulated depletion.

4) A long lived emissive state means there is a better probability for stimulated emission to be achieved.

Current commercial organic probes address only the photostability and high quantum yield necessary for STED. Therefore, there is much work to be done on the development of probes to improve the performance of STED microscopy.

### 1.12.2 Applications of STED microscopy

STED was first experimentally demonstrated by *Hell et al* in 1999, whereby they imaged nanocrystals using standard UV-confocal, then applied a STED laser to disable the fluorescence from the outer part of the focal spot.[169] Figure 1.27 shows the improvement in spatial resolution of nanocrystals achieved after using STED. A full width half maximum (FWHM) of the X-Y profile across the nanocrystals was measured to be 150 ± 8 nm in the standard confocal image, which improved to 106 ± 8 nm when STED was used. The STED image was also able to resolve two nanocrystals in the focal plane, whereas it appears that there is only one when confocal was used.

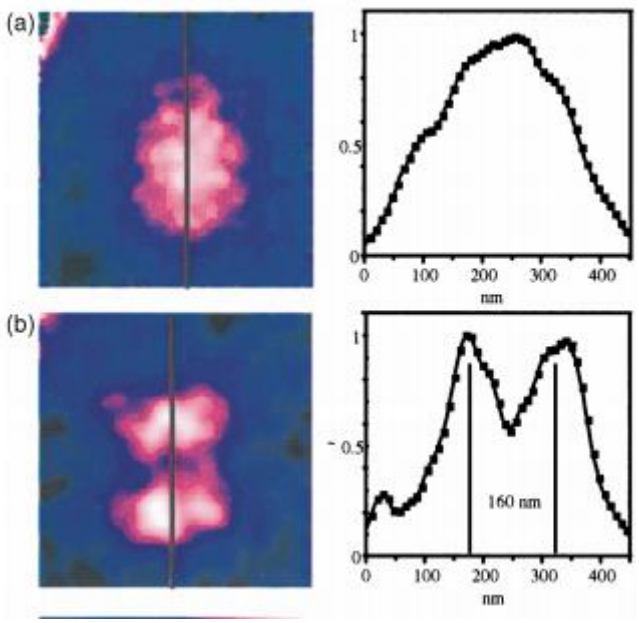


**Figure 1.27** Images of adjacent nanocrystals in (a) the standard UV-confocal and (b) the STED-confocal microscopes. Comparison of the images and the profiles reveals significantly improved spatial resolution in the far field. Excitation 388 nm, STED depletion laser 766 nm.[169]

The first application of STED to live cell imaging was reported by *Hell et al* in 2000.[168] They labelled the membrane of live *E.coli* and applied STED microscopy. Figure 1.28 demonstrates the improved resolution of the membrane compared to the confocal image (b). Here they have 'broken the diffraction barrier' by up to a factor of 2 in the lateral and 6 in the axial direction.

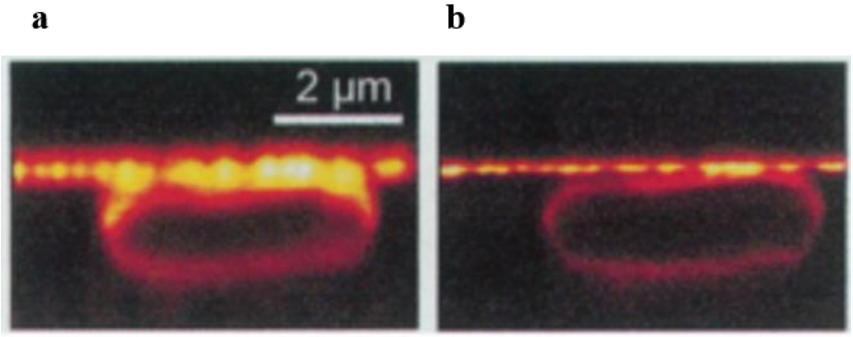


**Figure 1.28** Resolution improvement of labelled E.coli membrane. A 3-fold improvement was demonstrated using STED (b) compared to the simultaneously recorded confocal image (a).[168]

Many improvements in STED imaging techniques have been made since this early work. In 2009, reports from the same group demonstrated sub-diffraction STED nanoscopy

images of mitochondrial cristae structure inside a cell.[170] Here they were able to non-invasively image the arrangements of the translocase of the outer membrane (TOM) of the mitochondria, shown in Figure 1.29. Figure 1.29a demonstrates the complexity of the mitochondria in the cell. The sketch described in (b) illustrates that the size of the mitochondrial tubule is beyond the diffraction limit of a general confocal microscope. Upon scanning of the mitochondrial tubules, the confocal image gives no structural detail of the antibody-labelled mitochondria. However, the STED images reveal individual TOM complexes on the mitochondria membrane, demonstrating 30 nm resolution for the first time using optical methods.

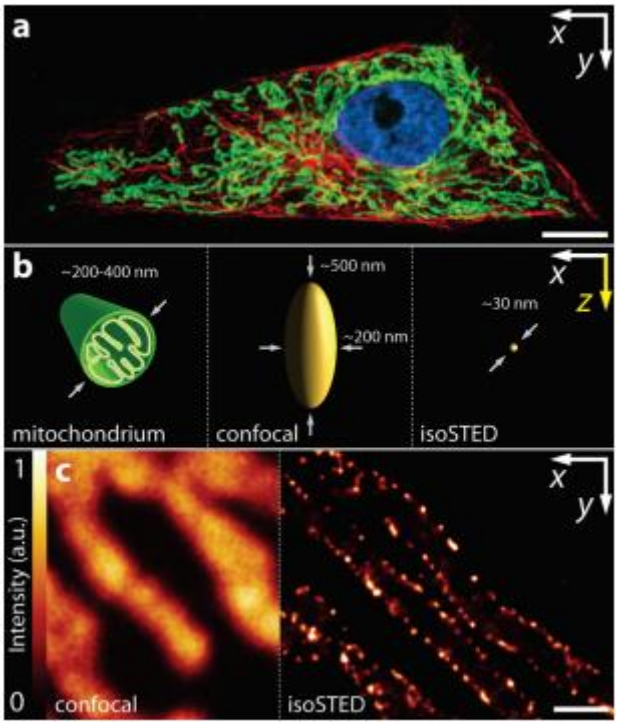


**Figure 1.29** STED nanoscopy of mitochondrial cristae. (a) The mitochondrial network of a PtK2 (kangaroo rat) cell. The mitochondria were labelled with antibodies against the TOM-complex (green) and the microtubule cytoskeleton with antibodies against -tubulin (red). The nucleus was labelled with DAPI (blue). (b) Sketch comparing the dimensions of a mitochondrial tubule (left) with the confocal (middle) and the STED focal volume (right), drawn to scale. (c) Mitochondria labelled with antibodies specific for the TOM complex comparing the confocal image (left) with the STED image (right). Scale bars: 10 µm (a) and 500 nm (c). [170]

Time-lapse STED, a newer extension of STED, was employed by the group of *Nägerl et al* to image changes in synapse functions in live brain tissue.[171] Figure 1.30

demonstrates a resolution of 60 – 80 nm of actin present at depths of 120 μM in brain slices. They established an average resolution of 190 nm for confocal microscopy and 60 nm for STED microscopy at depths up to 90 $\mu$m in brain slices. Such penetrating depths and improved resolutions highlights the diversity of STED applications, which will be increasingly be applied to the biomedical imaging of normal and abnormal functions.

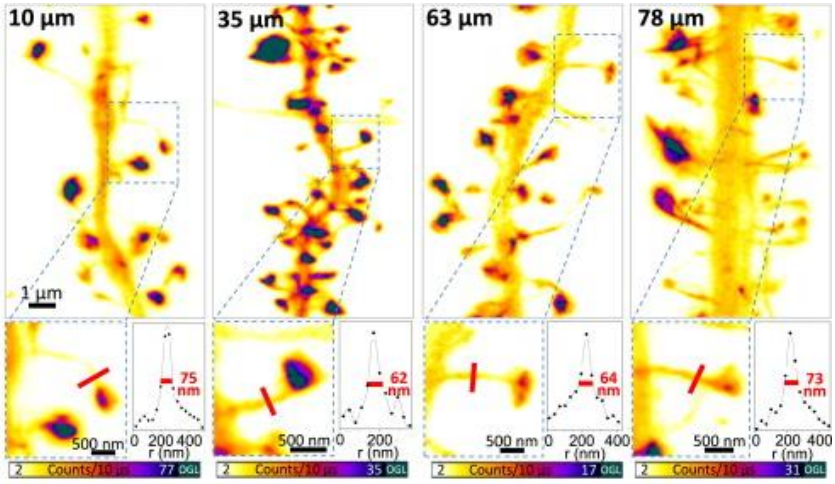


**Figure 1.30** Live STED images of dendrites of hippocampal neurons recorded at various depths 10, 35, 63, and 78 $\mu$m below the tissue surface. Samples were labelled with pSCA-Lifeact-EYFP vector. They were excited at 490 nm, and the 595 nm STED depletion laser.[171]

Long-term changes to synapse function is a central challenge for neurobiological research. Imaging of the synapse in Figure 1.30 is one of the few examples where STED has been used to study biological functions. To date STED reports have focused on method development with improved resolutions and the development of imaging dyes, rather than the discovery of new biological functions.

Nuclear pores located on the nuclear surface of a cell are typically 80 nm long and 145 nm in diameter.[172] The nuclear pore prevents the passage of non-specific molecules to enter the nuclear envelope while still allowing the diffusion of water, sugars and ions. It also plays a key role in cellular processes such as gene activation. Imaging such structures using conventional confocal cannot be achieved because of the diffraction limit. However, *Hell et al* were able to achieve high resolution images of nuclear pores using single-colour STED nanoscopy.[165] Figure 1.31 demonstrates the confocal versus STED images acquired of the nuclear pore complex in a fixed HeLa cell. Atto 647N was

used to stain the nuclear pore for imaging. A high contrast image was achieved, and the background noise has been significantly reduced, along with the improved resolution following STED. However, this report only focuses on the development of new imaging dyes and achieving improved spatial resolutions, using the nuclear pore to do so. There have been no dynamic biological studies carried out on the nuclear pore using STED microscopy.

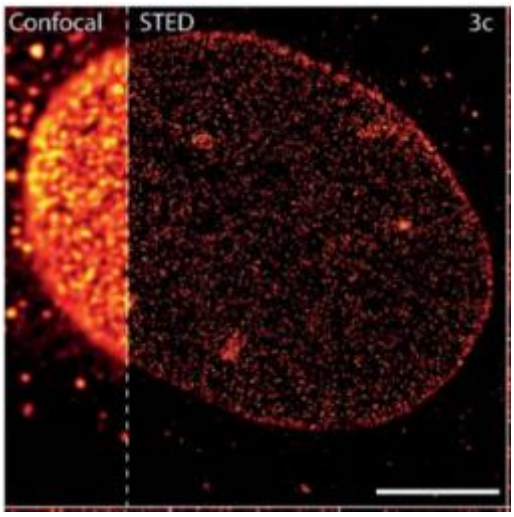


**Figure 1.31** Nuclear pore complex stain with Atto647N in a fixed HeLa cell. The detailed structure can be clearly resolved compare to the confocal equivalent. [165]

To date, the greatest improvement in resolution was reported by *Hell et al* in 2013 where they demonstrated resolutions as low as 20 nm in unprocessed data images.[173] Figure 1.32 describes dual-stained protein complexes of the nuclear pore complex (NPC) with immuno-labelled homodimers. Upon applying STED, the detail of the NPCs structure could be clearly resolved from the dual-labelling, with the diameter of an NPC was found to be around 160 nm in diameter. The STED image of a single NPC revealed that it consists of 8 subunits, each with a size of between 20-40 nm, surrounding an 80 nm sized centre.

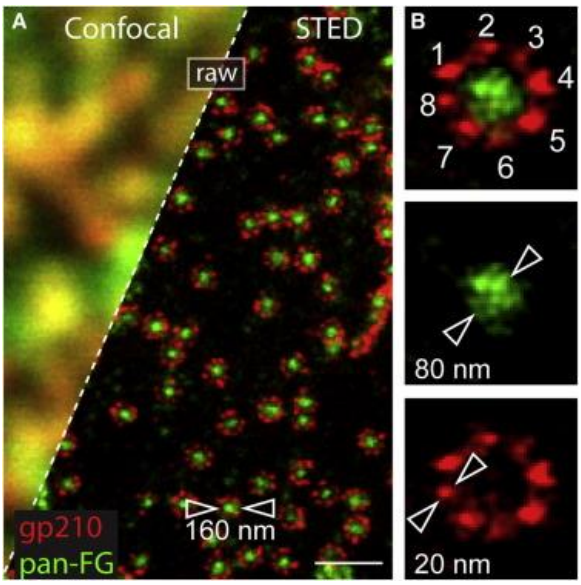


**Figure 1.32** Fluorescence nanoscopy of protein complexes with a compact near-infrared nanosecond-pulsed STED microscope. (*A*) STED reveals immuno-labelled subunits in the nuclear pore complex. The diameter of the ring was established as ~160 nm. Scale bar, 500 nm. (*B*) An individual nuclear pore complex image showing eight antibody-labelled gp210 homodimers as 20–40 nm in diameter, with an 80 nm-sized centre. [173]

The abilities to dual-stain protein structures allows for in-depth imaging at sub-diffraction resolution using STED. Up until now, all of the reports of STED microscopy have been based on organic probes. To date, there have been no reports of transition metal complexes applied to STED. Transition metal complexes possess all the previously described attributes of a good STED probe such as large Stokes shifts, long lived emissive states, red emission and photostability. Chapter 5 will look at the application of two Ru(II) complexes as a novel STED imaging probes.

## 1.13 Fluorescence Lifetime Microscopy (FLIM)

Fluorescence lifetime microscopy (FLIM), or in the context of metal complex luminophores are sometimes referred to as phosphorescence lifetime imaging (PLIM), is a quantitative microscopy technique which maps the spatially resolved average luminescence lifetime of a probe across a sample. The application of fluorescence lifetime imaging to live cells was first reported in 1992.[174] and, although it is not yet

widely adopted in cell biology laboratories its use is growing. FLIM systems are typically used in tandem set-ups implemented in conventional confocal and multi-photon microscopes.[175,176] The biggest advantage of FLIM is that the lifetime of a luminophore is independent of its concentration, making FLIM is the most reliable way of assessing the probe environment without need for ratiometric signal. In other words changes to lifetime can be attributed to changes in the local environment and not probe loading.

FLIM can be used as a Time domain (TD) or Frequency domain (FD) system. In FD FLIM, the light source is pulsed at a high frequency and modulates the fluorescence. The delay in the fluorescence between the pulses causes a phase shift. The lifetime can be determined from the shift or decrease in the phase.[177] TD FLIM typically employs time correlated single-photon counting (TCSPC), where short pulses of light excite the sample and the fluorescence decay is directly measured with a time gated system. This is the principle behind TCSPC.[178] This is the system used throughout this thesis. In TCSPC, the sample is excited using a pulsed-laser diode (LDs) to create short pulses of light. The time between the excitation pulse and the emission of a fluorescent photon is recorded. The data is collected by detecting single photons of the fluorescent and marking their arrival times at the detector with respect to the laser pulse.[177,179] The time-dependent intensity is measured between the excitation pulse and the photon.[17] Each detected photon creates a histogram or decay curve which builds up over time to give the lifetime decay, shown in Figure 1.33. Typically, the detection rate is 1 photon per 100 excitation pulses. The decay time $\tau$ is calculated from the slope of the plot *log (I) t versus t*. Or, more commonly by non-linear least squares fitting of the decay curve.

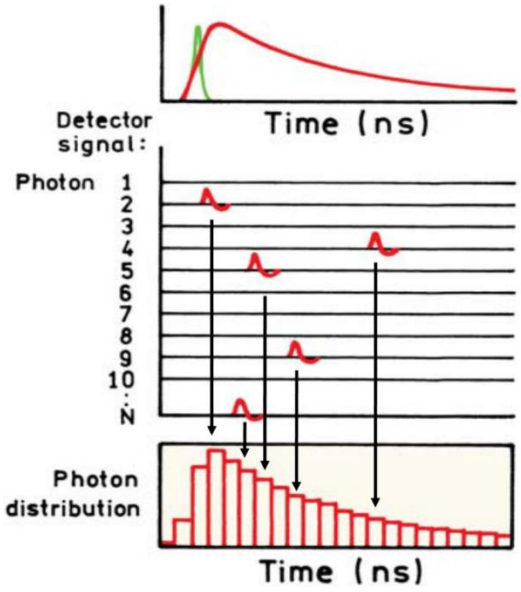


**Figure 1.33** Lifetime measurement using Time-domain system. Single photons are detected based on their arrival times (middle image) and collected to create a histogram decay curve [17]

In imaging mode, the detected photons are sorted into time bins according to their arrival time, resulting in a lifetime decay plot of photon distribution and arrival time after each laser pulse and in the resulting FLIM image, each pixel is made up of the detected photons in that region, making up a false-colour image.[180] The advantage of this method over time domain and gated systems as that it counts all the photons that reach the detector, giving much higher efficiency, and typically requires low excitation intensity compared to conventional fluorescence imaging. It is useful for photosensitive samples as photo-bleaching or sample damage during longer acquisition times is avoided.[17] TCSPC FLIM delivers the highest time resolution with the best lifetime accuracy of the time resolved fluorescence imaging methods.[181] Because of the high resolution of the the lifetime data it can resolve complex decay profiles from a sample and it is compatible with confocal laser scanning microscope systems.[182] However acquisition times can be long, particularly for long lived probes because the cycle time depends on average wavelength lifetime, and this can limit the dynamic range of TCSPC systems. [183]

The acquired FLIM image is a contrast image where each pixel contains a fluorescent decay lifetime, not intensity. The data is analysed by fitting to fluorescence decay models, and can be mono- or bi-exponential.[184] Mono-exponential (single-exponential) is used when there is only one expected fluorophore present in the complex, for example

$Ru(bpy)_3^{2+}$. A bi-exponential decay is used for a complex with two fluorophores with a single emitting state but can be de-convoluted based on their lifetimes. For example, Ru(BODIPY) complexes are bi-exponential. The shorter component BODIPY has a lifetime of around 3-4 ns and can be separated from the Ru component whose lifetime is around 500 ns. The lifetime of a fluorphore can change, and can be fitted to a bi- or multi-exponentail decay when exposed to different environments. For example, dipyridophenazine (dppz) complexes in organic solevents generally have a mono-exponential luminescent lifetime, or no luminescent lifetime when in aqueous solution, as described preveiously in *section 1.2*. However, when bound to DNA, the lifetime can significantly increases, or can be fitted to a bi-exponentail decay. *Barton et al* showed that $[Ru(phen)_2dppz](PF_6)_2]$ comlex exhibited no luminecsnet lifetime in water. However, upon binding to DNA, it could be fir to a bi-exponential decay, resulting in two luminescent lifetimes of 120 ns and 750 ns, with the shorter lifetime being the more dominant of the two.[178]

### 1.13.1 Applications of Metal Complexes Luminophores in FLIM

In contrast to organic dyes whose lifetimes are relatively short, typically between 1 and 5 ns, the long luminescent lifetime of transition metals such as Ru, Ir, and Re, typically on the scale of hundreds of nanoseconds, is well outside the auto-fluorescence of biomaterials. This offers the opportunity to time-gate out such contributions to the decay. In addition, metal complexes frequently show better photostability than organic luminophores which is a particular advantage in lifetime imaging where in order to collect a representative lifetime image, several images need to be collected to reduce noise, correct for background fluorescence, and auto-fluorescence from the cell. This can lead to long acquisition times and photobleaching leading to artefacts in the lifetime data if the probe is photo-unstable.[175]

Environmental sensing in cell biology using luminescent lifetime is highly advantageous as it is a non-invasive method of monitoring oxygen,[185] pH,[186,187] and ion concentration[188] where the right probes are available, based on the changes of a fluorophore's lifetime. Many fluorophores used in microscopy show lifetime variations upon binding to different targets. This can be exploited to study binding with cellular proteins such as DNA. Recently, *Baggalely et al* reported on a [Ru(tpphz)] complex that entered the nucleus of HeLa cells.[189] They used phosphorescent lifetime imaging

microscopy (PLIM) to determine if the probe had bound to chromosomal DNA. Figure 1.34 shows that the probe has a luminescent lifetime of 124 ± 13 ns in the cytoplasm, which increased to 200 ± 12 ns upon binding to DNA, where binding was confirmed by confocal microscopy. The probe also had no toxic effects towards the cells, and ideal attribute for a cell sensing probe. Given the biological significance of DNA and its role in genetic diseases, such probes can potentially be used to specifically target and report on the micro-environment of DNA.

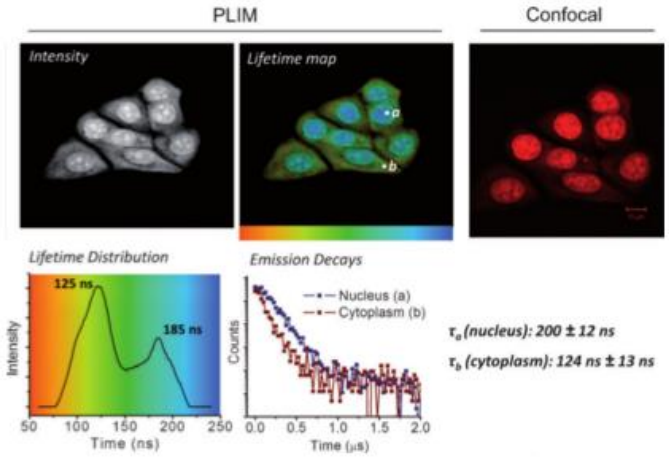


**Figure 1.34** PLIM (left) and confocal (right) comparison of fixed, permeabilized MCF7 cells treated with complex 1 (100 mm, 45 min, PBS buffer). [189]

Protein-protein interactions can be studied using Förster resonance energy transfer (FRET). FRET occurs when two fluorophores, a donor and acceptor, are in close proximity to each other (<10nm) and their emission spectra overlap. FRET is detected when the donor and acceptor come into contact and the excited energy from the donor is transferred non-radiactively to the acceptor who is in its ground state[190], for example when two tagged proteins interact. This gives conformational changes of lifetime quenching detected using FLIM. It has also been used to monitor post-translational modifications (PTMs) such as phosphorylation.[191] PTMs are of huge interest at the moment as it is believed that certain PTMs are the molecular beginning of certain cancer states.

As discussed previously, oxygen is the key metabolite in cellular functions. $O_2$ sensors are based on fluorescent quenchers. Quenching reduces the fluorescent lifetime, which

can be detected accurately using FLIM techniques.[192] This has been discussed in more detail in *section 1.8*.

The luminescent lifetime of transition metal complexes is sensitive to its environment, including viscosity, whereby the complex is polarized. Changes in the viscosity within the cell membrane have been linked to various diseases such as Alzheimer's, cystic fibrosis, and diabetes.[94] FLIM imaging can therefore be used to accurately monitor and study the local viscosity, cell membrane fluidity, and lipid packing in cells using suitable polypyridyl complexes.[193,194]

## 1.14 Resonance Raman Spectroscopy

Resonance Raman spectroscopy is a form of vibrational spectroscopy where, rather than absorbing light, light is scattered by a vibrating molecule creating vibrational transition frequency bands that are characteristic of the structure of the compound. This analytical method can be employed to determine the chemical structure of molecules, and examine their interactions at a molecular level.

Figure 1.35 shows a simplified energy level diagram which illustrates the vibrational and electronic energy levels of a molecule and the origin of a Raman transition. In conventional Raman, vibrational transitions occur when there is an energy exchange between the photon and the scattering molecule. The exciting laser, which is too low in energy to stimulate an electronic transition, stimulates the molecule to transit to a short-lived virtual state. The molecule relaxs from this state, exchanges energy with the incident photon, and returns to a different vibrational state. It is the difference in this energy shift from the absorbed and emitted photon that gives rise to Raman scattering. If the molecule gains energy and returns to a higher stat, the emitted photon will shift to a lower frequency, resulting in Stokes scattering. If the molecule returns to a lower state, it will shift to a higher frequency, known as an anti-Stokes shift. If there is no scattering of light and the molecule returns to the same vibrational state, then Raleigh scattering will occur. The vibrational information is analogous to IR spectroscopy. However, as Raman is a scattering phenomenon, unlike IR spectroscopy which is an absorbance spectroscopy, the incident light does not have to match the energy of the vibrational

transition it is instigating. In conventional Raman, a laser, often visible light which is at a frequency outside of the absorbance spectrum, is used. [195]

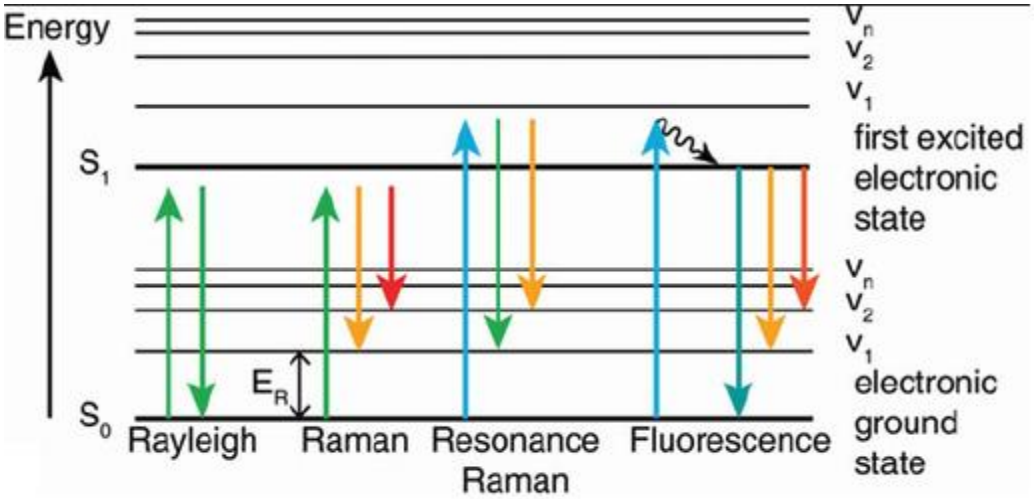


**Figure 1.35** Jablonski diagram showing the typical vibrational and electronic energy levels of a molecule. The upward arrows depict excitation by a light source, and the downward arrows depict the resulting emitted photon detected.[196]

### 1.14.1 Resonance Raman Spectroscopy

Resonance Raman spectroscopy, which is used in this thesis, is a special case of Raman spectroscopy which occurs when the exciting laser matches an electronic transition of a molecule, leading to the population of an electronically excited state. The principle of resonance Raman spectroscopy is illustrated above in Figure 1.34. Because the exciting laser excites the sample to a vibronic state, vibrational modes associated with that transition are greatly enhanced. This enhancement of the scattering gives higher frequency signals than traditional Raman, with intensities up to 6 orders of magnitudes higher, which allows for components at low concentrations to be detected.[197] Only the parts of the molecule involved in the transition are enhanced. Therefore, the resonance Raman spectra associated with this absorption region of the molecule will be enhanced and distinguished. This yields much simpler Raman spectra, which reveal the molecular origin of the optical transition. Figure 1.36 shows the resonance Raman spectra of the complex $[(bpy)_2Ru(MQ')_2]^{2+}$ in 0.1 M $CH_3CN$ solution when excited into the different wavelengths 363 nm, 457 nm, and 568 nm. This demonstrates an example where exciting into the different optical transitions of the complex results in resonance spectra

with different absorbances. For example, when excited at 363 nm, there is a peak centred on 800 $cm^{-1}$, which does not appear when excited at the other wavelengths. The vibrational band 920 $cm^{-1}$ is used as the non-resonant marker as this peak was unaffected at the different wavelengths.[198]

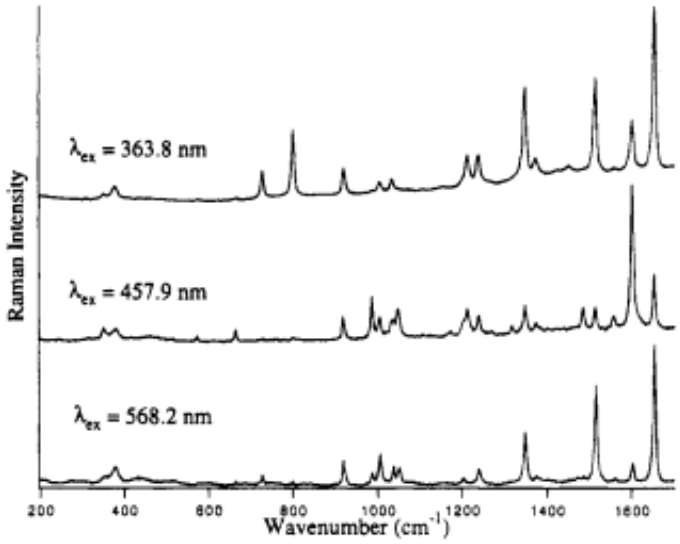


**Figure 1.36** Resonance Raman spectra of $[(bpy)_2Ru(MQ')_2]^{2+}$ complex in 0.1 m $CH_3CN$ solution excited at different wavelengths.[198]

Using resonance Raman makes it possible to identify optical transitions, and because of increased sensitivity over conventional Raman, to directly probe and monitor molecule interactions within cellular proteins and membranes. In the visible range, resonance Raman is used to probe biological samples such as carotenoids. In the UV range, aromatic molecules and functional groups are specifically detected.[199]

Resonance Raman of live cells has the ability to provide detailed information on cellular biochemical and in analysing the compositions of the different cell compartments within the cell label free, although the cell components such as proteins tend to require UV excitation for resonance enhancement.

Label free resonance Raman of live cells has the ability to provide detailed information on cellular biochemicals and in analysing the compositions of the different cell compartments within the cell. The dye distribution and structure can be tracked and probed from within the cell with great sensitivity.[149, 200] Raman is not influenced by oxygen concentration or other environmental factors. Figure 1.37 shows a Raman map of a CHO cell and the corresponding spectra from the nucleus, cytoplasm and membrane.[201] here they have calibrated specific peaks associated with the DNA, proteins, and lipids in the different regions. This information can be used to track changes to specific peaks when monitoring interactions or the effects of changes to the cells environment.

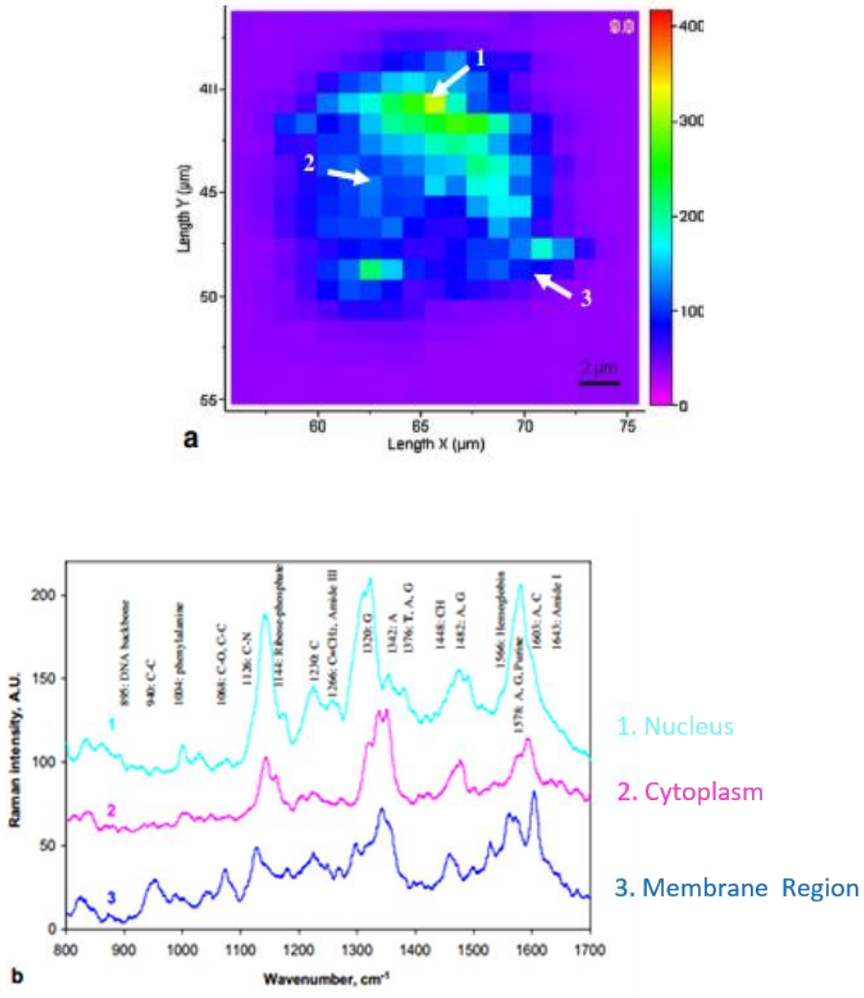


**Figure 1.37** Raman map of a CHO cell (a) and the corresponding spectra of the nucleus (1), cytoplasm (2), and membrane (3) respectively (b).[149]

Labels can be introduced to a sample to map distributions and interactions within a sample. Ideal labels possess strong Raman signals with specific unique marker bands to track in the sample. For example, introducing a C=C (≤ 1800 cm-1) or C≡C (≥ 2900 cm-1) stretching modes are very useful as they are seen at very isolated spectral regions that do not interfere with the sample.[199]

The MLCT transitions of polypyridyl complexes such as Ruthenium and Osmium give strong resonance Raman signals and, due to their large Stokes shift, there is very little fluorescence interference, making them ideal labels for Raman mapping. Ligands such as bipyridine exhibit strong Raman signals at specific peak positions when resonant with the MLCT such as 1603, 1560, 1480, 1315 1270, 1025, and 665 $cm^{-1}$. These signature peaks are useful in tacking the complex in the cell.

Labelling probes have been used to monitor the cellular environment in response to changes in oxygen and pH. Our group have shown that the resonance Raman spectra of $Ru(bpy)_2(pic\text{-}arg_8)]^{2+}$ complex was pH dependent in the cell, but was insensitive to oxygen. By working out a ratio of a pH dependent marker peak and pH independent peak and calibration plot of Raman spectra varying pH was developed. Therefore, the pH of the different cellular components can be probed and measured without directly compromising with the cell.[149]

## 1.15 Conclusions

Luminescent transition metal complexes are finding increasing application across cell imaging and sensing. This is driven by their very attractive photophysical properties and growing understanding regarding their permeability and targeting within cells. As shown in this review, the theory behind transition metal complex photophysics has highlighted their valuable characteristics as applied to cell imaging. Their long luminescent lifetimes, large Stokes shifts, good photostability and sensitivity to the environment make attractive candidates in the field of bio-imaging and diagnostics. There has been extensive literature reports on transition metal complexes, in particular Ru(II) polypyridyl complexes, as novel probes cell imaging and sensing. The ability to target such complexes to cross the cell membrane, localise in specific organelles, and sense from within has been improved dramatically in the past decade, by using ancillary

ligands for lipophilicity, sugar conjugates, PEGylation, and cell penetrating peptide sequences. The future of transition metal fluorescent probes lies in the development of such probes to be applied to new emerging imaging techniques such as super-resolution microscopy, for example STED, to allow for live cell imaging while obtaining high contrast images with little background noise. To date, there has been little application of STED to studying biological activities. Most of the reported work is on the improved spatial resolution over general confocal, and the development of STED probes in live cells. But these probes have not shown any sensing abilities in vivo. Therefore, future work will have to focus on developing STED-suitable fluorescent probes with high quantum yields and photostability that can also be utilised as environmental sensors in live cells and tissues.

The aim of this thesis is to apply novel luminescent metal-ligand complexes to cell use. To carry out our optical/photophysical characterization of complexes, novel $[Os(bpy)_2(pic\text{-}arg_8)]^{10+}$ complex will be assessed as a multimodal imaging tool and compared to the widely used Ru(II) equivalent, demonstrated in Chapter 2.

Chapter 3 will highlight the characteristics of oxygen sensor probe $Ru(bpy)_2$phen-COOH and its peptide conjugate $Ru(bpy)_2$phen-FrFKFrFK. The aim of this chapter is to direct the complex across the cell membrane and to the mitochondria to measure $O_2$ concentration from within the cell.

Chapter 4 will focus on a ratio-metric, core shell nano particle probe to measure oxygen concentration in cells. It consists of BODIPY complex as a reference probe located in the core of the sturcture, and an oxygen-sensitive Ru(II) complex on the outside. Based on the ratiometric emission intensites of the two probes, oxygen concentration can be measured using confocal microscopy.

Finally, Chapter 5 will explore the application of Ru(II) polypyridyl complexes for STimulated Emission Depletion microscopy. The Ru(II) probes are conjugated to CPPs, for precise targeting of the endoplasmic reticulum and the nucleus, which allows excellent high resolultion images to be acquired by discriminating against any background noise in the cell.

## *References*


1. Gill MR, Thomas JA. Ruthenium(II) polypyridyl complexes and DNA—from structural probes to cellular imaging and therapeutics. *Chemical Society Reviews*. 2012;41:3179.

2. Ebrecht R, Paul CD, Wouters FS. Fluorescence lifetime imaging microscopy in the medical sciences. *Protoplasma*. 2014;251:293-305.

3. Juris A, Balzani V, Barigelletti F, Campagna S, Belser P, von Zelewsky A. Ru(II) polypyridine complexes: Photophysics, photochemistry, eletrochemistry, and chemiluminescence. *Coord Chem Rev*. 1988;84(0):85-277.

4. Caspar JV, Meyer TJ. Photochemistry of ru(bpy)$_3^{2+\cdot}$ solvent effects. *J Am Chem Soc*. 1983;105:5583-5590.

5. Balzani V, Juris A. Photochemistry and photophysics of ru(II) polypyridine complexes in the bologna group. from early studies to recent developments. *Coord Chem Rev*. 2001;211(1):97-115.

6. Nakamaru K. Synthesis, luminescence quantum yields, and lifetimes of trischelated ruthenium (II) mixed-ligand complexes including 3,3'-dimethyl-2,2'-bipyridyl. *Bull Chem Soc Jpn*. 1982;55:2697.

7. Ma D, He H, Leung K, Chan DS, Leung C. Bioactive luminescent transition-metal complexes for biomedical applications. *Angew Chem Int Ed*. 2013;52:7666-7682.

8. Delaney S, Pascaly M, Bhattacharya PK, Han K, Barton JK. Oxidative damage by ruthenium complexes containing the dipyridophenazine ligand or its derivatives: A focus on intercalation. *Inorganic Chemistry*. 2002;41:1966-1974.

9. Friedman AE, Chambron J, Sauvage J, Turro NJ, Barton JK. Molecular ‘‘Light switch” for DNA: Ru(bpy)2(dppz)$^{2+}$. *J Am Chem Soc*. 1990;112:4960-4962.

10. McConnell AJ, Song H, Barton JK. Luminescence of [ru(bpy)2(dppz)]2+ bound to RNA mismatches. *Inorg Chem*. 2013;52:10131-10136.

11. Ferna´ndez-Moreira V, Thorp-Greenwood FL, Coogan MP. Application of d6 transition metal complexes in fluorescence cell imaging. *Chem. Commun.* 2010;46:186.

12. Turro C, Bossmann SH, Jenkins Y, Barton JK, Turro NJ. Proton transfer quenching of the MLCT excited state of ru(phen)2dppz2+ in homogeneous solution and bound to DNA. *J Am Chem Soc*. 1995;117:9026-9032.

13. Chen W, Turro C, Friedman LA, Barton JK, Turro NJ. Resonance raman investigation of ru(phen)2(dppz)2+ and related complexes in water and in the presence of DNA. *J Phys Chem B*. 1997;101:6995-7000.

14. Pellegrin Y, Forster RJ, Keyes TE. pH dependent photophysics and role of medium on photoinduced electron transfer between ruthenium polypyridyl complex and anthraquinone. *Inorg Chim Acta*. 2009;362(6):1715-1722.

15. Shaw GB, Styers-Barnett DJ, Gannon EZ, Granger JC, Papanikolas JM. Interligand electron transfer dynamics in [os(bpy)3]2+: Exploring the excited state potential surfaces with femtosecond spectroscopy. *J Phys Chem A,*. 2004;108:4998-5006.

16. Moucheron C, Kirsch-De Mesmaeker A, Kelly JM. Photoreactions of ruthenium (II) and osmium (II) complexes with deoxyribonucleic acid (DNA). *Journal of Photochemistry and Photobiology B: Biology*. 1997;40(2):91-106

17. Lakowicz JR. *Principles of fluorescence spectroscopy*. Vol Third Edition. Springer; 2006:954.

18. van Rijt SH, Kostrhunova H, Brabec V, Sadler PJ. Functionalization of osmium arene anticancer complexes with (poly)arginine: Effect on cellular uptake, internalization, and cytotoxicity. *Bioconjugate Chem*. 2011;22:218-226.

19. van Rijt SH, Mukherjee A, Pizarro AM, Sadler PJ. Cytotoxicity, hydrophobicity, uptake, and distribution of osmium(II) anticancer complexes in ovarian cancer cells. *J Med Chem*. 2010;53:840-849.

20. Kostrhunova H, Florian J, Novakova O, Peacock AFA, Sadler PJ, Brabec V. DNA interactions of monofunctional organometallic osmium(II) antitumor complexes in cell-free media. *J Med Chem 2008, 51, 3635–3643*. 2008;51:3635-3643.

21. van Rijt SH, Romero-Canelón I, Fu Y, Shnyder SD, Sadler PJ. Potent organometallic osmium compounds induce mitochondria-mediated apoptosis and S-phase cell cycle arrest in A549 non-small cell lung cancer cells. *Metallomics*. 2014;6:1014-1022.

22. Hearn JM, Romero-Canelón I, Munro AF, et al. Potent organo-osmium compound shifts metabolism in epithelial ovarian cancer cells. *Proc Natl Acad Sci U S A*. 2015;112:3800-3805.

23. Dobrucki JW. Interaction of oxygen-sensitive luminescent probes ru(phen) and 3 21 ru(bipy) with animal and plant cells in vitro 3 mechanism of phototoxicity and conditions for non-invasive oxygen measurements. *Journal of Photochemistry and Photobiology B: Biology*. 2001;65:136-144.

24. Peacock AFA, Habtemariam A, Ferna´ndez R, et al. Tuning the reactivity of osmium(II) and ruthenium(II) arene complexes under physiological conditions. *J. Am. Chem. Soc.* 2006;128:1739.

25. Fuchs SM, Rainesa RT. Internalization of cationic peptides: The road less (or more?) travelled. *Cell Mol Life Sci*. 2006;63:1819-1822.

26. Jones SW, Christison R, Bundell K, et al. Characterisation of cell-penetrating peptide-mediated peptide delivery. *British Journal of Pharmacology*. 2005;145:1093-1102.

27. Li SP, Lau CT, Louie M, Lam Y, Cheng SH, Lo KK. Mitochondria-targeting cyclometalated iridium(III)–PEG complexes with tunable photodynamic activity. *Biomaterials*. 2013;34:7519-7532.

28. Marin V, Holder E, Hoogenbooma R, Schubert US. Functional ruthenium(II)- and iridium(III)-containing polymers for potential electro-optical applications. *Chem Soc Rev*. 2007;36:618-635.

29. Komatsu H, Yoshihara K, Yamada H, et al. Ruthenium complexes with hydrophobic ligands that are key factors for the optical imaging of physiological hypoxia. *Chem Eur J*. 2013;19:1971-1977.

30. Lo KK, Hui W. Design of rhenium(I) polypyridine biotin complexes as a new class of luminescent probes for avidin. *Inorg Chem*. 2005;44:1992-2002.

31. Horobin RW, Rashid-Doubell F, Pediani JD, Milligan G. Predicting small molecule fluorescent probe localization in living cells using QSAR modeling. 1. overview and models for probes of structure, properties and function in single cells. *Biotechnic & Histochemistry,*. 2013;88:440-460.

32. Horobin RW, Stockert JC, Rashid-Doubell F. Fluorescent cationic probes for nuclei of living cells: Why are they selective? A quantitative structure–activity relations analysis. *Histochem Cell Biol*. 2006;126:165-175.

33. Horobin RW, Stockert JC, Rashid-Doubell F. Uptake and localisation of small-molecule fluorescent probes in living cells: A critical appraisal of QSAR models and a case study concerning probes for DNA and RNA. *Histochem Cell Biol*. 2013;139:623-637.

34. Horobin RW, Rashid-Doubel F. Predicting small molecule fl uorescent probe localization in living cells using QSAR modeling. 2. specifying probe, protocol and cell factors; selecting QSAR models; predicting entry and localization. *Biotechnic & Histochemistry*. 2013;88:461-476.

35. Madani F, Lindberg S, Langel U, Futaki S, Graslund A. Mechanisms of cellular uptake of cell-penetrating peptides. *J Biophys*. 2011;2011:414729.

36. Komor AC, Barton JK. The path for metal complexes to a DNA target. *Chemical Communications*. 2013;49(35):3617.

37. Lodish H, Berk A, Zipursky SL, Matsudaira P, Baltimore D, Darnell JE, eds. *Molecular cell biology*. 2000. W.H. Freeman New York, ed. ; No. 4th ed.

38. Puckett CA, Barton JK. Mechanism of cellular uptake of a ruthenium polypyridyl complex. *Biochemistry*. 2008;47:11711-11716.

39. Puckett CA, Ernst RJ, Barton. J.K. Exploring the cellular accumulation of metal complexes. *Dalton Trans*. 2010;39:1159-1170.

40. Heitz F, Morris MC, Divita G. Twenty years of cell-penetrating peptides: From molecular mechanisms to therapeutics. *British Journal of Pharmacology*. 2009;157:195-206.

41. Deshayes S, Morris MC, Divita G, Heitz F. Cell-penetrating peptides: Tools for intracellular delivery of therapeutics. *Cell Mol Life Sci*. 62;2005:1839-1849.

42. Lu Y, Low PS. Folate-mediated delivery of macromolecular anticancer therapeutic agents. *Advanced Drug Delivery Reviews*. 2002;54:675-693.

43. Arnott JA, Planey SL. The influence of lipophilicity in drug discovery and design. *Expert Opin Drug Discov*. 2012;7:863-875.

44. Tang TS, Yip AM, Zhang KY, et al. Bioorthogonal labeling, bioimaging, and PhotocytotoxicityStudies of phosphorescent ruthenium(II) PolypyridineDibenzocyclooctyne complexes. *Chem Eur J*. 2015;21:1-13.

45. Law WH, Lee LC, Louie M, Liu H, Ang TW, Lo KK. Phosphorescent cellular probes and uptake indicators derived from cyclometalated iridium(III) bipyridine complexes appended with a glucose or galactose entity. *Inorg Chem*. 2013;52:13029-13041.

46. Lv G, Guo L, Qiu L, et al. Lipophilicity-dependent ruthenium N-heterocyclic carbene complexes as potential anticancer agents. *Dalton Trans*. 2015;44:7324.

47. Mazuryk O, Magiera K, Rys B, Suzenet F, Kieda C, Brindell M. Multifaceted interplay between lipophilicity, protein interaction and luminescence parameters of non-intercalative ruthenium(II) polypyridyl complexes controlling cellular imaging and cytotoxic properties. *J Biol Inorg Chem*. 2014;19:1305-1316.

48. Ross MF, Filipovska A, Smith RA, Gait MJ, Murphy MP. Cell-penetrating peptides do not cross mitochondrial membranes even when conjugated to a lipophilic cation: Evidence against direct passage through phospholipid bilayers. *Biochem J*. 2004;383:457-468.

49. Mahon KP, Potocky TB, Blair D, et al. Deconvolution of the cellular oxidative stress response with organelle-specific peptide conjugates. *Chemistry & Biology*. 2007;14:923-930.

50. Dickerson M, Sun Y, Howerton B, and Glazer EC. Modifying charge and hydrophilicity of simple ru(II) polypyridyl complexes radically alters biological activities: Old complexes, surprising new tricks. *Inorg Chem*. 2014;53:10370-10377.

51. Svensson FR, Matson M, Li M, Lincoln P. Lipophilic ruthenium complexes with tuned cell membrane affinity and photoactivated uptake. *Biophys Chem*. 2010;149(3):102-106.

52. Mandal S, Poria DK, Ghosh R, Ray PS, Gupta P. Development of a cyclometalated iridium complex with specific intramolecular hydrogen-bonding that acts as a fluorescent marker for the endoplasmic reticulum and causes photoinduced cell death. *Dalton Trans*. 2014;43:17463.

53. Mandal S, Poria DK, Ghosh R, Ray PS, Gupta P. Development of a cyclometalated iridium complex with specific intramolecular hydrogen-bonding that acts as a fluorescent marker for the endoplasmic reticulum and causes photoinduced cell death. *Dalton Trans*. 2014;43:17463.

54. Samanta D, Kratz K, Zhang X, Emrick T. A synthesis of PEG- and phosphorylcholine-substituted pyridines to afford water-soluble ruthenium benzylidene metathesis catalysts. *Macromolecules*. 2008;41:530-532.

55. Lo KK. Luminescent rhenium(I) and iridium(III) polypyridine complexes as biological probes, imaging reagents, and photocytotoxic agents. *Acc Chem Res*. 2015;48:2985-2995.

56. Li SPY, Liu HW, Zhang KY, Lo KK. Modification of luminescent iridium(III) polypyridine complexes with discrete poly(ethylene glycol) (PEG) pendants: Synthesis, emissive behavior, intracellular uptake, and PEGylation properties. *Chem Eur J*. 2010;16:8329-8339.

57. Li PY, Lau CTS, Louie MW, Lam YW, Cheng SH, Lo KKW. Mitochondria-targeting cyclometalated iridium(III)-PEG complexes with tunable photodynamic activity. *Biomaterials*. 2013;34:7519-7532.

58. Louie M, Liu H, Lam MH, Lam Y, Lo KK. Luminescent rhenium(I) polypyridine complexes appended withan a-d-glucose moiety as novel biomolecular and cellular Probes. *Chem Eur J*. 2011;17:8304-8308.

59. Ndinguri MW, Solipuram R, Gambrell RP, Aggarwal S, Hammer RP. Peptide targeting of platinum anti-cancer drugs. *Bioconjugate Chem*. 2009;20:1869-1878.

60. Brooks H, Lebleu B, Vivès E. Tat peptide-mediated cellular delivery: Back to basics. *Adv Drug Deliv Rev*. 2005;57(4):559-577.

61. Yousif LF, Stewart KM, O. Kelley S. Targeting mitochondria with organelle-specific compounds: Strategies and applications. *ChemBioChem*. 2009;10:1939-1950.

62. Horton KL, Stewart KM, Fonseca SB, Guo G, O. Kelley S. Mitochondria-penetrating peptides . *Chemistry & Biology*. 2008;15:375-382.

63. Jean SR, Tulumello DV, Wisnovsky SP, Lei EK, Pereira MP, O. Kelley S. Molecular vehicles for mitochondrial chemical biology and drug delivery. *ACS Chem Biol*. 2014;9:323-333.

64. Blackmore L, Moriarty R, Dolan C, et al. Peptide directed transmembrane transport and nuclear localization of ru(II) polypyridyl complexes in mammalian cells. *Chem Commun*. 2013;49:2658.

65. Boulikas T. Putative nuclear localization signals (NLS) in protein T ran scr i pt io n factor. *Journal of Cellular Biochemistry*. 1994;55:32-58.

66. Fuchs SM, Raines RT. Pathway for polyarginine entry into mammalian cells. *Biochemistry*. 2004;43:2438-2444.

67. Neugebauer U, Pellegrin Y, Devocelle M, et al. Ruthenium polypyridyl peptide conjugates: Membrane permeable probes for cellular imaging. *Chem Commun*. 2008;42:5307-5309.

68. Al-Taei S, Penning NA, Simpson JC, et al. Intracellular traffic and fate of protein transduction domains HIV-1 TAT peptide and octaarginine. implications for their utilization as drug delivery vectors. *Bioconjugate Chem*. 2006;17:90-100.

69. Kloß A, Henklein P, Siele D, et al. The cell-penetrating peptide octa-arginine is a potent inhibitor of proteasome activities. *European Journal of Pharmaceutics and Biopharmaceutics*. 2009;72(1):219-225.

70. Pisani MJ, Weber DK, Heimann K, Collins JG, Keene RF. Selective mitochondrial accumulation of cytotoxic dinuclear polypyridyl ruthenium(II) complexes. *Metallomics*. 2010;2:393-396.

71. Ragin AD, Morgan RA, Chmielewski J. Cellular import mediated by nuclear localization signal peptide sequences. *Chem Biol*. 2002;9(8):943-948.

72. Brandén LJ, Mohamed AJ, Smith CIE. A peptide nucleic acid–nuclear localization signal fusion that mediates nuclear transport of DNA. *Nature Biotechnology*. 1999;17:784-787.

73. Heller A, Brockhoff G, Goepferich A. Targeting drugs to mitochondria. *European Journal of Pharmaceutics and Biopharmaceutics*. 2012;82(1):1-18

74. Pisani MJ, Weber DK, Heimann K, Collins JG, Keene FR. Selective mitochondrial accumulation of cytotoxic dinuclear polypyridyl ruthenium(II) complexes. *Metallomics*. 2010;2:393-396.

75. Kondrashina AV, Dmitriev RI, Borisov SM, et al. A phosphorescent nanoparticle-based probe for sensing and imaging of (intra)cellular oxygen in multiple detection modalities. *Adv Funct Mater*. 2012;22:4931-4939.

76. Frantz M, Wipf P. Mitochondria as a target in treatment . *Environmental and Molecular Mutagenesis*. 2010;51:462-475.

77. Ferna´ndez-Carneado J, Van Gool M, Martos V, et al. Highly efficient, nonpeptidic oligoguanidinium vectors that selectively internalize into mitochondria . *J Am Chem Soc*. 2005;127:869.

78. Malhi SS, Murthy RSR. Delivery to mitochondria: A narrower approach for broader therapeutics. *Expert Opin Drug Deliv*. 2012;9:909.

79. Yousif LF, Stewart KM, Horton KL, O. Kelley S. Mitochondria-penetrating peptides: Sequence effects and model cargo transport. *ChemBioChem*. 2009;10:2081-2088.

80. Tan C, Wu S, Lai S, et al. Synthesis, structures, cellular uptake and apoptosis-inducing properties of highly cytotoxic ruthenium-norharman complexes. *Dalton Trans*. 2011;40:8611.

81. Nepomnyashchii AB, Cho S, Rossky PJ, Bard AJ. Dependence of electrochemical and electrogenerated chemiluminescence properties on the structure of BODIPY dyes. unusually large separation between sequential electron transfers . *J Am Chem Soc*. 2010;132:17550-17559.

82. Jiao L, Yu C, Uppal T, et al. Long wavelength red fluorescent dyes from 3,5-diiodo-BODIPYs. *Org Biomol Chem*. 2010;8:2517-2519.

83. Martin A, Long C, Forster RJ, Keyes TE. Near IR emitting BODIPY fluorophores with mega-stokes shiftsw . *Chem Commun*. 2012;48:5617-5619.

84. Kowada T, Maedab H, Kikuch K. BODIPY-based probes for the fluorescence imaging of biomolecules in living cells. *Chem Soc Rev*. 2015;44:4953.

85. Zheng Q, Xu G, Prasad PN. Conformationally restricted dipyrromethene boron difluoride (BODIPY) dyes: Highly fluorescent, multicolored probes for cellular imaging. *Chem Eur J*. 2008;14:5812-5819.

86. Izumi H, Torigoe T, Ishiguchi H, et al. Cellular pH regulators: Potentially promising molecular targets for cancer chemotherapy. *Cancer Treat Rev*. 2003;29(6):541-549.

87. Schindler M, Grabski S, Hoff E, Simon SM. Defective pH regulation of acidic compartments in human breast cancer cells (MCF-7) is normalized in adriamycin-resistant cells (MCF-7adr)† . *Biochemistry*. 1996;35:2812-2817.

88. Urano Y, Asanuma D, Hama Y, et al. Selective molecular imaging of viable cancer cells with pH-activatable fluorescence probes . *Nature Medicine*. 2009;15:104-109.

89. Boens N, Leen V, Dehaen W. Fluorescent indicators based on BODIPY. *Chem Soc Rev*. 2012;41:1130-1172.

90. Boens N, Qin W, Baruah M, et al. Rational design, synthesis, and spectroscopic and photophysical properties of a visible-light-excitable, ratiometric, fluorescent near-neutral pH indicator based on BODIPY . *Chem Eur J*. 2011;17:10924-10934.

91. Hoogendoorn S, Blom AEM, Willems LI, van der Marel GA, Overkleeft HS. Synthesis of pH-activatable red fluorescent BODIPY dyes with distinct functionalities. *Organic Letters*. 2011;13:5656-5659.

92. Kuimova MK, Yahioglu G, Levitt JA, Suhling K. Molecular rotor measures viscosity of live cells via fluorescence lifetime imaging. *J Am Chem Soc*. 2008;130:6672-6673.

93. Zhou Q, Lei W, Hou Y, et al. BODIPY-modified ru(II) arene complex—a new ligand dissociation mechanism and a novel strategy to red shift the photoactivation wavelength of anticancer metallodrugs†. *Dalton Trans*. 2013;42:2786.

94. Benniston AC, Copley G. Lighting the way ahead with boron dipyrromethene (bodipy) dyes . *Phys Chem Chem Phys*. 2009;21:4124-4131.

95. Yamada Y, Tomiyama Y, Morita A, Ikekita M, Aoki S. BODIPY-based fluorescent redox potential sensors that utilize reversible redox properties of flavin. *ChemBioChem*. 2008;9:853.

96. Bertout JA, Patel SA, Simon MC. The impact of O2 availability on human cancer. *Nat Rev Cancer*. 8;2008:967-975.

97. Ruggi A, van Leeuwen FWB, Velders AH. Interaction of dioxygen with the electronic excited state of ir(III) and ru(II) complexes: Principles and biomedical applications. *Coord Chem Rev*. 2011;255(21–22):2542-2554.

98. Zhong W, Urayama P, Mycek M. Imaging fluorescence lifetime modulation of a ruthenium-based dye in living cells: The potential for oxygen sensing. *J Phys D: Appl Phys*. 2003;1689:1695.

99. Papkovsky DB, O'Riordan TC. Emerging applications of phosphorescent metalloporphyrins. *Journal of Fluorescence,*. 2005;15:569-584.

100. Borisov SM, Nuss G, Klimant I. Red light-excitable oxygen sensing materials based on platinum(II) and palladium(II) benzoporphyrins. *Anal Chem*. 2008;80:9435-9442.

101. O'Mahony FC, O'Riordan TC, Papkovskaia N, Kerry JP, Papkovsky DB. Non-destructive assessment of oxygen levels in industrial modified atmosphere packaged cheddar cheese. *Food Control*. 2006;17(4):286-292.

102. Papkovsky DD, Ponomarev GV. Spectral-luminescent study of the porphyrin-diketones and their complexes. *Spectrochim Acta A*. 2001;57:1897-1905.

103. Dmitriev RI, Papkovsky DB. Optical probes and techniques for $O_2$ measurement in live cells and tissue . *Cell Mol Life Sci*. 2012;69:2025-2039.

104. Dmitriev RI, Zhdanov AV, Jasionek G, Papkovsky DB. Assessment of cellular oxygen gradients with a panel of phosphorescent oxygen-sensitive probes. *Anal Chem*. 2012;84:2930-2938.

105. Fercher A, Borisov SM, Zhdanov AV, Klimant I, Papkovsky DB. Intracellular $O_2$ sensing probe based on cell-penetrating phosphorescent nanoparticles. *ACS Nano*. 2011;5:5499-5508.

106. Dmitriev RI, Ropiak HM, Ponomarev GV, Yashunsky DV, Papkovsky DB. Cell-penetrating conjugates of coproporphyrins with oligoarginine peptides: Rational design and application for sensing intracellular $O_2$. *Bioconj Chem*. 2011;22:2507-2518.

107. Lebedev AY, Cheprakov AV, Sakadzˇic´ S, Boas DA, Wilson DF, Vinogradov SA. Dendritic phosphorescent probes for oxygen imaging in biological systems. *Appl Mater Interfaces*. 2009;1:1292-1304.

108. Gomes A, Fernandes E, Lima JLFC. Fluorescence probes used for detection of reactive oxygen species. *J Biochem Biophys Methods*. 2005;65(2–3):45-80.

109. Tiede LM, Cook EA, Morsey B, Fox HS. Oxygen matters: Tissue culture oxygen levels affect mitochondrial function and structure as well as responses to HIV viroproteins. *Cell Death Dis*. 2012;3:274.

110. Petros JA, Baumann AK, Ruiz-Pesini E, et al. mtDNA mutations increase tumorigenicity in prostate cancer. *Proc Natl Acad Sci USA*. 2005;102:719-724.

111. Penta JS, Johnson FM, Wachsman JT, Copeland WC. Mitochondrial DNA in human malignancy. *Mutation Research/Reviews in Mutation Research*. 2001;488(2):119-133.

112. Nagano T. Bioimaging probes for reactive oxygen species and reactive nitrogen species. *J Clin Biochem Nutr*. 2009;45:111-124.

113. Dickinson BC, Srikun D, Chang CJ. Mitochondrial-targeted fluorescent probes for reactive oxygen species. *Current Opinion in Chemical Biology*. 2010;14:50-56.

114. Murphy MP. How mitochondria produce reactive oxygen species. *Biochem J*. 2009;417:1-13.

115. Apel K, Hirt H. Reactive Oxygen Species: Metabolism, oxidative stress, and signal transduction . *Annu Rev Plant Biol*. 2004;55:373-399.

116. Kowaltowski AJ, de Souza-Pinto NC, Castilho RF, Vercesi AE. Mitochondria and reactive oxygen species. *Free Radical Biology and Medicine*. 2009;47(4):333-343.

117. Gerritsen HG, Sanders R, Draaijer A, Ince C, Levine YK. Fluorescence lifetime imaging of oxygen in living cells. *Journal of Fluorescence*. 1997;7(1):11.

118. Jacobson MD. Reactive oxygen species and programmed cell death. *TIBS*. 1996:83-86.

119. Barnham KJ, Masters CL, Bush AI. Neurodegenerative diseases and oxidative stress. *Nature Reviews Drug Discovery*. 2004;3:205-214.

120. Jenner P. Oxidative stress in parkinson's disease. *Annals of Neurology*. 2003;53:26-38.

121. Kalyanaraman B, Darley-Usmar V, Davies KJA, et al. Measuring reactive oxygen and nitrogen species with fluorescent probes: Challenges and limitations. *Free Radical Biology and Medicine*. 2012;52(1):1-6.

122. Zhao N, Wu Y, Wang R, Shia L, Chen Z. An iridium(III) complex of oximated 2,20 - bipyridine as a sensitive phosphorescent sensor for hypochlorite. *Analyst*. 2011;136:2277-2282.

123. Setsukinai K, Urano Y, Kakinuma K, Majima HJ, Nagano T. Development of novel fluorescence probes that can reliably detect reactive oxygen species and distinguish specific species. *The Journal of Biological Chemistry*. 2003;278:3170-3175.

124. Koide Y, Urano Y, Kenmoku S, Kojima H, Nagano T. Design and synthesis of fluorescent probes for selective detection of highly reactive oxygen species in mitochondria of living cells. *J Am Chem Soc*. 2007;129:10324-10325.

125. Mukhopadhyay P, Rajesh M, Yoshihiro K, Haskó G, Pacher P. Simple quantitative detection of mitochondrial superoxide production in live cells. *Biochem Biophys Res Commun*. 2007;358(1):203-208.

126. Park W, Han Y, Kim S, Kim S. *J Cellular BioChem*. 2007;102:98-109.

127. Balaban RS, Nemoto S, Finkel T. Mitochondria, oxidants, and aging. *Cell*. 2005;120:483-495.

128. Dmitriev RI, and Papkovsky DB. Optical probes and techniques for O2 measurement in live cells and tissue. *Cell Mol Life Sci*. 2012;69(12):2025-2039.

129. Feng Y, Cheng J, Zhou L, Zhou X, and Xiang H. Ratiometric optical oxygen sensing: A review in respect of material design. *Analyst*. 2012;137:4885.

130. Hara D, Komatsu H, Son A, Nishimoto S, Tanabe K. Water-soluble phosphorescent ruthenium complex with a fluorescent coumarin unit for ratiometric sensing of oxygen levels in living cells. *Bioconjugate Chem*. 2015;26:645-649.

131. Yoshihara T, Murayama S, Tobita S. Ratiometric molecular probes based on dual emission of a blue fluorescent coumarin and a red phosphorescent cationic iridium(III) complex for intracellular oxygen sensing. *Sensors 2015*. 2015;15:13503-13521.

132. Zhang G, Palmer GM, Dewhirst MW, Fraser CL. A dual-emissive-materials design concept enables tumour hypoxia imaging. *Nat Mat*. 2009;8:747-751.

133. Wu C, Bull B, Christensen K, McNeill J. Ratiometric single-nanoparticle oxygen sensors for biological imaging. *Angew Chem*. 2009,;121:2779-2783.

134. Doussineau T, Schulz A, Lapresta-Fernandez A, et al. On the design of fluorescent ratiometric nanosensors authors. *Chem –Eur J*. 2010;16:10290.

135. Koo YL, Cao Y, Kopelman R, Koo SM, Brasuel M, Philbert MA. Real-time measurements of dissolved oxygen inside live cells by organically modified silicate fluorescent nanosensors**.** *Anal Chem*. 2004;76:2498-2505.

136. Xu H, Aylott JW, Kopelman R, Miller TJ, Philbert MA. A real-time ratiometric method for the determination of molecular oxygen inside living cells using Sol−Gel-based spherical optical nanosensors with applications to rat C6 glioma. *Anal Chem*. 2001;73:4124-4133.

137. Lee YK, Ulbrich EE, Kim G, et al. Near infrared luminescent oxygen nanosensors with nanoparticle matrix tailored sensitivity. *Anal Chem*. 2010;82:8446-8455.

138. Choi NW, Verbridge SS, Williams RM, et al. Phosphorescent nanoparticles for quantitative measurements of oxygen profiles in vitro and in vivo. *Biomaterials*. 2012;33(9):2710-2722

139. Buck SM, Koo YL, Park E, et al. Optochemical nanosensor PEBBLEs: Photonic explorers for bioanalysis with biologically localized embedding. *Curr Opin Chem Biol*. 2004;8(5):540-546.

140. Wang X, Gorris HH, Stolwijk JA, et al. Self-referenced RGB colour imaging of intracellular oxygen. *Chem. Sci.* 2011(2):901.

141. Yoshihara T, Yamaguchi Y, Hosaka M, Takeuchi T, Tobita S. Ratiometric molecular sensor for monitoring oxygen levels in living cells. *Angew Chem Int Ed*. 2012;51:4148-4151.

142. Vonesch C, Aguet F, Vonesch J, Unser M. An introducction into fluorescence microscopy: The colored revolution of bioimaging. *IEEE Signal Processing Magazine*. 2006:20-31.

143. Nakano A. Spinning-disk confocal microscopy - a cutting-edge tool for imaging of membrane traffic. *Cell Struct Funct*. 2002;5:349-355.

144. Wang E, Babbey CM, Dunn KW. Performance comparison between the high-speed yokogawa spinning disc confocal system and single-point scanning confocal systems. *Journal of Microscopy*. 2005;218:148-159.

145. Sakurai T, Lanahan A, Woolls MJ, Li N, Tirziu D, Murakami M. Live cell imaging of primary rat neonatal cardiomyocytes following adenoviral and lentiviral transduction using confocal spinning disk microscopy. *J Vis Exp*. 2014;88:51666.

146. Egeblad M, Ewald AJ, Askautrud HA, et al. Visualizing stromal cell dynamics in different tumor microenvironments by spinning disk confocal microscopy. *Dis Model Mech*. 2008;2-3:155-167.

147. Forster RJ, Keyes TE, Vos In JG, eds. *Interfacial supermolecular assemblies, wiley:* . Wiley; 2003.

148. Paddock SW. Principles and practices of laser scanning confocal microscopy. *Molecular Biotechnology*. 16;2000:127-149.

149. Neugebauer U, Cosgrave L, Pellegrin Y, Devocelle M, forster RJ, Keyes TE. Mulitmodal, muliparameter cell imaging using ruthenium polypyridyl peptide conjugates. *Proc SPIE*. 2012;8427:84270C.

150. Xu W, Zuo J, Wang L, Ji L, Chao H. Dinuclear ruthenium(II) polypyridyl complexes as single and two-photon luminescence cellular imaging probes. *Chem Commun*. 2014;50:2123.

151. Zhao Q, Yu M, Shi L, et al. Cationic iridium(III) complexes with tunable emission color as phosphorescent dyes for live cell imaging. *Organometallics*. 2010;29:1085-1091.

152. Xiong L, Zhao Q, Chen H, et al. Phosphorescence imaging of homocysteine and cysteine in living cells based on a cationic iridium(III) complex. *Inorg Chem*. 2010;49:6402-6408.

153. Dolan C, Moriarty RD, Lestini E, Devocelle M, Forster RJ, Keyes TE. Cell uptake and cytotoxicity of a novel cyclometalated iridium(III) complex and its octaarginine peptide conjugate. *J Inorg Biochem*. 2013;119:65-74.

154. Balasingham RG, Coogan MP, Thorp-Greenwood FL. Complexes in context: Attempting to control the cellular uptake and localisation of rhenium fac-tricarbonyl polypyridyl complexes. *Dalton Trans.* 2011;40:11663.

155. Choi AW, Liu H, Lo KK. Rhenium(I) polypyridine dibenzocyclooctyne complexes as phosphorescent bioorthogonal probes: Synthesis, characterization, emissive behavior, and biolabeling properties. *J Inorg Biochem*. 2015;148(0):2-10

156. Hell SW, Wichmann J. Breaking the diffraction resolution limit by stimulated emission: Stimulated-emission-depletion fluorescence microscopy. *Opt Let*. 1994;19:780-782.

157. Hess ST, Girirajan TPK, Mason MD. Ultra-high resolution imaging by fluorescence photoactivation localization microscopy. *Biophys J*. 2006;91(11):4258-4272

158. Godin A, Lounis B, Cognet L. Super-resolution microscopy approaches for live cell imaging. *Biophys J*. 2014;107(8):1777-1784.

159. Heilemann M, Margeat E, Kasper R, Sauer M, Tinnefeld P. Carbocyanine dyes as efficient reversible single-molecule optical switch. *J Am Chem Soc 2005 Mar 23;127(11):3801-6*. 2005;127:3801-3806.

160. Rust MJ, Bates M, Zhuang X. Stochastic optical reconstruction microscopy (STORM) provides sub-diffraction-limit image resolution. *Nat Methods 2006 Oct; 3(10): 793–795*. 2006;3:793-795.

161. Kasper R, Harke B, Forthmann C, Tinnefeld P, Hell SW, Sauer M. Single-molecule STED microscopy with photostable organic fluorophores. *Small*. 2010;6:1379-1384.

162. Blom H, Brismar H. STED microscopy: Increased resolution for medical research? *Journal of Internal Medicine*. 2014;276:560-578.

163. Moneron G, Medda R, Hein B, Giske A, Westphal V, Hell SW. Fast STED microscopy with continuous wave fiber lasers. *Optics Express*. 2010;18:1302-1309.

164. Fernández-Suárez M, Ting AY. Fluorescent probes for superresolution imaging in living cell. *Nature Reviews Molecular Cell Biology*. 2008;9:929.

165. Kolmakov K, Wurm CA, Meineke DNH, et al. Polar red-emitting rhodamine dyes with reactive groups:Synthesis, photophysical properties, and two-color STED Nanoscopy applications. *Chem Eur J*. 2014;20:146-157.

166. Wildanger D, Medda R, Kastrup K, Hell SW. A compact STED microscope providing 3D nanoscale resolution. *Journal of Microscopy*. 2009;236:35-43.

167. Meyer L, Wildanger D, Medda R, et al. Dual-color STED microscopy at 30-nm focal-plane resolution. *Small*. 2008;4:1095-1100.

168. Klar TA, Jakobs S, Dyba M, Egner A, Hell SW. Fluorescence microscopy with diffraction resolution barrier broken by stimulated emission. *Proc Natl Acad Sci USA*. 2000;97:8206-8210.

169. Klar TA, Hell SW. Subdiffraction resolution in far-field fluorescence microscopy. *Optics Letters*. 1999;24:954-956.

170. Schmidt R, Wurm CA, Punge A, Egner A, Jakobs S, Hell SW. Mitochondrial cristae revealed with focused light. *Nano Lett*. 2009;9:2508-2510.

171. Urban N, Willig K, Hell S, Nägerl U . STED nanoscopy of actin dynamics in synapses deep inside living brain slices. *Biophys J*. 2011;101(5):1277-1284

172. Adam SA. The nuclear pore complex. *Genome Biol*. 2001;2:1-6.

173. Göttfert F, Wurm C, Mueller V, et al. Coaligned dual-channel STED nanoscopy and molecular diffusion analysis at 20 nm resolution. *Biophys J*. 2013;105(1):L01-L03

174. Lakowicz JR, Szmacinski H, Nowaczyk K, Johnson ML. Fluorescence lifetime imaging of calcium using quin-2. *Cell Calcium*. 1992;3:131-147.

175. Levitt JA, Kuimova MK, Yahioglu G, Chung P, Suhling K, Phillips D. Membrane-bound molecular rotors measure viscosity in live cells via fluorescence lifetime imaging. *J Phys Chem C,*. 2009, 113 (27);113:11634-11642.

176. Ryder AG, Glynn TJ, Przyjalgowski M, Szczupak B. A compact violet diode laser-based fluorescence lifetime microscope. *Journal of Fluorescence*. 2002;12:177-180.

177. Borst JW, Visser AJWG. Fluorescence lifetime imaging microscopy in life sciences. *Meas Sci Technol* 2010;21:1-21.

178. Suhling K, French PMW, Phillips D. Time-resolved fluorescence microscopy. *Photochem Photobiol Sci*. 2005;4:13-22.

179. Becker W. Fluorescence lifetime imaging – techniques and applications. *Journal of Microscopy*. 2012;247:119-136.

180. Becker W, ed. *Advanced time-correlated single-photon counting techniques.* Berlin/Heidelberg/New York: Springer; 2005.

181. Ballew RM, Demas JN. An error analysis of the rapid lifetime determination method for the evaluation of single exponential decays. *Anal Chem*. 1989;61:30-33.

182. Pawley J, ed. *Handbook of biological confocal microscopy.* Springer; 2006; No. 3rd edt.

183. Becker W. Fluorescence lifetime imaging – techniques and applications. *Journal of Microscopy*. 2012;247:119-136.

184. Festy F, Ameer-Beg SM, Ngab T, Suhling K. Imaging proteins in vivo using fluorescence lifetime microscopy. *Mol BioSyst*. 2007;3:381-391.

185. Dmitriev R, Kondrashina A, Foley T, Papkovsk DB. Imaging of molecular oxygen at subcellular resolution in mammalian cell culture: From 2D to 3D models (764.1). *The FASEB Journal*. 2014;28.

186. Sanders R, Draaijer A, Gerritsen HC, Houpt PM, Levine YK. Quantitative pH imaging in cells using confocal fluorescence lifetime imaging microscopy. *Anal Biochem*. 1995;227(2):302-308.

187. Hanson KM, Behne MJ, Barry NP, Mauro TM, Gratton E, Clegg RM. Two-photon fluorescence lifetime imaging of the skin stratum corneum pH gradient. *Biophys J*. 2002;83(3):1682-1690.

188. Gilbert D, Franjic-Würtz C, Funk K, Gensch T, Frings S, Möhrlen F. Differential maturation of chloride homeostasis in primary afferent neurons of the somatosensory system. *International Journal of Developmental Neuroscience*. 2007;25(7):479-489

189. Baggaley E, Gill MR, Green NH, et al. Dinuclear ruthenium(II) complexes as two-photon, time-resolved emission microscopy probes for cellular DNA. *Angew Chem Int Ed.* 2014;53:3367-3371.

190. Valeur B. *Molecular fluorescence: Principles and applications.* Wiley-VCH; 2001:399.

191. Stubbs CD, Botchway SW, Slater SJ, Parker AW. The use of time-resolved fluorescence imaging in the study of protein kinase C localisation in cells. *BMC Cell Biol*. 2005;6:1-12.

192. Dmitriev RI, Papkovsk DB. Optical probes and techniques for O2 measurement in live cells and tissue. *Cell Mol Life Sci*. 2012;69:2025-2039.

193. Suhling K, Cade NI, Levitt JA, et al. Fluorescence lifetime imaging applied to microviscosity mapping and fluorescence modification studies in cells . *Biomedical Imaging : The Chemistry of Labels, Probes and Contrast Agents*. 2012:371-390.

194. Stöckl MT, Herrmann A. Detection of lipid domains in model and cell membranes by fluorescence lifetime imaging microscopy. *Biochimica et Biophysica Acta (BBA) - Biomembranes*.2010;1798(7):1444-1456.

195. Robert B. Resonance raman spectroscopy. *Photosynth Res*. 2009;101:147-155.

196. Hooijschuura JH, Verkaaika MFC, Davies GR, Ariese F. Will raman meet bacteria on mars? an overview of the optimal raman spectroscopic techniques for carotenoid biomarkers detection on mineral backgrounds. *Netherlands Journal of Geosciences*. 2016;95:141-151.

197. Hong Z, Asher SA. Dependence of raman and resonance raman intensities on sample self-absorption. *App Spec*. 2015;69:75-83.

198. Bates WD, Chen P, Bignozzi CA, Schoonover JR, Meyer TJ. Resonance raman spectroscopy of ruthenium(II) and osmium(I1) polypyridyl complexes containing the N-methyl-4,4'-bipyridinium radical (MQ) as a ligand: Evidence for a M(dn) - MQ(R*) methl-to-ligand charge transfer (MLCT) transition . *Inorg Chem 1995,34, 6215-6217*. 1995;34:6215-6217.

199. Opilik L, Schmid T, Zenobi R. Modern raman imaging: Vibrational spectroscopy on the micrometer and nanometer scales . *Annu Rev Anal Chem*. 2013;6:379-398.

200. Cosgrave L, Devocelle M, Forster RJ, Keyes TE. Multimodal cell imaging by ruthenium polypyridyl labelled cellpenetrating peptides. *Chem Commun*. 2010;46:103-105.

201. Zhang X, Yin H, Cooper JM, Haswell SJ. Characterization of cellular chemical dynamics using combined microfluidic and raman techniques. *Anal Bioanal Chem*. 2008;390:833.

# Chapter Two: A Comparison of Ruthenium (II) and Osmium (II) Polypyridyl complex as a Luminophore for Cellular Imaging

## 2.1 Introduction

The demand for well-designed luminescent probes for live cell imaging and sensing is growing due to the improvements of luminescent-based imaging technologies available. Traditionally, organic fluorophores are the primary materials used as probes in fluorescence microscopy. However, such probes suffer drawbacks such as poor photostability, small Stokes shifts, poor solubility in aqueous solutions, and short lived emissive states. Inorganic probes based on transition metal complexes overcome these limitations, making them potentially very valuable as alternative probes for imaging purposes. To date, luminescent inorganic probes have focused on platinum group metals such as ruthenium and iridium complexes, which have been fairly widely studied in this context.[1-6] Osmium (II) polypyridyl complexes share many properties with the widely studied Ru(II) complexes, making them, in theory, useful imaging probes. In fact, some of their properties are superior to that of Ru(II). While Ru(II) polypyridyl complexes emit in the spectral range 600 to 700 nm, Os(II) complexes emit in the NIR region, well outside the auto fluorescence window, with an emission maximum typically between 700 and 850 nm. This strongly coincides with the biological window, ideal for imaging. They, like Ru(II) polypyridyl complexes, have a large Stokes shift which reduces self-quenching. Although they tend to have relatively short-lived emission lifetimes, Os(II) complexes are less likely to be quenched by oxygen. This can be an advantage in a cell imaging probe as quenching by oxygen in a cell can lead to the production of singlet oxygen, causing phototoxicity during the imaging process. Another advantage of Os(II) complexes is that their d-d states cannot be accessed by thermal cross-over from its excited triplet state, making Os(II) complexes more photostable than Ru(II) complexes. This also renders their photophysics temperature independent, ideal for studies which require incubating cells at 37 °C.[6, 7]

Until now, reports of osmium complexes in a biological context have been largely based on Os(II) as potential chemotherapeutic agents, and there have been no reports regarding Os(II) as an imaging agent. For example, the group of *Sadler et al* have extensively studied a group of Os(II) arene complexes as an anti-cancer agents.[8, 9] One of which they reported on was an Os(II) arene complex that was conjugated to an octa-arginine peptide sequence.[10] They demonstrated increased uptake and binding to nuclear DNA as a result of using the cell penetrating peptide (CPP) sequence octa-arginine ($Arg_8$). As discussed

in Chapter 1, cell penetrating peptides such as octa-arginine are widely used to carry molecular cargo across the cell membrane. With the appropriate modification to use ligands that are less labile, high toxicity can be avoided to generate a general probe suited to cell imaging rather than anti-cancer purposes.

The aim of this chapter was to evaluate a new NIR emitting Os(II) complex as a potential probe for cell imaging and sensing. The $[Os(bpy)_2(picCOOH)]^{2+}$ parent complex and its peptide conjugate $[Os(bpy)_2(pic\text{-}arg_8)]^{10+}$ were assessed as luminescent imaging probes, and compared to the ruthenium equivalent $[Ru(bpy)_2(pic\text{-}arg_8)]^{10+}$ which had been previously studied by *Neugebauer et al*.[11] The photophysical properties of $[Os(bpy)_2(pic\text{-}arg_8)]^{10+}$ were examined, and its ability to penetrate the cell membrane was assessed by means of confocal microscopy and using high through put analysing techniques. Its sensitivity to cellular environments was explored by fluorescence lifetime imaging microscopy (FLIM) techniques, as well as using Raman spectroscopy to examine the complex interactions inside the cell to assess, overall, its suitability as an imaging probe.

## 2.2 Materials and Methods

### 2.2.1 Materials

The $[Os(bpy)_2(picCOOH)]^{2+}$ parent complex was synthesized and characterized by Dr Ciaran Dolan (DCU).[12] The conjugation to the octa-arginine peptide was carried out by Dr Aaron Martin (DCU). Chemicals and solvents used in experimental procedures were all purchased from Sigma Aldrich (Ireland) unless otherwise stated. All solutions were made using deionised water, which was purified by a Milli-Q plus 18.5 Millipore purifying system.

Sp2/0-Ag 14 murine myeloma spleen cells (ATCC no. CRL-1518) and Chinese Hamster Ovarian (CHO) (CHO-K1 ATCC no. CCL-61) were purchased from ATCC Cell Biology Collection (UK). Resazurin reagents were acquired from Promokine. Cell culture media, serum and penicillin/streptomycin were purchased from Sigma. Cell culture flasks were purchased from Corning Incorporated.

### 2.2.2 Spectroscopic Measurements

The UV/Vis spectra were recorded on a Jasco V-679 UV/Vis/NIR spectrophotometer. Fluorescence emission and excitation were measured using a Cary Eclipse Fluorescence Spectrometer, both at a slit width of 5 nm. Solution measurements were carried out in 1% DMSO with PBS for the parent complex, and PBS only for the conjugate in a Hellma quartz cuvette of 1 cm optical path length.

### 2.2.3 Quantum Yield

The phosphorescent quantum yields of $[Os(bpy)_2(picCOOH)]^{2+}$ and $[Os(bpy)_2(pic\text{-}arg_8)]^{10+}$ were estimated by matching the MLCT absorbance transition with a standard $[Ru(bpy)_3]^{2+}$ in PBS solution [$\Phi_P = 0.028$ in PBS].[13] Both solutions were excited into the MLCT region of matched absorbance and the corresponding emission was recorded. The luminescent quantum yield was calculated by using the following formula in Equation 2.1:

$$\Phi_{P(x)} = (A_x/A_s)\,(F_s/F_x)\,(n_x/n_s)^2\,\Phi_{Ps} \quad \ldots\ldots \text{(Equation 2.1)}$$

Where $\Phi_P$ is the phosphorescent quantum yield, A is the absorbance at the excitation wavelength, F is the area under the corrected emission spectrum, and n is the refractive index of the solvent used. The subscripts s and x refer to the standard and unknown respectively. The quantum yield experiment was carried out three times and the average quantum yield is the reported value

### 2.2.4 Luminescent Lifetimes

The lifetimes were collected using a FluoTime 100 Time-Correlated Single Photon Counting (TCSPC) instrument. The 370 nm laser line was used to excite both the osmium and ruthenium complexes, provided from a Picoquant 'PDL 800-jB' pulsed diode laser. 10,000 counts were collected for each lifetime measurement. The measurements were carried out using either Picoquant Nanoharp software for ruthenium, or Picoquant Timeharp software for osmium. The luminescent lifetimes were calculated using the PicoQuant FluoFit software by fitting an exponential decay function to each decay plot. The data was then fit to a mono-exponential decay curve. The goodness of fit was evaluated by visual inspection of the residuals and by confirming the fit had a $\chi^2$ value between 0.9-1.1.

### 2.2.5 Cell Culture

The SP2 Myeloma suspension cell line were grown in Dulbecco's modified Eagle's medium (DMEM) with stable L-glutamine and the CHO cells in DMEM/Hams F-12, both supplemented with 10 % foetal calf serum and 1 % penicillin/streptomycin. Cells were kept at 37 °C with 5 % $CO_2$, and harvested when they 90 % confluency for CHO, and 1 x $10^6$ cells/mL for SP2 cells. CHO cells were harvested using 0.25 % trypsin for 5 minutes at 37 °C. CHO cells were seeded at 2.5 x $10^5$ cells in 2 mL media and SP2 cells were seeded at 2.5 x $10^5$ cells in 1.5 mL media on 35 mm glass bottom culture dishes and grown for 24 h. The media was removed and cells were washed with PBS solution supplemented with 1.1 mM $MgCl_2$ and 0.9 mM $CaCl_2$.

### 2.2.6 Real time confocal imaging

CHO and SP2 cells were seeded at 2.5 x $10^5$ cells in 1.5 mL Lebovitz on poly-L-lysine coated, 16 mm coverslips in a 12-well plate or 35 mm glass bottom culture dishes and left for 24 h at 37

ºC with 5 % $CO_2$. Either $[Os(bpy)_2(picCOOH)]^{2+}$ or $[Ru(bpy)_2(picCOOH)]^{2+}$ parent complexes (0.05 % v/v DMSO in PBS) or the octa-arginine conjugates (in aqueous PBS alone) were added to the cells to achieve a final concentration of 40 µM, and were left to incubate for various time intervals. The cells were washed with PBS (supplemented with 1.1 mM $MgCl_2$ and 0.9 mM $CaCl_2$) and imaged immediately, using a Zeiss LSM510 Meta Confocal microscope with a 63x oil immersion objective lens on a temperature-controlled stage at 37 °C. To assess temperature dependence of uptake, cells were prepared as described above, and incubated with the complex at 4 ºC. The cells were excited at 488 nm by an Argon ion laser and emission was collected using the long pass 650 nm filter set. For real-time imaging, 70 µM dye was added and cells were imaged immediately using the Time Series mode to capture images every 10 minutes over 120 minute period.

### 2.2.7 High-throughput Uptake Studies

Live high throughput (HTP) uptake study was carried out to monitor uptake over 2 hours. CHO cells were seeded at 2 x $10^4$ cells per well in a 96-well plate, and incubated overnight at 37 °C with 5 % $CO_2$. Nuclei were stained using Hoescht (200 µg/ml) which was added 20 minutes before measurements. The media was removed and the cells were washed once with PBS (supplemented with 1.1 mM $MgCl_2$ and 0.9 mM $CaCl_2$). The dye uptake rate was measured by reading five random fields of view per well, using an Insight Cell Analyzer 1000 by GE, with a 20x objective. The data was analysed using In Cell Analyzer 1000 Investigator program by measuring the intensity of the complex within the cell and taking away any background noise.

### 2.2.8 Cytotoxicity Studies

Both cell lines were seeded in a 96-well plate at 1 x $10^4$ in 100 µL of media, and left to incubate at 37 ° C at 5 % $CO_2$ for 24 hours. The compounds were added to the wells to give final concentrations of 200, 150, 100, 40, 10, 1 and 0.1 µM. The cells were incubated over night with the dyes. 10 µL Resazurin reagent (PromoKine) was added to each well, and incubated for 7 h in the dark at 37 °C. Absorbance readings were recorded using a Tecan 96-well plate reader at 570 nm and 600 nm for background subtraction. All cytotoxicity experiments are reported in terms of % viability, where 100% viability = 100% of viable cells in the well. Each experiment was carried out in triplicate (n=3 ± SD).

### 2.2.9 Phototoxicity Study

CHO cells were seeded at 2 x $10^5$ in 2 mL media on a 35 mm glass-bottom dish and grown for 24 h at 37 °C with 5 % $CO_2$. 500 µL media was removed and 70 µM of the parent and conjugate was added and left for a further 24 h. Images were recorded using a Zeiss LSM 510 Meta Confocal microscope with a 63x oil immersion objective lens and the heated stage was set up to 37 °C. DRAQ 7, a nuclear staining dye, was added to the culture dish (1:100 dilution). The 633 nm HeNe laser and 488 nm Argon laser were used to excite DRAQ 7 and osmium respectively. Emission was collected using the long pass 650 nm filter set for both dyes. An initial image was taken at t = 0 using the multi-track feature to show the loading of the osmium and that the cells were viable. The light was set to 1.36 x $10^{-15}$ mJ and the cells were left exposed for 3 h. Control cells were set up in the same manner, but without the addition of the osmium complex. DRAQ 7 nuclear stain was added and was exposed to 1.36 x $10^{-15}$ mJ light until DRAQ 7 had entered the cells.

### 2.2.10 Phosphorescent Lifetime Imaging Microscopy (PLIM)

For PLIM studies cell lines were seeded on 35 mm glass bottom culture dishes at densities stated in *section 2.2.5*. PLIM images were acquired using a Microtime 200 instrument by PicoQuant, with a 63x oil immersion objective lens with 256 x 256 resolution. The sample was imaged for 20 minutes to ensure high counts were obtained. The sample was excited using the 405 nm laser line, and the emission was collected using the filter suited for the complex. Data was analysed using PicoQuant Symphotime software to extract the lifetimes in different areas of the cell. An exponential decay function was fitted against the sample decay plot to get a tail fit with a $\chi^2$ between 0.9-1.1 for each location.

### 2.2.11 Resonance Raman spectroscopy and cell mapping

To acquire a resonance Raman spectra of $[Os(bpy)_2(picCOOH)]^{2+}$ and $[Ru(bpy)_2(picCOOH)]^{2+}$ parent and peptide conjugates, 70 µM solutions in 1 % ACN and PBS for parent complex, and PBS only for peptide conjugates, were pipetted on to 16x16 mm cover slips. Three separate locations of the solution on the slide were

measured to obtain an average spectrum of the complexes. For cell mapping, CHO cells were seeded on 35 mm glass bottom culture dishes and incubated with $[Os(bpy)_2(pic\text{-}arg_8)]^{10+}$ (70 μM) for 24 h. Raman spectra within different regions of live CHO was collected using a 50x Olympus objective coupled to a 488nm Argon laser. The Raman spectrometer was calibrated using the centre frequency of a silicon band at 520 $cm^{-1}$ from a silicon sample and the Rayleigh line. Three locations per cellular region were measured to obtain an average spectrum of each compound at that location. The spectra were baseline corrected and analysed using NSG LabSpec 5.0 software.

## 2.3 Photophysics

Scheme 2.1 illustrates the structures of $[Os(bpy)_2(picCOOH)]^{2+}$ (A), $[Os(bpy)_2(pic\text{-}arg_8)]^{10+}$ (B) and $[Ru(bpy)_2(pic\text{-}arg_8)]^{10+}$ (C) which are the focus of this study. The complexes are structurally analogous but for the identity of the coordinated metal. Both complexes belong to the d block of transition metals on the periodic table and have isoelectronic configurations, i.e. $d^6$ in their M(II) states. However ruthenium is a second and osmium a third row metal., the nuclear mass of osmium is therefore greater.

The parent complexes are conjugated to an octa-arginine ($Arg_8$) peptide sequence, *via* an amide bond, which renders the complexes cationic with an overall charge of 10+.

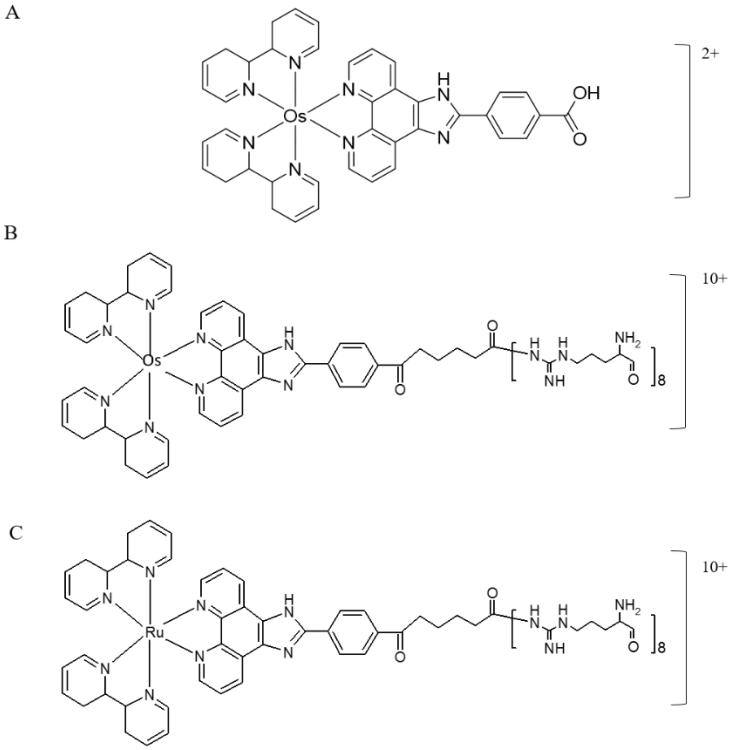


**Scheme 2.1** Chemical structures of $[Os(bpy)_2(picCOOH)]^{2+}$ parent complex (A), $[Os(bpy)_2(pic\text{-}arg_8)]^{10+}$ (B), and $[Ru(bpy)_2(pic\text{-}arg_8)]^{10+}$ (C).

Figure 2.1 shows representative optical spectroscopy of $[Os(bpy)_2(pic\text{-}arg_8)]^{10+}$ and $[Ru(bpy)_2(pic\text{-}arg_8)]^{10+}$ in PBS solution. $[Os(bpy)_2(pic\text{-}arg_8)]^{10+}$ complex exhibits a strong absorbance band at 486 nm ($\varepsilon \sim 4.7 \times 10^3$ L mol$^{-1}$ cm$^{-1}$) attributed to the $^1$MLCT transition. When excited into this $^1$MLCT absorbance, $[Os(bpy)_2(pic\text{-}arg_8)]^{10+}$ exhibits an emission maxima centred at 720 nm which is outside the auto-fluorescence window. The emission was shown to be unaffected by the conjugation of the $Arg_8$ peptide (Table 2.1). Both $[Os(bpy)_2(pic\text{-}arg_8)]^{10+}$ and $[Ru(bpy)_2(pic\text{-}arg_8)]^{10+}$ also have a strong absorbance band at approximately 285 nm, which may be assigned to the $\pi$-$\pi$* transitions within the bipyridine ligand, while a shoulder at approximately 330 nm is attributed to the pic ligand. As expected, the parent complexes exhibit large Stokes shifts in 1% DMSO and PBS. $[Os(bpy)_2(pic\text{-}arg_8)]^{10+}$ exhibited slightly red-shifted emission in PBS centered at 726 nm on conjugation. $[Ru(bpy)_2(pic\text{-}arg_8)]^{10+}$ exhibited an emission maximum centered at 610 nm. The luminescence from $[Os(bpy)_2(pic\text{-}arg_8)]^{10+}$ is at a lower energy than that from $[Ru(bpy)_2(pic\text{-}arg_8)]^{10+}$ due to the smaller gap between the Os(II) metal centre and the bpy ligand, and therefore the emission of $[Os(bpy)_2(pic\text{-}arg_8)]^{10+}$ is significantly lower in Figure 2.1 compared to $[Ru(bpy)_2(pic\text{-}arg_8)]^{10+}$ at the same concentration.

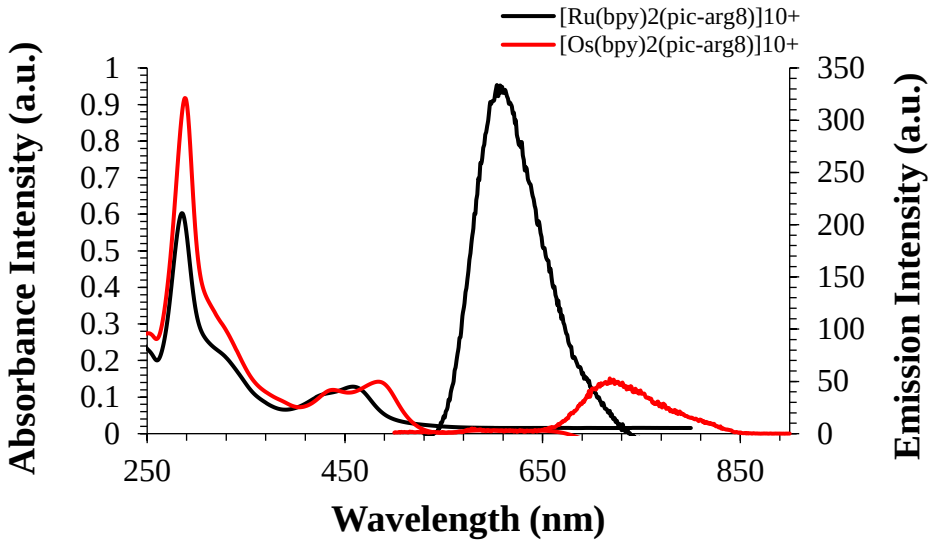


**Figure 2.1** Absorbance and emission spectra of $[Os(bpy)_2(pic\text{-}arg_8)]^{10+}$(—) and $[Ru(bpy)_2(pic\text{-}arg_8)]^{10+}$ (—) in aerated PBS solution (30 μM). $[Os(bpy)_2(pic\text{-}arg_8)]^{10+}$ was excited into the MLCT at 488 nm and the emission was collected between 500 – 900 nm. $[Ru(bpy)_2(pic\text{-}arg_8)]^{10+}$ was excited at 458 nm and the emission was collected between 520 – 750 nm, both at a slit width = 5nm.

Table 2.1 compares the spectroscopic properties of the complexes. The emission lifetimes were measured using Time Correlated Single Photon Counting (TCSPC). Figure 2.2 shows representative TCSPC emission lifetime decay traces of $[Os(bpy)_2(picCOOH)]^{2+}$ (A) and $[Os(bpy)_2(pic\text{-}arg_8)]^{10+}$ (B) in PBS solution at room temperature. A background measurement, an IRF, which is shown in red, was recorded using Ludox solution. This is deconvoluted from the Osmium decay to eliminate any contribution from the laser or electronics of the optical system. The lifetimes were obtained by iterative deconvolution so that the fit conformed to a $\chi^2$ value as close to 1 as possible. $[Os(bpy)_2(picCOOH)]^{2+}$ has a luminescent lifetime of 33 ± 0.1 ns (A). Upon conjugation, $[Os(bpy)_2(pic\text{-}arg_8)]^{10+}$ emission lifetime decreased slightly to 31 ± 0.2 ns, indicating that the peptide conjugation had a slight effect on the complex photophysical properties (B).The emission lifetime traces were fit to give a $\chi^2$ value between 0.9 and 1.1, and fit was also evaluated by visual inspection of the residuals of the fit.

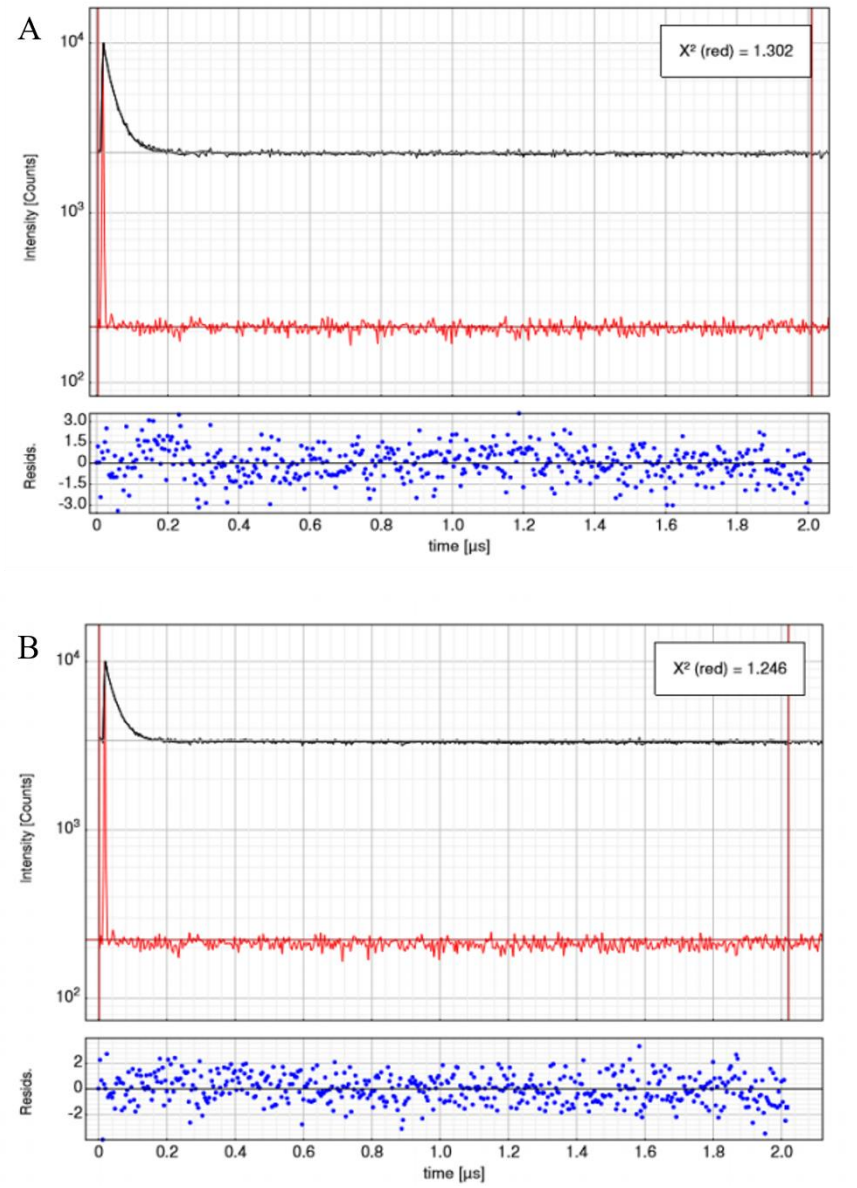


**Figure 2.2** TCSPC emission lifetime traces of $[Os(bpy)_2(picCOOH)]^{2+}$ (A) and $[Os(bpy)_2(pic\text{-}arg_8)]^{10+}$ (B) in PBS solution at room temperature. The complexes were excited using the 370 nm laser, and the data was acquired using the PicoQuant Time Harp system. The IRF was measured using Ludox solution (—). The lifetime traces (—) (•) were fit to give a $\chi^2$ value between 0.9 and 1.3, and residuals showed no structure, indicating an excellent fit.

On the other hand, $[Ru(bpy)_2(picCOOH)]^{2+}$ has a considerably longer lifetime than the $[Os(bpy)_2(picCOOH)]^{2+}$ complex of 540 ns which did not change with peptide conjugation. The shorter lifetime of $[Os(bpy)_2(pic\text{-}arg_8)]^{10+}$ is due to the strong spin orbit coupling of the osmium centre. To investigate sensitivity to oxygen, samples were purged with nitrogen for 20 minutes and the emission lifetimes were measured again. Neither the lifetime nor emission of $[Os(bpy)_2(picCOOH)]^{2+}$ and peptide conjugate were

affected by the absence of oxygen (Figure 2.3). In contrast, $[Ru(bpy)_2(picCOOH)]^{2+}$ emission lifetime increased from 540 ns to 872 ns under de-aerated conditions, which is typical behaviour of ruthenium complexes. The quantum yield ($\varphi_f$) of $[Os(bpy)_2(picCOOH)]^{2+}$ and its peptide conjugate was found to be 0.002 ± 0.0007 in aerated PBS solution. Consistent with the emission lifetime, the quantum yield was found to be independent of oxygen concentration. This was obtained using $[Ru(bpy)_3]^{2+}$ as a standard solution.[13]

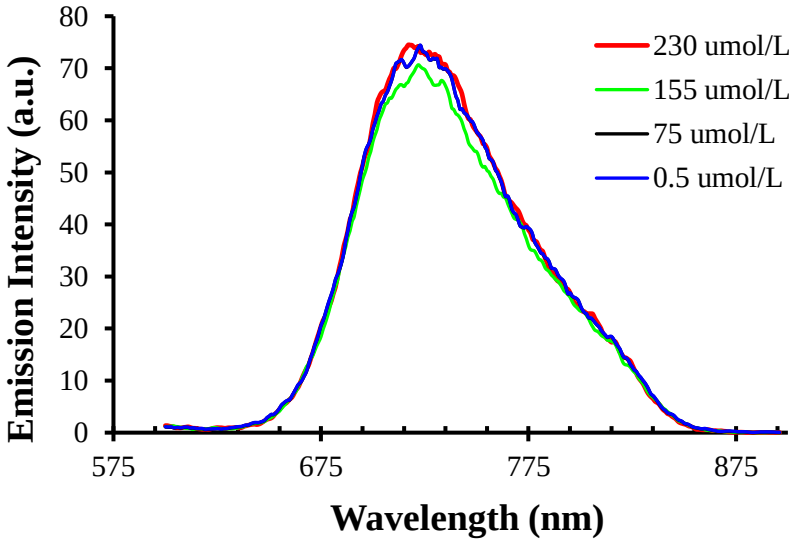


**Figure 2.3** Emission intensity of Os(II) complex independent to oxygen concentrations. $[Os(bpy)_2(pic\text{-}arg_8)]^{10+}$ (40 μM in PBS solution) was depleted of oxygen using nitrogen gas for 20 minutes. Oxygen concentrations were measured using a micro needle fiber-optic probe (Presens) before and after emission intensity was read (using a Varian Fluorimeter, slit width 5 nm).

Although $[Os(bpy)_2(pic\text{-}arg_8)]^{10+}$ has a short lifetime, rendering it oxygen-independent, its photophysical properties such as its large Stokes shift and NIR emission, suggest that osmium may be a suitable imaging probe. If designed correctly, Os(II) complexes may be used for other sensing applications, such as pH, without the interference of oxygen concentration.

**Table 2.1** Spectroscopic and photophysical data for $Os(bpy)_2(pic\text{-}COOH)]^{2+}$ and $Ru(bpy)_2(pic\text{-}COOH)]^{2+}$ complexes in aqueous PBS solution. Lifetimes were measured at (a) room temperature, (b) 20 °C, and (c) 37 °C for the peptide conjugates.

*From *Neugebauer et al* [11] ξ In de-aerated acetonitrile ¶ Quantum yields measured in aerated PBS solution. $\Phi_f$ values measured using $Ru(bpy_3)^{2+}$ = 0.028 as standard solution.[19]

| **Compound** | **$\lambda_{abs}/\lambda_{ex}$ (nm)** | **$\lambda_{em}$/nm** | **$\Phi_f$** **(quantum yeild)** | **$\tau_f$/ns** [a] |
|---|---|---|---|---|
| **$[Os(bpy)_2(pic)]^{2+}$** | 484 | 720 | 0.0022 ± 0.0007¶ | 33 ± 0.1 [a]<br>33 ± 1.1 [b]<br>31 ± 1.9 [c] |
| **$[Os(bpy)_2(pic)]^{2+}$**ξ | 488 | 726 | 0.01 ± 0.02 | 57 ± 0.4 |
| **$[Os(bpy)_2(pic\text{-}arg_8)]^{10+}$** | 486 | 726 | 0.0025 ± 0.0008¶ | 31 ± 0.2 [a]<br>33 ± 2.47 [b]<br>29 ± 2.05 [c] |
| **$[Ru(bpy)_2(pic)]^{2+}$** * | 458 | 608 | 0.067 | 540 [a]<br>570 ± 74.8 [b]<br>624 ± 70.2 [c] |
| **$[Ru(bpy)_2(pic\text{-}arg_8)]^{10+}$*** | 470 | 610 | 0.06 | 478 [a]<br>536 [b]<br>514 ± 4.9 [c] |

## 2.4 Cell Uptake Studies of Os(II) versus Ru(II) using Confocal Microscopy

In order to investigate the application of Os(II) as an imaging probe compared to Ru(II), real time uptake studies were carried out. Two cell lines were used; Chinese hamster ovary (CHO) cells and Sp2/0 mouse myeloma cell. Mammalian cell lines such as CHO and murine myelomas generate proteins that closely resemble that of humans.[14] Therefore the uptake and interactions of $Os(bpy)_2(pic\text{-}arg_8)]^{10+}$ complex can be explored and compared across the two cell types. Cells were seeded at 2 x $10^5$ cells on a 35 mm glass bottom culture dish and left to incubate at 37 °C with 5 % $CO_2$ for 24 h. $[Os(bpy)_2(pic\text{-}COOH)]^{10+}$ (0.05 % DMSO and PBS) or $[Os(bpy)_2(pic\text{-}arg_8)]^{10+}$ (PBS) were added to the cells in Lebovitz media. Confocal images were obtained using a 488 nm laser to excite the complex, and emission was collected using long pass 650 nm filter set.

To evaluate the optimum working concentrations, a range of concentrations between 20 and 100 μM of both the parent and peptide complexes were incubated with CHO and Sp2 cells for varying time periods. The $[Os(bpy)_2(picCOOH)]^{2+}$ parent complex did not permeate the cell membrane. Uptake of the parent complex was only observed when cells were exposed to a 0.1 % Trition/PBS solution which permeabilises the cell membrane. Similar observations were reported for the $[Ru(bpy)_2(pic\text{-}arg_8)]^{10+}$ analogue by *Neugebauer et al*.[11] It was found that 70 μM for 2 h were the optimum conditions for imaging $[Os(bpy)_2(pic\text{-}arg_8)]^{10+}$.

Live cell uptake studies were carried out to assess how efficiently the compound is taken up by CHO and Sp2 cells. For both cell lines, entry into the cell was observed within minutes of addition, as described in Figure 2.4.

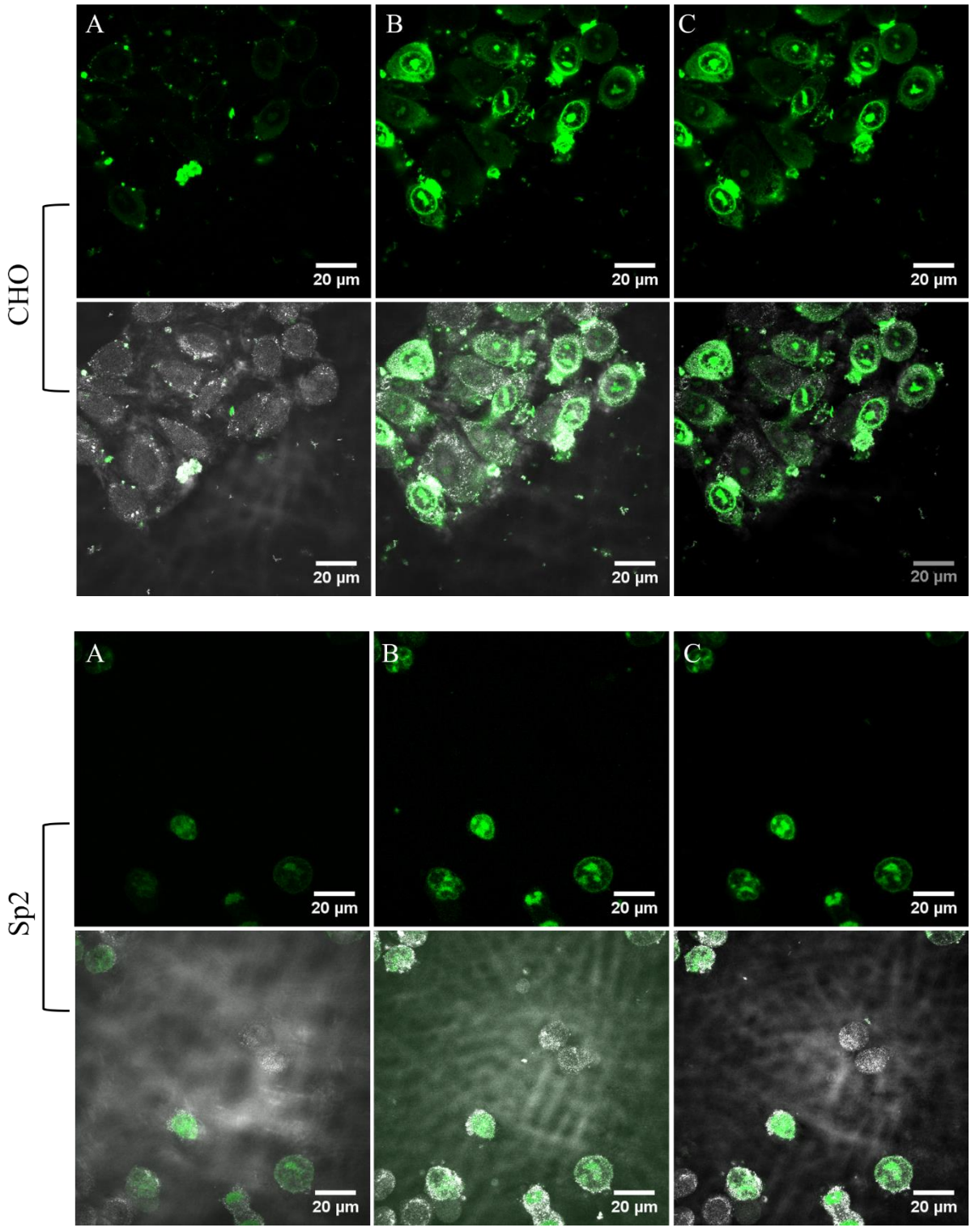


**Figure 2.4** Live uptake of $[Os(bpy)_2(pic\text{-}arg_8)]^{10+}$ by CHO and Sp2 cells. 70 µM complex in phenol red-free media was added, and cells imaged continuously using Time Series mode. Uptake was instantaneous for both cell lines. The initial uptake was seen after 2 minutes exposure (A), with further uptake seen after 10 minutes (B), and at 17 minutes (C) of continuous confocal scanning. Cells were excited with a 488 nm argon laser and the emission was collected using a long pass 650 nm filter set. Fluorescent images and background overlay images are presented.

Uptake was broadly similar in both cell lines, however $[Os(bpy)_2(pic\text{-}arg_8)]^{10+}$ appeared to cross the CHO membrane more rapidly. After 2 minutes of exposure to $[Os(bpy)_2(pic\text{-}arg_8)]^{10+}$ the complex appeared to concentrate in the cytoplasm (Figure 2.4a), distributing throughout different cellular components, such as the nucleolus (Figure 2.4b). The same uptake was observed for the equivalent $[Ru(bpy)_2(pic\text{-}arg_8)]^{10+}$ complex in Sp2 myeloma cells.[11] *Neugebauer et al* reported uptake after 2 minutes of exposure to $[Ru(bpy)_2(pic\text{-}arg_8)]^{10+}$ , and it distributed throughout the cytoplasm, however with one distinction, it did not penetrate the nuclear envelope.

After 2 h incubation with 70 µM $[Os(bpy)_2(pic\text{-}arg_8)]^{10+}$, the complex was readily taken up by both Sp2 and CHO the cells. Figure 2.5 (A and B) focuses on a group of Sp2 cells which is representative of the sample, illustrating the uptake of $[Os(bpy)_2(pic\text{-}arg_8)]^{10+}$. The complex appears to penetrate the membrane and localize within different cellular compartments of the cytoplasm. However, it was found that nuclear penetration was light or heat activated by the laser as in the absence of light it did not enter the nuclear envelope as demonstrated previously during real-time uptake in Figure 2.4. Similar distribution was observed in CHO cells (Figure 2.5 E and F), however the complex emission is much brighter in CHO cells compared to Sp2 under the same imaging conditions. A possible suggestion for this is that $[Os(bpy)_2(pic\text{-}arg_8)]^{10+}$ is being quenched from within the Sp2 cells, for example, by the pH of the cell. Sp2 cells are a cancer cell line. Cancer cells tend to have a slightly more acidic pH as they produce more lactic acid as a result of their increased metabolism, which could be quenching the emission.[15] A single Sp2 cell (C and D) and a single CHO cell (G and H), which are representative of the broader behaviour in the sample, show a more punctate distribution in both cell lines, with no entry into the nucleolus. This shows that entry into the nuclear envelope was photo-activated as localization within the nucleolus was observed only upon continuous irradiation with the confocal laser during the live uptake measurements.

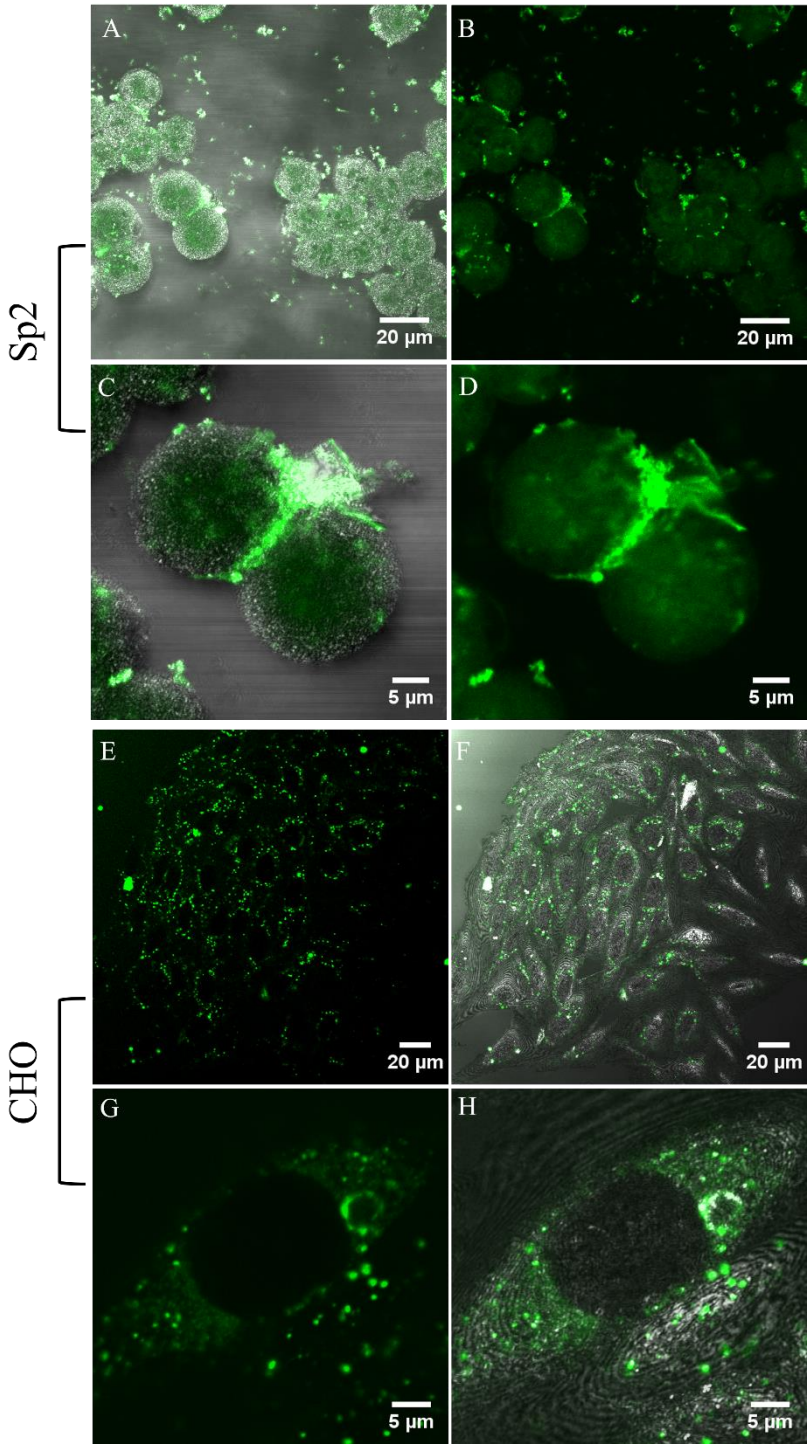


**Figure 2.5** Confocal imaging of $[Os(bpy)_2(pic\text{-}arg_8)]^{10+}$ in Sp2 and CHO cells, incubated with 70 µM for 2 h at 37 °C in the absence of light. The distribution of $[Os(bpy)_2(pic\text{-}arg_8)]^{10+}$ in a group of Sp2 cells (A and B), and the localisation within a single Sp2 cell (C and D). The distribution of $[Os(bpy)_2(pic\text{-}arg_8)]^{10+}$ in a group of CHO cells (E and F), and the localisation within a single CHO cell (G and H), both representative of the population of cells in the sample. $[Os(bpy)_2(pic\text{-}arg_8)]^{10+}$ was excited using a 488 nm argon laser, and the emission was collected using a 650 nm long pass filter.

Temperature studies were carried out to investigate the mechanism of uptake as described in Chapter 1. Cells were prepared as described in *section 2.2.5*, but were incubated at 4 °C for 2 h instead of 37 °C. Under these conditions it was found that the cells did not take up $[Os(bpy)_2(pic\text{-}arg_8)]^{10+}$, indicating strongly that the complex is taken up by active transport.[16] Furthermore, the punctate distribution of the complex implies it is taken up by endocytosis, where the cell membrane forms a vesicle around the molecule to carry into the cell. This correlates well with the temperature study results, as endocytosis is a form of active transport.[17] However this would need to be looked at it in greater detail to irrevocably confirm endocytosis as the mode of uptake.

### 2.4.1 Co-localisation studies of $[Os(bpy)_2(pic\text{-}arg_8)]^{10+}$ in CHO cells

As discussed in Chapter 1, polyarginines do not generally localize in specific organelles but tend to distribute throughout the cytoplasm. In order to address if and where $[Os(bpy)_2(pic\text{-}arg_8)]^{10+}$ was localising in the cell, co-localisation studies were carried out using commercial organelle-specific dyes. CHO cells were incubated with 70 μM $[Os(bpy)_2(pic\text{-}arg_8)]^{10+}$ for 2 h before the commercial dyes were introduced. The smallest working concentration of the commercial dyes was used to ensure they did not stain other organelles. LysoTracker Green™ (50 nM) was used to stain the lysosomes, and MitoTracker Deep Red™ (150 nM) was used to stain mitochondria. Figure 2.6 demonstrates the co-localisation of $[Os(bpy)_2(pic\text{-}arg_8)]^{10+}$ in live CHO cells. It appears to have entered some mitochondria and lysosomes, but not all of them according to the staining of the commercial dyes.

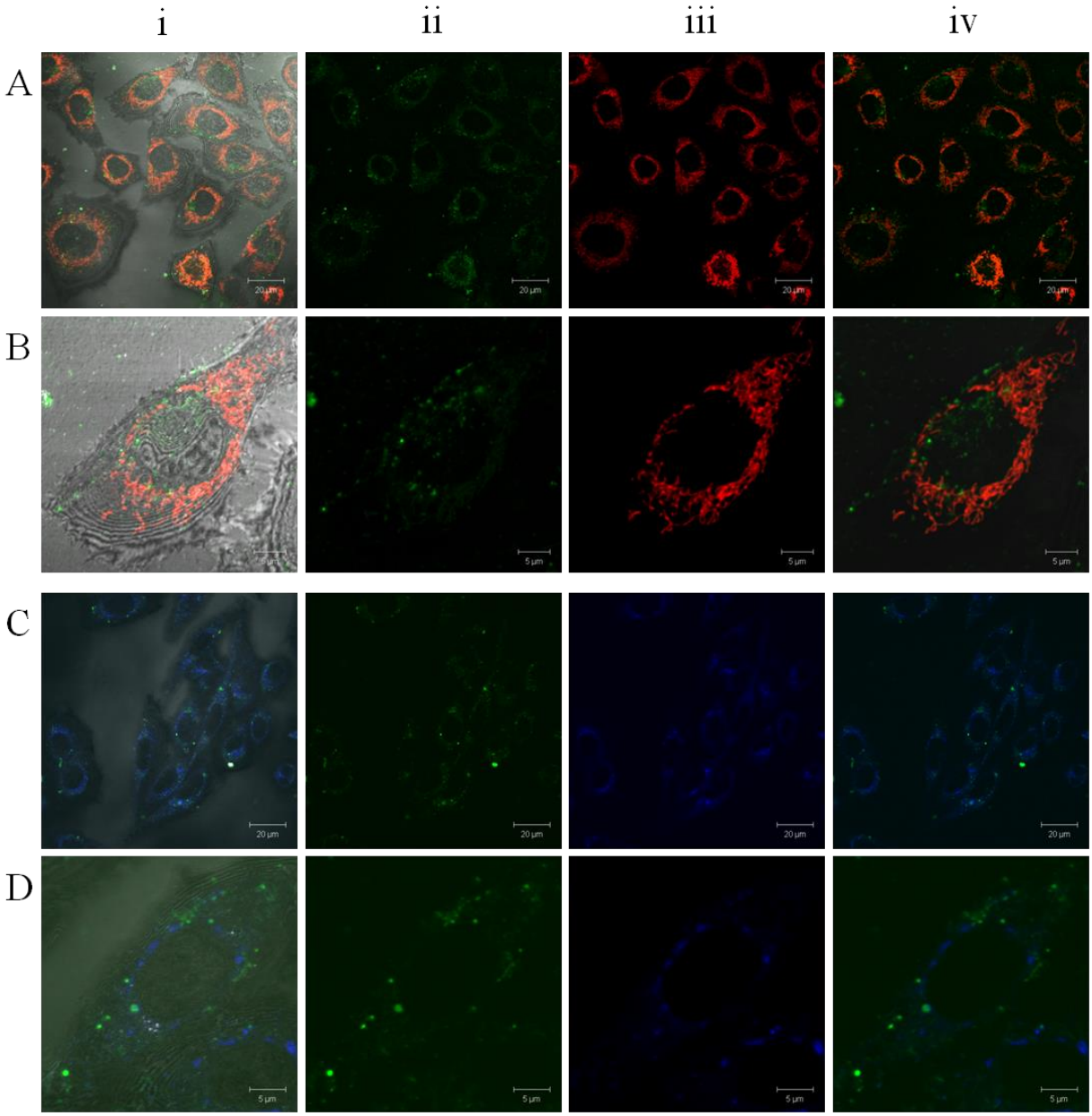


**Figure 2.6** Co-localising studies of $[Os(bpy)_2(pic\text{-}arg_8)]^{2+}$ with MitoTracker Deep Red (150 nM) (A and B) and LysoTracker Green (50 nM) (C and D) in PBS solution. Column (i) exhibits both the Osmium channel, localising dye channel and background channel; column (ii) osmium channel only; column (iii) localising dye channel only; column (iv) overlap of osmium with localising dye excluding background channel. $[Os(bpy)_2(pic\text{-}arg_8)]^{10+}$ was excited using a 488 nm argon laser and the emission was collected using a long pass 650 nm filter. LysoTracker Green was excited using a 488 nm argon laser and the emission was collected using a band pass 505 – 530 nm filter. MitoTracker Deep Red was excited using a 633 nm HeNe laser and the emission was collected using a long pass 650 nm laser.

Os(II) arene anticancer complexes have been found to target DNA, accumulating in DNA rich areas such the nuclear membrane, nucleolus, and mitochondria. For example, Sadler and group have reported on an Os(II) arene complex, [(biphenyl -arene)Os(4-methyl-picolinate)Cl], and introduced it to A2780 ovarian cancer cells. [9] Figure 2.7 compares the structures of [(biphenyl -arene)Os(4-methyl-picolinate)Cl] (A) with $[Os(bpy)_2(pic\text{-}arg_8)]^{10+}$ (B). [(biphenyl -arene)Os(4-methyl-picolinate)Cl] has a free –Cl group, which is one possible route for this complexes in vivo activation, where –Cl can be replaced by $H_2O$ making the complex more reactive.

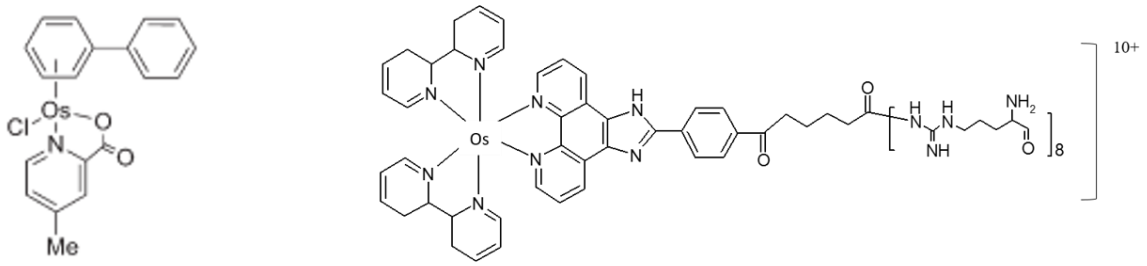


**A** **B**

**Figure 2.7** Chemical structures comparing [(biphenyl -arene)Os(4-methyl-picolinate)Cl] arene complex (A), taken from *Sadler et al,* [9] with $[Os(bpy)_2(pic\text{-}arg_8)]^{10+}$ complex (A).

Although the two complexes are very different in structure, *Sadler et al* demonstrated that [(biphenyl-arene)Os(4-methyl-picolinate)Cl] complex accumulated within the nucleolus and mitochondria after exposure for 12 h (Figure 2.8).

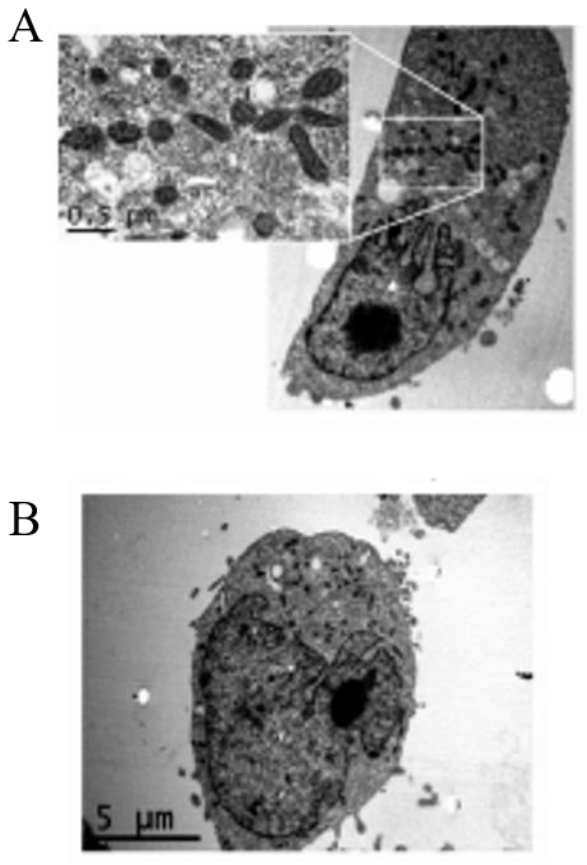


**Figure 2.8** TEM image of Os(II) arene biphenyl complex (20 μM) localising within the nucleolus and mitochondria of an A2780 ovarian carcinoma cell, incubated for 12 h.[9]

The mitochondria accumulation shown in Figure 2.8 is common to the localisation of $[Os(bpy)_2(pic\text{-}arg_8)]^{10+}$ in CHO cells investigated in this chapter. This could suggest that osmium has an affinity for mitochondria once it crosses the cell membrane. However, upon incubation with $[Os(bpy)_2(pic\text{-}arg_8)]^{10+}$ in the absence of light, no localisation was found in the nucleolus. This could reflect on the lipophilicity of the two complexes. This is something that would have to be in investigated further.

### 2.4.2 HTP Uptake Studies

As the complexes appeared to penetrate the nuclear envelope under direct and continuous exposure to the confocal laser, live high throughput (HTP) uptake study was carried out to obtain a more detailed insight into the dynamics of uptake over 2 h. The advantage of using HTP is it allows for the monitoring of cell uptake without long exposure times to laser scanning. Therefore, uptake can be studied without the impact

of light seen, which was observed previously in Figure 2.4, under continuous scanning during confocal microscopy. The experiment was carried out at the School of Medicine, CRANN and AMBER Centres as part of Trinity College Dublin with the help of Dr. Anthony Davies. CHO cells were prepared in a 96-well plate as described in *section 2.2.6*. $[Os(bpy)_2(pic\text{-}arg_8)]^{10+}$ and $[Ru(bpy)_2(pic\text{-}arg_8)]^{10+}$ were added separately to the cells, and the uptake was measured using an Insight Cell Analyser 1000 (GE Healthcare). The complex solutions were present for the duration of the experiment. Uptake was recorded *via* fluorescence intensity from 5 random fields of view per well at 37 °C. The results are presented in Figure 2.9. Initially, both complexes were taken up quickly, and the emission intensity continuously increased over time. Interestingly, $[Ru(bpy)_2(pic\text{-}arg_8)]^{10+}$ appears to be taken up in two steps, whereas $[Os(bpy)_2(pic\text{-}arg_8)]^{10+}$ uptake appears to be more continuous. The difference in emission intensities between the complexes is a reflectance of their quantum yields (Φ) within the cells. The continuous increase in intensities indicates no self-quenching occurred. Over the course of the experiment, both complexes accumulate within the cells. After 2 h, it was found that uptake plateaued for $[Ru(bpy)_2(pic\text{-}arg_8)]^{10+}$ but $[Os(bpy)_2(pic\text{-}arg_8)]^{10+}$ continued to enter the cells.

The rate of uptake (k) for each complex was determined by finding the slope of the plot Ln (I) v *t*, where I is the emission intensity and *t* is the time in seconds. From the uptake plot in Figure 2.7, there appears to be a lead in time as there is no uptake of $[Ru(bpy)_2(pic\text{-}arg_8)]^{10+}$ in the first 30 minutes of incubation. However, this is not the case for $[Os(bpy)_2(pic\text{-}arg_8)]^{10+}$ which is taken up instantaneously once introduced to the cells. As everything in the experiment is equal; i.e. the concentration of the complexes, the number of cells seeded in the wells, and the time when the complexes are added to the cells, this interesting effect must be due to the lipophilicity of the complexes. The heavy osmium is likely to be more lipophilic than ruthenium, due to nuclear shielding.

The rate of uptake was determined for both complexes. As $[Ru(bpy)_2(pic\text{-}arg_8)]^{10+}$ appears to not enter the cells in the first 30 minutes of addition, the uptake rates for both $[Ru(bpy)_2(pic\text{-}arg_8)]^{10+}$ and $[Os(bpy)_2(pic\text{-}arg_8)]^{10+}$ were determined between 40 minutes and 120 minutes. The rate of uptake for $[Ru(bpy)_2(pic\text{-}arg_8)]^{10+}$ was found to be 0.57 $s^{-1}$. On the other hand, $[Os(bpy)_2(pic\text{-}arg_8)]^{10+}$ has a slower uptake rate of 0.21 $s^{-1}$, which can appears to be more linear and steady, which can be seen from the plots in Figure 2.7.

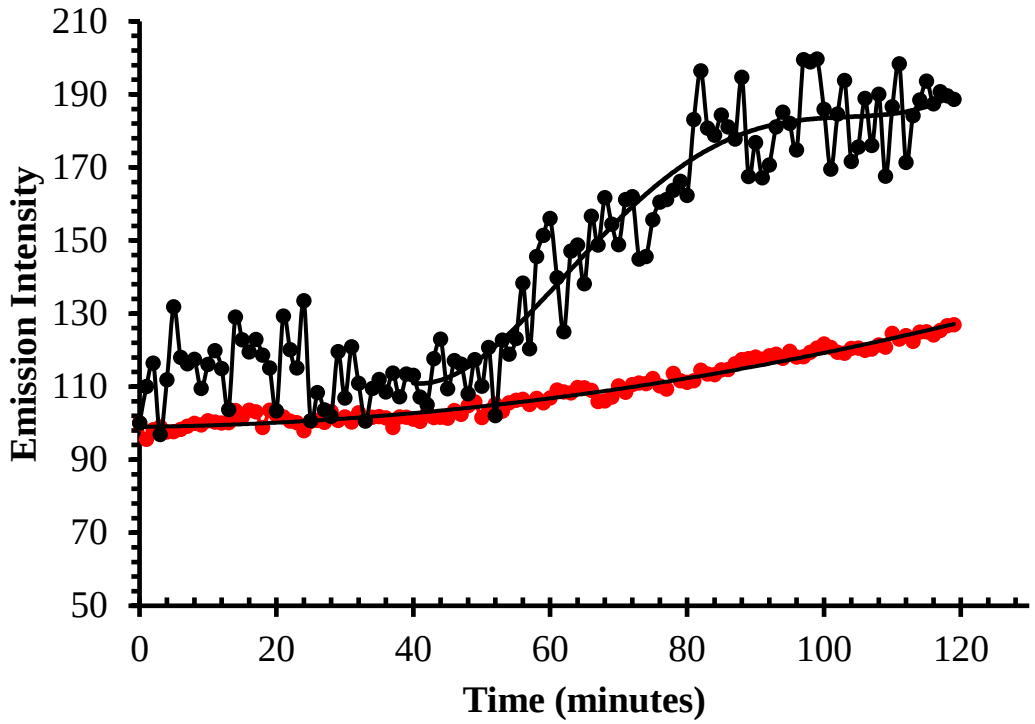


**Figure 2.9** Cellular uptake of $[Os(bpy)_2(pic\text{-}arg8)]^{10+}$ (—) and $[Ru(bpy)_2(pic\text{-}arg8)]^{10+}$ (—) in live CHO cells using the InCell Analyzer High Throughput method at 37 °C. The complexes were excited using a 480 nm laser at 5 random fields of view of each sample, and the emission was collected using a long pass 620 nm filter. (Data normalised to no dye)

Methods such as HTP can allow us to see the cell-complex uptake rate more efficiently than confocal microscopy as the cells are scanned for 20 seconds and at multiple fields of view to record the average emission at each time point with little laser exposure. Photo bleaching and photo toxicity can be avoided as the compound is not being continuously exposed to laser scanning. Cells are less likely to be damaged by the laser, which can force them to take up the compound or redistribute it over time through thermal damage from direct light exposure, or through the generation of singlet oxygen by the complex.

## 2.5 Cytotoxicity

From the uptake studies described previously in *section 2.4*, neither $[Os(bpy)_2(pic\text{-}arg_8)]^{10+}$ nor $[Ru(bpy)_2(pic\text{-}arg_8)]^{10+}$ appear to be toxic towards the cells at short exposure times. The cytotoxicity of $[Os(bpy)_2(pic\text{-}arg_8)]^{10+}$ and $[Ru(bpy)_2(pic\text{-}arg_8)]^{10+}$

was then examined and compared in CHO and Sp2 cells using the Resazurin (Alamar Blue) assay. Resazurin (7-hydroxy-3H-phenoxazin-3-one-10-oxide) is a non-fluorescent dye that is used as an oxidation-reduction indicator in cells. It measures the metabolic activity of the cells. Viable cells reduce the non-fluorescent resazurin to the highly fluorescent resorufin and dihydroresorufin. Therefore, it is a method of measuring cellular ATP. The extent of reduction, and therefore the fluorescent intensity, is directly proportional to the number of viable cells over time.

Cells were prepared in 96-well plates as described in *section 2.2.7,* and was carried out in the absence of light. Figure 2.10 illustrates a plot of absorbance versus metal complex concentration (μM) in Sp2 (A) and CHO (B) cells. $[Os(bpy)_2(picCOOH)]^{2+}$ and $[Ru(bpy)_2(picCOOH)]^{2+}$ parent complex's (0.1 % vol. DMSO) did not induce toxicity towards the cells, even up to concentrations as high as 200 μM over 16 h. Similarly, the octa-arginine conjugates induced little toxicity towards the cells, with cells remaining viable at concentrations as high as 150 μM in CHO cells (B). Interestingly, $[Os(bpy)_2(pic\text{-}arg_8)]^{10+}$ did have a cytotoxic effect on Sp2 cells at concentrations greater than 100 μM (A). In comparison, the assay indicated that $[Ru(bpy)_2(pic\text{-}arg_8)]^{10+}$ was slightly more toxic towards the CHO cells, showing a 10 % decrease in cell viability compared to cells treated with $[Os(bpy)_2(pic\text{-}arg_8)]^{10+}$. Nonetheless, the low cytotoxicity of the $[Os(bpy)_2(pic\text{-}arg_8)]^{10+}$ conjugate further indicates that this compound is a valuable molecular probe for multimodal imaging.

**A**

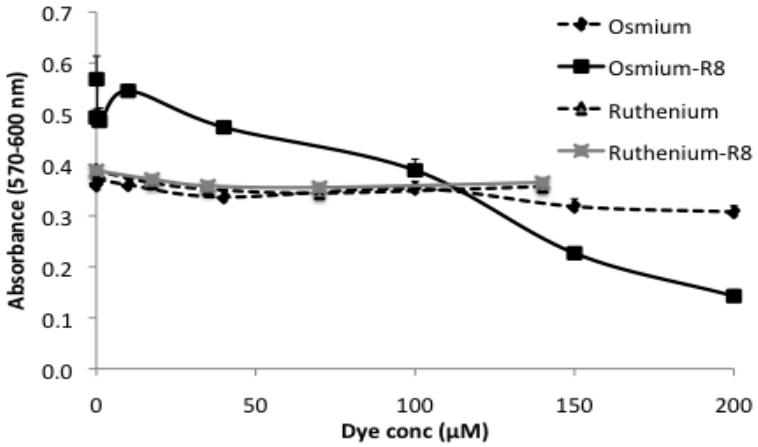


**B**

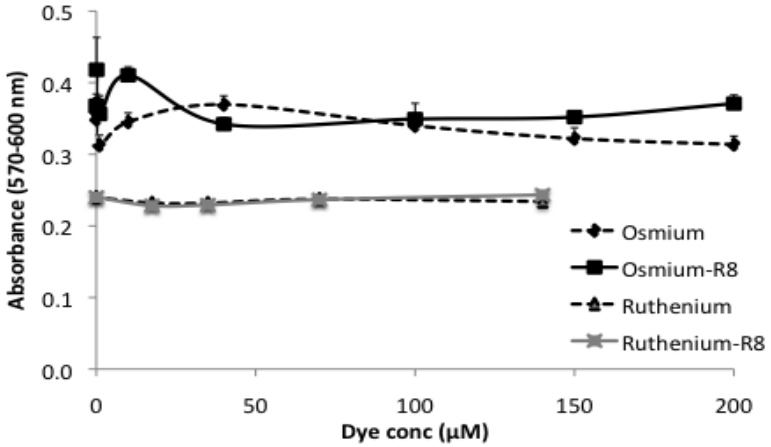


**Figure 2.10** Cell viability in Sp2 (A) and CHO cells (B). Live cells were treated with $[Os(bpy)_2(pic\text{-}COOH)]^{10+}$ (Osmium), $[Os(bpy)_2(pic\text{-}arg_8)]^{10+}$ (Osmium-R8), $[Ru(bpy)_2(pic\text{-}COOH)]^{10+}$ (Ruthenium) and $[Ru(bpy)_2(pic\text{-}arg_8)]^{10+}$ (Ruthenium-R8) for 16 h followed by addition of resazurin reagent for a further 6 h. Absorbance was read at 570 nm with background at 600 nm subtracted, n=3 in triplicate

The group of *Sadler et al* compared Ru(II) and Os(II) arene complexes that were structurally analogous except for the metal centre, shown in Figure 2.11.[18] They demonstrated that the Ru(II) arene complex exhibited toxicity towards cancer cells while the Os(II) arene complex did not.

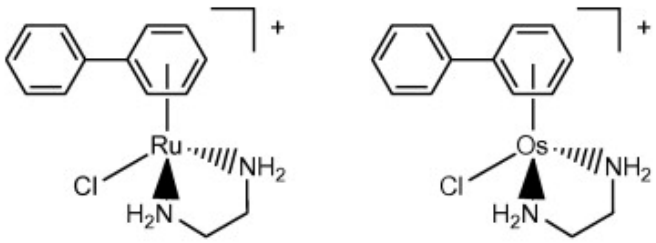


**Figure 2.11** Structure of a Ru(II) arene complex and the analogous Os(II) arene complex. [18]

Although arene complexes are designed to be highly toxic towards cells, and they are structurally very different to the complexes studies in this chapter, the results show the same trend seen here, indicating very interestingly, that the heavier third-row transition metal ion Os(II) is less toxic than Ru(II). The lack of biological activity is possibly due to it being relatively more inert compared to Ru(II). However, in a separate report of an Os(II)-arene-$arg_8$ complex, it showed significant cytotoxicity towards CHO cells.[10] The $Arg_8$ conjugate demonstrated higher toxicity than $Arg_5$ and the parent complex as it increased the cell uptake abilities of the complex. By comparing these very different complexes and their effects on cells, it shows that the ligands play an important role in the cytotoxic effects of different Os(II) complexes, as well as between Os(II) and Ru(II) analogue complexes.

## 2.6 Phototoxicity

As the application of $[Os(bpy)_2(pic\text{-}arg_8)]^{10+}$ in the context of this thesis is in luminescence imaging, the complex stability and particularly its cellular toxicity under exposure to light is an important factor. As demonstrated previously in *section 2.5*, $[Os(bpy)_2(pic\text{-}arg_8)]^{10+}$ showed no significant toxicity towards both cells lines when incubated in the absence of light. Therefore the phototoxicity of $[Os(bpy)_2(pic\text{-}arg_8)]^{10+}$ was investigated in CHO cells. The cells were prepared as described in *section 2.2.8.* CHO cells were exposed to a white light source at 1.36 x $10^{-15}$ mJ intensity, using the confocal microscope white light. Control CHO cells were examined with DRAQ 7 in PBS (1:100 dilution) in the absence of $[Os(bpy)_2(pic\text{-}arg_8)]^{10+}$. After 3 h, no DRAQ 7 had entered the cells indicating they were still viable. Next, in a separate glass-bottom culture dish, $[Os(bpy)_2(pic\text{-}arg_8)]^{10+}$ (70 μM in phenol-red free media) was added to

CHO cells and left to incubate for 24 h (37 °C with 5 % $CO_2$) to ensure maximum uptake. Prior to imaging, DRAQ 7 was added to the cells. The cells were exposed to the white light source (1.36 x $10^{-15}$ mJ) for 3 h. No change in the location of $[Os(bpy)_2(pic\text{-}arg_8)]^{10+}$ in the cells was observed, and the cells remained viable. Similar results were observed in *section 2.5*, where CHO cells were still viable after being exposed to 70 μM $[Os(bpy)_2(pic\text{-}arg_8)]^{10+}$ for 24 h in the absence of light. There was no change in cell morphology associated with toxicity, such as surface blebbing, which is a sign of photo toxic effects[19] indicating that $[Os(bpy)_2(pic\text{-}arg_8)]^{10+}$ is not phototoxic to the cells under the conditions described here.

## 2.7 Photostability

Good photostability of a fluorophore is a desired characteristic of an imaging probe. This ensures it will not photo bleach under continuous excitation over long imaging times, for example in dynamic studies. One of the key disadvantages of organic chromophores for live cell imaging is that they are frequently prone to photo bleach over extended periods of light exposure. The photostability of $[Os(bpy)_2(picCOOH)]^{2+}$ in solution was explored and compared to $[Ru(bpy)_2(picCOOH)]^{2+}$ as this complex had been shown previously under imaging conditions to exhibit significantly superior performance in terms of photostability compared to fluorescein.[11]

To explore photostability under imaging conditions, solutions of each complex in PBS (70 μM) were pipetted onto a cover slip. The samples were excited using a 488 nm argon laser at 0.24 μW/$cm^2$ laser power. The samples were then continuously irradiated for 10 minute intervals in one area at 7.2 μW/$cm^2$ laser power. Figure 2.9 illustrates the results after 20 minutes of continuous excitation.

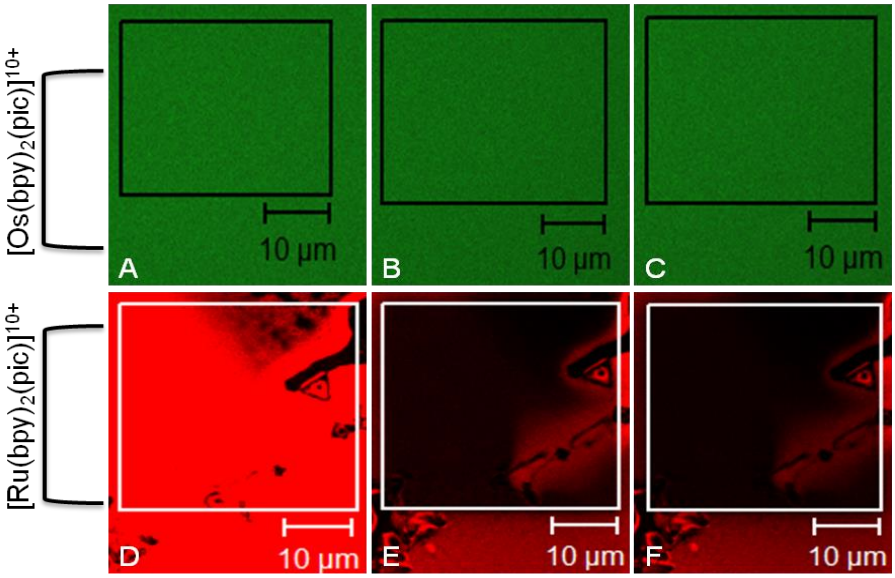


**Figure 2.12** Photostability of $[Os(bpy)_2(picCOOH)]^{2+}$ and $[Ru(bpy)_2(picCOOH)]^{2+}$ in PBS solution was assessed using confocal microscopy laser scanning. Bleaching was performed by exciting $[Os(bpy)_2(picCOOH)]^{2+}$ with 488 nm laser and 458 nm laser for $[Ru(bpy)_2(picCOOH)]^{2+}$. Both complexes were scanned using 30 % laser power at 10 minute intervals. The complexes were imaged at the lowest laser power of 1 % before scanning (A and D), after 10 minutes (B and E), and 20 minutes scanning (C and F).

Remarkably, it was found that $[Os(bpy)_2(picCOOH)]^{2+}$ did not bleach at all after 20 minutes of continuous high intensity laser scanning, seen in Figure 2.12 A-C, whereas $[Ru(bpy)_2(picCOOH)]^{2+}$ underwent significant bleaching after 10 minutes of scanning (E), and further bleaching after a final exposure time of 20 minutes (F). *Neugebauer et al* reported that $[Ru(bpy)_2(pic\text{-}arg_8)]^{10+}$ retained more than 50 % of its initial luminescence after 20 minutes of continuous irradiation from within a platelet, and that this probe is significantly more stable than the commonly used imaging probe fluorescein.[11] The photostability of the Os complex, is therefore outstanding. The origin of this photostability is the large ligand field splitting of the dd levels of Os(II) complexes. Unlike Ru(II) complexes its $^3$MC state cannot be thermally populated from its lowest excited state making them more photostable than Ru(II) complexes.[20]

These results suggest Os(II) polypyridyl complexes like $[Os(bpy)_2(pic\text{-}arg_8)]^{10+}$ may be valuable imaging probes particularly for dynamic or imaging studies over extended periods due to low toxicity towards cells and extreme photostability.

## 2.8 Phosphorescent Lifetime Imaging Microscopy (PLIM)

Phosphorescent lifetime imaging microscopy (PLIM) is a useful method for measuring the emission lifetime of a probe from within the cell. The advantage of using Ru(II) and Os(II) metal complexes for lifetime applications is that their emission lifetimes are environmentally sensitive. Cellular environments, such as oxygen concentration and pH, can be monitored using changes in the luminescent lifetimes as the lifetime is independent of probe concentration. Luminescent lifetime measurements in solution showed that $[Ru(bpy)_2(pic\text{-}arg_8)]^{10+}$ has a lifetime of 540 ns, while $[Os(bpy)_2(pic\text{-}arg_8)]^{10+}$ has a lifetime of 33 ns (Table 2.1). PLIM was carried out to investigate the variation of the lifetime of each complex within a cell. CHO and Sp2 cells were prepared as described in *section 2.2.9*, particularly given that $[Os(bpy)_2(pic\text{-}arg_8)]^{10+}$ is not sensitive to $O_2$.The PLIM images were acquired using a Microtime 200 instrument. The samples were excited with a 405 nm laser line and emission was collected using a long pass 530 filter set. Each cell image was exposed to scanning for 20 minutes to ensure a high number counts were collected for accurate decay statistics. Even though the sample is scanned for long periods of time to generate the lifetime data, the laser power is low, at 0.7 $\mu W/cm^2$ compared to 7 $\mu W/cm^2$ for confocal imaging. Therefore, the cell is not compromised by thermal damage from the laser or by the generation of free radicals such as singlet oxygen by the metal complex. $[Os(bpy)_2(pic\text{-}arg_8)]^{10+}$ and $[Ru(bpy)_2(pic\text{-}arg_8)]^{10+}$ lifetimes were compared in Sp2 cells, while $[Os(bpy)_2(pic\text{-}arg_8)]^{10+}$ lifetimes were measured in Sp2 and CHO cells to assess any differences between cell lines.

Figure 2.13 shows the false-colour lifetime distributions of $[Os(bpy)_2(pic\text{-}arg_8)]^{10+}$ (A) and $[Ru(bpy)_2(pic\text{-}arg_8)]^{10+}$ (B) measured separately in a live single Sp2 cell. The lifetime distribution in this cell is representative of the cells throughout the sample. The overall average lifetimes in the cells were analysed using SymPhoTime software, where each pixel represents the average lifetime at that point in the cell. This creates the false colour images of the cell.

Table 2.2 summarises the average luminescent lifetimes of $[Os(bpy)_2(pic\text{-}arg_8)]^{10+}$ and $[Ru\ (bpy)_2(pic\text{-}arg_8)]^{10+}$ in the membrane and cytoplasm of the cells. The average lifetime of $[Os(bpy)_2(pic\text{-}arg_8)]^{10+}$ in the cell was found to be 20 ± 0.9 ns, which is slightly shorter than in aqueous PBS solution at 29 ± 2.05 at 37 °C. The lifetime within the membrane was measured to be 18.8 ± 0.6 ns and 14.5 ± 1.5 ns in the cytoplasm. As

$[Os(bpy)_2(pic\text{-}arg_8)]^{10+}$ lifetime was shown to be unaffected by oxygen, it is an alternative environmental parameter, such as local viscosity at the membrane that is causing the increase in lifetime there compared to the cytoplasm.[20] $[Ru(bpy)_2(pic\text{-}arg_8)]^{10+}$ demonstrated different lifetime distributions to the osmium complex, with the lifetime decreasing from 540 ± 12 ns in the cytoplasm to 453 ± 25 ns in the membrane.[11] In this case, as $[Ru(bpy)_2(pic\text{-}arg_8)]^{10+}$ is sensitive to oxygen concentrations, therefore this is likely to play a role in the varying lifetimes between the cell regions. For example, a higher oxygen concentration would be expected in the lipophilic membrane, quenching the luminescent lifetime there.

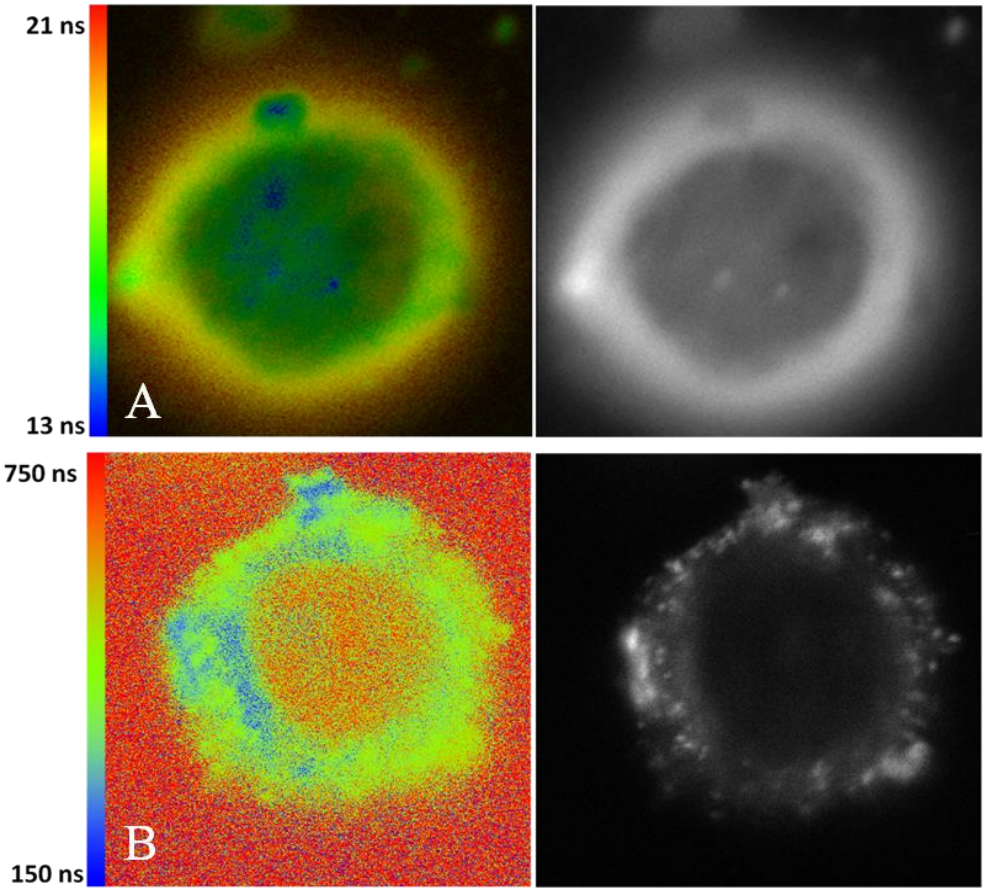


**Figure 2.13** False-colour luminescent lifetime images of $[Os(bpy)_2(pic\text{-}arg_8)]^{10+}$ (A) and $[Ru(bpy)_2(pic\text{-}arg_8)]^{10+}$ (B) (taken from *Neugebauer et al* [11]) and the corresponding intensity images in Sp2 cells. Prior to imaging, Sp2 cells were incubated with 70 μM complex for 24 h and images were acquired using a Microtime 200 system by PicoQuant for 20 minutes on a temperature controlled stage set to 37 °C. The samples were excited with a 405 nm laser line and the emission was collected using a long pass 530 nm filter. (Image zoom=10)

The luminescent lifetime of images $[Os(bpy)_2(pic\text{-}arg_8)]^{10+}$ were acquired in live CHO cells and compared to the lifetime distributions in Sp2 cells. Figure 2.14 shows the acquired PLIM false-colour images of $[Os(bpy)_2(pic\text{-}arg_8)]^{10+}$ in a single CHO cell (A) and Sp2 cell (B) with their corresponding lifetime distribution charts. These cells are representative of the samples. The lifetime profiles of $[Os(bpy)_2(pic\text{-}arg_8)]^{10+}$ between the cell lines is surprisingly different, summarised in Table 2.2. The average lifetime was obtained using SymPho Time Analysis software, and provides the average lifetime of all the pixels of the selected cell area. Interestingly, the overall average lifetime in Sp2 cells was found to be longer than that in the CHO cell, which is reflected in the differences in the lifetime distribution throughout each cell type, shown in Figure 2.11. The lifetime in the membrane is from 18.8 ± 0.6 ns in the Sp2 cell, compared to 13 ± 1.5 ns in the CHO cell. The lifetime in the cytoplasm was found to be 14.5 ± 1.5 ns in the Sp2 cell, and 11.6 ± 0.4 ns in the CHO cell. This is a significant difference between the two cell lines, although the trends in lifetime distribution are the same for each cell line, i.e. the lifetime increases in the cell membrane, relative to the lifetime of the cytoplasm. This is attributed to tight lipid packing in the plasma membrane which prevents $[Os(bpy)_2(pic\text{-}arg_8)]^{10+}$ from relaxing to ground state as fast as it does in the cytoplasm.[21]

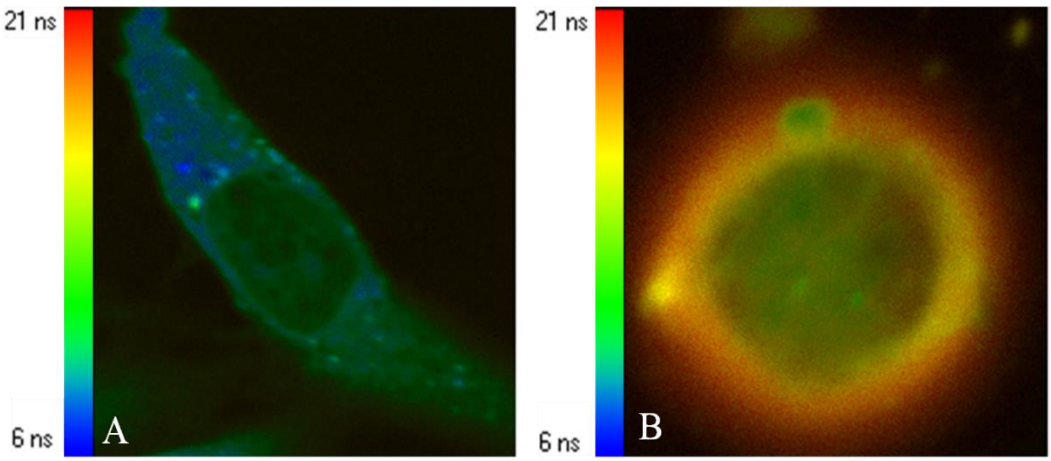


**Figure 2.14** Luminescent lifetime imaging of $[Os(bpy)_2(pic\text{-}arg_8)]^{10+}$ in a live CHO (A) and a live Sp2 cell (B). Prior to imaging, Sp2 cells were incubated with 70 μM $[Os(bpy)_2(pic\text{-}arg_8)]^{10+}$ complex for 24 h in cell culture media, and images were acquired using a Microtime 200 system by PicoQuant for 20 minutes on a temperature controlled stage set to 37 °C. The samples were excited with a 405 nm laser line and the emission was collected using a long pass 530 nm filter. (Image zoom=10)

**Table 2.2** Average luminescent lifetimes (ns) of $[Os(bpy)_2(pic\text{-}arg_8)]^{10+}$ in CHO and Sp2 cells, and $[Ru(bpy)_2(pic\text{-}arg_8)]^{10+}$ in Sp2 cells. Each value represents the mean ± SD for 3 separate experiments.

*Values taken from *Neugebauer et al* for comparison [11]

| Average τ (ns) | $[Os(bpy)_2(pic\text{-}arg_8)]^{10+}$ (ns) | | $[Ru(bpy)_2(pic\text{-}arg_8)]^{10+}$ (ns) |
|---|---|---|---|
| | **CHO** | **Sp2** | **Sp2** |
| **Overall Cell** | 10.7 ± 0.7 | 20 ± 0.9 | 479 |
| **Membrane** | 13 ± 1.5 | 18.8 ± 0.6 | 453 ± 25* |
| **Cytoplasm** | 11.6 ± 0.4 | 14.5 ± 1.5 | 540 ± 12* |
| **TCSPC τ in solution (at 37 °C in PBS solution)** | 29 ± 2.05 | | 514 ± 4.9 |

The variations in the luminescent lifetimes of $[Os(bpy)_2(pic\text{-}arg_8)]^{10+}$ within the two cell lines suggests that osmium is influenced by its local environment. These changes are not influenced by oxygen as it was demonstrated previously in *section 2.3* that $[Os(bpy)_2(pic\text{-}arg_8)]^{10+}$ shows no sensitivity to oxygen concentrations. During PLIM, images were acquired at 37 °C using a heated stage to keep the temperature constant throughout the process. Ruling out the possibilities of temperature and oxygen, it suggests that the emission lifetime differences may be attributed to the local environments and cell structure between the two cell lines; CHO, a mammalian cell line, and Sp2, a cancerous cell line. Lipid modifications in the cell membrane, such as accumulation of cholesterol, are associated with cancer cells due to the increased proliferation rates.[22] The over-expression of fatty acids, which make up the phospholipids in the cell membrane, is also found in cancer cells, such as prostate cancer. It is tempting to speculate that these structural differences might be affecting the changes in lifetime of $[Os(bpy)_2(pic\text{-}arg_8)]^{10+}$ in the two cell lines.[23]

## 2.9 Resonance Raman Spectroscopy

As demonstrated in *section 2.3*, $[Os(bpy)_2(pic\text{-}arg_8)]^{10+}$ exhibits a broad visible absorbance and a large Stokes shift. These properties make Os(II) highly suitable for resonance Raman. The advantage of using resonance Raman is its ability to selectively monitor a probe against a complex background, for example, against a background of lipid, carbohydrate and protein in cells. Resonance Raman in CHO cells was conducted and compared with a drop cast solution of the complex on a glass slide. The resonance Raman spectra of $[Os(bpy)_2(pic\text{-}COOH)]^{2+}$ and $[Os(bpy)_2(pic\text{-}arg_8)]^{10+}$ are presented in Figure 2.15. For comparison, solutions of both complexes in PBS in solution were pipetted on to a glass slide, and excited with a 488 nm argon laser into the $^1$MLCT absorbance band. The spectra were normalized to the 1317 $cm^{-1}$ bipyridine (bpy) peak as it exhibits little dependence on the environment.[24]

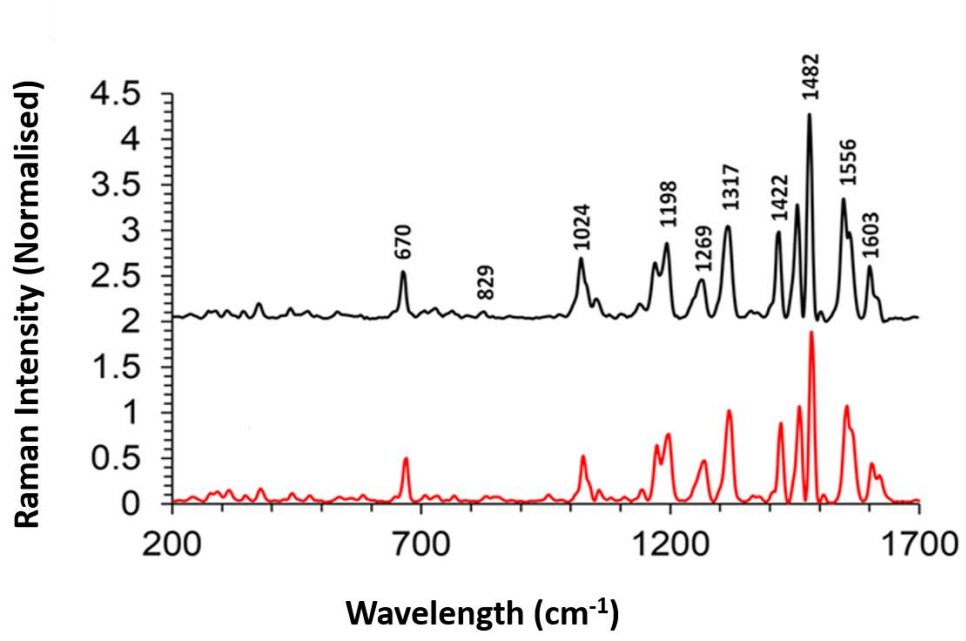


**Figure 2.15** Raman spectra of $[Os(bpy)_2(pic\text{-}COOH)]^{2+}$ (—) and $[Os(bpy)_2(pic\text{-}arg_8)]^{10+}$ (—) in PBS solution (70 µM) excited using a 488 nm laser. Data was normalised to the 1317 $cm^{-1}$ bpy peak and offset for clarity. (n=3)

As demonstrated in Figure 2.15, $[Os(bpy)_2(pic\text{-}arg_8)]^{10+}$ exhibits a remarkably strong resonance Raman signal when excited at 488 nm in PBS solution. Signature vibrational modes for the bipyridine (bpy) ligand appear at 1603, 1552, 1482, 1317, 1269, 1173, 1024 and 670 $cm^{-1.}$ Interestingly, unlike the analogous $[Ru(bpy)_2(pic\text{-}arg_8)]^{10+}$ complex where the pic moiety was weaker at this excitation, vibrational modes for the pic moiety are equally as intense, seen at 1556, 1506 $cm^{-1}$, and a 1458, 1422, 1248, 1198 and 829 $cm^{-1}$. This suggests Os(dπ) to bpy π* transition and Os(dπ) to pic π* MLCT transition are both resonant at 488 nm. The spectra of $[Os(bpy)_2(pic\text{-}COOH)]^{2+}$ and its peptide conjugate do not show any significant changes as expected, as the peptide does not contribute to the visible optical transition.

Resonance Raman mapping of $[Os(bpy)_2(pic\text{-}arg_8)]^{10+}$ in a CHO cell was then examined. Figure 2.16 shows representative Raman mapping of $[Os(bpy)_2(pic\text{-}arg_8)]^{10+}$ in a single CHO cell. The CHO cells were prepared as described in *section 2.2.10* with 70 µM $[Os(bpy)_2(pic\text{-}arg_8)]^{10+}$. Point spectra were acquired at the cell membrane, cytoplasm, and nucleus, and compared to $[Os(bpy)_2(pic\text{-}arg_8)]^{10+}$ spectrum in solution. The sample was excited using a 488 nm laser line, as this is coincident with the $^1$MLCT absorbance, and the spectra were acquired for 64 seconds. Spectra were normalized to 1317 $cm^{-1}$ peak.

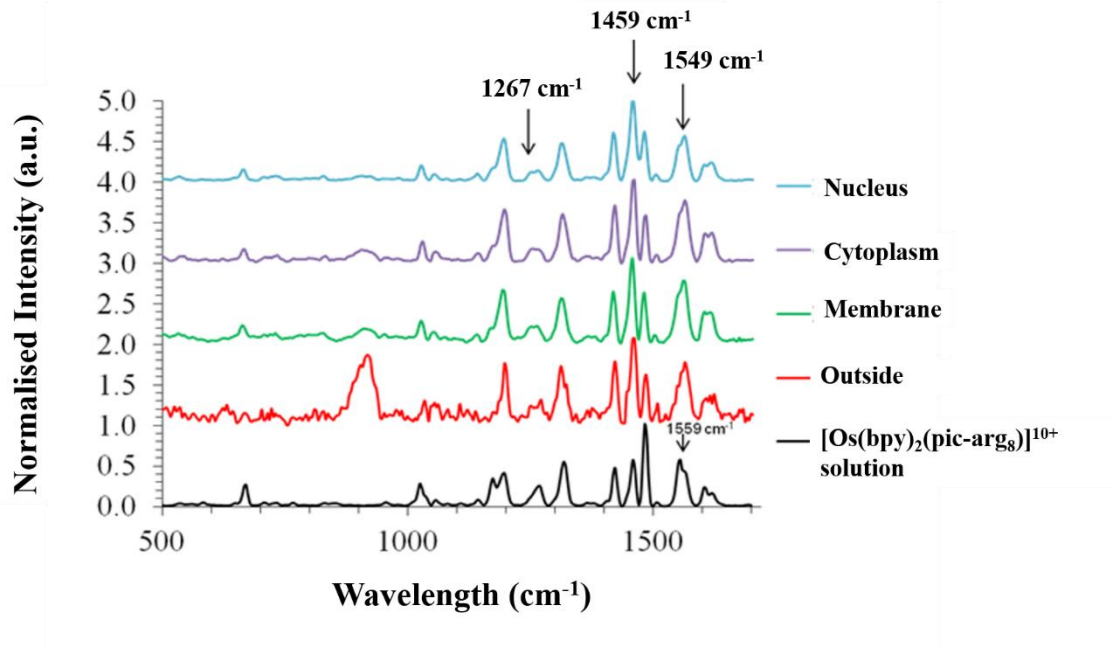


**Figure 2.16** Raman spectra of $[Os(bpy)_2(pic\text{-}arg_8)]^{10+}$ accumulation in a CHO cell. Cells were incubated with 70 μM complex for 24 h (37 °C with 5 % $CO_2$). Media was removed and cells were washed twice with PBS buffer supplemented with 1.1 mM $MgCl_2$ and 0.9 mM $CaCl_2$. Spectra compared to $[Os(bpy)_2(pic\text{-}arg_8)]^{10+}$ solution in PBS. (n = 3).

Consistent with emission confocal images, the resonance Raman confirms that $[Os(bpy)_2(pic\text{-}arg_8)]^{10+}$ accumulates within the cell and distributes widely. Interestingly, the 1459 $cm^{-1}$ pic vibrational band shows a 2-3 fold relative increase in intensity in the cell compared to the bpy reference at 1482 $cm^{-1}$ in the cell compared to when in solution. The 1267 $cm^{-1}$ bpy vibrational band broadens as $[Os(bpy)_2(pic\text{-}arg_8)]^{10+}$ enters the cell. The peak broadens and the intensity decreases as the complex is internalized and enters the cell organelles. Broadening of Raman peaks is often associated with a heterogeneous environment. The aromatic ring stretch coupled CH mode at 1552 $cm^{-1}$ exhibits a shoulder at 1559 $cm^{-1}$ in PBS solution, which disappears upon entering the cell. Instead, a shoulder at 1549 $cm^{-1}$ appears.[25] This may be as a result of changes to the pH of the environment. Similar effects were noted for the Ru(II) analogue but were not as strong as $[Os(bpy)_2(pic\text{-}arg_8)]^{10+}$.[24]

$[Os(bpy)_2(pic\text{-}arg_8)]^{10+}$ has demonstrated excellent Raman signal from within the cell. The changes in which $[Os(bpy)_2(pic\text{-}arg_8)]^{10+}$ undergoes once inside the cell makes it a useful Raman probe for tracking cellular functions at the various organelles via cell mapping.

## 2.10 Conclusions

Chapter 2 explored, for the first time, Os(II) complexes as multimodal imaging probes, and compared the complex $[Os(bpy)_2(pic\text{-}arg_8)]^{10+}$ to its Ru(II) analogue $[Ru(bpy)_2(pic\text{-}arg_8)]^{10+}$.

The photophysical, cell uptake, and in-cell optical properties of a novel $[Os(bpy)_2(pic\text{-}COOH)]^{2+}$ and conjugate $[Os(bpy)_2(pic\text{-}arg_8)]^{10+}$ were investigated. Like ruthenium, osmium has a large Stokes shift, but it emits outside the biological window at $\lambda_{max}$ 720 nm. This is an ideal characteristic of an imaging probe as it avoids the auto-fluorescence of a cell and self-quenching. It was found to have a much lower lifetime of 33 ns, and to be oxygen independent, unlike its ruthenium analogue that possesses a much longer lifetime of 560 ns and is sensitive to $O_2$ concentrations. A disadvantage is the relatively low quantum yield, nonetheless, good quality images were acquired without self-quenching occurring.

Confocal microscopy demonstrated that $[Os(bpy)_2(pic\text{-}arg_8)]^{10+}$ was easily taken up by cells, internalized in the first 2 minutes of exposure. Similar results were shown by *Neugebauer et al* of $[Ru(bpy)_2(pic\text{-}arg_8)]^{10+}$.[11] Both complexes accumulated in the cytoplasm, and distributed throughout the cell with no specificity for particular organelles. Co-localization studies confirmed that $[Os(bpy)_2(pic\text{-}arg_8)]^{10+}$ had entered some lysosomes and mitochondria of the cell, but not all, which is consistent with octa-arginine as a general cytoplasmic targeting peptide. Nuclear penetration by $[Os(bpy)_2(pic\text{-}arg_8)]^{10+}$ was observed during live uptake studies, possibly as a result of photo activation, and increased lipophilicity. The lipophilicity is something that needs to be explored further in $[Os(bpy)_2(pic\text{-}arg_8)]^{10+}$ uptake, localisation, and toxicity towards cells.

Although it has a much shorter lifetime than that of $[Ru(bpy)_2(pic\text{-}arg_8)]^{10+}$ at 33 ns in solution, the lifetime is still considerably long compared to organic dyes. $[Os(bpy)_2(pic\text{-}arg_8)]^{10+}$ lifetime in CHO cells was examined using PLIM imaging. Both $[Os(bpy)_2(pic\text{-}arg_8)]^{10+}$ and $[Ru(bpy)_2(pic\text{-}arg_8)]^{10+}$ showed changes in their lifetimes when internalized. A lower lifetime was seen in the cytoplasm compared to the membrane for both complexes, which could be a result of tight lipid packing in the plasma membrane. As $[Os(bpy)_2(pic\text{-}arg_8)]^{10+}$ is insensitive to oxygen concentrations, the significant changes in $[Os(bpy)_2(pic\text{-}arg_8)]^{10+}$ luminescent lifetime that were observed in the cell are

attributed to other environmental factors in the cell, such as pH. This is something that will have to be explored further. This suggests that $[Os(bpy)_2(pic\text{-}arg_8)]^{10+}$ may be useful as an environmental sensing probe without the interference of oxygen.

Finally, the large large Stokes shift allowed for the resonance Raman of $[Os(bpy)_2(pic\text{-}arg_8)]^{10+}$ to be explored. Useful confirmation of probe structure can be obtained using resonance Raman. In aqueous solution it exhibited a strong resonance Raman spectrum, with no interference from the peptide conjugate. Raman mapping of $[Os(bpy)_2(pic\text{-}arg_8)]^{10+}$ in a CHO cell demonstrated clear spectra from the membrane, cytoplasm, and nucleus. The bpy moiety showed to be affected by internalization, with clear changes to its vibrational bands compared to when in solution. The changes may also be a result of the changing pH of the cell environment. This is something to be looked at in greater detail in the future.

The $[Os(bpy)_2(pic\text{-}arg_8)]^{10+}$ peptide conjugate shows promise as a multi-modal imaging probe, and proved to be as effective as its Ru(II) equivalent. In terms of its ease of uptake and lack of phototoxicity and cytotoxicity towards cells, this will allow for long term confocal scanning to be carried out without compromising the state of the cell. Although it is oxygen independent, $[Os(bpy)_2(pic\text{-}arg_8)]^{10+}$ shows promise as a successful probe in studying the local viscosity, cell membrane fluidity, and lipid membranes in the cell using FLIM imaging techniques. This will have to be explored in greater detail. Overall, its NIR emission and excellent photostability have shown Os(II) complexes to be a suitable metal complex in cell imaging over its Ru(II) equivalent.

## *References*


1. Gill MR, Thomas JA. Ruthenium(II) polypyridyl complexes and DNA—from structural probes to cellular imaging and therapeutics. *Chemical Society Reviews*. 2012;41:3179.

2. Ferna´ndez-Moreira V, Thorp-Greenwood FL, Coogan MP. Application of d6 transition metal complexes in fluorescence cell imaging. *Chem. Commun.* 2010;46:186.

3. Zhao Q, Yu M, Shi L, et al. Cationic iridium(III) complexes with tunable emission color as phosphorescent dyes for live cell imaging. *Organometallics*. 2010;29:1085-1091.

4. Xiong L, Zhao Q, Chen H, et al. Phosphorescence imaging of homocysteine and cysteine in living cells based on a cationic iridium(III) complex. *Inorg Chem*. 2010;49:6402-6408.

5. Dolan C, Moriarty RD, Lestini E, Devocelle M, Forster RJ, Keyes TE. Cell uptake and cytotoxicity of a novel cyclometalated iridium(III) complex and its octaarginine peptide conjugate. *J Inorg Biochem*. 2013;119:65-74.

6. Liu YJ, Zeng CH, Huang HL, He LX, Wu FH. Synthesis, DNA-binding, photocleavage, cytotoxicity and antioxidant activity of ruthenium (II) polypyridyl complexes. *European Journal of Medicinal Chemistry*. 2010;45:564-571.

7. Barton JK, Olmon ED, Sontz PA. Metal complexes for DNA-mediated charge transport. *Coord Chem Rev*. 2011;255:619-634.

8. Kostrhunova H, Florian J, Novakova O, Peacock AFA, Sadler PJ, Brabec V. DNA interactions of monofunctional organometallic osmium(II) antitumor complexes in cell-free media. *J Med Chem 2008, 51, 3635–3643*. 2008;51:3635-3643.

9. van Rijt SH, Mukherjee A, Pizarro AM, Sadler PJ. Cytotoxicity, hydrophobicity, uptake, and distribution of osmium(II) anticancer complexes in ovarian cancer cells. *J Med Chem*. 2010;53:840-849.

10. van Rijt SH, Kostrhunova H, Brabec V, Sadler PJ. Functionalization of osmium arene anticancer complexes with (poly)arginine: Effect on cellular uptake, internalization, and cytotoxicity. *Bioconjugate Chem*. 2011;22:218-226.

11. Neugebauer U, Pellegrin Y, Devocelle M, et al. Ruthenium polypyridyl peptide conjugates: Membrane permeable probes for cellular imaging. *Chem Commun , 2008, 5307–5309*. 2008;42:5307-5309.

12. Byrne A, Dolan C, Moriarty RD, et al. Osmium(II) polypyridyl polyarginine conjugate as a probe for live cell imaging; a comparison of uptake, localization and cytotoxicity with its ruthenium(II) analogue. *Dalton Trans*. 2015;44:14323-14332.

13. Nakamaru K. Synthesis, luminescence quantum yields, and lifetimes of trischelated ruthenium (II) mixed-ligand complexes including 3,3'-dimethyl-2,2'-bipyridyl. *Bull Chem Soc Jpn*. 1982;55:2697.

14. Yoo EM, Yu LJ, Wims LA, Goldberg D, Morrison SL. Differences in N-glycan structures foundon recombinant IgA1 and IgA2 producedin murine myeloma and CHO cell lines *MAbs*. 2010;2:320-334.

15. Ngo DC, Ververis K, Tortorella SM, Karagiannis TC. Introduction to the molecular basis of cancer metabolism and the warburg effect. *Mol Biol Rep*. 2015;42:819-823.

16. Komor AC, Barton JK. The path for metal complexes to a DNA target. *Chemical Communications*. 2013;49(35):3617.

17. Puckett CA, Barton JK. Fluorescein redirects a ruthenium-octaarginine conjugate to the nucleus. *J Am Chem Soc*. 2009;131:8738-8739.

18. Bergamo A, Masi A, Peacock AFA, Habtemariam A, Sadler PJ, Sava G. In vivo tumour and metastasis reduction and in vitro effects on invasion assays of the ruthenium RM175 and osmium AFAP51 organometallics in the mammary cancer model. *J Inorg Biochem*. 2010;104(1):79-86.

19. Hannan S, Wilkins ME, Dehghani-Tafti E, Thomas P, Baddeley SM, Smart TG. γ-aminobutyric acid type B (GABAB) receptor internalization is regulated by the R2 subunit. *Journal of Biological Chemistry*. 2011;286:24324.

20. Moucheron C, Kirsch-De Mesmaeker A, Kelly JM. Photoreactions of ruthenium (II) and osmium (II) complexes with deoxyribonucleic acid (DNA). *Journal of Photochemistry and Photobiology B: Biology*. 1997;40(2):91-106.

21. Suhling K, Cade NI, Levitt JA, et al. Fluorescence lifetime imaging applied to microviscosity mapping and fluorescence modification studies in cells. *Biomedical Imaging : The Chemistry of Labels, Probes and Contrast Agents*. 2012:371-390.

22. Stöckl MT, Herrmann A. Detection of lipid domains in model and cell membranes by fluorescence lifetime imaging microscopy. *Biochimica et Biophysica Acta (BBA) - Biomembranes*. 2010;1798(7):1444-1456.

23. Lladó V, López DJ, Ibarguren M, et al. Regulation of the cancer cell membrane lipid composition by NaCHOleate: Effects on cell signaling and therapeutical relevance in glioma. *Biochimica et Biophysica Acta (BBA) - Biomembranes*. 2014;1838(6):1619-1627.

24. Swinnen JV, Vanderhoydonc F, Elgamal AA, et al. Selective activation of the fatty acid synthesis pathway in human prostate cancer. *Int J Cancer*. 2000;88:176-179.

25. Neugebauer U, Cosgrave L, Pellegrin Y, Devocelle M, forster RJ, Keyes TE. Mulitmodal, muliparameter cell imaging using ruthenium polypyridyl peptide conjugates. *Proc SPIE*. 2012;8427:84270C.

26. Mallick PK, Danzer GD, Strommen DP, Kincaid JR. Vibrational spectra and normal-coordinate analysis of tris(bipyridine)ruthenium(II) *J Phys Chem* ,. 1988;92:5628-5634.

# Chapter Three: Ru (II) polypyridyl complex conjugated to a mitochondria penetrating peptide (MPP) as an oxygen sensor

## 3.1 Introduction

Intracellular oxygen is the key metabolite in energy generation in mammalian cells. It is also a substrate of numerous enzymatic reactions within the cell which are vital for normal cell function. Therefore, monitoring oxygen concentrations within living cells is a valuable way of assessing cellular respiration and metabolism.

Oxygen can be detected in luminescence imaging through its ability to quench the excited state of the given luminophore, and thus reducing emission intensity and lifetime. However, the emission intensity is also affected by probe concentration, making emission intensity via imaging an unreliable quantitative method. Whereas, the luminescent lifetime of a luminophore is independent of probe concentration and therefore is a more suitable measurement parameter.[1-3] Platinum group metal complexes, such as ruthenium and osmium, emit from a triplet excited state which can interact with a triplet acceptor, in this case oxygen allowing for quenching *via* energy transfer.

There have been relatively few oxygen probes reported that are capable of crossing the cell membrane without the need for permeabilisation using solvents, for example DMSO or detergents such as Triton X. These complexes can be rendered water soluble by incorporating conjugation peptides, PEG groups and other bio-compatible functional groups, as discussed previously in Chapter 1. This chapter will focus on using signal peptide sequences to promote water solubility and enhance cell uptake whilst targeting the probe specifically to the mitochondria.

As discussed earlier, the advantages of using transition metals such as ruthenium are their photostability, high quantum yield, and oxygen sensitivity. In order to selectively target specific cellular organelles, in this case, the mitochondria, a specific mitochondria penetrating peptide (MPP) sequence will be used in order to measure oxygen from within the mitochondria.[4] The mitochondria are the energy centres of the cell. All of the ATP required for cellular functions is formed there. In order to produce ATP, the mitochondria consumes ~90 % of the cells oxygen. [5] Thus $O_2$ concentrations in the mitochondria directly reflect the health of the cell. Mitochondrial dysfunctions have been found to play a part in a range of debilitating diseases including Alzheimer's, Parkinson's, and Multiple Sclerosis, typically as a result of abnormal $O_2$ metabolism in the mitochondria. [6, 7] The coupling of a Ru(II), $O_2$ probe with an MPP would be

advantageous in directing the complex across the cell membrane without compromising the cell. It would provide real-time information on oxygen concentrations in the mitochondria monitored by methods such as phosphorescent lifetime imaging microscopy (PLIM). This would make imaging of cellular $O_2$ useful in the biochemical toxicity of diseases caused by the dysfunction in the mitochondria.

Due to the relatively low lipophilicity and the cationic charge of metal based probes, difficulties arise in successfully directing a metal-based probe to the mitochondria and penetrating the organelle. [8] To date, there have been a number of examples of luminophores reported to reach the mitochondria.[9-11] For example, *Lo et al* recently described a family of PEGylated cyclometalated iridium complexes which reached the mitochondria and exhibited strong phototoxicity.[12] *Keene et al* reported on di-nuclear ruthenium complexes that showed to selectively locate in the mitochondria of L1210 murine leukaemia cells.[11] But in all of these studies, the complexes were not specifically designed to target the mitochondria. The nature of their designs allowed serendipity to play a role as they localised within the mitochondria. Recently, *Chao et al* synthesised a series of Ru(II) complexes designed to target the mitochondria by possessing a 2-phenylimidazo[4, 5–f][1, 10]phenanthroline (PIP) ligand.[13] However, their aim was to induce apoptosis from within the mitochondria as an anti-cancer agent rather than as an imaging sensor probe.

The aim of this chapter was to evaluate a Ru(II) complex as an oxygen sensing probe and to generate a calibration plot reflecting its response to oxygen concentrations. The Ru(II) complex conjugated to peptide sequence FrFKFrFK (r = D-arginine) where previously shown to be investigated as a mitochondrial targeting probe, as a means to report on oxygen levels from within the mitochondria.

This chapter details the $[Ru(bpy)_2phen\text{-}Ar\text{-}COOH]^{2+}$ complex, conjugated to two peptide sequences for in-cell sensing. The probe's luminescent emission intensity and lifetime was measured in response to oxygen concentrations to generate calibration curves which could then be applied to cells. Detailed cell studies were carried out, looking at the general uptake of the complexes by cells, and the co-localistaion within the mitochondria. Oxygen concentrations from within the mitochondria were measured using PLIM, and the oxygen concentrations were modulated using the antibiotic Antimycin A. Antimycin A is an inhibitor of electron transfer at complex III in mitochondria. It blocks the mitochondria from consuming oxygen in the cell. Therefore,

there is a build up of oxygen in the cell, increasing the natural concentration. This was used in order to test the probes ability to respond dynamically to the changing environments from within the mitochondria.

## 3.2 Materials and Methods

### 3.2.1 Materials

$[Ru(bpy)_2phen\text{-}Ar\text{-}COOH]^{2+}$ parent complex and the peptide conjugate were synthesised by Dr. Aaron Martin (DCU). All chemicals and solvents used in experimental procedures were purchased from Sigma Aldrich (Ireland). All solutions were made using deionised water, which was purified by a Milli-Q plus 18.5 Millipore purifying system.

Resazurin reagents were acquired from Promokine. Cell culture media, serum and penicillin / streptomycin were purchased from Sigma Aldrich. Cell culture flasks were purchased from Corning Incorporated

### 3.2.2 Spectroscopic Measurements

The UV/Vis spectra were recorded on a Jasco V-679 UV/Vis/NIR spectrometer. Fluorescence emission and excitation were measured using a Cary Eclipse Fluorescence Spectrometer, both at a slit width of 5 nm. Solution measurements were carried out in 1 % v/v DMSO with PBS, and neat PBS in a Hellma quartz cuvette of 1 cm optical path length.

### 3.2.3 Luminescent Lifetimes

The lifetimes were collected using a FluoTime 100 Time-Correlated Single Photon Counting (TCSPC) instrument. The 405 nm laser was used to excite parent and conjugate complexes, provided from a Picoquant ‘PDL 800B’ pulsed diode laser. 10,000 counts were collected for each lifetime measurement. Analysis of measurements was carried out using either Nanoharp or Timeharp software. The luminescent lifetimes were calculated using the PicoQuant FluoFit software by fitting an exponential decay function

to each decay plot. The data was then fitted to a mono-exponential decay to the background decay curve, using a tail fit with a $\chi^2$ value between 0.9-1.1.

### 3.2.4 Real-time confocal luminescent imaging

HeLa cells were seeded at 1.5 x $10^5$ cells in 2 mL media on 35 mm glass-bottom culture dishes. Cells were grown for 48 h at 37 ºC at 5 % $CO_2$. The growth medium was removed and 75 µM of the $[(Ru(bpy)_2phen\text{-}Ar)_2\text{-}FrFKFrFK]^{7+}$ or $[Ru(bpy)_2\text{-}Phen\text{-}Ar\text{-}Arg_8]^{10+}$ in phenol red indicator-free media was added and allowed to incubate for 2 h at 37 ºC at 5 % $CO_2$ in the dark. The dye/media solution was removed and cells were washed with PBS supplemented with 1.1 mM $MgCl_2$ and 0.9 mM $CaCl_2$. Cells were imaged using a Zeiss LSM510 Meta confocal microscope using a 63X oil immersion objective lens and heated stage set to 37 ºC. A 488 nm Argon ion laser was used to excite the complex, and emission was collected using a long pass 560 nm filter set.

### 3.2.5 Cytotoxicity Studies

HeLa cells were seeded in a 96-well plate at 1 x $10^4$ in 100 µL of media, and left to incubate at 37 °C at 5 % $CO_2$ for 24 hours. The compounds were added to the wells resulting in final concentrations of 200, 150, 100, 40, 10, 1 and 0.1 µM. The cells were incubated overnight with the dyes. 10 µL Resazurin reagent (PromoKine) was added to each well, and incubated for 7 h in the dark at 37 °C. Absorbance readings were recorded using a Tecan 96-well plate reader at 570 nm and 600 nm for background subtraction. All cytotoxicity experiments are reported in terms of percentage (%) viability, where 100 % viability = 100 % of viable cells in the well. Each experiment was carried out in triplicate (n = 3 ± SD).

### 3.2.6 Phosphorescent Lifetime Imaging Microscopy (PLIM)

HeLa cells were seeded at 1.5 x $10^5$ on a sterile 35 mm glass bottom culture dish and were incubated for 48 h. 75 µM of $[(Ru(bpy)_2phen\text{-}Ar)_2\text{-}FrFKFrFK]^{7+}$ in phenol red-free media was added for 2 h incubation in the dark at 37 ºC at 5 % $CO_2$. The media was removed and cells were washed with PBS (supplemented with 1.1 mM $MgCl_2$ and 0.9 mM $CaCl_2$). Live PLIM images were acquired usung MicroTime 200, PicoQuant, attached to a Zeiss LSM510 confocal microscope using a 63 x oil immersion objective and heated stage set to 37ºC. Each PLIM image was acquired for 10 minutes with 256 x 256 resolution. 405 nm laser was used to excite the sample, and emission collected using a long pass 530 nm filter. The data was analysed using PicoQuant Symphotime software. Lifetimes were fit to a mono-exponential decay until a $\chi^2$ value of 0.9 - 1.1 was achieved. The average lifetime was taken from 2 separate experiments (n = 2).

### 3.2.7 Oxygen studies in HeLa cells

HeLa cells were seeded as described previously and incubated with 75 µM complex $[(Ru(bpy)_2phen\text{-}Ar)_2\text{-}FrFKFrFK]^{7+}$ in phenol red-free media for 2 h at 37 ºC and washed with PBS/$MgCl_2$/$CaCl_2$ solution. PLIM images were aquired immediately using Microtime 200, PicoQuant attached to a Zeiss LSM510 confocal microscope using 63x oil immersion objective, using a heated stage at 37 ºC. Each PLIM image was acquired for an average of 10 minutes to reach 10,000 counts, with 256 x 256 resolution. A 405 nm laser was used to excite the sample, and emission collected using a long pass 530 filter. 200 µg/mL Antimycin A in PBS (supplemented with 0.9 mM $CaCl_2$ and 1.1 mM $MgCl_2$) was added to live HeLa cells and left for 10 minutes at 37 ºC to accumulate, and the PLIM image was acquired over time. Cells were incubated for a further 90 minutes with the Antimycin A, and PLIM image was acquired at a final exposure time of 100 minutes.

### 3.2.8 $[(Ru(bpy)_2phen\text{-}Ar)_2\text{-}FrFKFrFK]^{7+}$ phototoxicity towards HeLa cells

HeLa cells were seeded at 1.5 x $10^5$ in 2 mL cell media on 35 mm glass bottom culture dishes and incubated for 48 h. The media was removed and cells were washed with PBS

supplemented with 1.1 mM $MgCl_2$ and 0.9 mM $CaCl_2$ and transferred to a 37 ºC heated stage. 75 µM of $[(Ru(bpy)_2phen\text{-}Ar)_2\text{-}FrFKFrFK]^{7+}$ in phenol red-free media and DRAQ 7 (1:100) was added to the live cells and scanned immediately using the Time Series mode on a Zeiss LSM510 Meta confocal microscope. DRAQ 7, which stains the nucleus of dead cells, was excited using 633 nm HeNe laser 10 % transmission, and 488 nm Argon laser 3 % transmission for $[(Ru(bpy)_2phen\text{-}Ar)_2\text{-}FrFKFrFK]^{7+}$. Emission was collected using a long pass 650 nm filter set for DRAQ 7, and long pass 560 nm filter for $[(Ru(bpy)_2phen\text{-}Ar)_2\text{-}FrFKFrFK]^{7+}$. Cells were scanned continuously using the $[(Ru(bpy)_2phen\text{-}Ar)_2\text{-}FrFKFrFK]^{7+}$ settings for 5 minute intervals, imaging with the DRAQ 7 settings between intervals to assess viability. For the control, cells were set up as described above, and DRAQ 7 (1:100) in phenol red-free media was added to the live cells. They were scanned continuously using the ruthenium settings, and imaged after each interval to assess for DRAQ 7 uptake.

## 3.3 Photo physical properties and Characterisation of $[Ru(bpy)_2phen\text{-}Ar\text{-}COOH]^{2+}$ and Peptide Conjugates

Figure 3.1 shows the emission and absorbance spectroscopy of $[Ru(bpy)_2phen\text{-}Ar\text{-}COOH]^{2+}$ and $[(Ru(bpy)_2phen\text{-}Ar)_2\text{-}FrFKFrFK]^{7+}$, both in PBS aqueous solution (pH 7.4). They both exhibit an absorbance band at 460 nm, which is assigned to the ruthenium π to ligand π* MLCT transition. The strong absorbance band observed at ~280 nm is attributed to the π-π* transitions of the polypyridyl ligands. The absorbance spectra appear to be identical, but a more intense absorbance at the same concentration is detected for $[(Ru(bpy)_2phen\text{-}Ar)_2\text{-}FrFKFrFK]^{7+}$, which is attributed to the presence of two ruthenium centres at the peptide bridge (Scheme 3.1). When excited into the MLCT band at 460 nm, an intense emission band is exhibited at approximately 604 nm. Conjugation to the peptide appeared to have no effect on the photophysics of the dimeric complexcmpared to its parent.

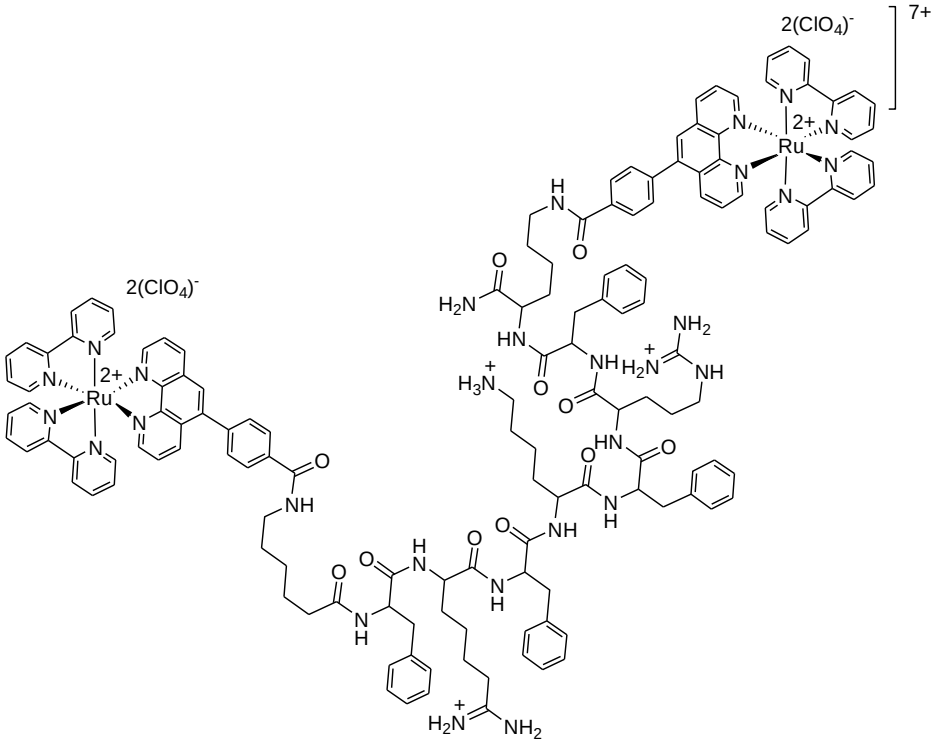


**Scheme 3.1** Chemical structure of dimeric $[(Ru(bpy)_2phen\text{-}Ar)_2\text{-}FrFKFrFK]^{7+}$ mitochondrial localising complex.

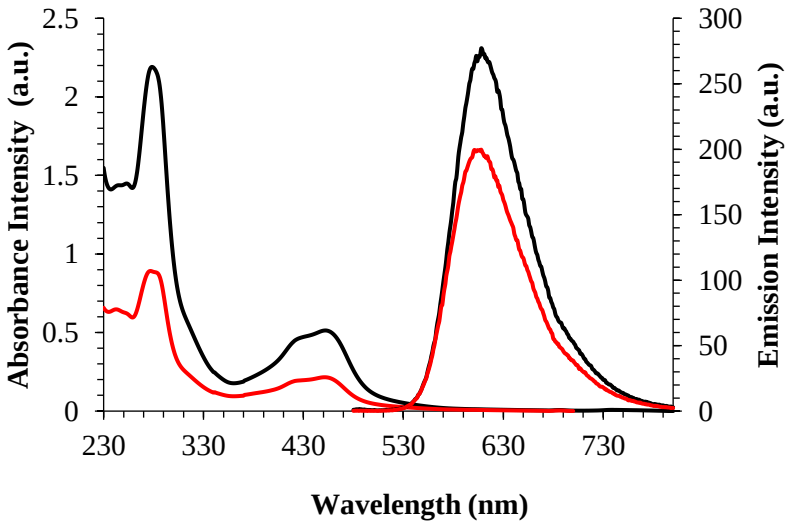


**Figure 3.1** Absorbance and emission spectra of ruthenium parent complex $[Ru(bpy)_2phen\text{-}Ar\text{-}COOH]^{2+}$ (—) and MPP conjugate $[(Ru(bpy)_2phen\text{-}Ar)_2\text{-}FrFKFrFK]^{7+}$ (—). Spectra were recorded at 50 μM in aqueous solution (PBS). Both complexes were excited into the MLCT band at 458 nm and the emission was collected between 500 – 750 nm, both at a slit width = 5nm.

The luminescent lifetimes were fit to a mono-exponential lifetime decay, signifying that there is only one luminescent lifetime present. The luminescent lifetime of **[**$Ru(bpy)_2$phen-Ar-COOH$]^{2+}$ parent complex increased from 455 ± 11 ns to 689 ± 6 ns upon peptide conjugation which is attributed to some modest protection of the metal centre from diffusing oxygen by the peptide. The samples were then deaerated by purging with nitrogen for 20 minutes and luminescent lifetime measurements were recorded again. Time correlated single photon counting (TCSPC) was used to measure the luminescent lifetimes. Following deaeration, the lifetimes of both complexes increased dramatically. The luminescent lifetime of [$(Ru(bpy)_2$phen-$Ar)_2$-FrFKFrFK$]^{7+}$ increased from 689 ± 6 ns to 1.23 μs ± 10 ns. Figure 3.2 shows the luminescent lifetime decays of [$(Ru(bpy)_2$phen-$Ar)_2$-FrFKFrFK$]^{7+}$ when aerated (A), and de-aerated (B) using time correlated single photon counting (TCSPC).

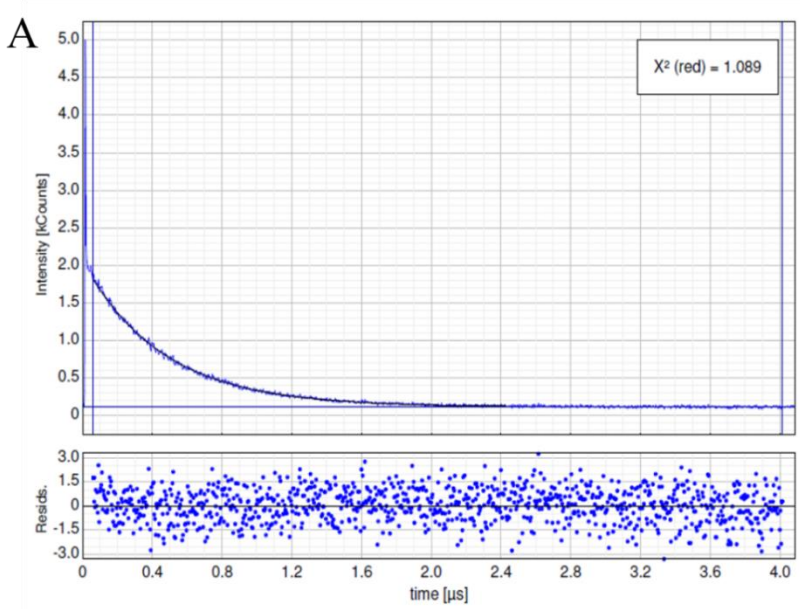

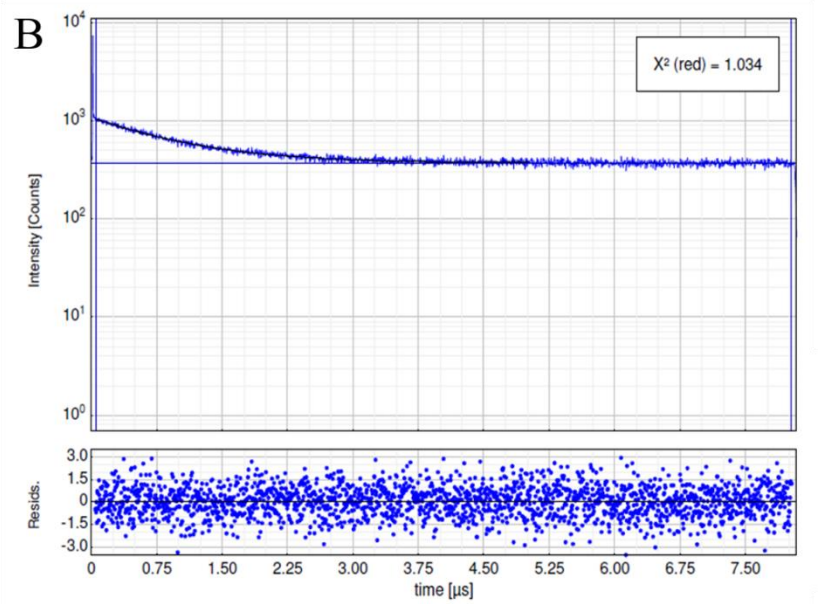


**Figure 3.2** TCSPC emission lifetime traces of $[(Ru(bpy)_2phen\text{-}Ar)_2\text{-}FrFKFrFK]^{7+}$ under aerated (A) and de-aerated (B) condiotions. $[(Ru(bpy)_2phen\text{-}Ar)_2\text{-}FrFKFrFK]^{7+}$ was de-aerated for 20 minutes with nitrogen. The complexes were excited using the 450 nm laser, and the data was acquired using the PicoQuant Nano Harp system. The lifetime traces (—) and residuals (•) were fit to give a $\chi^2$ value between 0.9 and 1.1.

The luminescent lifetimes were obtained by fitting the model to the curve (•) to give a $\chi^2$ value as close to 1 as possible and goodness of fit was also assessed by visual inspection of the residuals (e.g. Figure 3.2 bottom). In both cases, the decays were fit to give $\chi^2$ values of 1.089 when aerated, and 1.034 when de-aerated, indicating in agreement with the residuals shown above, an excellent fit. Table 3.1 summarises the photophysical properties of parent complex $[Ru(bpy)_2phen\text{-}Ar\text{-}COOH]^{2+}$ and MPP conjugate $[(Ru(bpy)_2phen\text{-}Ar)_2\text{-}FrFKFrFK]^{7+}$.

**Table 3.1** Photophysical properties of the $[Ru(bpy)_2phen\text{-}Ar\text{-}COOH]^{2+}$ parent complex, $[(Ru(bpy)_2phen\text{-}Ar)_2\text{-}FrFKFrFK]^{7+}$ mitochondrial complex, and $[(Ru(bpy)_2phen\text{-}Ar)_2\text{-}AHX\text{-}Arg_8]^{10+}$ complex in PBS solution (12.5 μM) at room temperature 18 °C.

| **Complex** | **Φ (%)** | **UV-Vis $Abs_{max}$** | **$\lambda_{max}$** | **τ aerated (18 °C)** | **τ deaerated (18 °C)** |
|---|---|---|---|---|---|
| **$[Ru(bpy)_2phen\text{-}Ar\text{-}COOH]^{2+}$** | 0.046 ± 0.003 | 460 | 604 | 455 ns ± 11 ns | 780 ns ± 9 ns |
| **$[(Ru(bpy)_2phen\text{-}Ar)_2\text{-}FrFKFrFK]^{7+}$** | 0.053 ± 0.002 | 460 | 604 | 698 ns ± 6 ns | 1.23μs ± 10 ns |
| **$[(Ru(bpy)_2phen\text{-}Ar)_2\text{-}Arg_8]^{10+}$** | 0.067 ± 0.005 | 460 | 604 | 579 ns ± 11 ns | 1.02 μs ± 9 ns |

## 3.4 Oxygen dependent studies

To further investigate the oxygen sensitivity of $[(Ru(bpy)_2phen\text{-}Ar)_2\text{-}FrFKFrFK]^{7+}$, the emission intensity and lifetimes were recorded over a range of oxygen concentrations *in vitro* at room temperature (18 °C). The oxygen saturation concentration of $[(Ru(bpy)_2phen\text{-}Ar)_2\text{-}FrFKFrFK]^{7+}$ (50 μM in PBS) was determined to be 220 μM/L using a PreSense oxygen probe, and the initial emission spectra was recorded in air saturated solution. The solution was then fully degassed using nitrogen for 15 minutes. This resulted in a final oxygen concentration measured from the PreSense probe of 2 μM/L in the solution, and the emission intensity was recorded. Oxygen was reintroduced slowly into the sample, recording the emission spectra at different oxygen concentrations. Figure 3.3A shows that the emission intensity increased dramatically by ~50 % when fully aerated (—) to when fully deaerated (—). As oxygen was reintroduced

in to the sample, the emission intensity decreased linearly. The same linear decrease was observed for the luminescent lifetime. Such behaviour in response to oxygen is typical of Ru(II) complexes.

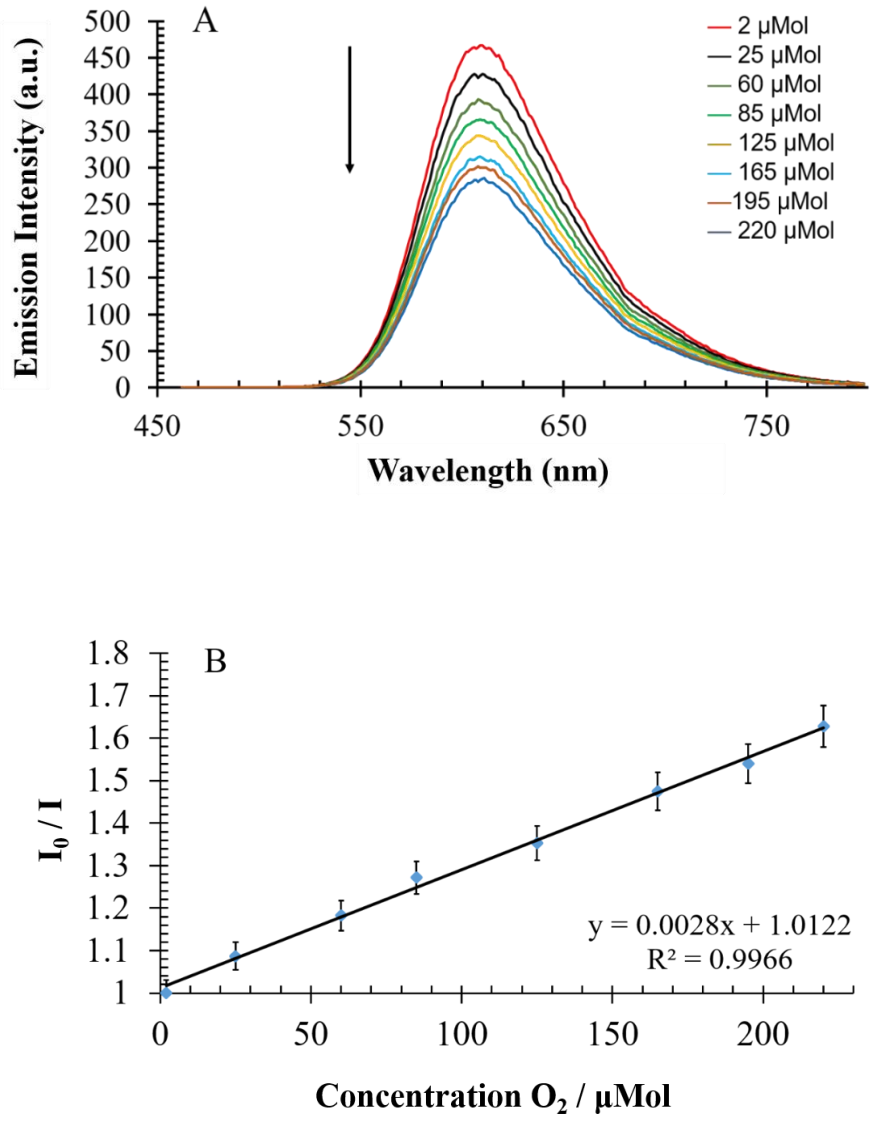


**Figure 3.3** Luminescent emission intensity measured as a function of $O_2$ for $[(Ru(bpy)_2phen\text{-}Ar)_2\text{-}FrFKFrFK]^{7+}$ in PBS (50 µM, 18 °C). Emission intensity versus $O_2$ from saturation to deaeration (A), where the legend shows concentrations of $O_2$ in the media as measured independently by $O_2$ sensor. The corresponding Stern-Volmer plot (B) of emission intensity as a function of oxygen concentration. The sample was de-aerated with nitrogen for 20 minutes and the emission intensities were measured at various oxygen concentrations. The arrow indicates the decrease in the luminescent emission intensity as the oxygen concentration increases.

To determine the rate of quenching by oxygen, the data was fit to a Stern Volmer plot applying the Stern Volmer equation given in equation 3.1:

$$I_0/I = \tau_0/\tau = 1 + K_{SV}\,[O_2] \text{ …. Equation 3.1}$$

Where $I_0$ is the emission intensity in the absence of oxygen, I is the emission intensity, $\tau_0$ is the lifetime in the absence of oxygen, $\tau$ is the lifetime, $K_{SV}$ is the Stern-Volmer quenching constant and $[O_2]$ is the concentration of oxygen, mol/dm$^3$. $K_{SV}$ can be used to determine the biomolecular quenching rate using the following equation 3.2:

$$K_{SV} = k_q.\tau_0 \text{ …. Equation 3.2}$$

where $K_{SV}$ is the slope of the Stern Volmer plot, $k_q$ is the rate of quenching and $\tau_0$ is the luminescent lifetime in the absence of oxygen.

Figure 3.4 shows the corresponding Stern Volmer plot of the oxygen dependent luminescent emission intensity of $[(Ru(bpy)_2phen\text{-}Ar)_2\text{-}FrFKFrFK]^{7+}$. The linear plot indicates that there is only one type of oxygen quenching occuring. Figure 3.4 shows the linear relationship between $[O_2]$, and $\tau_0/\tau$ and $I_0/I$ for $[(Ru(bpy)_2phen\text{-}Ar)_2\text{-}FrFKFrFK]^{7+}$. The matching plots for $\tau_0/\tau$ (•) and $I_0/I$ (•) shows that $[(Ru(bpy)_2phen\text{-}Ar)_2\text{-}FrFKFrFK]^{7+}$ is undergoing dynamic quenching by oxygen. Dynamic quenching occurs when the luminophore in its excited state comes into contact with the quencher through diffusion, and returns to the ground state with out emitting any luminescence. In this case, $[(Ru(bpy)_2phen\text{-}Ar)_2\text{-}FrFKFrFK]^{7+}$ is being quenched by the oxygen present in the solution.

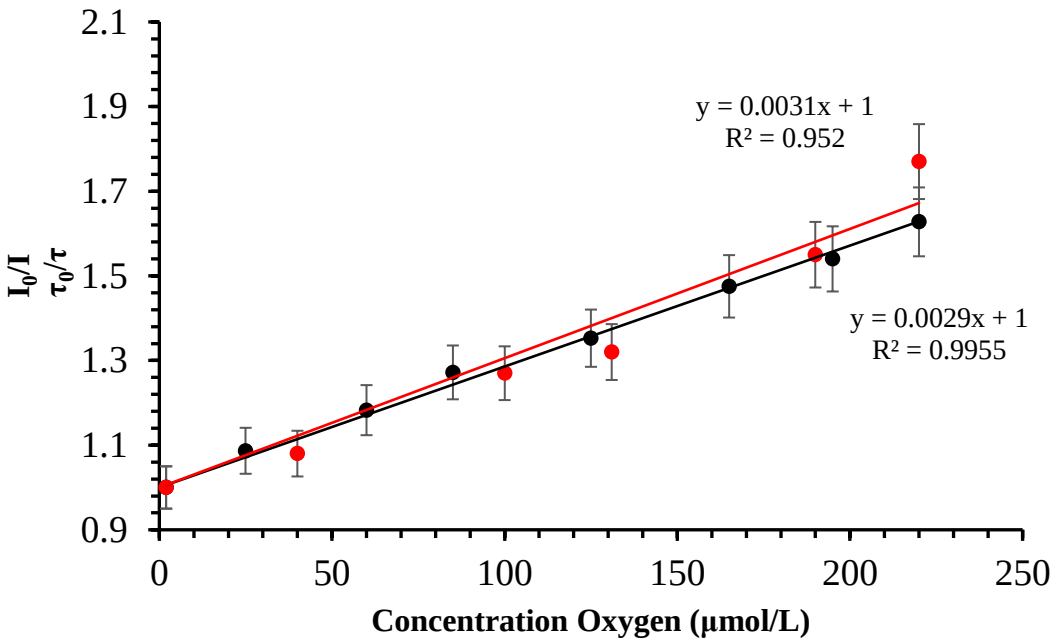


**Figure 3.4** Stern-Volmer plot of luminescent emission intensity as a function of oxygen, $I_0/I$ (•) and the corresponding luminescent lifetime as a function of oxygen, $\tau_0/\tau$ (•), for $[(Ru(bpy)_2phen\text{-}Ar)_2\text{-}FrFKFrFK]^{7+}$ in PBS (50 µM, 18 °C).

Oxygen studies were then investigated at 37 °C to mimic the probes response to biological conditions. Ruthenium polypyridyl complexes have been suggested to possess radical temperature dependence. This can affect the spectroscopic properties such as emission intensity and lifetime.[14] At high temperature, Ru(II) lifetimes undergo a photochemical or photophysical deactivation as a result of thermally activated surface crossing from the $^3$MLCT to the $^3$MC state.[15] In this case, $[(Ru(bpy)_2phen\text{-}Ar)_2\text{-}FrFKFrFK]^{7+}$ has a luminescent lifetime of 689 ± 6 ns in aerated PBS at 18 °C which decreases significantly to 458 ± 7 ns in aerated PBS at 37 °C. Therefore, for a more realistic interpretation of the analytical response of $[(Ru(bpy)_2phen\text{-}Ar)_2\text{-}FrFKFrFK]^{7+}$ under imaging conditions the luminescent emission and lifetimes over a range of oxygen concentrations were measured at 37 °C. Prior to the de-aeration process, the sample was incubated in a water bath so it reached 37 °C and nitrogen gas was bubbled into the sample for 15 minutes. During the de-aeration process and reintroduction of $O_2$, the sample remained in the water bath to maintain the temperature (37 °C) throughout the measurements. The fluorescent lifetimes (τ) and emission spectra were recorded at a range of oxygen concentrations. A linear relationship was observed at 37 °C, as indicated by the Stern-Volmer plot of $[O_2]$ versus lifetime decay. Figure 3.5 compares the relationships at 18 °C and 37 °C.

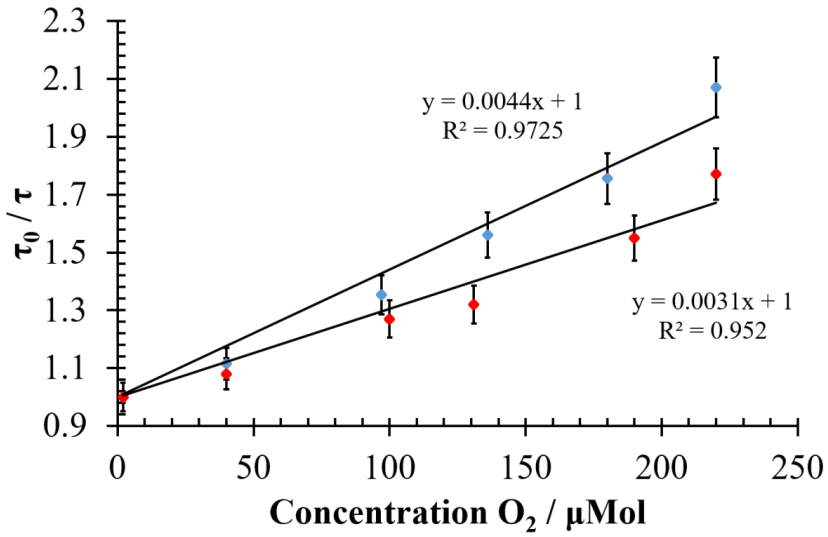


**Figure 3.5** Stern-Volmer plot of the luminescent lifetimes of $[(Ru(bpy)_2phen\text{-}Ar)_2\text{-}FrFKFrFK]^{7+}$ (50 µM) as a function of $[O_2]$ at 18 °C (•) and 37 °C (•) in PBS solution.

The oxygen quenching rate constants were obtained from $K_{SV}$ and the lifetime values in the absence of oxygen ($\tau_0$), and were determined to be 2.5 x $10^9$ M $s^{-1}$ at 18 °C and 4.64 x $10^9$ M $s^{-1}$ at 37 °C, summarised in Table 3.2. In comparison, *DeGraff et al* reported on oxygen quenching rates for $[Ru(bpy)_3]^{2+}$ to be 2.97 x $10^9$ M $s^{-1}$ at 19 °C, and 4.73 x $10^9$ M $s^{-1}$ at 39 °C in water.[16] These conform well to the values found for $[(Ru(bpy)_2phen\text{-}Ar)_2\text{-}FrFKFrFK]^{7+}$ but quenching rates for $[(Ru(bpy)_2phen\text{-}Ar)_2\text{-}FrFKFrFK]^{7+}$ are somewhat lower. This may be attributed to the large peptide conjugated to the complex, protecting the complex from quenching.

**Table 3.2** Changes in the lifetime of $[(Ru(bpy)_2phen\text{-}Ar)_2\text{-}FrFKFrFK]^{7+}$ in response to temperature and oxygen concentration, where aerated conditions have 220 µmol/L at oxygen saturation, and de-aerated conditions have 2 µmol/L oxygen present. The Stern Volmer rate $K_{SV}$ and quenching rate $k_q$ for 18 °C and 37 °C.

| | **18 °C** | **37 °C** |
|---|---|---|
| **$\tau$ aerated (ns)** | 689 ± 6 | 458 ± 7 |
| **$\tau$ de-aerated (ns)** | 1.23 µs ± 10 ns | 948 ± 6 |
| **$K_{SV}$** | 0.0044 | 0.0031 |
| **$k_q$** | 2.5 x $10^9$ M $s^{-1}$ | 4.64 x $10^9$ M $s^{-1}$ |

## 3.5 Cell Uptake and Mitochondria Localisation Studies

In order to assess the ability of $[(Ru(bpy)_2phen\text{-}Ar)_2\text{-}FrFKFrFK]^{7+}$ to cross the cell membrane and localise in the mitochondria, HeLa cells, an adherent cervical cancer cell line, were used. HeLa cells were seeded at 1.5 x $10^5$ in 2 mL culture media and grown 48 hours before imaging. All images were acquired using a Zeiss LSM510 confocal microscope with a 63 x oil immersion objective lens. Ru(II) was excited using a 488 nm laser line and emission was collected using a long pass 560 nm filter set.

### 3.5.1 Cell uptake of $[(Ru(bpy)_2phen\text{-}Ar)_2\text{-}FrFKFrFK]^{7+}$

In order to determine the optimum working concentration, a range of concentrations between 10 and 100 µM of both the parent and peptide complexes were incubated with HeLa cells for varying range of time periods of 1, 2, and 6 h at 37 °C and 5 % $CO_2$ in the absence of light. The parent complex $[Ru(bpy)_2phen\text{-}Ar\text{-}COOH]^{2+}$ showed poor cell penetration ability as no luminescence was observed in the HeLa cells. In comparison, $[(Ru(bpy)_2phen\text{-}Ar)_2\text{-}FrFKFrFK]^{7+}$ was readily taken up by the cells in a concentration

dependent manner. The optimum working conditions were found to be at a concentration of 75 μM in the cell media for an incubation time of 2 h.

Live uptake studies showed that the initial uptake was rapid. Figure 3.6 shows the complex binding to the cell membrane after 3 minutes (A and B), and entering the cell after 5 minutes exposure (C and D). The likely reason for rapid membrane binding and uptake is the cationic charge of the peptide sequence, which promotes electrostatic association with the negatively charged exterior cell membrane.

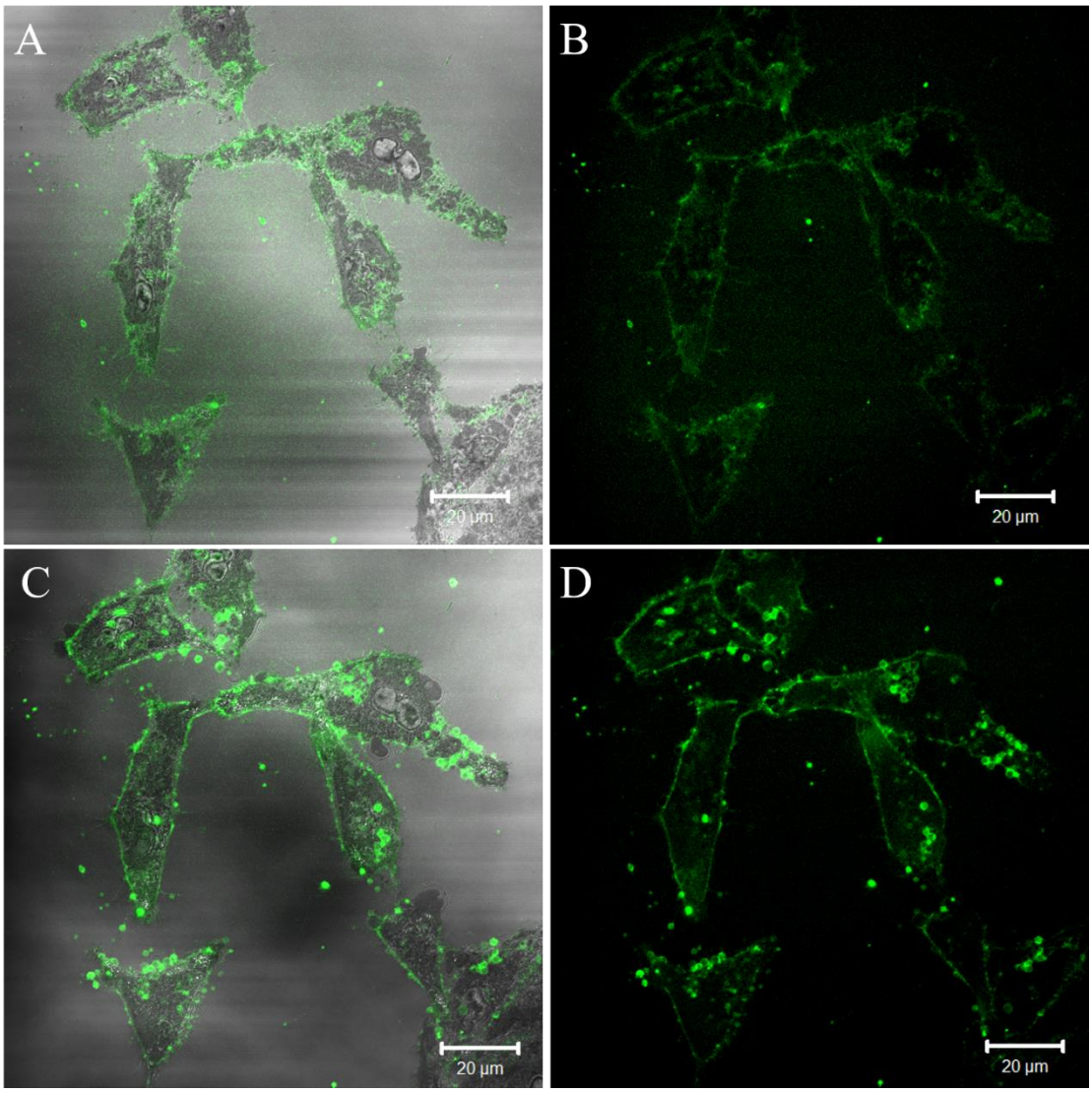


**Figure 3.6** Live uptake of $[(Ru(bpy)_2phen\text{-}Ar)_2\text{-}FrFKFrFK]^{7+}$ in HeLa cells. 70 μM $[(Ru(bpy)_2phen\text{-}Ar)_2\text{-}FrFKFrFK]^{7+}$ in phenol red-free media was added to HeLa cells. The complex crosses the membrane after 3 minutes (A and B), and diffuses in the cells after 5 minutes (C and D) upon

addition. The temperature was kept at 37 °C using a heated stage. The complex was excited using a 488 nm argon ion laser and the emission was collected using a long pass 560 nm filter.

After 1 h $[(Ru(bpy)_2phen\text{-}Ar)_2\text{-}FrFKFrFK]^{7+}$ exhibited strong luminescence from within the cell, and appeared to concentrate within the cytoplasm, excluding the nuclear region. After incubating for 2 h at 37 °C in the absence of light, it strongly localised within the mitochondria, as illustrated in Figure 3.7 A-C, which shows a group of HeLa cells, illustrating the same distribution of the complex across all of the cells. This is representitive of the probe distribution throughout the sample. D-F looks closely at a single HeLa cell, where there is evidence of localization within specific cellular compartments in the cytoplasm.

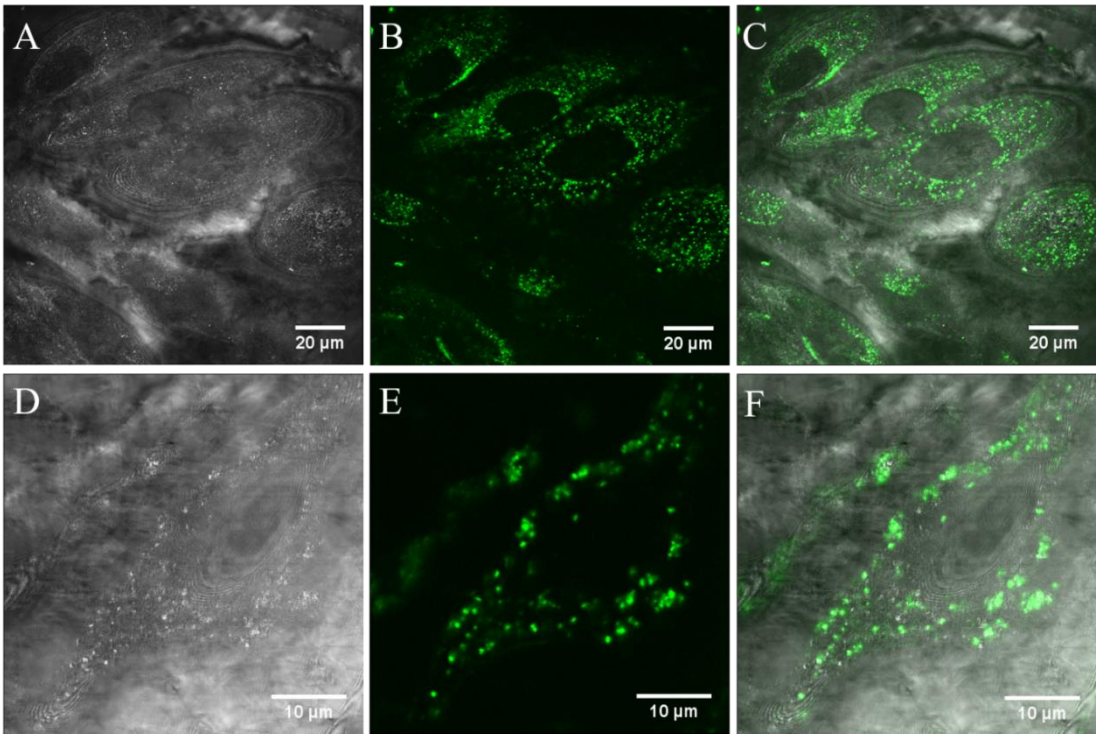


**Figure 3.7** Confocal imaging of HeLa cells with 75 µM $[(Ru(bpy)_2phen\text{-}Ar)_2\text{-}FrFKFrFK]^{7+}$ for 2 h at 37 °C in the dark. A-C show representative uptake by HeLa cells (z = 1). D-F shows distribution within a single HeLa cell, suggesting that the complex is localising in specific cellular compartments (z = 3). A and D represent the bright-field confocal image of the cell. B and E represent complex intensity in the cell. C and F shows the overlay of the channels. The complex was excited using a 488 nm argon ion laser and the emission was collected using a long pass 560 nm filter.

As discussed in Chapter 1, probes can cross the cell membrane in either an energy dependent or independent manner. To determine the mode of uptake, the cells were incubated with 75 μM $[(Ru(bpy)_2phen\text{-}Ar)_2\text{-}FrFKFrFK]^{7+}$ for 2 h at 4 °C in the dark. Figures 3.8 A and B show that under these conditions, $[(Ru(bpy)_2phen\text{-}Ar)_2\text{-}FrFKFrFK]^{7+}$ failed to cross the cell membrane. Upon closer inspection of the cells, C and D show that the complex resides solely at the membrane. Comparing this to Figure 3.7 shows that uptake of $[(Ru(bpy)_2phen\text{-}Ar)_2\text{-}FrFKFrFK]^{7+}$ is temperature dependent. When initially introduced to the cells, $[(Ru(bpy)_2phen\text{-}Ar)_2\text{-}FrFKFrFK]^{7+}$ may bind electrostatically to the plasma membrane due to its high charge, as described earlier. This observation, combined with the temperature dependent studies suggests that uptake occurs *via* an activated process such as endocytosis.

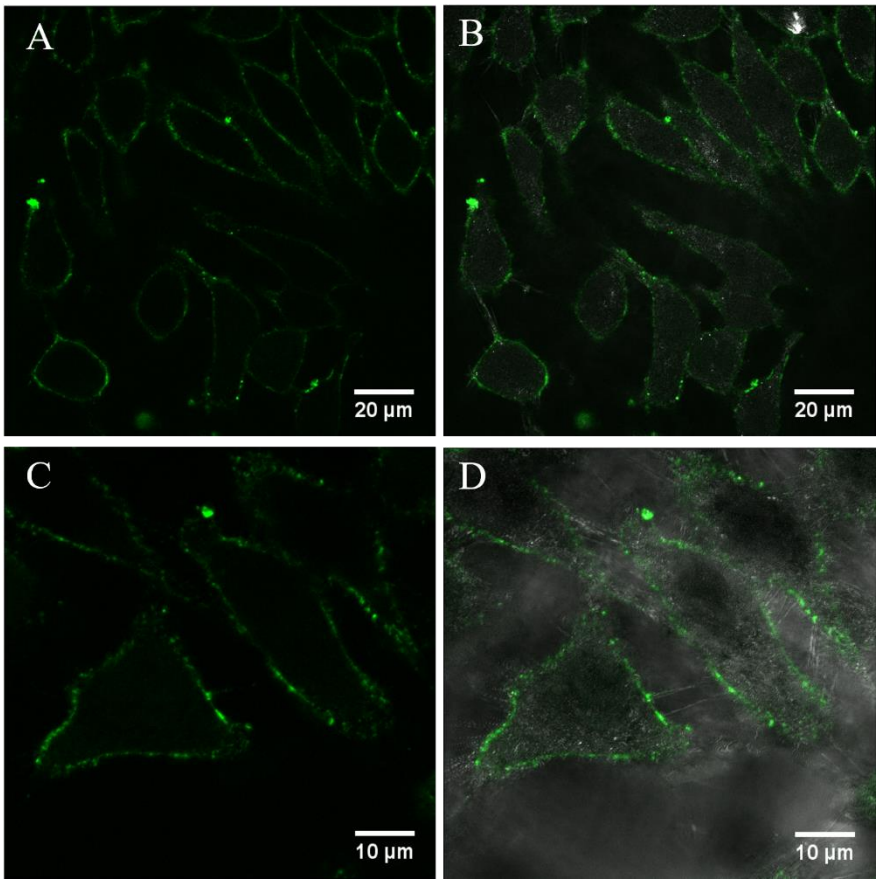


**Figure 3.8** Confocal imaging of HeLa cells after incubation with 75 μM $[(Ru(bpy)_2phen\text{-}Ar)_2\text{-}FrFKFrFK]^{7+}$ at 4 °C for 2 h. A and B represent the general distribution throughout the sample. C and D look closely at a group of cells to show localisation. (A and C represent the ruthenium channel only, B and D show an overlay with the white light channel). The complex was excited using a 488 nm argon ion laser and the emission was collected using a long pass 560 nm filter.

To assess the effect of different peptide sequences on uptake of the complex, $[(Ru(bpy)_2phen\text{-}Ar)_2\text{-}Arg_8]^{10+}$ was introduced to HeLa cells in the same manner as $[(Ru(bpy)_2phen\text{-}Ar)_2\text{-}FrFKFrFK]^{7+}$ to compare the behaviour of a cell penetrating peptide (CPP) with the mitochondrial peptide sequence. As described in Chapter 1, octa-arginine ($Arg_8$) is a general CPP that localises within the cytoplasm and enters some, but not all organelles. $[(Ru(bpy)_2phen\text{-}Ar)_2\text{-}Arg_8]^{10+}$ displayed a similar distribution in HeLa cells when incubated under the same conditions as $[(Ru(bpy)_2phen\text{-}Ar)_2\text{-}FrFKFrFK]^{7+}$. Figure 3.9 shows a representative image of the manner in which $[(Ru(bpy)_2phen\text{-}Ar)_2\text{-}Arg_8]^{10+}$ appears to localize within the cytoplasm, and does not enter the nucleus. 1(A-C) and 2(D-F) illustrate that the uptake of $[(Ru(bpy)_2phen\text{-}Ar)_2\text{-}Arg_8]^{10+}$ and its distributions within the cell were the same for all cells across the sample.

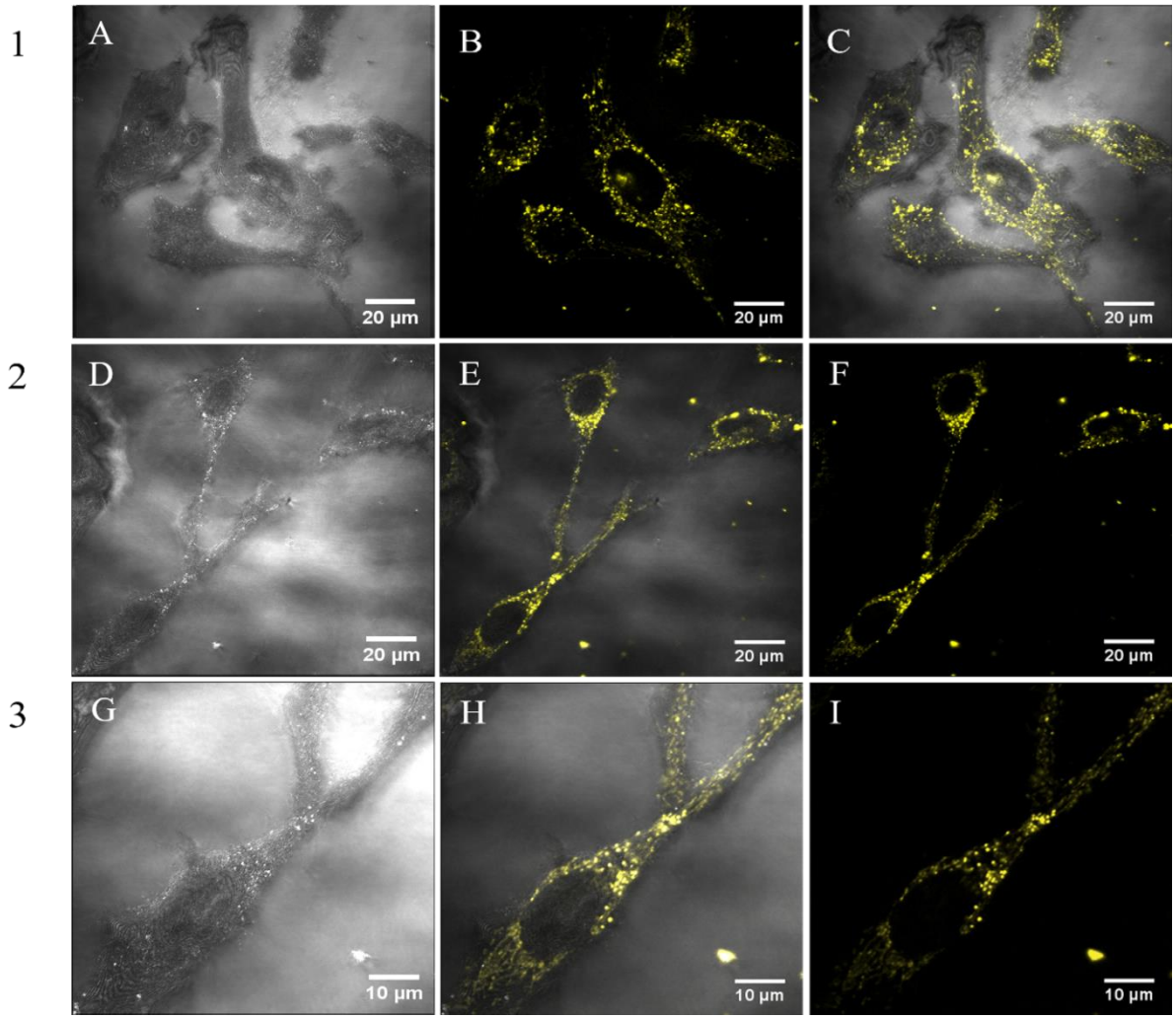


**Figure 3.9** Confocal imaging of $[(Ru(bpy)_2phen\text{-}Ar)_2\text{-}Arg_8]^{10+}$ in HeLa cells. HeLa cells were incubated with 75 µM $[(Ru(bpy)_2phen\text{-}Ar)_2\text{-}Arg_8]^{10+}$ in phenol red free media for 2 h in the absence of light. 1A-C and 2D-F focus on several cells for a representative uptake image of the complex across the sample. 3G-I presents a single HeLa cell and the localisation of the complex. A, D and G represent the bright-field confocal image of the cell. B, E and H shows the overlay of the channels. C, F and I represent complex intensity in the cell. The complex was excited using a 488 nm argon ion laser and the emission was collected using a long pass 560 nm filter. Yellow false colour used to distinguish $[(Ru(bpy)_2phen\text{-}Ar)_2\text{-}Arg_8]^{10+}$ from $[(Ru(bpy)_2phen\text{-}Ar)_2\text{-}FrFKFrFK]^{7+}$ in previous images.

3(G-I) looks closely at a single HeLa cell. The complex shows a more punctate distribution throughout the cytoplasm, suggesting that it has entered many cellular organelles, which is characteristic of the distribution of $Arg_8$ peptide sequence, where similar localisation was also demonstrated in Chapter 2 for the complex $[Ru(bpy)_2PIC\text{-}Arg_8]^{10+}$.

### 3.5.2 Mitochondria Localisation Studies

To assess the localisation of $[(Ru(bpy)_2phen\text{-}Ar)_2\text{-}FrFKFrFK]^{7+}$, 75 μM was incubated with HeLa cells for 2 h at 37 °C. MitoTracker Deep Red, a commercial mitochondrial targeting dye, was added to the cells for the final 30 minutes of incubation for dual staining. Figure 3.10 shows the accumulation of both $[(Ru(bpy)_2phen\text{-}Ar)_2\text{-}FrFKFrFK]^{7+}$ and MitoTracker Deep Red (150 nM) in the mitochondria, where $[(Ru(bpy)_2phen\text{-}Ar)_2\text{-}FrFKFrFK]^{7+}$ is in green, MitoTracker in red, and their colocalization in yellow.

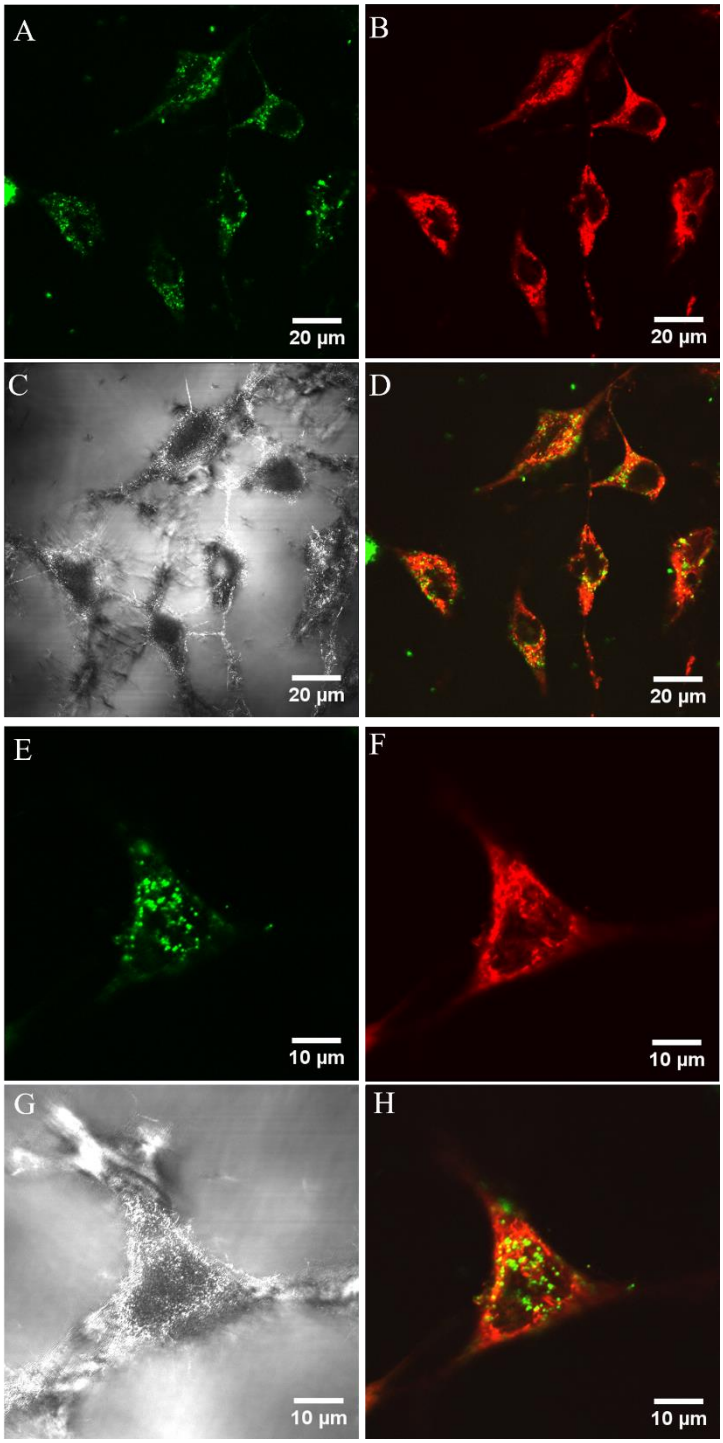


**Figure 3.10** Confocal images showing co-localisation of $[(Ru(bpy)_2phen\text{-}Ar)_2\text{-}FrFKFrFK]^{7+}$ in the green channel (A), MitoTracker Deep Red in the red channel (B) in HeLa cells, and the backscatter (C). The co-localisation represented in yellow where the two complexes co-localise in the mitochondria (D). Similarly, E-H is based on the distribution within a single HeLa cell. HeLa cells were incubated with 75 µM $[(Ru(bpy)_2phen\text{-}Ar)_2\text{-}FrFKFrFK]^{7+}$ in phenol red free indicator for 2 h in the absence of light. MitoTracker Deep Red (150 nM) was added to the cells for 30 minutes prior to imaging in PBS buffer. $[(Ru(bpy)_2phen\text{-}Ar)_2\text{-}FrFKFrFK]^{7+}$ was excited using a 488 nm laser and the emission was collected using a long pass 560 nm filter. MitoTracker Deep Red was excited at 633 nm and the emission was collected using a long pass 650 nm filter.

To confirm that [(Ru(bpy)$_2$phen-Ar)$_2$-FrFKFrFK]$^{7+}$ and MitoTracker Deep Red are both coincident in the mitochondria, a profile cross section of a fluorescence image of a HeLa cell was examined and its corresponding fluorescent intensity profile plotted. This plot in Figure 3.11 confirms that they are both localising within the same cellular components and that both are nuclear excluding. The profile also suggests that [(Ru(bpy)$_2$phen-Ar)$_2$-FrFKFrFK]$^{7+}$ has a more selective and specific localization within the mitochondria, while the commercial MitoTracker appears to be more dispersed and diffused suggesting that it is residing in the mitochondrial membrane.

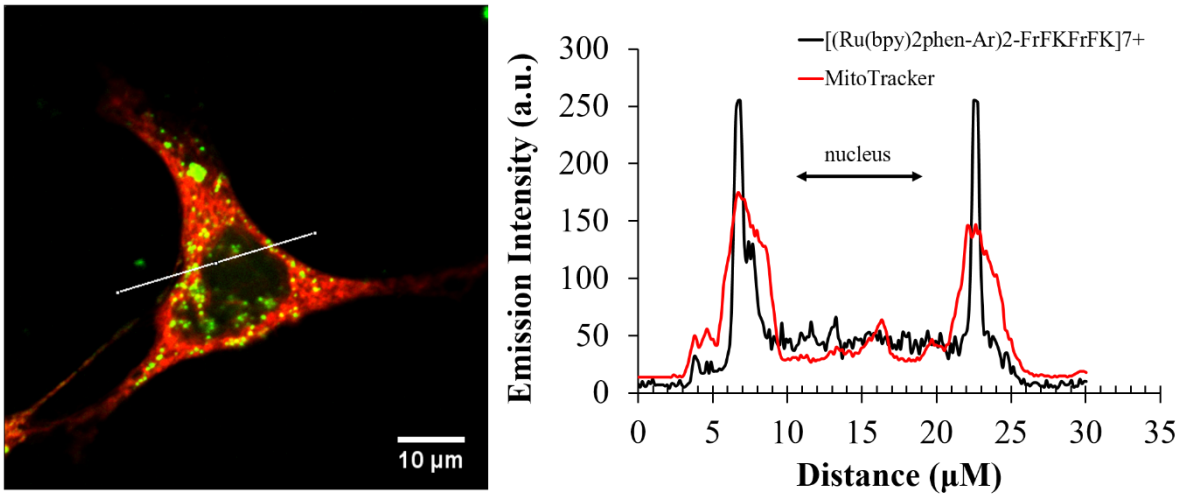


**Figure 3.11** Co-localization of [(Ru(bpy)$_2$phen-Ar)$_2$-FrFKFrFK]$^{7+}$ in green and MitoTracker Deep Red in red and their co-localisation in yellow. The line profile across the cell and the corresponding fluorescence intensity profile demonstrate co-localisation of the two complexes HeLa cells were incubated with 75 µM [(Ru(bpy)$_2$phen-Ar)$_2$-FrFKFrFK]$^{7+}$ in phenol red free indicator for 2 h in the absence of light. MitoTracker Deep Red (150 nM) was added to the cells for 30 minutes prior to imaging in PBS buffer. [(Ru(bpy)$_2$phen-Ar)$_2$-FrFKFrFK]$^{7+}$ was excited using a 488 nm laser and the emission was collected using a long pass 560 nm filter. MitoTracker Deep Red was excited at 633 nm and the emission was collected using a long pass 650 nm filter.

Many groups have reported on metal complexes localising in the mitochondria, but the mitochondria were not typically the predicted target in these studies. For example, *Keene et al* demonstrated mitochondrial localisation of a dinuclear ruthenium in murine leukemia cells using confocal microscopy.[11] However, the complex localised in the mitochondria by chance as they did not use any mitochondrial penetrating peptides to

specifically target the mitochondria. Similarly, Puckett and Barton reported on a $[Ru(DIP)_2dppz]^{2+}$ complex, which after 2 h incubation with HeLa cells localised in the mitochondria without specifically targeting the mitochondria.[17]

Conversely, this result indicates that this peptide sequence, FrFKFrFK, is a successful mitochondria penetrating peptide (MPP) for carrying metal complexes in a predictable way. Not only can it direct a metal complex to the mitochondria, it can also enable it to penetrate the mitochondrial membrane. The luminescence from within the mitochondria is bright and distinguishable from the background, i.e. the rest of the cell. This allows for a precise and localised monitoring of oxygen from the mitochondria.

## 3.6 Oxygen dependent studies in HeLa cells using Phosphorescent Lifetime Imaging Microscopy

$[(Ru(bpy)_2phen\text{-}Ar)_2\text{-}FrFKFrFK]^{7+}$ showed excellent sensitivity to oxygen in vitro, and as described in *section 3.4*, successfully localized within the mitochondria. To assess $[(Ru(bpy)_2phen\text{-}Ar)_2\text{-}FrFKFrFK]^{7+}$ as a biological $O_2$ probe, Phosphorescent Lifetime Imaging Microscopy (PLIM) imaging was used to interogate its lifetime within the mitochondria of a HeLa cell.

At 37 °C in aqueous solution, the luminescent lifetime of $[(Ru(bpy)_2phen\text{-}Ar)_2\text{-}FrFKFrFK]^{7+}$ was found to be 458 ns ± 6 ns, as described earlier in *section 3.3*. The luminescent lifetime was measured at 37 °C as Ru(II) spectroscopic properties are sensitive to temperature, and to mimic the cellular environment as imaging is frequently carried out at this temperature. For *in vivo* studies, HeLa cells were prepared on 35 mm glass bottom culture dishes for 48 h, and 75 μM of $[(Ru(bpy)_2phen\text{-}Ar)_2\text{-}FrFKFrFK]^{7+}$ was added for 2 h. Live PLIM images were recorded using MicroTime 200, PicoQuant software, and excited with a 405 nm laser line. Figure 3.12 shows the acquired false-colour PLIM image of $[(Ru(bpy)_2phen\text{-}Ar)_2\text{-}FrFKFrFK]^{7+}$ in a single HeLa cell (A), which is representitve of the sample, and the corresponding luminescent lifetime decay plot (B). To aquire the luminescent lifetime of $[(Ru(bpy)_2phen\text{-}Ar)_2\text{-}FrFKFrFK]^{7+}$ from within the mitochondria, only the mitochondrial regions were imaged.

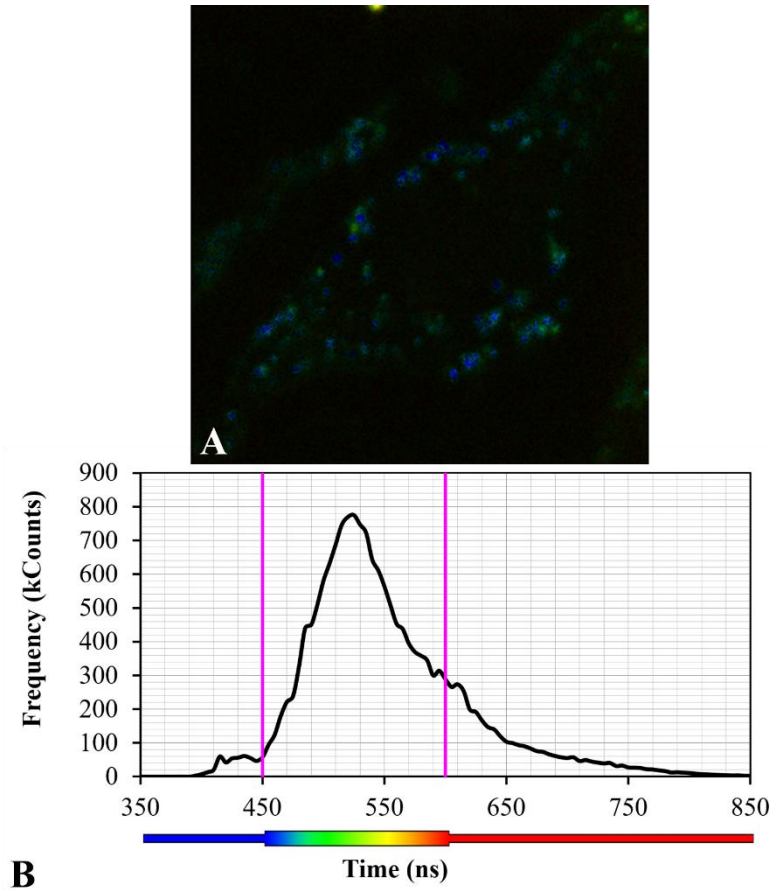


**Figure 3.12** PLIM image and distribution of lifetime of $[(Ru(bpy)_2phen\text{-}Ar)_2\text{-}FrFKFrFK]^{7+}$ in HeLa cells. HeLa cells were incubated with 75 μM complex for 2 h and washed with PBS supplemented with 1.1 mM $MgCl_2$ and 0.9 mM $CaCl_2$. The lifetime within the mitochondria is 525 ± ns (n = 2). The sample was excited with a 405 nm laser and the emission was collected using a long pass 530 nm filter.

The luminescent lifetime decay distribution shows a single exponential mode, with the average lifetime in the mitochondria to be 525 ± 10 ns. The increase in lifetime from 458 ns ± 6 ns when fully aerated in solution to 525 ± 10 ns in the mitochondria suggests that oxygen concentration in the mitochondria is slightly lower. Based on the calibration plot at 37 °C (Figure 3.5), the measured lifetime represents an intracellular oxygen concentration of ~183 μmol. The lower concentration at the mitochondria is expected for normal metabolizing cells as some of the oxygen taken up by the cell gets used up by other cellular organelles or is lost in the diffusion process to the mitochondria.

### 3.6.1 Antimycin A as an $O_2$ inhibitor in mitochondria

To further assess the ability of $[(Ru(bpy)_2phen\text{-}Ar)_2\text{-}FrFKFrFK]^{7+}$ to report on the dynamic changes to oxygen concentration cellular respiration, the $O_2$ concentration in the cell was altered using Antimycin A. Antimycin A is an inhibitor of electron transfer at complex III in mitochondria. It blocks the mitochondria from consuming oxygen in the cell. Therefore, there is a build up of oxygen in the cell, increasing the natural concentration.[18] This change in the cellular environment causes the cell to undergo oxidative stress, leading to reactive oxygen species (ROS) production. As discussed in Chapter 1, ROS are chemically reactive oxygen metabolites. They are highly reactive as they have one or more unpaired electrons in their outer shells. ROS are formed as a natural byproduct of cellular metabolism of oxygen. However, under oxidative stress there is an increase in ROS production which can have a damaging effect on the cell. As a result in the increase of ROS, there is a decrease in ATP production.[19] The most common ROS produced by the mitochondria under oxidative stress is singlet oxygen, $^1O_2$.

HeLa cells were prepared as described in *section 3.2.8*. Antimycin A (200 µg/mL) was added to the cells in PBS solution, which were then incubated for 10 minutes. The lifetime of $[(Ru(bpy)_2phen\text{-}Ar)_2\text{-}FrFKFrFK]^{7+}$ was then measured and mapped using PLIM imaging. The lifetime was measured at 10 minute intervals, to a total exposure time of 100 minutes. Figure 3.13 A-C shows the PLIM image of the region of mitochondria monitored following the addition of Antimycin A (A), after 10 minutes exposure (B), and 100 minutes (C). In Figure 3.11 (A), the luminescent lifetime decay map shows a gaussian distribtuion of lifetimes with a single maxima, with an average lifetime measured to be 525 ns. Antimycin A was added to the cells and after 10 minutes exposure, the luminescent lifetime decay changed, shown in Figure 3.13 (B). Here, the decay appears to be bi-modal distribution, suggesting that there are two distributions of lifetimes present in the mitochondria. The two peaks represent the two median luminescent lifetimes of approximately 220 ns nand 423 ns. The longer luminescent lifetime of 423 ns can be attributed to the increase in oxygen in the mitochondria as a result of the Antimycin A, quenching the lifetime of $[(Ru(bpy)_2phen\text{-}Ar)_2\text{-}FrFKFrFK]^{7+}$. The shorter lifetime of 220 ns is as a result of the formation of ROS by the cell. After 100 minutes exposure to Antimycin A, the luminescent lifetime decay distribution returns to a single peak, shown in Figure 3.13 (C), where the median luminescent

lifetime is 228 ns. It is highly unlikely that oxygen quenching is contributing to the shorter lifetime component as when $[(Ru(bpy)_2phen\text{-}Ar)_2\text{-}FrFKFrFK]^{7+}$ is is in air saturated solution it has a luminescent lifetime of 458 ns. Oxygen concentration cannot exceed saturation. Therefore, a separate quenching pathway is causing the futher reduction in $[(Ru(bpy)_2phen\text{-}Ar)_2\text{-}FrFKFrFK]^{7+}$ lifetime. The shorter luminescent lifetime is tentatively attributed to in the presence of ROS which is quenching the $[(Ru(bpy)_2phen\text{-}Ar)_2\text{-}FrFKFrFK]^{7+}$ emission. ROS production in the mitochondria is likely to be occuring in response to the oxidative stress caused by the Antimycin A. The superoxide anion ($O_2^{\bullet-}$), hydrogen peroxide ($H_2O_2$), and hydroxyl radical ($^{\bullet}OH$) have all been shown to be produced in response to Antimycin A in the mitochondria.[19] However, it is the superoxide anion $O_2^{\bullet-}$ that is the most likely ROS contributor in this quenching process. Superoxide $O_2^{\bullet-}$ is produced when $O_2$ becomes reduced and loses an electron, shown in equation 3.3.

$$O_2 + e^- = O_2^{\bullet-} \text{ …. Equation 3.3}$$

It is possible than when $[(Ru(bpy)_2phen\text{-}Ar)_2\text{-}FrFKFrFK]^{7+}$ comes in contact with oxygen, it becomes reduced gaining anelectron from the oxygen and as a result, produces $O_2^{\bullet-}$. This energy transfer is the possible cause of the quenching that is occuring to the luminescent lifetime. The likelyhood of this occurance is based on the redox potential of the compound. A similar complex $[Ru(bpy)_2(PIC)]^{2+}$, where PIC = 2-(4-Carboxylphenyl)imidazo[4,5-f][1,10]phenanthroline) was reported to have a redox potential of ~1.2 V.[20] Assuming that $[(Ru(bpy)_2phen\text{-}Ar)_2\text{-}FrFKFrFK]^{7+}$ has a similar redox potential, it would suggest that $[(Ru(bpy)_2phen\text{-}Ar)_2\text{-}FrFKFrFK]^{7+}$ is easily oxidised, as stated in Equation 3.3. This would account for generation of ROS, and the further quenching of $[(Ru(bpy)_2phen\text{-}Ar)_2\text{-}FrFKFrFK]^{7+}$ luminescent lifetime.

Figure 3.13 D-F shows the luminescent lifetime of $[(Ru(bpy)_2phen\text{-}Ar)_2\text{-}FrFKFrFK]^{7+}$ in the mitochondria of control cells, that were not exposed to Antimycin A, over the same time intervals. The luminescent lifetime decays are all of a single modal distribution with a median decay of 526 ± 21 ns. This suggests that the luminescent lifetime of $[(Ru(bpy)_2phen\text{-}Ar)_2\text{-}FrFKFrFK]^{7+}$ does not change in the mitochondria over time when the cell is metabolizing normally and it can be used to measure the oxygen concentration there over extended periods.

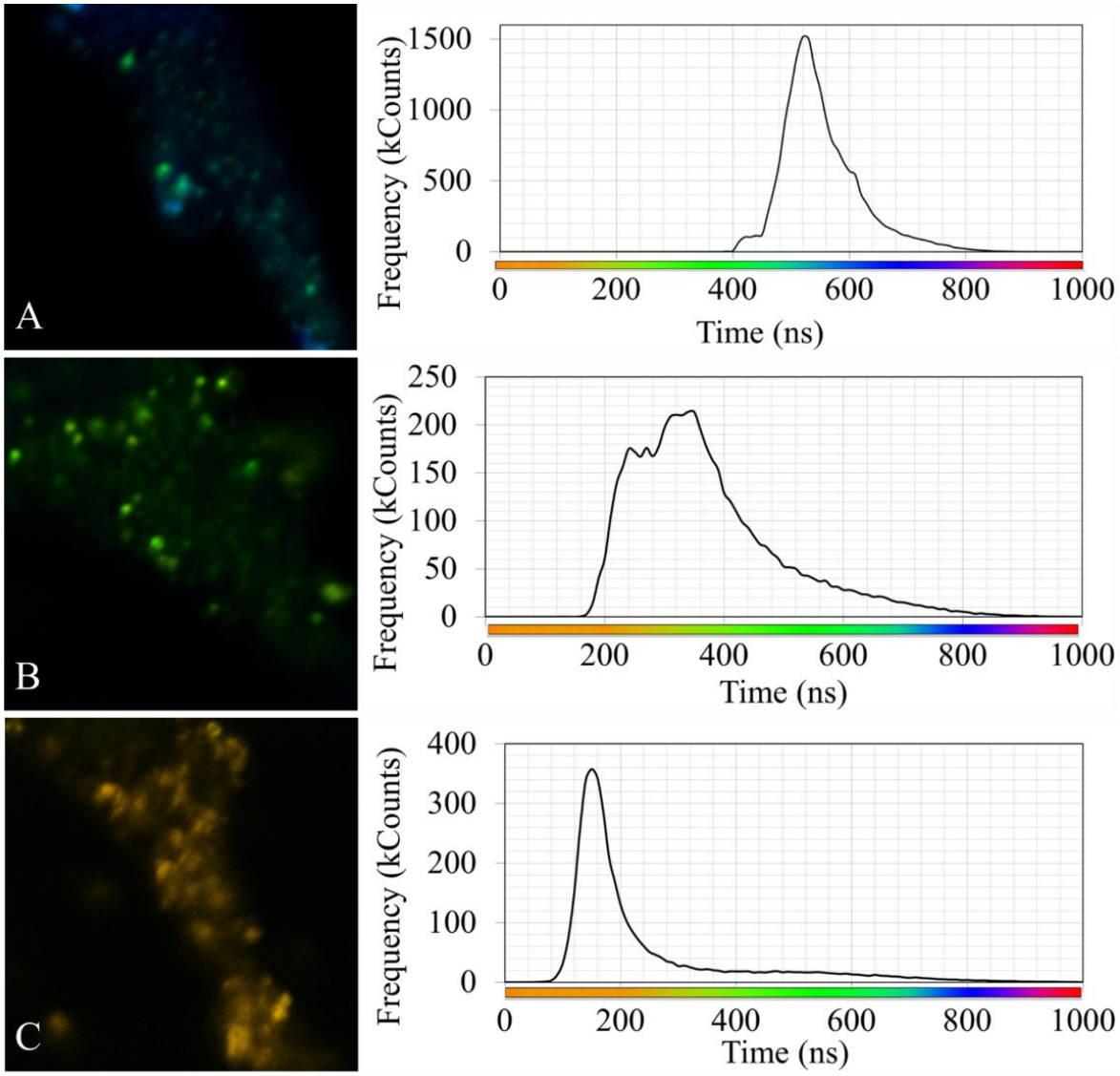
A
Frequency (kCounts)
1500
1000
500
0
0
200
400
600
800
1000
Time (ns)
B
Frequency (kCounts)
250
200
150
100
50
0
0
200
400
600
800
1000
Time (ns)
C
Frequency (kCounts)
400
300
200
100
0
0
200
400
600
800
1000
Time (ns)

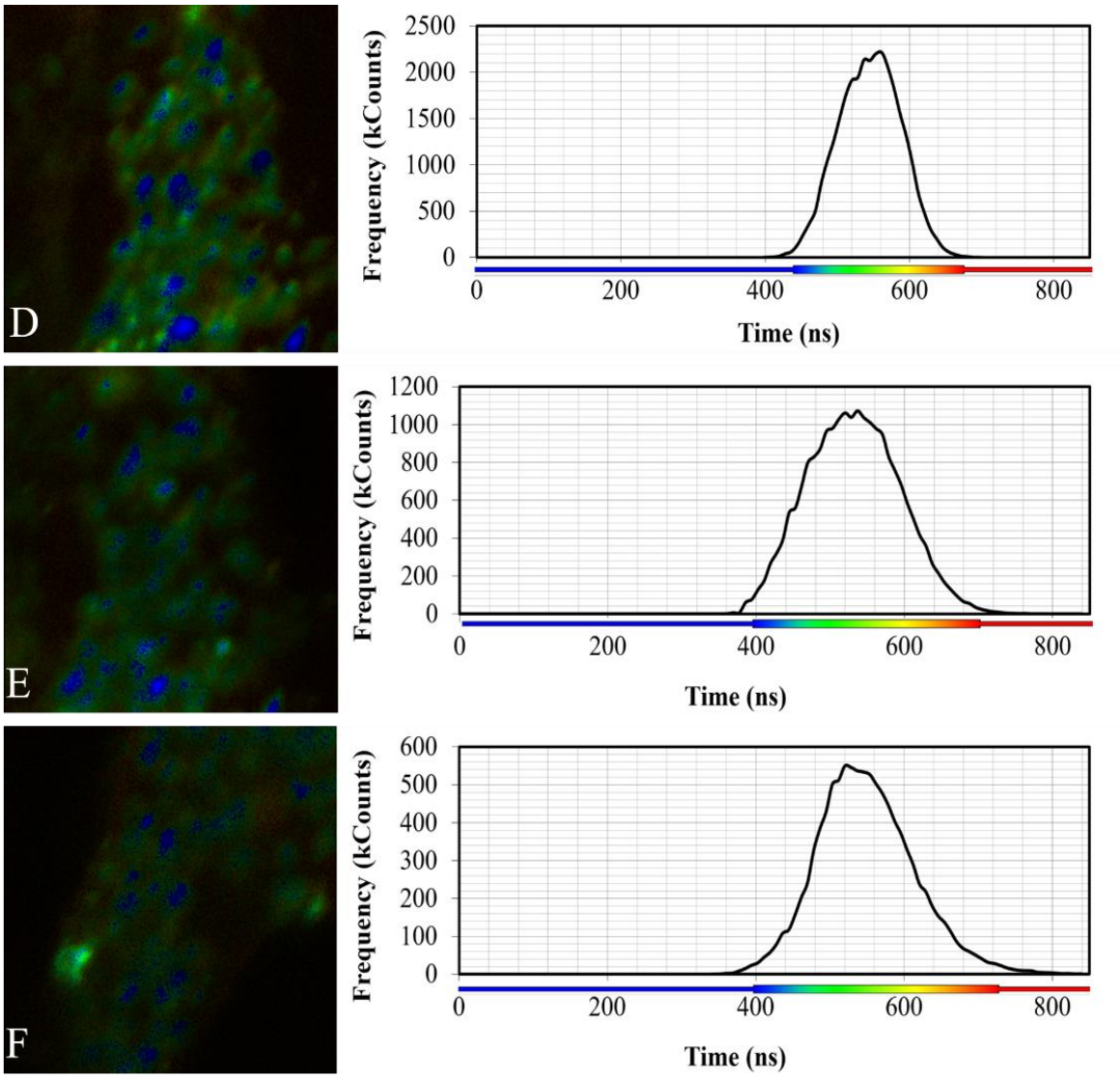


**Figure 3.13** PLIM lifetime distributions of $[(Ru(bpy)_2phen\text{-}Ar)_2\text{-}FrFKFrFK]^{7+}$ in HeLa cells in response to the addition of Antimycin A. HeLa cells were incubated with 75 µM of $[(Ru(bpy)_2phen\text{-}Ar)_2\text{-}FrFKFrFK]^{7+}$ in phenol red-free media for 2 h in the absence of light. Each PLIM image was acquired for 10 minutes. A 405 nm laser was used to excite the sample, and the emission was collected using a long pass 530 nm filter. The luminescent lifetime of $[(Ru(bpy)_2phen\text{-}Ar)_2\text{-}FrFKFrFK]^{7+}$ in HeLa cell (A) and the decrease in lifetime when Antimycin A (200 µM) is added after 10 min (B) and 100 min (C). Control HeLa cells, with no addition of Antimycin A, at 0 min (D), after 10 min (E), and 100 min (F). (z = 10)

Figure 3.14 shows a plot of lifetime (τ) versus time (minutes) of the control cells and those exposed to Anytimycin A over the 10 minute intervals. The results displayed an initial decrease in the average lifetime from 525 ns to 423 ns after the first 10 minutes. The decrease in the average lifetime continued until it reached a plateau at 228 ns after

100 minutes. Similar results were reported by *Fercher et al*. who introduced oxygen sensitive nanoparticles to mouse embryonic fibroblast (MEF) cells, using Antimycin A to stimulate the cell metabolism. Their results showed a decrease in the fluorescent intensity in response to the changing oxygen concentration.[3] They did report on the production of ROS as a result of using Antimycin A.

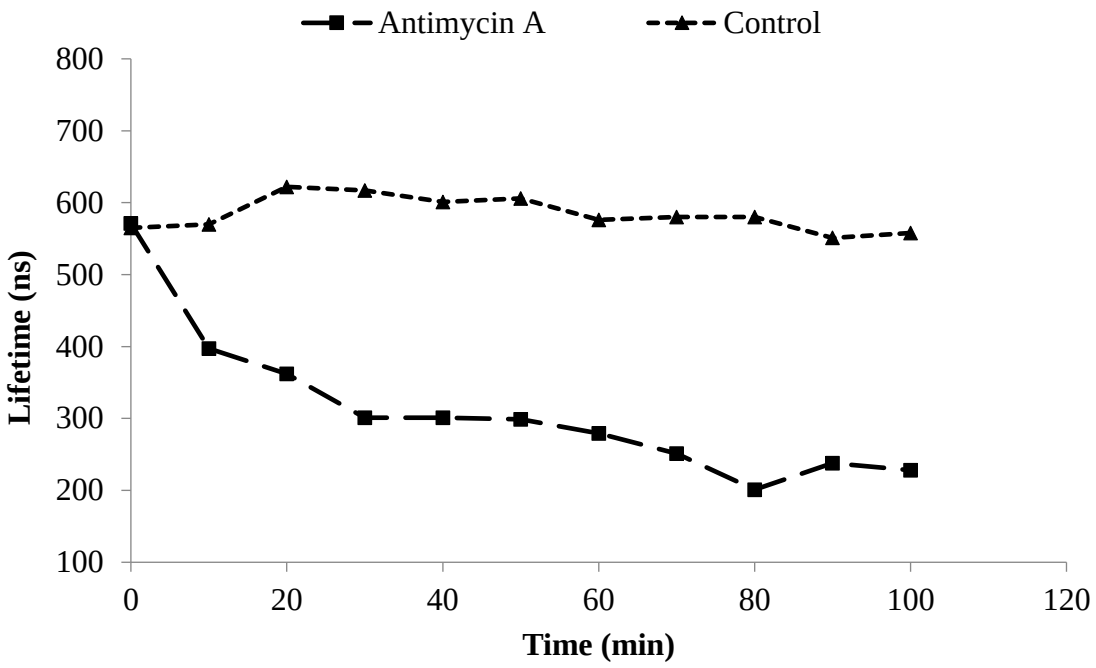


**Figure 3.14** Effects of Antimycin A on the lifetime of $[(Ru(bpy)_2phen\text{-}Ar)_2\text{-}FrFKFrFK]^{7+}$ over 100 min at 37ºC. PLIM images were acquired every 10 minutes to measure any changes in lifetime. The control sample of $[(Ru(bpy)_2phen\text{-}Ar)_2\text{-}FrFKFrFK]^{7+}$ only was measured without any addition of a mitochondrial uncoupling reagent.

ROS play crucial roles in both the physiological and pathological processes in the cell. For example, ROS play an important role in modulating signal transduction cascades and transcription factors in the mitochondria. However, overproduction of ROS leads to oxidative stress in the cell which has been implicated in many diseases, as discussed previously in Chapter 1. Therefore there is a need to develop novel probes for ROS sensing. However, detecting ROS in live cells is very difficult. They are highly reactive and short-lived, and therefore do not accumulate to high levels for accurate detection. There are any different types of ROS, which are produced and detoxified in subcellular

compartments. Their individual study would require probes that specifically target subcellular locations.[21] To date, there have been few reports on ROS sensors capable of quantitatively measuring ROS in live cells. Those that have been reported are based on organic probes not transition metal complexes. For example, the group of *Nagano et al* reported on a ROS sensor which was based on rhodamine.[22] They successfully targeted the complex to the mitochondria of HeLa cells. They stimulated ROS production by adding $H_2O_2$ to the cells, and recorded an enhancement in confocal fluorescence intensity as a result of ROS production. Similarly, *Tang et al* reported on a fluorescent superoxide anion $O_2^{\bullet-}$ probe for live cell imaging of ROS.[23] They were able to direct their complex, MF-DBZH, to the mitochondria of HepG2 cells, and measure $O_2^{\bullet-}$ there. They reported low cytotoxicity of their complex, which is ideal for sensing in live cells. However, in both cases, using the luminescence intensity in confocal imaging to measure ROS production has its limitations, since, as mentioned earlier, the luminescent intensity in imaging is dependent on the probe concentration in the cell. Therefore, it is very difficult to quantitatively measure ROS production in this manner. Also, the results would vary across different cell types depending on the loading conditions and how much of the probe is taken up by the cells. For this reason, using lifetime to quantitatively measure ROS production using techniques like PLIM is a more reliable method as luminescent lifetime is independent of probe concentration.

**Table 3.3** Luminescent lifetimes (ns) of $[(Ru(bpy)_2phen\text{-}Ar)_2\text{-}FrFKFrFK]^{7+}$ at 37 °C *in vitro* in PBS solution under aerated and de-aerated conditions compared to the biological lifetimes in the mitochondria before and after the addition of Antimycin A.

| **Compound** | **τ (ns) @ 37 °C aerated** | **τ (ns) @ 37 °C deaearated** | **τ (ns) mitochondria @ $T_0$** | **τ (ns) mitochondria @ $T_{100}$** |
|---|---|---|---|---|
| $[(Ru(bpy)_2phen\text{-}Ar)_2\text{-}FrFKFrFK]^{7+}$ | 458 ± 7 | 948 ± 6 | 525 ± 10 | 228 |

In order to ensure that the changes observed to $[(Ru(bpy)_2phen\text{-}Ar)_2\text{-}FrFKFrFK]^{7+}$ was as a result of the mitochondrial environment and not as a result of coming in contact with Antimycin A, the luminescent emission and lifetime of $[(Ru(bpy)_2phen\text{-}Ar)_2\text{-}FrFKFrFK]^{7+}$ with Antimycin A were measured in PBS solution (pH 7.4) at 37 °C. Figure 3.15 (A) shows the emission intensity of $[(Ru(bpy)_2phen\text{-}Ar)_2\text{-}FrFKFrFK]^{7+}$ in PBS solution, and $[(Ru(bpy)_2phen\text{-}Ar)_2\text{-}FrFKFrFK]^{7+}$ mixed with 200 µg/mL Antimycin A.

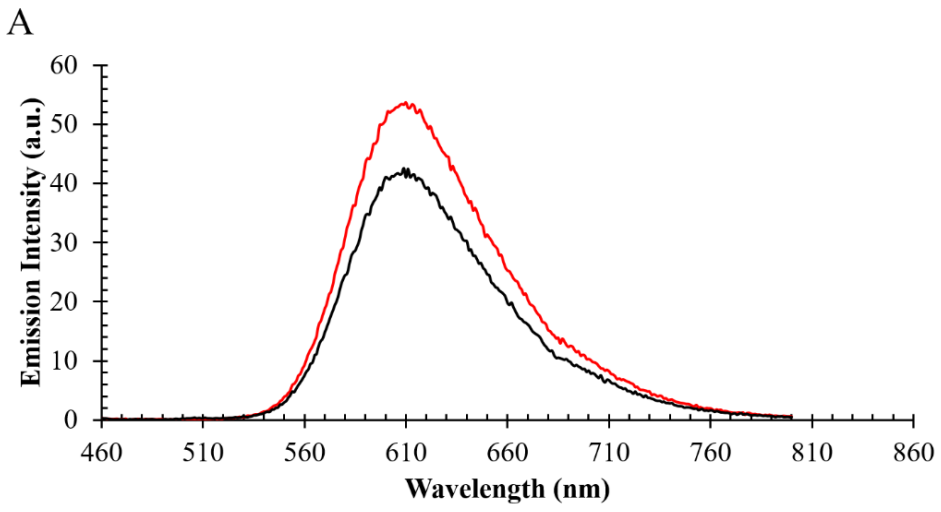

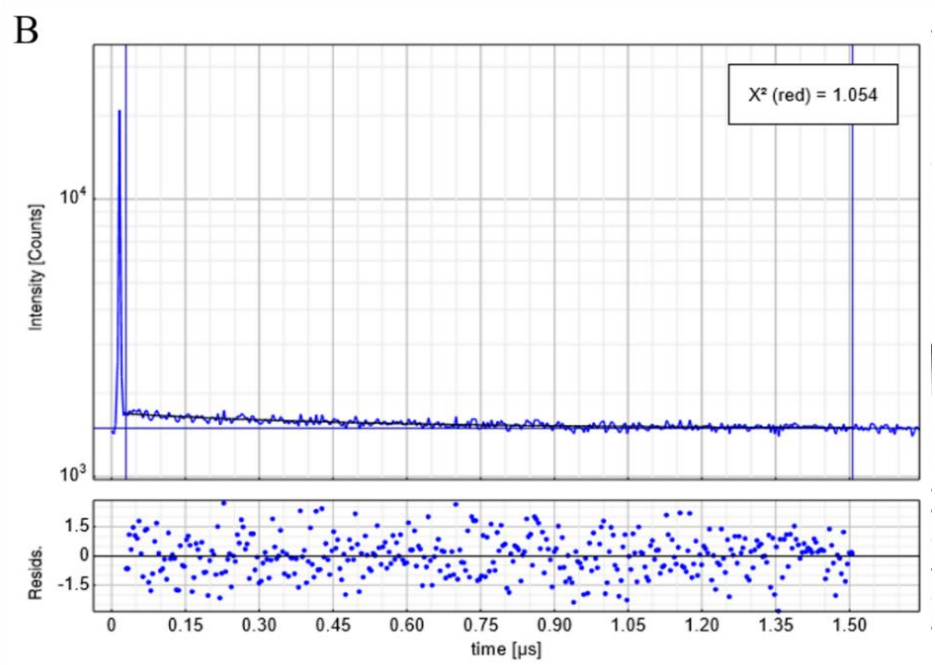


**Figure 3.15** Luminescent emission intensity of $[(Ru(bpy)_2phen\text{-}Ar)_2\text{-}FrFKFrFK]^{7+}$ in PBS solution (—), and $[(Ru(bpy)_2phen\text{-}Ar)_2\text{-}FrFKFrFK]^{7+}$ mixed with 200 µM/mL Antimycin A (—), at 37 °C (A). Both solutions were excited into the MLCT band at 458 nm and the emission was collected between 500 – 750 nm, both at a slit width = 5. Luminescent lifetime decay of $[(Ru(bpy)_2phen\text{-}Ar)_2\text{-}FrFKFrFK]^{7+}$ mixed with 200 µM/mL Antimycin A (B). . The complexes were excited using the 450 nm laser, and the data was acquired using the PicoQuant Time Harp system. The lifetime traces (—) and residuals (•) were fit to give a $\chi^2$ value between 0.9 and 1.1 The spectra were recorded at 15 µM in aqueous solution (PBS) that were heated to 37 °C using a water bath.

A slight decrease in the emission intensity was observed between the two solutions. Although both solutions were made up to give a final concentration of 15 µM, the concentration may have slightly decreased upon the addition of the Antimycin A. However, the luminescent lifetime was, within experimental error, unaffected by the Antimycin A, and was measured to be 468 ns (B), compared to 458 ± 7 ns without Antimycin A.

## 3.7 Cytotoxicity

The effect of $[(Ru(bpy)_2phen\text{-}Ar)_2\text{-}FrFKFrFK]^{7+}$ on the viability of the cells was carried out using the Alamar Blue (Resazurin) cytotoxicity assay as explained in *section 3.2.6*.

Figure 3.16 shows that the parent complex $[Ru(bpy)_2phen\text{-}Ar\text{-}COOH]^{2+}$ did not induce cytotoxicity in HeLa cells. 75 % of cells were viable when exposed to concentrations as high as 200 µM for 24 h in the dark. In comparison, cell viability decreased dramatically to 15 % at 200 µM when exposed to $[(Ru(bpy)_2phen\text{-}Ar)_2\text{-}FrFKFrFK]^{7+}$. 40 % viability was observed at the working concentration of 75 µM. The $IC_{50}$ value is the minimal amount of a drug needed to inhibit 50 % of cells. $[(Ru(bpy)_2phen\text{-}Ar)_2\text{-}FrFKFrFK]^{7+}$ was found to possess an $IC_{50}$ value of 47.45 µM. This result further suggests that the parent complex is not internalised by the cell unlike the peptide conjugate.

To assess if the toxicity was as a result of localising in the mitochondria, or induced by the complex itself, the toxicity of $[(Ru(bpy)_2phen\text{-}Ar)_2\text{-}FrFKFrFK]^{7+}$ and $[(Ru(bpy)_2phen\text{-}Ar)_2\text{-}Arg_8]^{10+}$ were compared. The complexes were added to HeLa cells for 24 h and assessed using the Resazurin assay as previously described. Figure 3.15 shows 0 % viability of HeLa cells at concentrations of 150 and 200 µM $[(Ru(bpy)_2phen\text{-}Ar)_2\text{-}Arg_8]^{10+}$, with an $IC_{50}$ value of 44.64 µM.

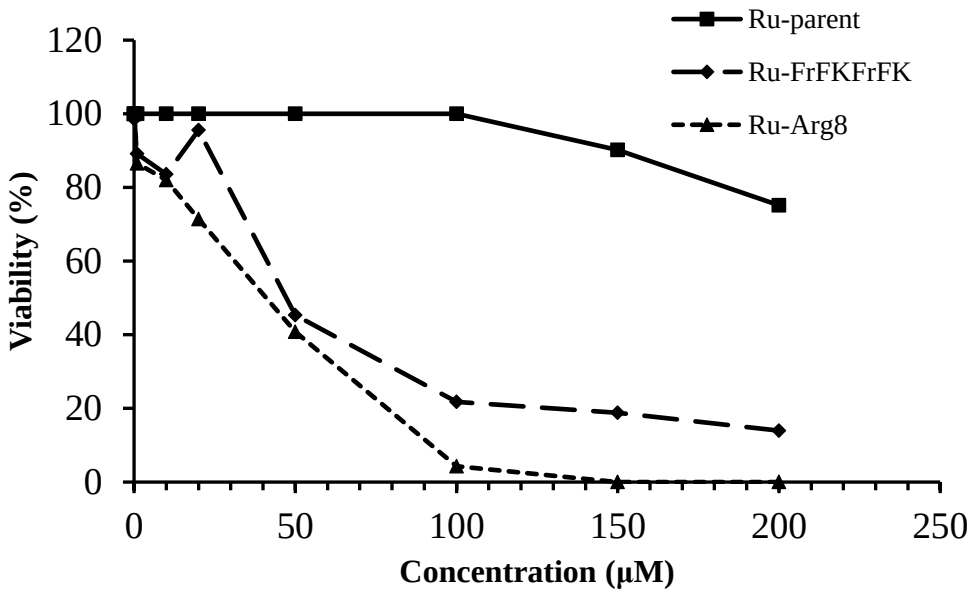


**Figure 3.16** Cytotoxicity of $[Ru(bpy)_2phen\text{-}Ar\text{-}COOH]^{2+}$ and $[(Ru(bpy)_2phen\text{-}Ar)_2\text{-}FrFKFrFK]^{7+}$ compared to that of $[(Ru(bpy)_2phen\text{-}Ar)_2\text{-}Arg_8]^{10+}$ at varying concentrations, incubated for 24 h in the dark at 37ºC at 5 % $CO_2$. HeLa viability was assessed using the Resazurin (Alamar Blue) assay (n=3).

A time-dependent cytotoxicity study was carried out on $[(Ru(bpy)_2phen\text{-}Ar)_2\text{-}FrFKFrFK]^{7+}$ at 75 µM over 1-7 h to assess cell viability during the working incubation time. After 2 h incubation with $[(Ru(bpy)_2phen\text{-}Ar)_2\text{-}FrFKFrFK]^{7+}$, which was the chosen working incubation time, 98 % of the cells remain viable. After 5 hours, cell viability decreased to 40 %, shown in Figure 3.17.

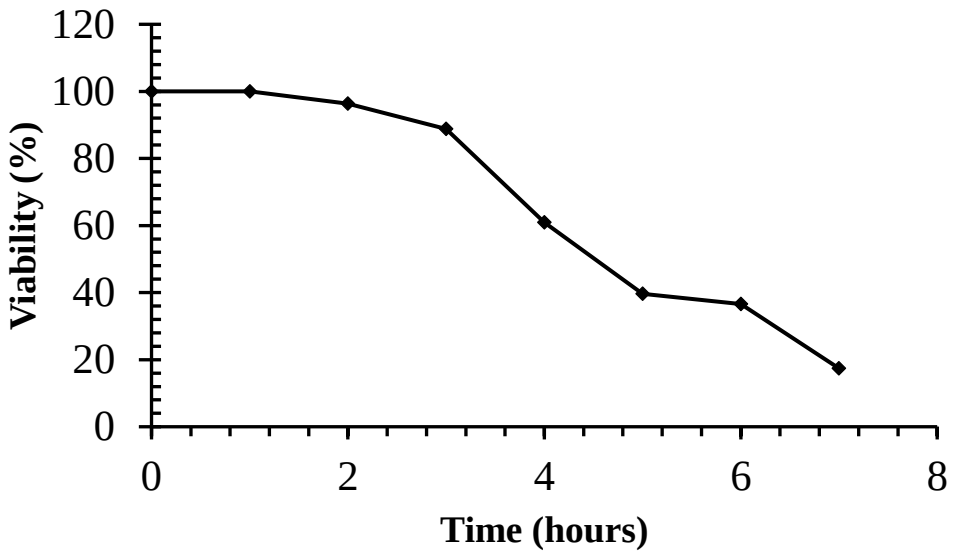


**Figure 3.17** Time dependence toxicity of $[(Ru(bpy)_2phen\text{-}Ar)_2\text{-}FrFKFrFK]^{7+}$ in HeLa cells. The cells were incubated with 75 μM $[(Ru(bpy)_2phen\text{-}Ar)_2\text{-}FrFKFrFK]^{7+}$ in the absence of light over 7 h. (n = 3)

As demonstrated in *section 3.4*, $[(Ru(bpy)_2phen\text{-}Ar)_2\text{-}FrFKFrFK]^{7+}$ localises in the mitochondria of cells after 2 h incubation. From the time dependence toxicity results, $[(Ru(bpy)_2phen\text{-}Ar)_2\text{-}FrFKFrFK]^{7+}$ is a useful mitochondrial imaging and sensing probe up to 5 h exposure to the complex. After 5 h, cell viability decreases dramatically. This suggests that $[(Ru(bpy)_2phen\text{-}Ar)_2\text{-}FrFKFrFK]^{7+}$ could be a useful qualitative probe in imaging compromised mitochondria, and therefore be used to compare the physical changes of healthy and unhealthy mitochondria. Furthermore, the result of the time dependent viability study indicates that it is the Ru(II) parent complex that is inducing the toxicity of the cells, not its localisation. As described in *section 1.6.1*, polyarginine sequences deliver complexes in a non-selective manner, where binding to the mitochondria, lysosomes, and endosomes can occur, resulting in cell death. The wide permeation abilities of $[(Ru(bpy)_2phen\text{-}Ar)_2\text{-}Arg_8]^{10+}$ are likely to be the reason for the higher toxicity results. *Section 2.5* outlines the cytotoxicity of a $[(Ru(bpy)_2PIC\text{-}Arg_8]^{10+}$ complex, which showed a similar distribution within the cell but did not induce toxicity towards the cell. This is further confirmation that it is the parent complex inducing toxicity, not the peptide or cellular localization. The high toxicity of the $[Ru(bpy)_2phen]^{2+}$ complex would suggest that it may possibly be a useful therapeutic agent when introduced to cells for longer periods of time.

## 3.8 Phototoxicity

Ru(II) complexes are ideal photosensitisers due to their strong absorbance and long-lived excited states. In *section 3.6* it was described that $[(Ru(bpy)_2phen\text{-}Ar)_2\text{-}FrFKFrFK]^{7+}$ induces toxicity after 24 h incubation in the absence of light. Given the fact that these complexes are intended for imaging, it was important to also assess their photocytotoxicity. From cellular uptake studies described in 3.4.1, HeLa cells remain viable after 2 h incubation in the dark. Cell viability following exposure of $[(Ru(bpy)_2phen\text{-}Ar)_2\text{-}FrFKFrFK]^{7+}$ to a light source of 488 nm (0.64 μW/cm$^2$) in live HeLa cells was examined.

Figure 3.18 shows live uptake of $[(Ru(bpy)_2phen\text{-}Ar)_2\text{-}FrFKFrFK]^{7+}$ by HeLa cells. Cells were continuously scanned at 5 minute intervals with a 488 nm laser to induce phototoxic effects. After the initial 5 minutes (1A-C), $[(Ru(bpy)_2phen\text{-}Ar)_2\text{-}FrFKFrFK]^{7+}$ entered the cells. After a further 15 minutes scanning (2D-F), the complex appeared to have permeablised all cellular compartments, including the nucleus. After 25 minutes (3G-I), the complex induced extensive cell death, indicated by the entry of DRAQ 7. Photo damage can occur to labelled cells nearby due to light scatter. As a control, an area that was not exposed to the light was examined (4J-L). No damage to the cells was observed. After the constant illumination, the luminescence of $[(Ru(bpy)_2phen\text{-}Ar)_2\text{-}FrFKFrFK]^{7+}$ showed a 5-fold increase in emission upon photo damage compared to the intensity of the complex that was not exposed to light. This suggests that the immediate uptake is caused by a loss in the plasma membrane integrity as the complex accumulates within the cell more rapidly than shown earlier in the live uptake studies in *section 3.4*. The loss of membrane integrity is as a result of phototoxicity which was induced by the constant illumination.

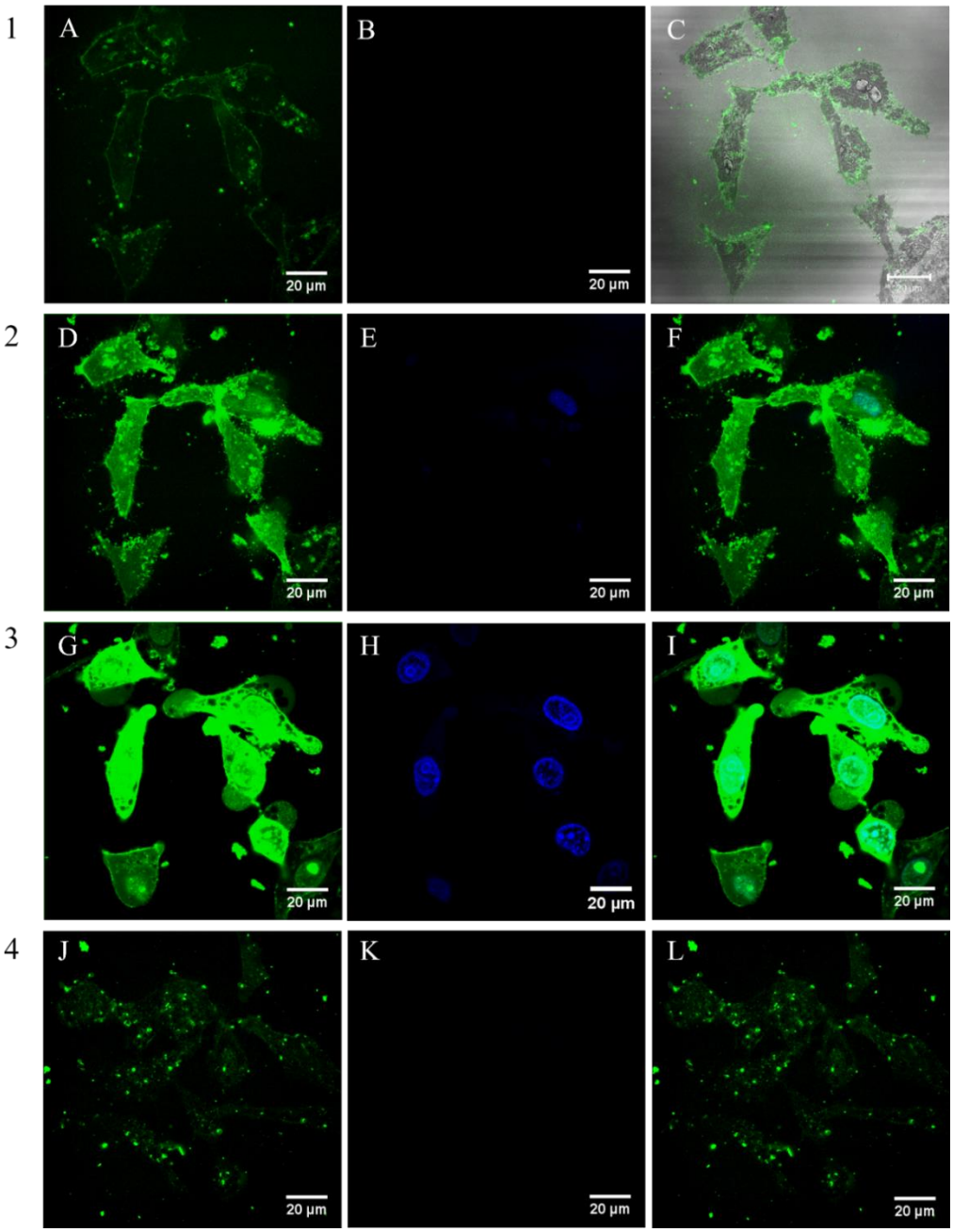


**Figure 3.18** Phototoxicity of $[(Ru(bpy)_2phen\text{-}Ar)_2\text{-}FrFKFrFK]^{7+}$ (75 µM in phenol red-free media) in HeLa cells. Uptake of $[(Ru(bpy)_2phen\text{-}Ar)_2\text{-}FrFKFrFK]^{7+}$ is presented in (1A-C) but no toxicity to cells was observed. After 20 minutes, some toxicity has ensued (2D-F), and after 25 minutes DRAQ 7 has entered the nucleus of all the cells indicating cell death (3G-I). After 35 minutes exposure to $[(Ru(bpy)_2phen\text{-}Ar)_2\text{-}FrFKFrFK]^{7+}$ complex in a new location that has not been exposed to the laser, there was no entry of DRAQ 7, shown in image K where no emission is detected as cells are still viable (4J-L). The laser power used was Ex 488 nm 0.64 µW/cm$^2$. Emission was collected using a long pass 560 nm filter. Channels for $[(Ru(bpy)_2phen\text{-}Ar)_2\text{-}FrFKFrFK]^{7+}$ only, DRAQ 7 only, and an overlay of the channels is shown for each time point.

Control experiments illustrated in Figure 3.19 demonstrate that when HeLa cells were exposed to the same light source in the absence of $[(Ru(bpy)_2phen\text{-}Ar)_2\text{-}FrFKFrFK]^{7+}$, no DRAQ 7 entered the cells up to 35 minutes of scanning under the same laser power exciting at 488 nm (0.64 $\mu W/cm^2$).

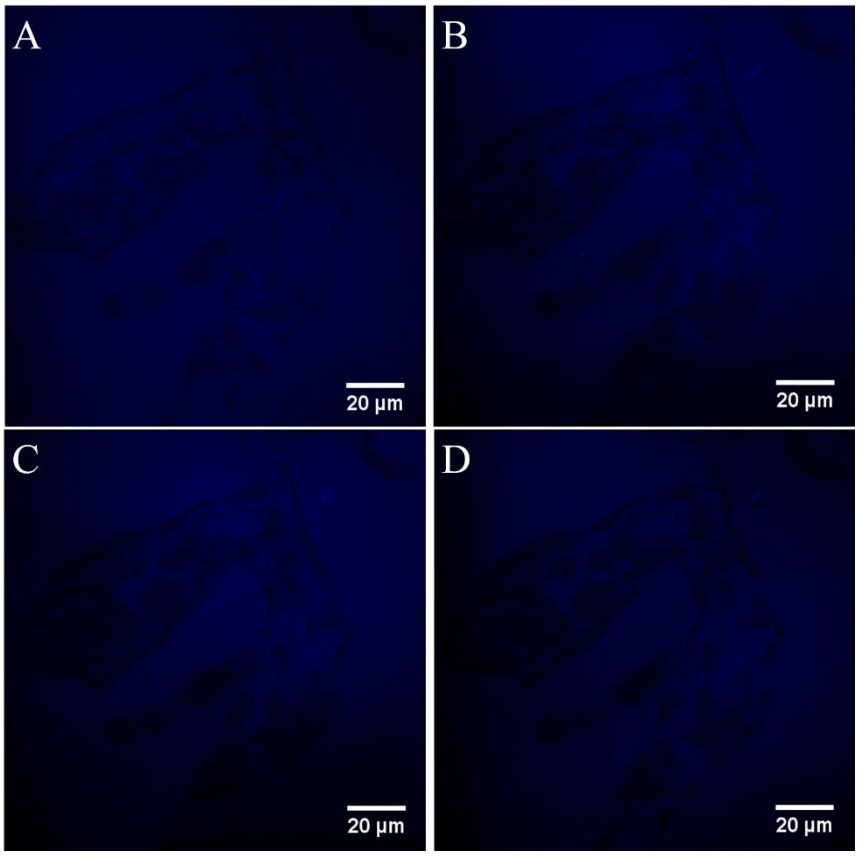


**Figure 3.19** Control HeLa cells for phototoxicity. Cells were scanned continuously, exciting at 488 nm, using the same confocal settings at a laser power of 0.64 $\mu W/cm^2$ at 5 min intervals, and imaged between each interval to assess for DRAQ 7 uptake (Ex 633 nm HeNe laser, long pass 650 nm filter set). (A) 0, (B) 20, (C) 25, and (D) 35 minutes of scanning.

As $[(Ru(bpy)_2phen\text{-}Ar)_2\text{-}FrFKFrFK]^{7+}$ is not toxic towards the cells when incubated for 2 h in the dark, it was necessary to assess if phototoxicity could be induced from within the mitochondria. Figure 3.20 (A-C) shows HeLa cells, incubated with $[(Ru(bpy)_2phen\text{-}Ar)_2\text{-}FrFKFrFK]^{7+}$ (75 µM) for 2 h in the dark. Cells were exposed to the light source and scanned continuously at 5 minute intervals. After 20 minutes of exposure, $[(Ru(bpy)_2phen\text{-}Ar)_2\text{-}FrFKFrFK]^{7+}$ induced cell death from within the mitochondria,

indicated by entry of the complex and DRAQ 7 into the nucleus (E-G). Again, phototoxicity was only detected in areas exposed to light. Luminescence intensity showed a 3-fold increase in emission after scanning (D) compared to intensity after incubation in the absence of light (A).

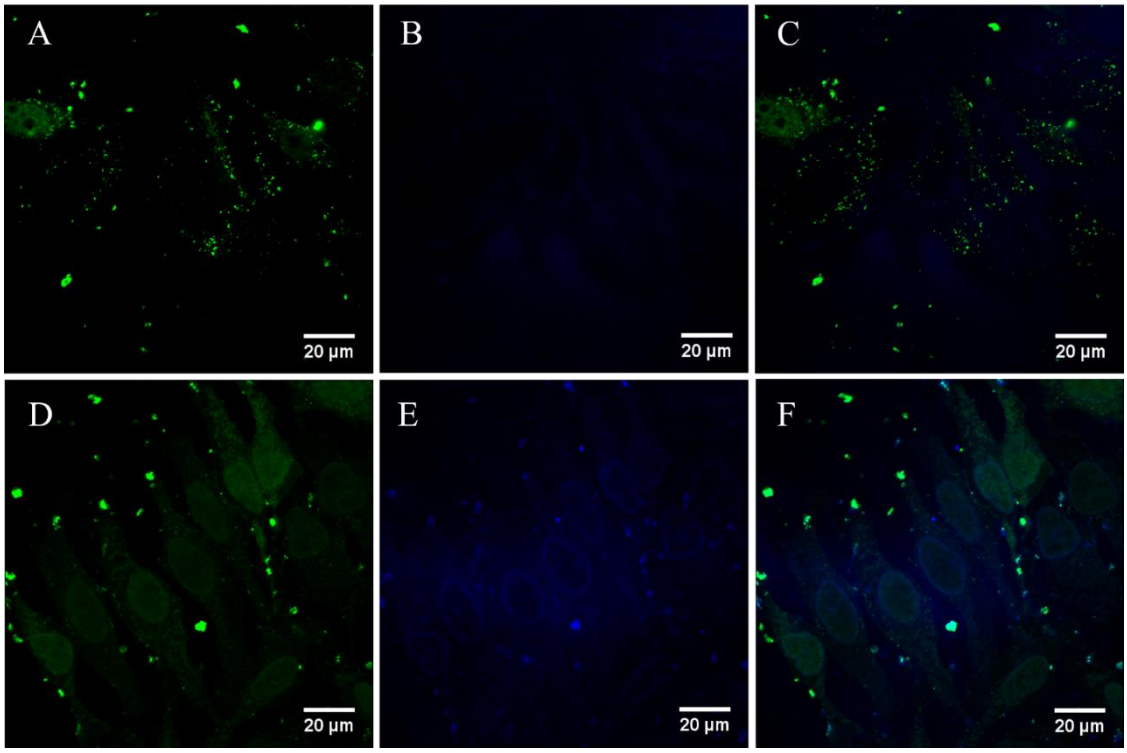


**Figure 3.20** HeLa cells were incubated with 75 µM $[(Ru(bpy)_2phen\text{-}Ar)_2\text{-}FrFKFrFK]^{7+}$ for 2 h, washed and DRAQ 7 added (A-C). Cells were exposed to continuous light source and DRAQ 7 entered the nucleus after 20 min scanning (D-F). Laser power used was Ex 488 nm 0.64 µW/cm$^2$. Channels for $[(Ru(bpy)_2phen\text{-}Ar)_2\text{-}FrFKFrFK]^{7+}$ only, DRAQ 7 only, and an overlay of the channels is shown for each time point.

One possible reason for the photo-induced damage in cells is the production of singlet oxygen. In order to produce singlet oxygen $^1O_2$, there needs to be oxygen present, photoexcitation of a triplet photosensitizer like Ru(II) can energy transfer to oxygen leading to formation of its single state. *Dobrucki* reported on the phototoxicity of $[Ru(phen)_3]^{2+}$ towards macrophages.[24] Here, it was demonstrated that there was an increase in cell uptake and luminescent emission from the nucleus upon irradiation. Furthermore, he showed that in the presence of histidine, a singlet oxygen scavenger,

that the phototoxicity towards the macrophages was reduced, suggesting that singlet oxygen was the mechanism of phototoxicity.

The increase in luminescent intensity on irradiation was surprising and we speculate it could be due to binding to DNA, RNA, or other proteins which are available after disruption of the cell. One possible mechanism of DNA binding might be between the bipyridine ligands of $[(Ru(bpy)_2phen\text{-}Ar)_2\text{-}FrFKFrFK]^{7+}$ and the DNA. $[Ru(bpy)_3]^{2+}$ has been studied in regards to binding to DNA.[25] The bipyridine ligand is likely to undergo electrostatic binding with DNA as it has reduced hydrophobic interactions compared to a phenanthroline ligand.[26] $[Ru(phen)_3]^{2+}$ has been shown to have an affinity towards DNA and RNA.[27,28] wherein it has been reported to bind stereoselectively to DNA through partial intercalation.[28-30] For example, the group of *Cardin et al* reported on the intercalation of a $[Ru(phen)_2dppz]^{2+}$ complex with DNA oligonucleotides.[31] Here they showed semi-intercalation of the phenanthroline ligand into the minor groove of B-DNA. However, it is unlikely to be phen binding here as $[(Ru(bpy)_2phen\text{-}Ar)_2\text{-}FrFKFrFK]^{7+}$ due to steric interference by the peptide.

As mentioned earlier, the emission intensity of $[(Ru(bpy)_2phen\text{-}Ar)_2\text{-}FrFKFrFK]^{7+}$ increased 5-fold when the complex/media solution was added to the cells (Figure 3.18 A-C), whereas the emission only incraesed 3-fold when the cells were incubated with the complex then washed (Figure 3.20 D-F). The differences in the increasing emission intensity suggests that the induced phototoxicity could be occuring in a concentration dependent manner. In the case of Figure 3.18, there is an abundence of $[(Ru(bpy)_2phen\text{-}Ar)_2\text{-}FrFKFrFK]^{7+}$ present in the sample, suggesting that there is more complex present to bind to the DNA/RNA/proteins of the cell. On the other hand, there is a limited aount of $[(Ru(bpy)_2phen\text{-}Ar)_2\text{-}FrFKFrFK]^{7+}$ present in Figure 3.20, i.e. the amount that was taken up by the cells during incubation. The damage appears to occur throughout the cells in Figure 3.18 compared to Figure 3.20, suggesting that more $^1O_2$ is being produced as a result of the different concentrations of $[(Ru(bpy)_2phen\text{-}Ar)_2\text{-}FrFKFrFK]^{7+}$ available. Also, the concentration of oxygen in the lipid membrane of a cell is expected to be higher than that in the cell. As $[(Ru(bpy)_2phen\text{-}Ar)_2\text{-}FrFKFrFK]^{7+}$ is taken up by the cell and is under constant illumination, it is likely that there is more $^1O_2$ being produced at the cell membrane than when $[(Ru(bpy)_2phen\text{-}Ar)_2\text{-}FrFKFrFK]^{7+}$ is in the mitochondria, causing more damage across the whole cell as a result.

## 3.9 Conclusions

Chapter 3 described the application of a novel dimeric Ru(II) probe conjugated to an MPP localising sequence FrFKFrFK to cell imaging, and $O_2$ and ROS sensing. The ability of the conjugate to cross the cell membrane and measure oxygen in the mitochondria were explored.

The photophysical properties of the parent and peptide conjugate were examined, and they exhibited a strong absorbance band at $\lambda_{max}$ = 460 nm, and emission maxima of 604 nm. The peptide conjugation did not affect the properties of the complex.

Confocal microscopy demonstrated that the parent complex was not capable of entering cells, whereas $[(Ru(bpy)_2phen\text{-}Ar)_2\text{-}FrFKFrFK]^{7+}$ exhibited efficient uptake, optimised for imaging at 75 µM incubated for 2 h in the absence of light. Co-localisation studies confirmed that the MPP sequence FrFKFrFK was successful in bringing the complex across the cell membrane and directing it to the mitochondria. Dual-staining with MitoTracker Deep Red confirmed co-localisation at the mitochondria.

PLIM studies established that the probes response to $O_2$ could successfully be translated to measuring $O_2$ in the cell. This was further investigated by using the mitochondria uncoupler Antimycin A to alter $O_2$ concentration in the mitochondria. The $[(Ru(bpy)_2phen\text{-}Ar)_2\text{-}FrFKFrFK]^{7+}$ lifetime decreased from 525 ns at 0 minutes to 423 ns after 10 minutes, and finally reached a lifetime of 228 ns after 100 minutes exposure. This was due to quenching by the build-up of oxygen and ROS production in the cell.

$[(Ru(bpy)_2phen\text{-}Ar)_2\text{-}FrFKFrFK]^{7+}$ also displays promise as a therapeutic agent. Its relatively low cytotoxicity at short incubation times in the absence of light, and induced high phototoxic effects upon exposure to light are the ideal properties of a photosensitiser used in photodynamic therapy (PDT), of which $[(Ru(bpy)_2phen\text{-}Ar)_2\text{-}FrFKFrFK]^{7+}$ has clearly demonstrated to have. The mechanism of cell death, either necrosis or apoptosis, needs to be explored further. Overall, not only has $[(Ru(bpy)_2phen\text{-}Ar)_2\text{-}FrFKFrFK]^{7+}$ exhibited great promise as a probe for monitoring the $O_2$ environment in the mitochondria, it has also shown to be a powerful ROS sensor in live cells, something that is currently very difficult to achieve.

## *References*


1. Morris KJ, Roach MS, Xu W, Demas JN, DeGraff BA. Extracellular oxygen concentration mapping with a confocal multiphoton laser scanning microscope and TCSPC card. *Anal Chem*. 2007;79:9310-9314.

2. Abdel-Shafi AA, Ward MD, Schmidt R. Mechanism of quenching by oxygen of the excited states of ruthenium(II) complexes in aqueous media. solvent isotope effect and photosensitized generation of singlet oxygen, $O_2$(1Deltag), by [ru(diimine)(CN)4]2- complex ions. *Dalton Trans*. 2007:2517-2527.

3. Fercher A, Borisov SM, Zhdanov AV, Klimant I, Papkovsky DB. Intracellular $O_2$ Sensing probe based on cell-penetrating phosphorescent nanoparticles. *ACS Nano*. 2011;5:5499-5508.

4. Horton KL, Stewart KM, Fonseca SB, Guo G, O. Kelley S. Mitochondria-penetrating peptides. *Chemistry & Biology*. 2008;15:375-382.

5. Papkovsky DB, Dmitriev RI. Biological detection by optical oxygen sensing. *Chem. Soc. Rev.* 2013(42):8700.

6. Duchen MR, Szabadkai G. Roles of mitochondria in human disease. *Essays Biochem*. 2010;47:115-137.

7. Tiede LM, Cook EA, Morsey B, Fox HS. Oxygen matters: Tissue culture oxygen levels affect mitochondrial function and structure as well as responses to HIV viroproteins. *Cell Death Dis*. 2012;3:274.

8. Smith RAJ, Porteous CM, Gane AM, Murphy MP. Delivery of bioactive molecules to mitochondria *invivo*. *Proc Natl Acad Sci U S A 2003, 100, 5407-5412*. 2003;100:5407-5412.

9. Komor AC, Schneider CJ, Weidmann AG, Barton JK. Cell-selective biological activity of rhodium metalloinsertors correlates with subcellular localization. *J Am Chem Soc*. 2012;134:19223-19233.

10. Chen T, Mei W, Wong Y, et al. Chiral ruthenium polypyridyl complexes as mitochondria-targetedapoptosis inducers. *Med Chem Comm*. 2010;1:73-75.

11. Pisani MJ, Weber DK, Heimann K, Collins JG, Keene RF. Selective mitochondrial accumulation of cytotoxic dinuclear polypyridyl ruthenium(II) complexes. *Metallomics*. 2010;2:393-396.

12. Li SP, Lau CT, Louie M, Lam Y, Cheng SH, Lo KK. Mitochondria-targeting cyclometalated iridium(III)–PEG complexes with tunable photodynamic activity. *Biomaterials*. 2013;34(30):7519-7532.

13. Wang J, Zhang P, Qian C, Hou X, Ji L, Chao H. Mitochondria are the primary target in the induction of apoptosis by chiral ruthenium(II) polypyridyl complexes in cancer cells. *J Biol Inorg Chem*. 2014;19:335-348.

14. Van Houten J, Watts RJ. Temperature dependence of the photophysical and photochemical properties of the tris( 2,2'-bipyridyl)ruthenium(11) ion in aqueous solution. *J Am Chem Soc*. 1976;98:4853-4858.

15. Barigelletti F, Juris A, Balzani V, Belser P, von Zelewsky A. Temperature dependence of the ru(bpy),(CN), and Ru(bpy),(i-biq)~+ luminescence. *The Journal of Physical Chemistry*. 1987;91:1095-1098.

16. Reynolds EW, Demas JN, DeGraff BA. Viscosity and temperature effects on the rate of oxygen quenching of tris-(2,2′-bipyridine)ruthenium(II). *J Fluoresc*. 2013;23:237-241.

17. Puckett CA, Barton JK. Methods to explore cellular uptake of ruthenium complexes. *J Am Chem Soc*. 2007;129:46-47.

18. Park W, Han Y, Kim S, Kim S. *J Cellular BioChem*. 2007;102:98-109.

19. Balaban RS, Nemoto S, Finkel T. Mitochondria, oxidants, and aging. *Cell*. 2005;120:483-495.

20. Forster RJ, Pellegrin Y, Keyes TE. pH effects on the rate of heterogeneous electron transfer across a fluorine doped tin oxide/monolayer interface. *Electrochemistry Communications*. 2007;9(8):1899-1906.

21. Shulaev V, Oliver DJ. Metabolic and proteomic markers for oxidative stress. new tools for reactive oxygen species research. *Plant Physiol*. 2006;141:367-372.

22. Koide Y, Urano Y, Kenmoku S, Kojima H, Nagano T. Design and synthesis of fluorescent probes for selective detection of highly reactive oxygen species in mitochondria of living cells. *J Am Chem Soc*. 2007;129:10324-10325.

23. Li P, Zhang W, Li K, et al. Mitochondria-targeted reaction-based two-photon fluorescent probe for imaging of superoxide anion in live cells and in vivo. *Anal Chem*. 2013;85:9877-9881.

24. Dobrucki JW. Interaction of oxygen-sensitive luminescent probes ru(phen) and 3 21 ru(bipy) with animal and plant cells in vitro 3 mechanism of phototoxicity and conditions for non-invasive oxygen measurements. *Journal of Photochemistry and Photobiology B: Biology*. 2001;65:136-144.

25. Kelly JM, Tossi AB, McConnell D, OhUigin C. A study of the interactions of some polypyridylrutheniumn(I) complexes with DNA using fluorescence spectroscopy, topoisomerisation and thermal denaturation. *Nucleic Acids Res*. 1985;13:6017-6034.

26. Eckstein F, Lilley DMJ, eds. *Nucleic acids and molecular biology.* Springer; 2012; No. 2.

27. Satyanarayana S, Dabrowiak JC, Chaires JB. Tris( phenanthroline)ruthenium( 11) enantiomer interactions with DNA: Mode and specificity of binding? *Biochemistry*. 1993;32:2573-2584.

28. Barton JK, Goldberg JM, Kumar CV, Turro NJ. Binding modes and base specificity of tris(phenanthroline)ruthenium(II) enantiomers with nucleic acids: Tuning the stereoselectivity. *J Am Chem Soc*. 1986;108:2081-2088.

29. Barton JK, Danishefsky A, Goldberg J. Tris(phenanthroline)ruthenium(II): Stereoselectivity in binding to DNA. *J Am Chem Soc*. 1984;106:2172-2176.

30. Yamagishi A. Evidence for stereospecific binding of tris(1,10-phenanthroline)-ruthenium(II) to DNA is provided by electronic dichroism. *J Chem Soc, Chem Commun.*1983;572:573.

31. Niyazi1 H, Hall JP, O'Sullivan K, et al. Crystal structures of L-[ru(phen)$_2$dppz]21 with oligonucleotides containing TA/TA and AT/AT steps show two intercalation modes. *Nat Chem*. 2012;4:621-628.

# Chapter 4: Dual-emission Ruthenium-BODIPY Ratiometric Complex for Oxygen Sensing

## 4.1 Introduction

The past decade has seen a widespread interest in optical sensing using fluorescence as a result of its sensitivity and ease of use. Fluorescence sensing has been employed to measure parameters such as temperature,[1] pH,[2] concentration of calcium ions,[3] and $O_2$.[4-6] Optical sensors for oxygen have found many different applications in biological domains such as (a) in food technology,[7,8] (b) biotechnology, [9,10] and (c) intracellular oxygen sensing.[11,12]

This interest in optical methods of intracellular oxygen sensing and determining oxygen concentration has spurred on the development of oxygen sensing techniques applied to cells and in-vivo methods.[13-15] The value of oxygen sensing in such domains has been discussed in the preceding chapters. Fluorescence based methods possess key features that make them ideal for measuring oxygen such as (a) full reversibility, (b) lack of consumption during measurement, (c) allows for remote sensing, and (d) the ability to image oxygen.[15]

Oxygen concentration can be measured from either the lifetime or emission intensity of the phosphor. Luminescent lifetime measurements *in vivo* require specialist detection strategies such as TCSPC or phase fluorimetery for example in fluorescence lifetime imaging microscopy (FLIM) as described in Chapter 1. FLIM is an ideal method for sensing as lifetime is independent of probe concentration and lifetime can be calibrated. However, intensity-based imaging probes makes sensing more widely accessible, since it requires conventional steady state detectors such as those used in conventional fluorescence microscopy rather than a specialized instrumentation. However, as emission intensity is influenced by probe concentration, a reference probe that is insensitive to oxygen must be introduced to which the intensity of the probe can be ratioed, to give quantitative measurements. Of course the ratio of probe and reference must be constant. The combination of an oxygen-sensitive probe with an insensitive reference probe results in a single excited, dual-emitting probe that can potentially be imaged to give ratio metrically determined intracellular oxygen imaging. These ratiometric methods allow for fluorescence-based intensity imaging.

As expanded below, effective molecular ratiometric probes are difficult to accomplish so the majority of reported ratiometric probes are particle based such as dyes encased in polymer structures PEBBLES,[16,17] and nanoparticles.[13,18-20] The ideal properties of a ratiometric probe include: 1) good spectral separation between the fluorescence or

phosphorescence of probe and reference 2) only the phosphorescent probe exhibits oxygen quenching; 3) reverse energy transfer does not occur from the phosphor to the fluorophore, avoiding cross-talk between the two complexes; 4) electron transfer quenching does not occur between the fluorophore and the phosphor; 5) it is taken up sufficiently by cells.

Single molecule probes are rare as it is difficult to design a single-excitation, dual-emitting probe with no cross-talk between the two. The advantages of using molecular systems though is that the sensitivity and detection of the sensor can be adjusted based on the dye concentrations and permeability/targeting within the cell is easier. Particle encasement though offers protection from interfering quenchers when introduced to live cells. The group of *Papkovsky et al* have carried out extensive work on oxygen sensing using both nanomaterials and porphyrins. They recently reported on phosphorescent Pt-porphyrins encased in a polyacrylate nanoparticle for oxygen sensing, shown in Figure 4.1. The particles were successfully taken up by neural cells. Upon stimulation with Antimycin A, they were able to measure a change in oxygen concentration using PLIM.[21] In a similar report they demonstrated ratiometric oxygen sensing based on phosphorescent quenching of Pt-porphyrins in neurospheres.[22] A neurosphere is a cluster of neural stem cells which are used to study neural precursor cells *in vitro*.

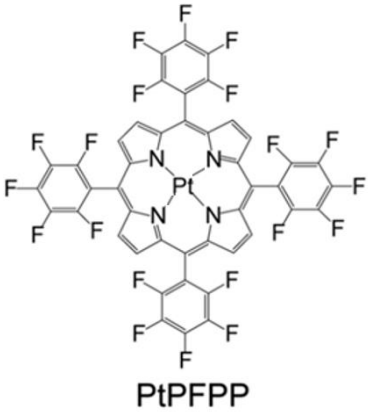


**Figure 4.1** Structure of a Pt(II)-tetrakis(pentafluorophenyl)porphyrin (PtPFPP) polyacrylate nanoparticle.[21]

Ratiometric probes based in the quenching of transition metal complexes by oxygen have been widely explored. [16,23-26] Real time monitoring of intracellular oxygen has been carried out using such probes as oxygen quenching in live cells is a reversible process.[14]

The long-lived phosphorescent emission increases the quenching efficiency of the probes. This has been discussed in more detail in Chapter 1.

This chapter focuses on two approaches to ratiometric optical oxygen sensing. The first is a ratiometric, dual emitting molecule. It consists of a ruthenium probe sensitive to oxygen, and a BODIPY reference which is insensitive to oxygen. The second is a core-shell poly(styrene) nanoparticle, where the reference BODIPY complex is located in the core of the structure, while the ruthenium oxygen probe is conjugated to the poly(L-lysine) surface. Ruthenium's long luminescent lifetime renders it environmentally sensitive to oxygen. Its oxygen sensitivity has been explored extensively as an oxygen sensing probe, which was discussed in Chapter 1.[6,27] This along with its photostability and other optical properties described, makes ruthenium an excellent choice as the oxygen sensitive component for these ratiometric approaches. BODIPY was chosen as the reference probe as its short luminescent lifetime renders it insensitive to oxygen. BODIPY complexes possess high quantum yields which is ideal for cell imaging. In the context of ratiometric sensing the sharp emission bands of the BODIPY are also useful in limiting overlap between probe and reference. However, the challenge of using BODIPYs alongside ruthenium for a ratiometric probe lies in the concentration ratio in which they are combined. Efforts must be made to ensure that the BODIPY (which usually have far greater quantum yields than ruthenium) does not outshine the ruthenium emission due to the difference in their quantum yields. Another challenge will be to avoid any cross talk between the two components. It is anticipated that any potential communication between the two probes will be limited in the core-shell nanoparticles as the BODIPY component is located in the poly-styrene core away from the ruthenium which is located at the shell. The molecular dyad was carefully designed to address both these issues by using a bromoBODIPY with reduced emission intensity and ensuring no energy or electron transfer between each moiety was thermodynamically feasible.[26] Both probes are assessed as quantitative optical oxygen sensing probes, generating calibration plots which can be translated to live cell imaging.

## 4.2 Materials and Methods

### 4.2.1 Materials

[Ru-(bpy-Ar-COOH)$_2$-phen-Ar-BODIPY-Br$_2$] complex was synthesised by Dr. Aaron martin (DCU) shown in Scheme 4.1. [Ru(bpy)$_2$-phen-COOH]$^{+2}$ and BODIPY-Br$_2$ complexes for the core-shell particles were synthesised by Christopher S. Burke (DCU). The polystyrene core-shell particles and dye loading were synthesised and carried out by Dr. Jaco Jacobs (DCU), shown in Figure 4.14.

All chemicals and solvents used in experimental procedures were purchased from Sigma Aldrich (Ireland). All solutions were made using deionised water, which was purified by a Milli-Q plus 18.5 Millipore purifying system. HeLa and CHO-K1 cells (ATCC) were used. Resazurin reagents were acquired from Promokine. Cell culture media, serum and penicillin / streptomycin were purchased from Sigma Aldrich. Cell culture flasks were purchased from Corning Incorporated.

From here on in [Ru-(bpy-Ar-COOH)$_2$-phen-Ar-BODIPY-Br$_2$] will be called [Ru(bpy)$_2$-phen-BODIPY-Br$_2$] complex, and the core-shell particles will be called RuBODIPY particles for distinction.

### 4.2.2 Spectroscopic Measurements

The spectroscopic properties of [Ru(bpy)$_2$-phen-BODIPY-Br$_2$] and the RuBODIPY particles were assessed in aqueous PBS solution (pH 7.4) at room temperature. The UV-vis spectra were obtained on a Jasco V-670 spectrophotometer. The steady state dual emission spectra were collected on a Varian Cary Eclipse fluorescence spectrophotometer with an excitation and emission slit width of 10 nm. The luminescent lifetimes of the ruthenium and BODIPY components were obtained using a time correlated single photon counting (TCSPC) PicoQuant system. The exciting laser for both components was 405 nm. 10,000 counts were collected for each lifetime measurement, and performed in triplicate. Lifetime decays were analysed using PicoQuant Nano Harp for the long lived ruthenium component, and Time Harp for the short lived BODIPY component.

### 4.2.3 Oxygen Calibration Studies

To measure the oxygen sensitivity, [$Ru(bpy)_2$-phen-BODIPY-$Br_2$] complex was purged with nitrogen for 20 minutes and RuBODIPY particle solutions in PBS were purged with nitrogen for 10 minutes, both at room temperature. The oxygen concentration was measured using a PreSense Oxygen Probe. The particles were slowly re-aerated to give a range of oxygen concentrations (measured in μmol/L). The emission spectra and lifetimes were measured to construct an oxygen calibration curve for the molecular system and the particles. The emission spectra were collected using a Varian Cary Fluorimeter, with an excitation and emission slit width of 10 nm. The lifetimes were collected using time correlated single photon counting (TCSPC).

### 4.2.4 RuBODIPY particle preparation for cell uptake

Cetyltrimethylammonium bromide (CTAB) from Sigma Aldrich, was used to induce a cationic surface charge on the particles for cell uptake. A 0.1 mM CTAB solution in PBS was added to the particles in a 3:2 ratio CTAB: particles, resulting in a final concentration of 150 μM, and was left to sonicate overnight to ensure sufficient particle coating.

### 4.2.5 Real-time confocal luminescent imaging

#### 4.2.5.1 [$Ru(bpy)_2$-phen-BODIPY-$Br_2$] Complex

CHO cells were seeded at 2.5 x $10^5$ cells in 2 mL media on 35 mm glass-bottom culture dishes. Cells were grown for 24 h at 37 °C at 5 % $CO_2$. The growth media was removed and 15 μM of [$Ru(bpy)_2$-phen-BODIPY-$Br_2$] complex in phenol red-free media was added and left to incubate for 24 h at 37 °C at 5 % CO2 in the dark. The dye/media solution was removed and the cells were washed with PBS supplemented with 1.1 mM $MgCl_2$ and 0.9 mM $CaCl_2$. Cells were imaged using a Zeiss LSM 510 Meta confocal microscope using a 63X oil immersion objective lens. A 458 nm argon ion laser was used to excite the complex. The BODIPY emission was collected using a band-pass 505-550 nm filter. The ruthenium complex emission was collected using a long pass 560 nm

filter. The excitation/λ scan was carried out using a 458 nm argon ion laser and the emission was collected between 497 nm and 754 nm with a step size of 10 nm.

#### 4.2.5.2 RuBODIPY particle uptake

CHO and HeLa cells were seeded at $1.5 \times 10^5$ cells in 2 mL media on 35 mm glass-bottom culture dishes. Cells were grown for 48 h at 37 °C at 5 % $CO_2$. The growth media was removed, and replaced with 2 mL Lebovitz media for 2 h. 5 % v/v nanoparticles in Lebovitz media were added to the cells and incubated for 5 minutes in the absence of light at 37 °C and 5 % $CO_2$. The nanoparticles/media solution was removed and replaced with Lebovitz media. Cells were left to incubate for 2, 4, and 6 h at 37 °C in the dark. Cells were washed twice with PBS supplemented with 1.1 mM $MgCl_2$ and 0.9 mM $CaCl_2$ and imaged immediately. Cells were imaged using a Leica TSP DMi8 confocal microscope, using a 100 X oil immersion objective lens. The nanoparticles were excited using a 470 nm white light laser. The BODIPY emission was collected using a band pass 505-550 nm filter, and the ruthenium emission was collected using a long pass 605 nm filter. DRAQ 7 (Biostatus, UK), which stains the nucleus of dead cells, was added to the culture dish (1:100 final concentration) to monitor cell viability. DRAQ 7 was excited using a 633 nm white light laser and emission was collected using a long pass 650 nm filter.

### 4.2.6 Phosphorescent lifetime imaging microscopy (PLIM) of RuBODIPY particles

CHO cells were seeded at 1.5 x $10^5$ cells in 2 mL media on 35 mm glass-bottom culture dishes. Cells were grown for 48 h at 37 °C at 5 % $CO_2$. The growth media was removed, and replaced with 2 mL Lebovitz media for 2 h. 5 % v/v nanoparticles in Lebovitx media were added to CHO cells and incubated for 5 minutes in the absence of light at 37 °C and 5 % $CO_2$. The nanoparticles/media solution was removed and replaced with Lebovitz media. Cells were left to incubate for 4 h at 37 °C in the dark. CHO cells were washed twice with PBS supplemented with 1.1 mM $MgCl_2$ and 0.9 mM $CaCl_2$. Live PLIM images were acquired using MicroTime System attached to a Leica TSP Dmi8 confocal microscope using a 100X oil immersion objective. Each PLIM image was acquired for 20 minutes at 512 x 512 resolution. A 405 nm laser was used to excite the sample. The BODIPY emission was collected using a 515-580 nm band pass filter at 8 ps resolution, and the $[Ru(bpy)_2\text{-Phen-Ar-COOH}]^{2+}$ was collected using a 570-700 nm

band pass filter at 256 ps resolution. The data was analysed using the PicoQuant Symphotime Software. Lifetimes were fit to a mono exponential decay until an $X^2$ value of 0.9-1.1 was achieved. The average lifetime was taken from 2 separate experiments.

### 4.2.7 Cytotoxicity assay

CHO cells were seeded in a 96-well plate in 100 μL media at 1 x $10^4$ cells per well for 24 h at 37 °C with 5 % $CO_2$. For [Ru(bpy)$_2$-phen-BODIPY-Br$_2$], the complex was added to the cells to give final concentrations of 150, 100, 50, 15, 1, 0.1 μM. Cells were incubated for 24 h at 37 ºC at 5% $CO_2$ in the absence of light. For RuBODIPY, the particles were added to give final concentrations of 1, 2, 5, 10, 25, and 50 % v/v in CHO media. The cells were incubated for 5 minutes. The particles were removed and replaced with CHO media and left to incubate in the absence of light for 24 h at 37 °C at 5 % $CO_2$. In both cases, 10 μL of Resazurin (Alamar Blue) reagent was added to each well and incubated for a further 7 h in the absence of light at 37 °C. The resazurin was converted to resorufin in viable cells and its absorbance was measured at 570 nm, with background measured at 600 nm using a Tecan 96-plate reader.

## 4.3 Photophysical properties and Characterisation of The Molecular System; [Ru(bpy)$_2$-phen-BODIPY-Br$_2$]

Scheme 4.1 illustrates the structure of [Ru(bpy)$_2$-phen-BODIPY-Br$_2$]. The ruthenium centre has two bipyridine (bpy) ligands with phenyl carboxylic acids. The phenanthroline-BODIPY moiety is brominated at the 2 and 6 positions.

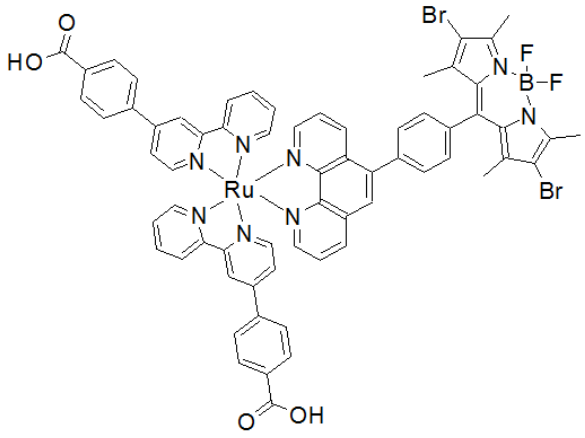


**Scheme 4.1** Structure of [Ru(bpy)$_2$-phen-BODIPY-Br$_2$] complex.[26]

Figure 4.2 shows the absorbance and emission spectra of [Ru(bpy)$_2$-phen-BODIPY-Br$_2$] in non-aqueous methanol solution (–), acetonitrile (–) and in aqueous PBS solution (–). In methanol the complex exhibits a shoulder at 466 nm which is attributed to the ruthenium moiety. A sharp, intense absorbance feature is observed at 526 nm, which is typical of BODIPY. The strong absorbance is due to the dipyrromethane based $S_0 \rightarrow S_1$ $\pi - \pi^*$ transition.[28] When excited into the absorbance shoulder at 458 nm, a dual-emission is observed, with an intense emission peak at 552 nm attributed to the BODIPY and a peak centred at 610 nm assigned to the ruthenium $^1$MLCT absorbance. However, interestingly, in aqueous solution, the BODIPY emission switches off. In PBS solution, the ruthenium absorbance appears to be slightly more intense than in non-aqueous solution, when measured at 50 μM. The excitation of the BODIPY absorbance peak at 525 nm decreases by almost 50 %. When excited at 458 nm, the BODIPY emission disappears and the ruthenium, now centred at 623 nm, remains.

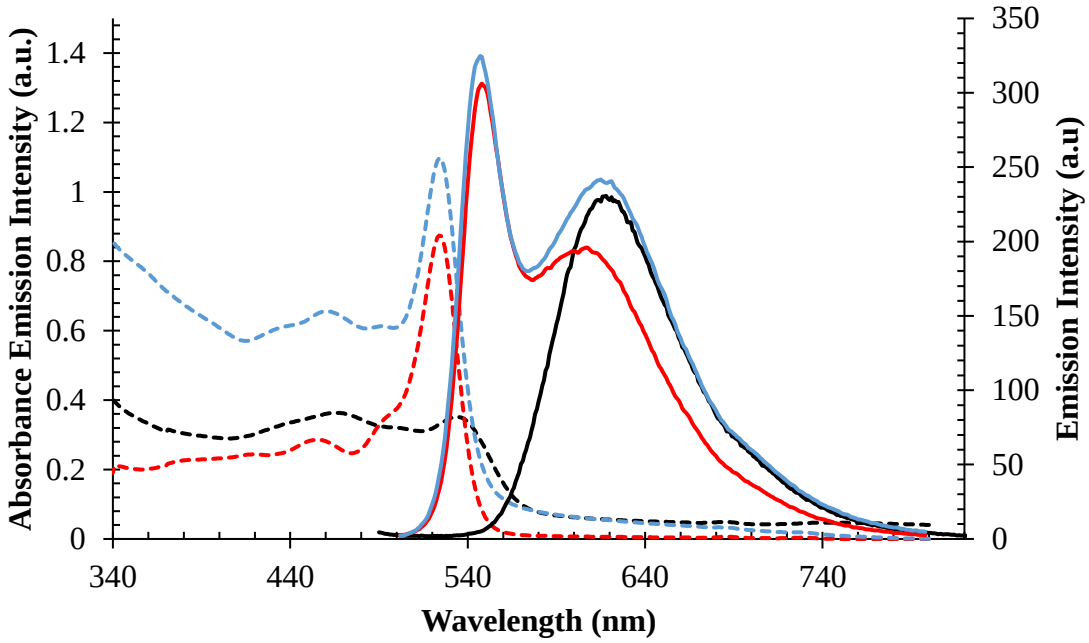


**Figure 4.2** Absorbance and emission spectra of [Ru(bpy)$_2$-phen-BODIPY-Br$_2$] complex at 50 µM in methanol solution (–), acetonitrile solution (–) and aqueous PBS solution (–). The emission was collected by exciting at 458 nm, slit width 5nm.

The emission of [Ru(bpy)$_2$-phen-BODIPY-Br$_2$] was also assessed in the aprotic solvent acetonitrile, to compare to the emission spectra of [Ru(bpy)$_2$-phen-BODIPY-Br$_2$] with the protic solvent methanol. As shown in Figure 4.2, the relative luminescent emission intensity between the ruthenium and BODIPY is slightly greater when in methanol (–) solution compared to acetonitrile (–), but importantly both units of the dyad remain emissive in both acetonitrile and methanol To assess if this switch was reversible and due to environmental sensitivity and not a chemical reaction such as decomposition, a solution of [Ru(bpy)$_2$-phen-BODIPY-Br$_2$] was made up in methanol and its emission was recorded (—), as described in Figure 4.3.

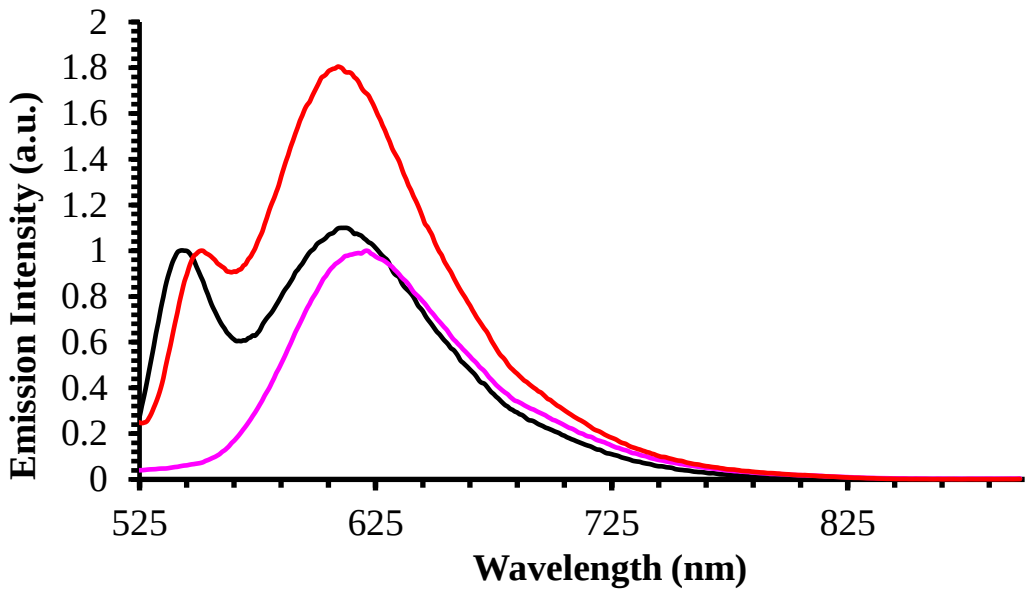


**Figure 4.3** Normalised emission intensity of [Ru(bpy)$_2$-phen-BODIPY-Br$_2$] illustrating the initial dual emission in methanol (—), the switching off of the BODIPY moiety in water (—), and its recovery upon changing back to methanol (—).

Water was added and the emission spectrum showed no contribution from the BODIPY as expected (—). 100 μL of the aqueous solution was remixed with methanol, and the BODIPY emission was recovered (—). The intensity of the recovered spectrum is lower in Figure 4.3 because of this dilution. This water sensitivity was rather unexpected, particularly given that the BODIPY emits in methanol, which is a protic solvent. Subsequent work in our lab on the isolated BODIPY has shown that it is this component alone that is water sensitive and work is ongoing to understand the origin of the switching mechanism (to be published). However in the context of imaging it may be useful as recovery of the BODIPY can be used as a 'switch' reference complex for imaging non-aqueous environments. The shift in the emission spectra of [Ru(bpy)$_2$-phen-BODIPY-Br$_2$] when introduced to water is attributed to the influence of solvent as some methanol solution still present.

The emission lifetimes of the two components of the complex were measured in methanol, acetonitrile, and PBS using time correlated single photon counting (TCSPC), as outlined in Table 4.1.

**Table 4.1** Luminescent spectra of [Ru(bpy)$_2$-phen-BODIPY-Br$_2$] in PBS [a], methanol [b], and acetonitrile [c] solution. Solutions were degassed with nitrogen for 15 minutes before reading the de-aerated values. Emissions were collected when excited at 458 nm, slit width = 10 nm. (Amp = amplitude)

| Compound | $\lambda_{abs}/\lambda_{ex}$ (nm) | $\lambda_{em}$ (nm) | $\tau_f$/ns aerated | $Amp_{aer}$ (%) | $\tau_f$/ns de-aerated | $Amp_{de\text{-}aer}$ (%) |
|---|---|---|---|---|---|---|
| **Ru(II)** | 468 [a] | 623 [a] | 587 ± 13 [a] | 100 | 1.08 μs ± 15 [a] | 100 [a] |
| | 466 [b] | 610 [b] | 306 ± 28 [b] | 40.81 [b] | 825 ± 28 [b] | 33.2 [b] |
| | 466 [c] | 617 [c] | 131 ± 13 [c] | | 319 ± 31 [c] | |
| **BODIPY** | 525 [a] | ____ [a] | ____ [a] | ____ [a] | ____ [a] | ____ [a] |
| | 526 [b] | 552 [b] | 24 ± 2 [b] | 59.19 [b] | 24 ± 2 [b] | 66.8 [b] |
| | 526 [c] | 548 [c] | 1.14 ± 0.15 [c] | | 1.22 μs ± 0.12 [c] | |

The lifetime data, collected by TCSPC, gave best fit in organic solvent and the particle to a dual exponential decay which allowed for identification of the lifetime of each component in the dyad. The molecular complex, in methanol or PBS, were purged with nitrogen for 15 minutes prior to measurement to obtain the de-aerated lifetime. Consistent with the emission spectra, in methanol, the lifetime fit a bi-exponential decay, while in PBS it fit to only a single exponential decay which corresponded to the lifetime of the ruthenium moiety. As expected, ruthenium displayed excellent oxygen sensitivity. When fully de-aerated, the lifetime of the ruthenium component increased from 306 ± 28 ns to 825 ± 28 ns in methanol, and from 587 ± 23 ns to 1.082 μs ± 15 ns in PBS. However, the ruthenium component exhibits a much shorter lifetime of 131 ± 13 ns when in aerated acetonitrile, which increased to 319 ± 31 ns when de-aerated. Acetonitrile is more polar. In multi-exponential lifetime decays, the lifetimes are extracted from the decay, as well the fractional amplitudes of each lifetime component. The amplitude is given as % value. The amplitude of the ruthenium and BODIPY components in methanol solution are shown in Table 4.1. When in aerated methanol

solution, the fractional amplitudes contributing to the lifetime of [Ru(bpy)$_2$-phen-BODIPY-Br$_2$] are almost equal, with ruthenium amplitude slightly smaller. When de-aerated, the fractional amplitude of ruthenium decreases further, making up only a third of the overall lifetime consistent with the reduction in emission intensity observed. The longer lifetime in PBS is surprising but consistent with intensity studies of other related complexes where ruthenium emission is more intense in water.[29] On the other hand, the BODIPY showed no change in intensity or lifetime in response to oxygen concentration. Its relatively short lifetime renders the BODIPY component insensitive to oxygen, making it an ideal reference probe in and oxygen ratiometric sensor. Figure 4.4 shows an example of the emission lifetime decays of [Ru(bpy)$_2$-phen-BODIPY-Br$_2$] in methanol when aerated (A) and de-aerated (B). In both cases, $\tau_1$ is attributed to the ruthenium lifetime contribution, and $\tau_2$ to the BODIPY.

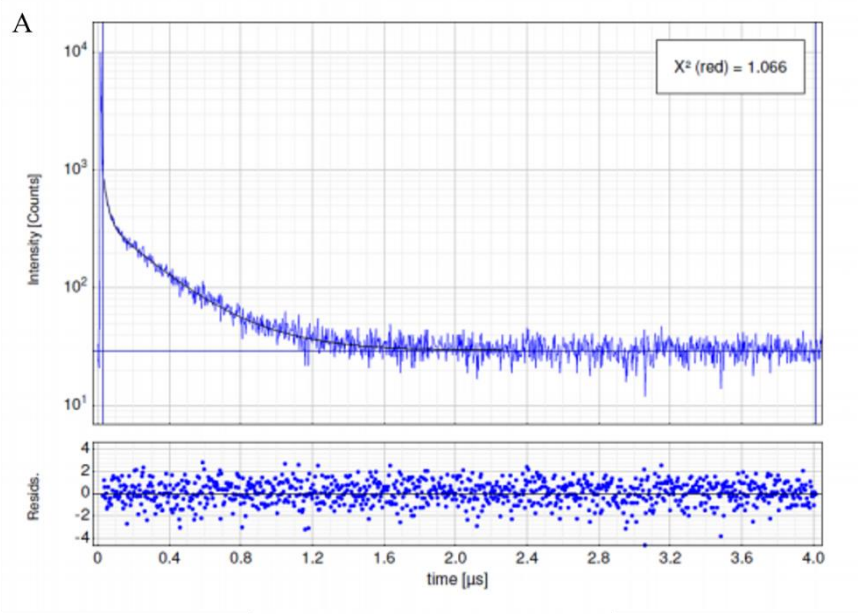


| Parameter | Value |
|---|---|
| $A_1$ [Cnts] | 335.0 |
| $\tau_1$ [µs] | 0.3063 |
| $A_2$ [Cnts] | 487.4 |
| $\tau_2$ [µs] | 0.02471 |
| Bkgr. $_{Dec}$ [Cnts] | 29.29 |

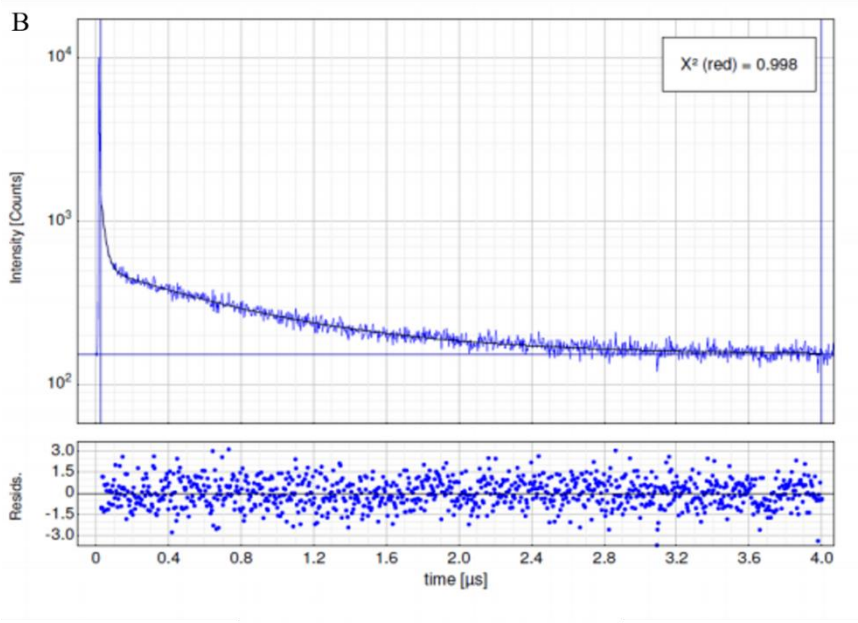


| Parameter | Value |
|---|---|
| $A_1$ [Cnts] | 355.04 |
| $\tau_1$ [µs] | 0.8250 |
| $A_2$ [Cnts] | 730.5 |
| $\tau_2$ [µs] | 0.02366 |
| Bkgr. $_{Dec}$ [Cnts] | 153.18 |

**Figure 4.4** TCSPC emission lifetime traces of [Ru(bpy)$_2$-phen-BODIPY-Br$_2$] under aerated (A) and de-aerated (B) condiotions in methanol. [Ru(bpy)$_2$-phen-BODIPY-Br$_2$] was de-aerated for 15 minutes with nitrogen. The complex was excited using the 450 nm laser, and the data was acquired using the PicoQuant Nano Harp system. The lifetime traces (—) were fit to give a $\chi^2$ value between 0.9 and 1.1 and visual inspection of residuals (•) also confirmed goodness of fit.

## 4.4 [Ru(bpy)$_2$-phen-BODIPY-Br$_2$] oxygen dependent studies

The luminescent lifetime and emission intensity data indicated that [Ru(bpy)$_2$-phen-BODIPY-Br$_2$] displays excellent response to oxygen concentration and this was investigated further as an oxygen sensing probe. The initial emission and lifetime of the probe in methanol were recorded as a function of oxygen concentration. When aerated, the maximum oxygen concentration in the solution was determined to be 256 µmol/L, measured using a commercial optical sensor – Presens $O_2$ probe. The complex was purged for 15 minutes, and the emission and lifetime recorded. The minimum dissolved oxygen concentration following de-aeration was found to be 30 µmol/L. The emission of the BODIPY remained unaffected by oxygen concentration, whereas the ruthenium emission increased by 50 %, as demonstrated by the emission profile in Figure 4.5.

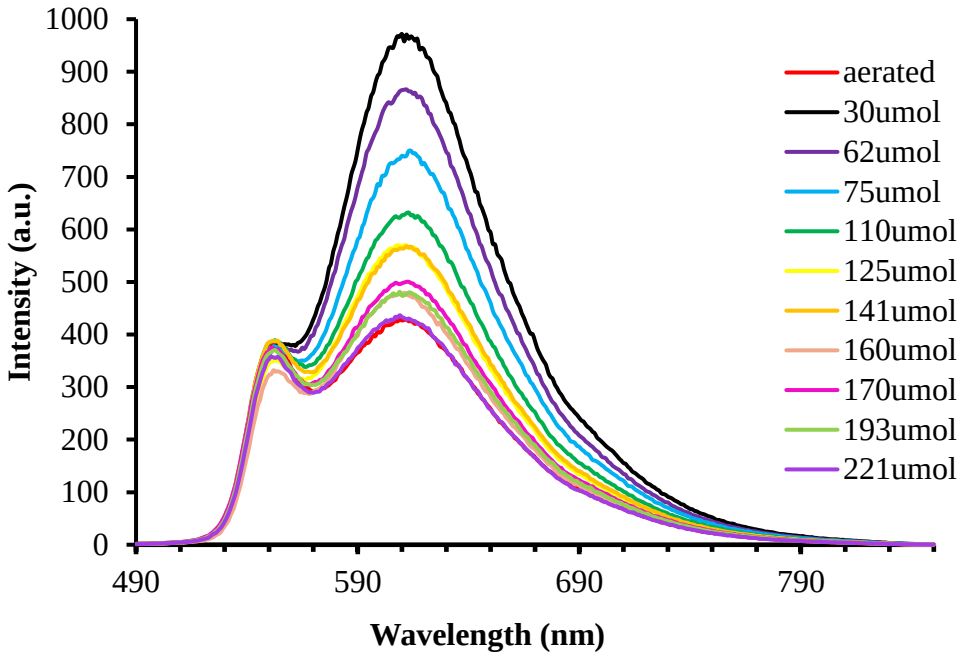


**Figure 4.5** Luminescent emission spectra of [Ru(bpy)$_2$-phen-BODIPY-Br$_2$] in methanol as a function of oxygen concentration (50 μM, 18 °C). The complex was excited at 458 nm, slit width 5 nm.

Oxygen was gradually reintroduced to the solution by allowing it to re-aerate through slow re-equilibration with ambient air, and the emission and lifetimes were measured at varying oxygen concentrations over time as the oxygen concentration recovered. The resulting spectra are shown in Figure 4.5. Over the course of re-aeration, the BODIPY emission profile remained constant throughout, and its lifetimes were unaffected. However, the emission from the ruthenium centre decreased linearly with increasing oxygen concentration, and this behaviour was mirrored in the lifetime data.

To obtain quantitative insights into $O_2$ quenching, the lifetime as a function of oxygen was plotted using the Stern-Volmer equation shown in Equation 4.1:

$$\frac{I_0}{I} = \frac{\tau_0}{\tau} = 1 + K_{SV} \,.\, [O_2] \quad \ldots\ldots\ldots \textbf{Equation 4.1}$$

Figure 4.6 describes the Stern Volmer plots of the luminescent lifetime (—), and luminescent emission intensity (—) versus oxygen concentration at 18 °C. The

relationship between the lifetime and oxygen concentration is linear, suggesting, as expected, that there is only one type of quenching occurring, dynamic quenching.

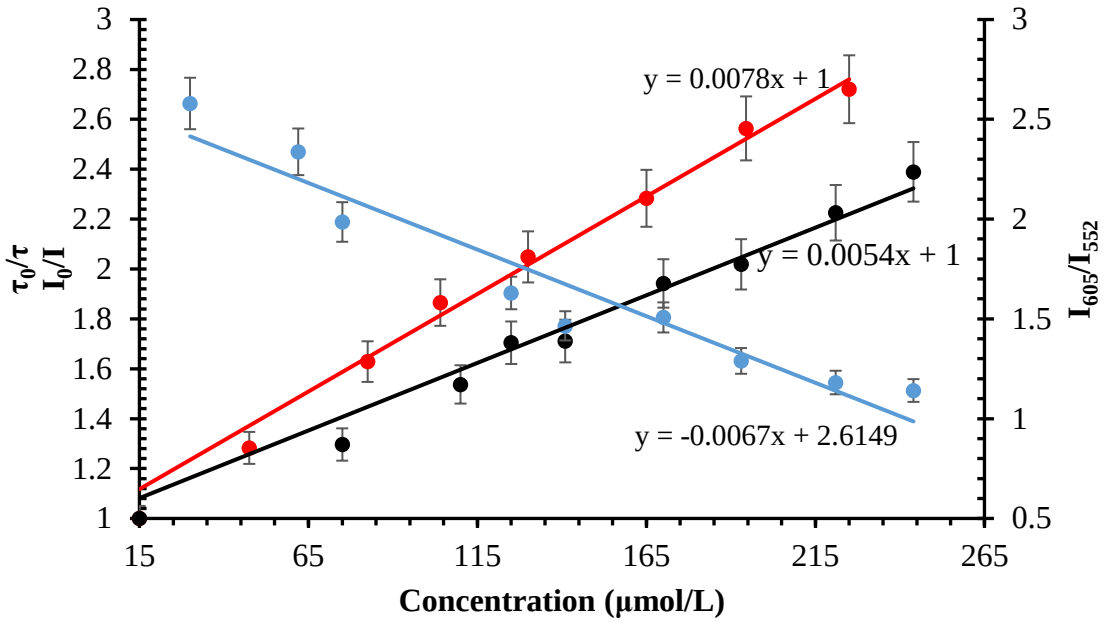


**Figure 4.6** Stern-Volmer plot of [Ru(bpy)$_2$-phen-BODIPY-Br$_2$] luminescent lifetime (—) and luminescent emission intensity (—) as a function of oxygen concentration in methanol (25 µM) at 18 °C. The complex was excited at 450 nm over a range of oxygen concentrations. Calibration ratiometric plot intensities of the BODIPY and ruthenium centred emissions as a function of oxygen concentration in methanol (—). The complex was excited at 458 nm and the ratio of the two emission centres was plot.

The Stern-Volmer constant, $K_{sv}$, can be obtained from the slope of the plot in Figure 4.6 (—), in this case $K_{sv}$ = 0.0078. The rate of quenching, $k_q$, for [Ru(bpy)$_2$-phen-BODIPY-Br$_2$] in methanol can be determined using Equation 4.2:

$$K_{SV} = k_q . \tau_0 \quad \ldots \textbf{ Equation 4.2}$$

Where $k_q$ is the quenching rate, $K_{SV}$ is the slope of the Stern Volmer plot, and $\tau_0$ is the luminescent lifetime in the absence of oxygen. In methanol solution, [Ru(bpy)$_2$-phen-

BODIPY-$Br_2$] has a quenching rate, $k_q$, of 9.45 x $10^9$ $M^{-1}$ $s^{-1}$. Figure 4.6 also shows the ratiometric luminescence response of the BODIPY and ruthenium centred emissions as a function of oxygen concentration in methanol (—).

The probes response to oxygen in PBS was then explored under the same conditions. Figure 4.7 shows the emission intensities of the complex over a range of oxygen concentrations, with the Stern Volmer plot of $\tau_0/\tau$ versus oxygen concentration in the inset (•).

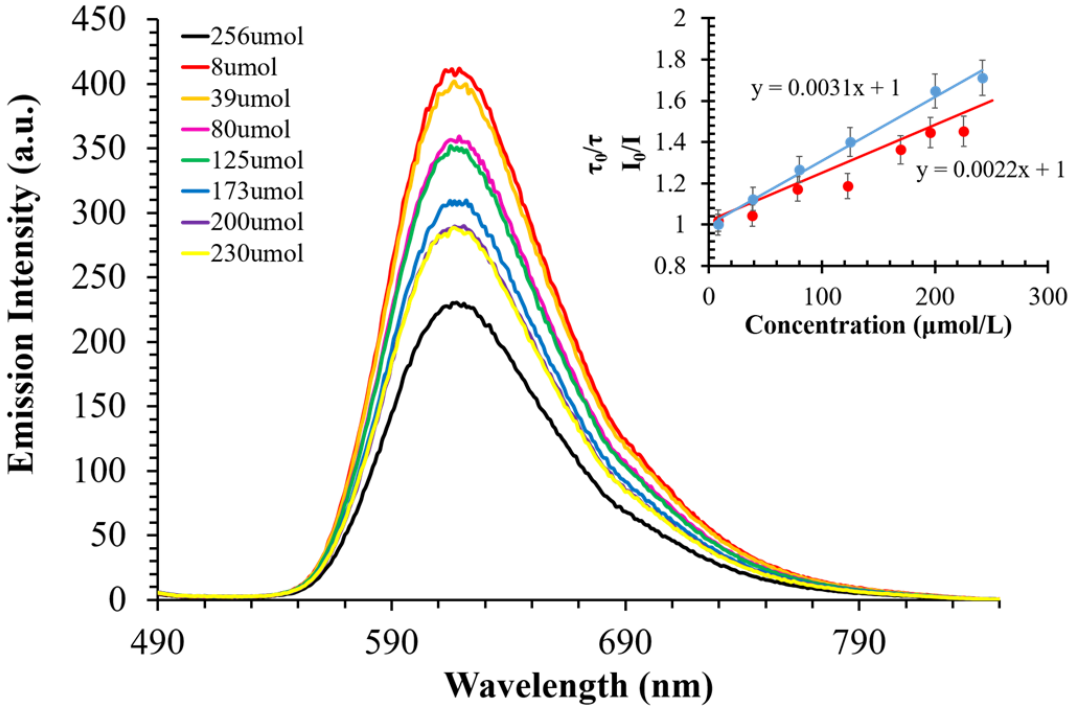


**Figure 4.7** Luminescent emission spectra of [Ru(bpy)$_2$-phen-BODIPY-$Br_2$] in PBS solution (25 µM) as a function of oxygen concentration. The corresponding Stern Volmer plot of the luminescent lifetimes (—) and emission intensity (—) over the range of oxygen concentrations. The complex was excited at 458 nm, slit width 5 nm.

Here, it was observed that the BODIPY component has switched off, while the ruthenium emission displayed a similar, linear response to oxygen, unaffected in aqueous solution. The rate of quenching for [Ru(bpy)$_2$-phen-BODIPY-$Br_2$] PBS was determined to be 2.87 x $10^9$ $M^{-1}$ $s^{-1}$, which is slightly slower than when it is methanol solution, which was measured to be $k_q$, of 9.45 x $10^9$ $M^{-1}$ $s^{-1}$. This is as a result of the

longer luminescent lifetime of ruthenium in aqueous solution. *Demas et al* obtained a quenching rate of 3.2 x $10^9$ $M^{-1}$ $s^{-1}$ for $[Ru(bpy)_3]^{2+}$ in water.[30] *Pellegrin et* al reported on a Ru(II) polypyridyl complex with a $k_q$ value of 6.7 x $10^9$ $M^{-1}$ $s^{-1}$ in water, which is of the same order, but slightly faster as the luminescent lifetime of their complex was much longer at 973 ± 3 ns compared to 587 ± 13 ns in PBS for our [$Ru(bpy)_2$-phen-BODIPY-$Br_2$] complex.[29]

## 4.5 Introduction of [$Ru(bpy)_2$-phen-BODIPY-$Br_2$] to cells

As demonstrated in *section 4.4,* [$Ru(bpy)_2$-phen-BODIPY-$Br_2$] showed promising self-referenced oxygen sensing capabilities in non-aqueous solution. Although the BODIPY reference switches off in aqueous solution, this could be used as a contrast reference for imaging non-aqueous regions in a cell, for example, lipid membranes.

In order to explore the uptake, distribution and sensing abilities in cells, Chinese hamster ovarian (CHO) cells, an adherent mammalian cell line, were used. CHO cells were seeded at 2.5 x $10^5$ cells in 2 mL culture media on 35 mm glass-bottom culture dishes, and were grown for 24 h at 37 °C with 5 % $CO_2$.

All images were acquired using a Zeiss LSM 510 confocal microscope with a 63 x oil immersion objective lens. A 458 nm argon ion laser was used to excite the complex. The BODIPY emission was collected using a band-pass 505 – 550 nm filter. The ruthenium emission was collected using a long pass 560 nm filter.

### 4.5.1 Cell Uptake of [$Ru(bpy)_2$-phen-BODIPY-$Br_2$]

A range of working concentrations and incubation times were assessed. 1 % DMSO was used to solubilise the complex and concentrations were made up in PBS. Initially, uptake dynamics were studied using 15 μM of [$Ru(bpy)_2$-phen-BODIPY-$Br_2$] in cell media and was added to live CHO cells where its uptake was monitored. Uptake was initially slow, with emission seen in some cells after 10 minutes exposure, shown in Figure 4.8 A. The cells were imaged every 5 minutes. After 15 minutes the complex has appeared to have crossed the membrane of all the cells (B), and dispersed throughout the cytoplasm by 25 minutes (C), with a plateau observed in uptake after 35 minutes (D).

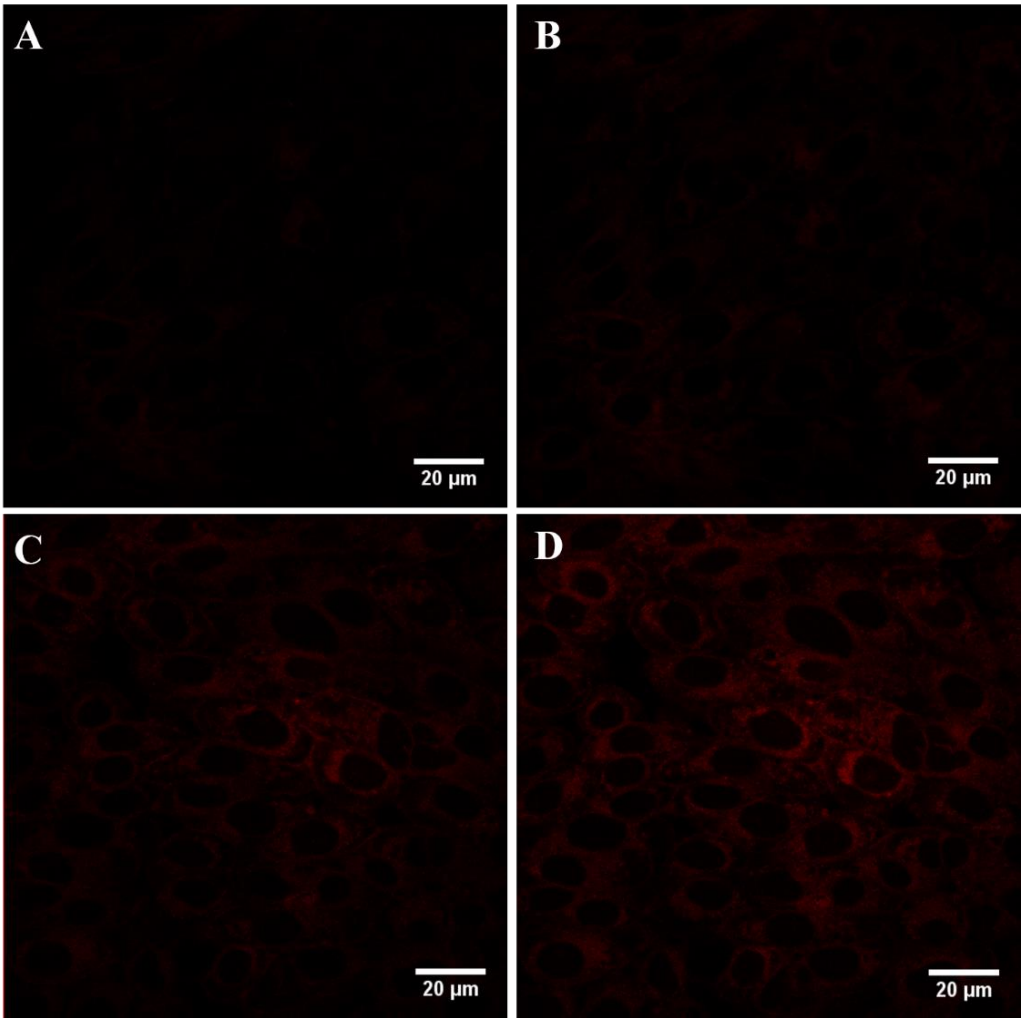


**Figure 4.8** Confocal microscopy of the live uptake of [Ru(bpy)$_2$-phen-BODIPY-Br$_2$] in CHO cells. 15 µM in cell culture media was added to CHO cells and uptake was observed after 10 minutes (A). Uptake was monitored at 15 (B), 25 (C), and 35 minutes (D). The sample was excited using a 458 nm argon laser. The BOPDIPY emission was collected using a 505-550 nm band-pass filter, and the ruthenium emission was collected using a long pass 560 nm filter.

To study distribution following uptake, the cells were incubated with [Ru(bpy)$_2$-phen-BODIPY-Br$_2$] (15 µM) for 24 h in the absence of light at 37 °C with 5 % $CO_2$. The solution was removed and the cells were washed with PBS supplemented with 0.9 mM $CaCl_2$ and 1.1 mM $MgCl_2$. Figure 4.9 shows representative images of the probe in CHO cells.

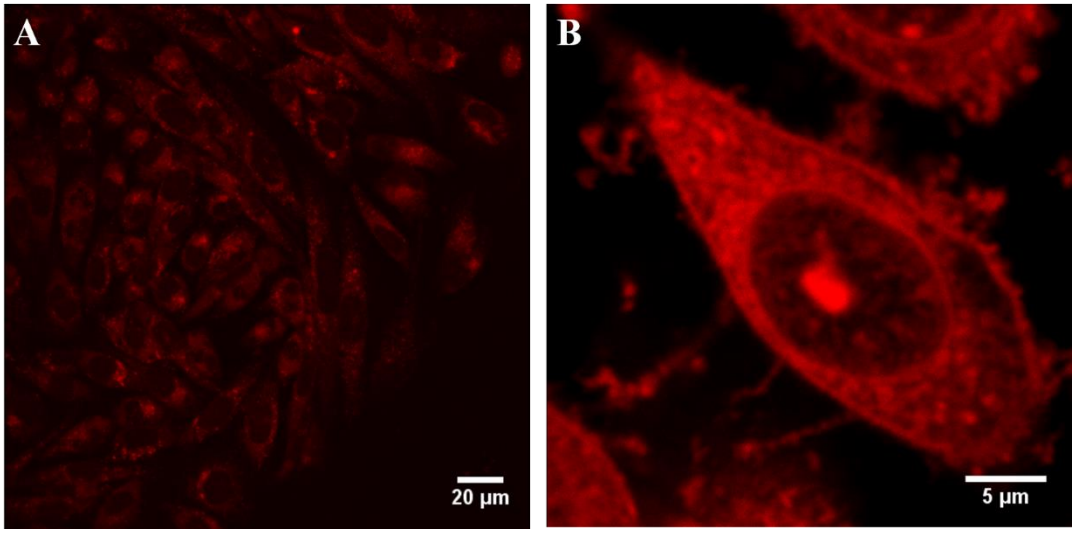


**Figure 4.9** Live CHO cells incubated with 15 µM [Ru(bpy)$_2$-phen-BODIPY-Br$_2$] complex for 24 h in the absence of light. Distribution can be seen in the cytoplasm (A) and in the nucleoli (B) of CHO cells. The sample was excited using a 458 nm argon laser. The BOPDIPY emission was collected using a 505-550 nm band-pass filter, and the ruthenium emission was collected using a long pass 560 nm filter.

As shown in the images, uptake is excellent with high contrast images achieved at low concentrations. [Ru(bpy)$_2$-phen-BODIPY-Br$_2$] permeated the cell membrane and appeared to be essentially non-selective in its localisation, distributing throughout the cytoplasm, although it also appears to permeate the nuclear envelope with evidence for localization of the probe in the nucleoli. *Barton et al* reported on a [Ru(phen)(bpy')(dppz)]$^{2+}$ complex conjugated to an octa-arginine sequence (Ru-D-R8), and to an octa-arginine-fluorescein sequence (Ru-D-R8-fluor). When incubated with Ru-D-R8, the complex localised in the cytoplasm of HeLa cells. However, it was found that Ru-D-R8-fluor located in the nucleoli of the cells. The greater lipophilicity of the fluorescein redirected the complex to the nucleus. The BODIPY, which is lipophilic, may be exerting the same influence here.[31] The concentration of 15 µM was determined to be ideal for imaging [Ru(bpy)$_2$-phen-BODIPY-Br$_2$], given the good images at relatively low concentrations, and low cytotoxicity. Working concentrations of 50 µM and greater appeared to be toxic towards the cells, demonstrated in Figure 4.10. Large vacuoles can be seen throughout the sample, which are indicative of apoptosis occurring at higher dye concentrations.

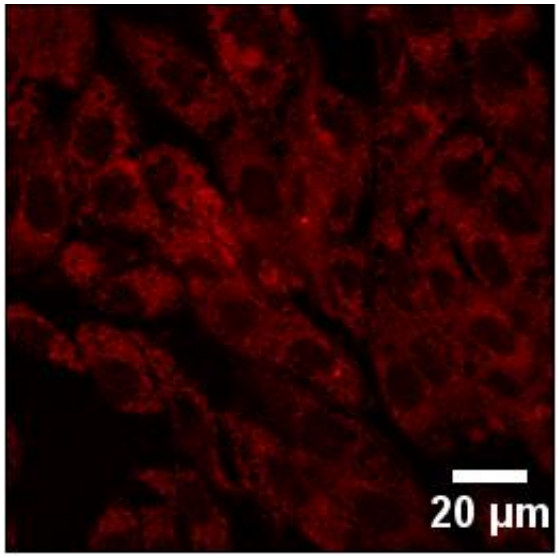


**Figure 4.10** Live CHO cells incubated with 50 µM [Ru(bpy)$_2$-phen-BODIPY-Br$_2$] for 24 h in the absence of light. Large vacuoles that have formed in the cells are indicative of apoptosis. The sample was excited using a 458 nm argon laser. The BOPDIPY emission was collected using a 505-550 nm band-pass filter, and the ruthenium emission was collected using a long pass 560 nm filter.

When incubated with the optimum concentration of 15 µM of [Ru(bpy)$_2$-phen-BODIPY-Br$_2$] the complex displayed strong luminescence from within the cell when excited at 458 nm. To determine if the BODPIY emission was present, an excitation scan was carried using the 458 nm argon laser line, and the emission was collected between 497 and 754 nm with a step size of 10 nm. Figure 4.11 A shows the results of the excitation scan. There is no emission seen in the range of 524 – 566 nm where the BODPIY would be expected to be. A slight emission can be seen in these windows, but it is attributed to contributions from the auto fluorescence of the cell.

A

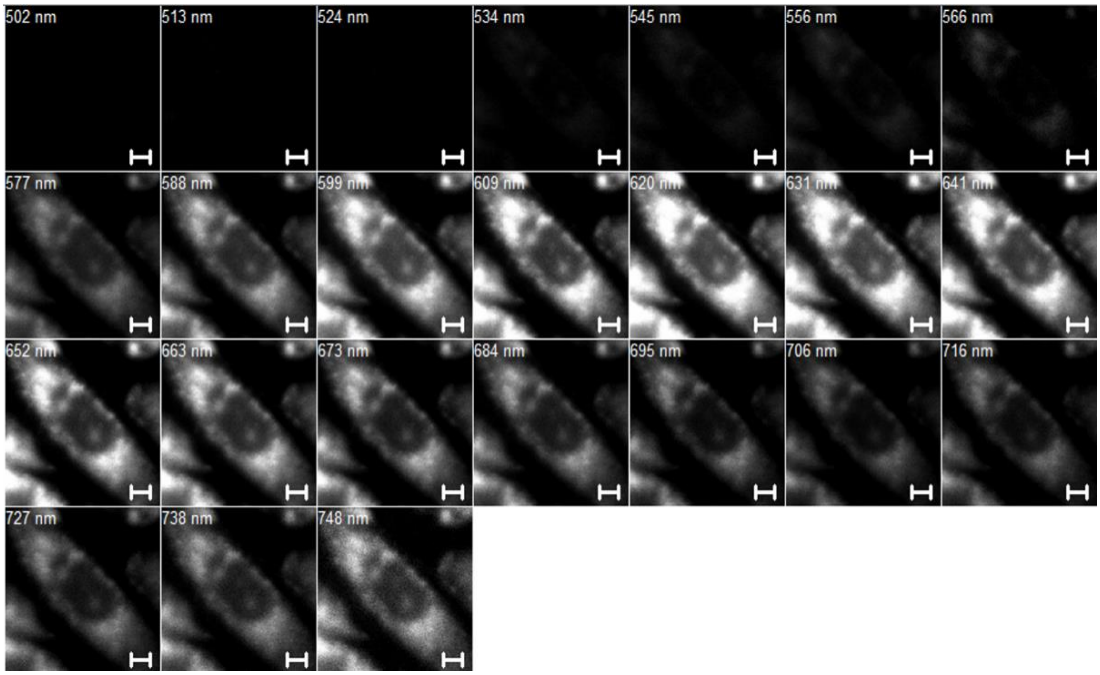
502 nm
513 nm
524 nm
534 nm
545 nm
556 nm
566 nm
577 nm
588 nm
599 nm
609 nm
620 nm
631 nm
641 nm
652 nm
663 nm
673 nm
684 nm
695 nm
706 nm
716 nm
727 nm
738 nm
748 nm

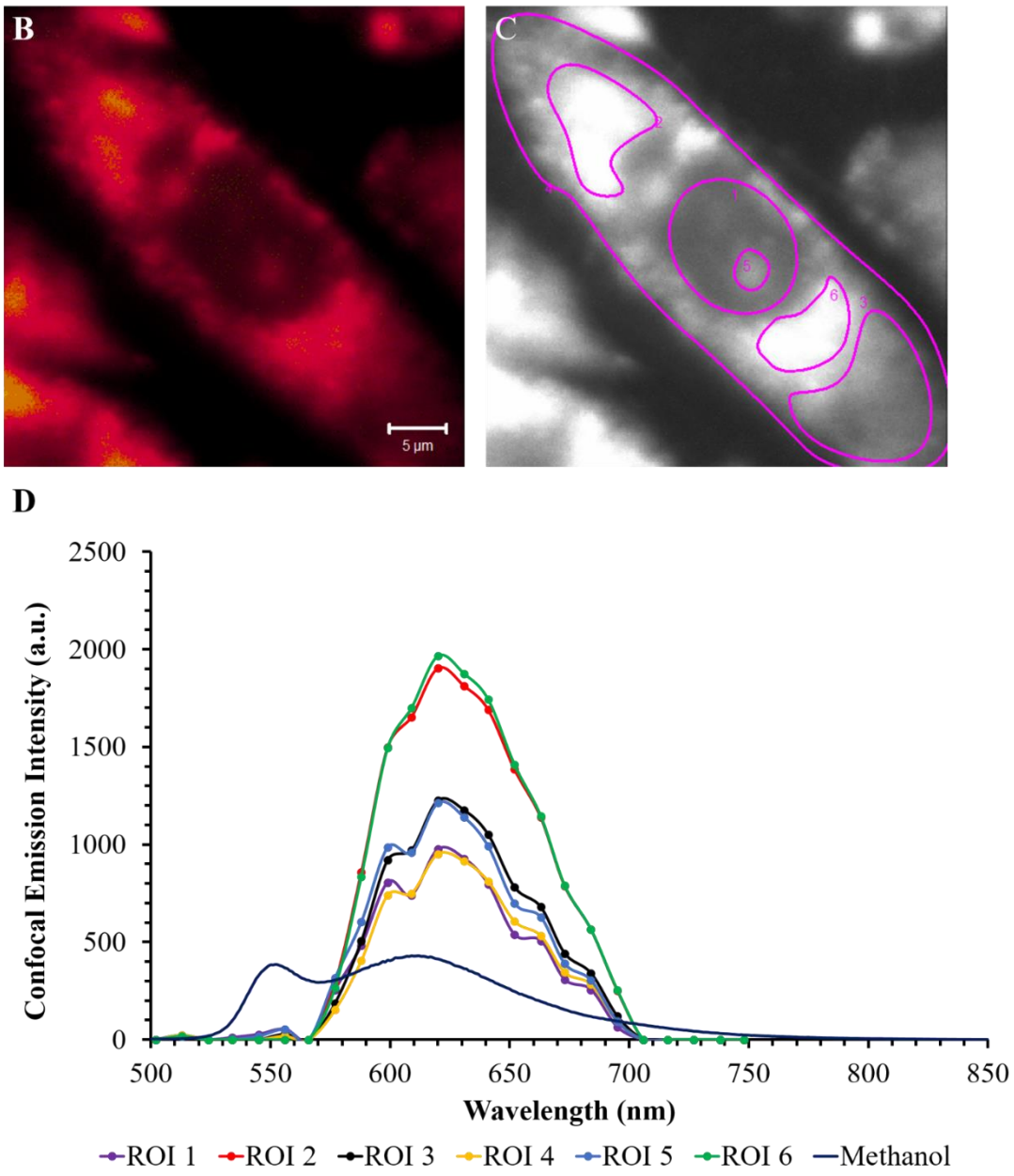


**Figure 4.11** Excitation scan of [Ru(bpy)$_2$-phen-BODIPY-Br$_2$] (15 µM) in a live CHO cell. Complex was excited at 458 nm and the emission was collected between 497-754 nm at 10 nm slit widths (A). Selected regions of interest (ROIs) were analysed further (B and C) to give an emission plot profile (D), demonstrating no BODIPY emission in the cell compared to when in aerated methanol solution. (Scale bars = 5 µM)

A range of regions of interest (ROIs) were selected and analysed to obtain a profile of the emission wavelengths present in different parts of the cell (Figure 4.11 B and C) and compared to the complex in aerated methanol. As demonstrated by the plot in Figure 4.11 D, there appears to be very little contribution from the BODIPY emission and certainly what is evident is below the calibration range used for referenced $O_2$ detection,.

The BODIPY emission intensity is greatest in ROI 5, which represents the nucleolus. It was measured to be 52.4 a.u. However, the ruthenium intensity is several orders of magnitude greater at 1212.6 a.u. Therefore, although there is some contribution measured from the emission of the BODIPY, it is too small compared to the ruthenium intensity to give accurate ratiometric measurements from within the cell compared to when in aerated methanol solution. We can therefore conclude that the complex is primarily in aqueous locations within the cell, and has not appeared to bind to a target.

On the other hand, the ruthenium emission intensity fluctuates depending on where it is located in the cell, which can be attributed to variations oxygen concentrations and the cellular environment. ROI 2 and 6 show the highest emission intensities, while the nuclear region represented by ROI 1 displays a lower emission intensity. ROI 3 represents the general cytoplasmic region of the cell, where ROI 4 represents the cell as a whole. Each ROI exhibits emission from the ruthenium moiety, but not from the BODIPY.

### 4.5.2 [Ru(bpy)$_2$-phen-BODIPY-Br$_2$] localisation studies

To determine more precisely where [Ru(bpy)$_2$-phen-BODIPY-Br$_2$] localised within the cells, CHO cells were prepared with 15 μM for 24 h. Before imaging, DiOC6, a commercial probe that emits in the green at 501 nm and stains the endoplasmic reticulum (ER), was introduced to the cells. 5 μM was added to the cell media and this was left at room temperature for 20 minutes. The solution was removed and the cells were washed with supplemented PBS. Figure 4.12 shows representative images of CHO cells incubated with [Ru(bpy)$_2$-phen-BODIPY-Br$_2$] represented in red (A), DiOC6 represented in green (B), and their co-localisation represented in yellow (C).

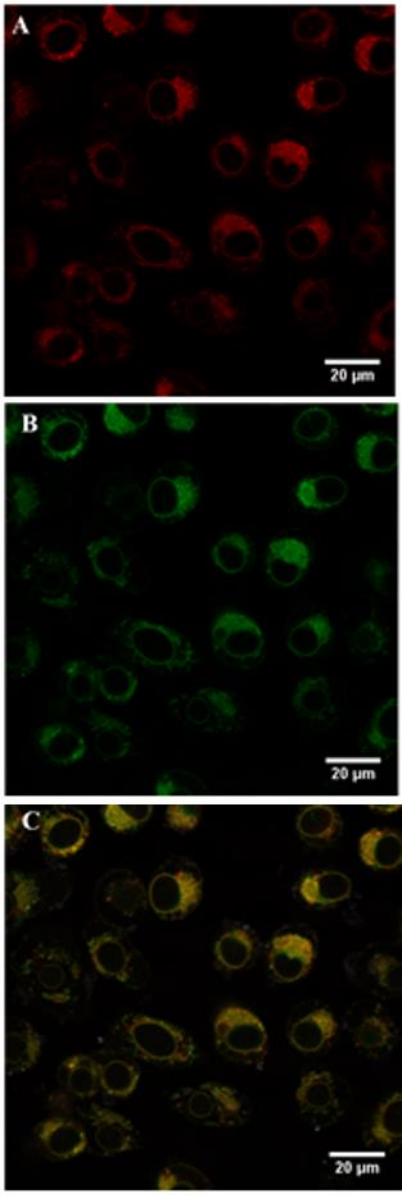


**Figure 4.12** Co-localisation of [Ru(bpy)$_2$-phen-BODIPY-Br$_2$] (15 µM) in live CHO cells. The cells were incubated with the complex for 24 h, and DiOC6 was added for 30 minutes at 5 µM. [Ru(bpy)$_2$-phen-BODIPY-Br$_2$] represented in red (A), DiOC6 in green (B), and their co-localisation in yellow (C). [Ru(bpy)$_2$-phen-BODIPY-Br$_2$] was excited at 458 nm and emission was collected using a long pass 560 nm filter. DiOC6 was excited at 488 nm and the emission was collected using a band pass 505 – 530 nm filter.

To confirm that the complexes are coincident in the ER, an X-Y cross section of a single CHO cell and its corresponding fluorescent intensity profile was examined (Figure 4.13). This confirms that they are both localising within the same cellular components. However, [Ru(bpy)$_2$-phen-BODIPY-Br$_2$] appears to be non-selective in entering the ER alone as it can be seen throughout the cytoplasm as described earlier was shown to enter

the nucleoli too. Localisation in the ER suggests that uptake was by endocytosis. However further studies would have to be carried out to establish more conclusively the mechanism of uptake.

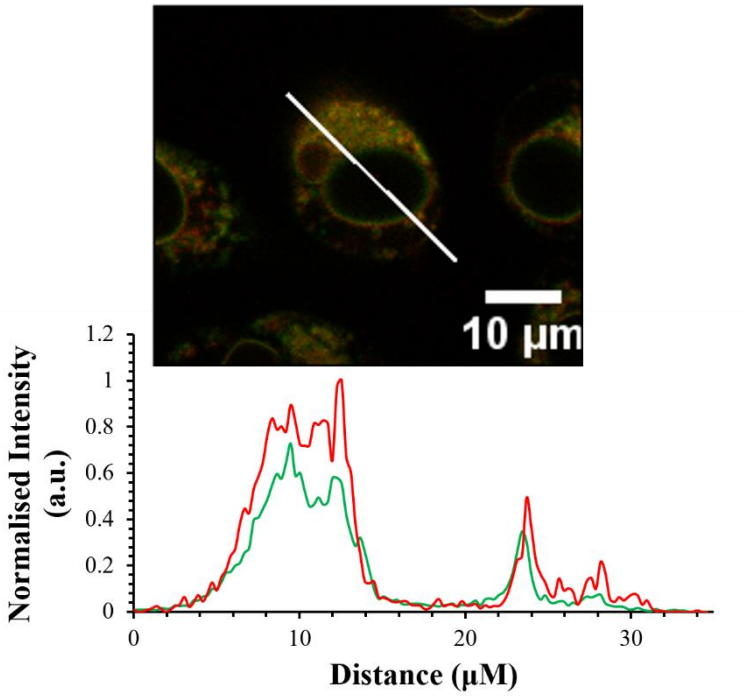


**Figure 4.13** Co-localisation of [Ru(bpy)$_2$-phen-BODIPY-Br$_2$] (15 µM, 24 h) and DiOC6 (5 µM, 30 minutes) in a live CHO cell, and its corresponding X-Y plot of intensity demonstrating their co-localisation. [Ru(bpy)$_2$-phen-BODIPY-Br$_2$] was excited at 458 nm and emission was collected using a long pass 560 nm filter. DiOC6 was excited at 488 nm and the emission was collected using a band pass 505 – 530 nm filter.

## 4.6 Cytotoxicity

The effect of [Ru(bpy)$_2$-phen-BODIPY-Br$_2$] on cell viability was determined in CHO cells, using the Alamar Blue (Resazurin) cytotoxicity assay, as explained in *section 4.2.7.* Figure 4.14 outlines the results of the assay. Remarkably, the probe proved to be highly toxic towards the cells

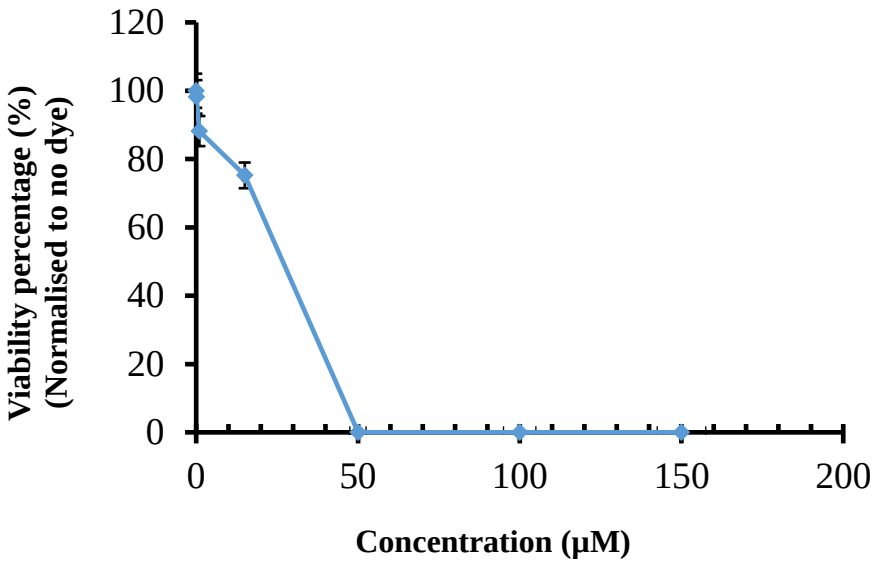


**Figure 4.14** Cell viability studies of [Ru(bpy)$_2$-phen-BODIPY-Br$_2$] in live CHO cells. Cells were incubated with the complex in the absence of light for 24 h. Viability was measured using the Resazurin (Alamar Blue) assay. (n = 3)

At concentrations greater than 50 µM, there were no viable cells remaining (0 ± 1.5 %) after 24 hours. At the working concentration of 15 µM, 75.2 ± 3.8 % of CHO cells were viable after 24 h exposure, while still giving excellent luminescence for cell imaging as demonstrated previously in *section 4.5*. For comparison with another $O_2$ sensing compound, *Papkovsky et al* reported on a platinum-porphyrin, PtCP-NH2, for intracellular oxygen sensing. Following 24 h exposure to the complex, 95 – 100 % of cells remained viable. Although this complex demonstrated virtually no toxic effects on the cells, it was not readily taken up without the use of reagents.[32] The superior uptake of [Ru(bpy)$_2$-phen-BODIPY-Br$_2$] may be related to the relative lipophilicity of this compound, but this lipophilicity may also contribute to cytotoxicity.

It has been demonstrated previously that the ligand combination 'bpy-phen' is highly toxic towards cells at high concentrations.[6] From the work carried out in Chapters 2 and 3, it is likely to be the phenanthroline ligand causing the high toxic affect towards the cells, as a 'bpy-pic' ligand combination described in Chapter 2 was not toxic towards CHO cells, and BODIPY complexes alone have demonstrated low toxic effects towards cells.[33,34] *Chen et al* reported on a bis-methoxyphenyl-BODIPY fluorescent probe for nitric oxide detection. The complex was introduced to macrophages for 24 h, and the viability was assessed using the MTT assay. The MTT assay is a reduction reaction by

viable cells. Following 24 h incubation with the probe, 55 % of cells remained viable at 100 μM of the complex.[35] *Zhang et al* reported on similar results where by 84 % of cells remained viable at concentrations as high as 100 μM of their BODIPY fluorescent probe.[33]

The [Ru(bpy)$_2$-phen-BODIPY-Br$_2$] dual emitting dyad discussed in the first half of this chapter has shown excellent, reversible oxygen sensing abilities in non-aqueous solution. It was readily taken up by CHO cells with a bright emission from the ruthenium moiety at low concentrations of 15 μM from inside the cytoplasm and nucleoli. Although the BODIPY emission switches off in aqueous solutions, this ratiometric oxygen probe would be ideal in imaging non-aqueous environments such as the lipid bilayer.

## 4.7 Core-shell RuBODIPY particles

In *section 4.4* it was demonstrated that the combination of oxygen-sensitive ruthenium and oxygen-insensitive BODIPY in non-aqueous solution displayed excellent oxygen sensing capabilities. However, the switching off of the BODIPY moiety means that it can only be used as an oxygen sensor in non-aqueous solutions, or as a reference for imaging non-aqueous environments, although alone it may ultimately prove to be a useful membrane sensor. To avoid this switching off effect and any cross talk between the oxygen sensor ruthenium and the BODIPY reference, the complexes were introduced in to a novel core shell structure. It was anticipated that this would allow oxygen sensing in aqueous environments. Furthermore, it was hoped that by introducing the complexes to a particle that the toxicity would be reduced. Figure 4.15 describes the structure of the poly(styrene) core shell particle. The poly(styrene) core particles were synthesised via a mini-emulsion polymerization by Dr. Jaco Jacobs. [36] The BODIPY moiety, which is composed of oxygen insensitive phen-Ar-BODIPY-Br$_2$ complex, is encased in the poly(styrene) core to protect it from an aqueous environment and avoid switching off. It also limits any cross talk with the oxygen sensitive probe. It is hoped that the encasement in a poly(styrene) core will avoid any leaching from the particle, which will give accurate ratiometric measurements in vivo. The oxygen sensor, composed of [Ru-(bpy)$_2$-phen-Ar-COOH], is conjugated to a poly(L-lysine) shell surface. 1-ethyl-3-[3-(dimethylamino)propyl]carbodiimide hydrochloride (EDC)/N-hydroxysuccinimide (NHS) coupling chemistry was employed to attach [Ru-(bpy)$_2$-phen-Ar-COOH] to the lysine residues. The carboxylate (COO-) of [Ru-(bpy)$_2$-phen-

Ar-COOH], with NHS, in the presence of EDC, forms a semi-stable NHS active ester which can then bind with the $NH_2$ of the lysine residue. This forms an amide crosslink between the [Ru-$(bpy)_2$-phen-Ar-COOH] and the lysine residues. Selective deprotection of the triblock ensured that the Ru (II) complex would be situated at the outer periphery of the formed NPs. This allows the ruthenium to access environmental oxygen for optimum sensing, and avoids contact with the reference probe in the core.

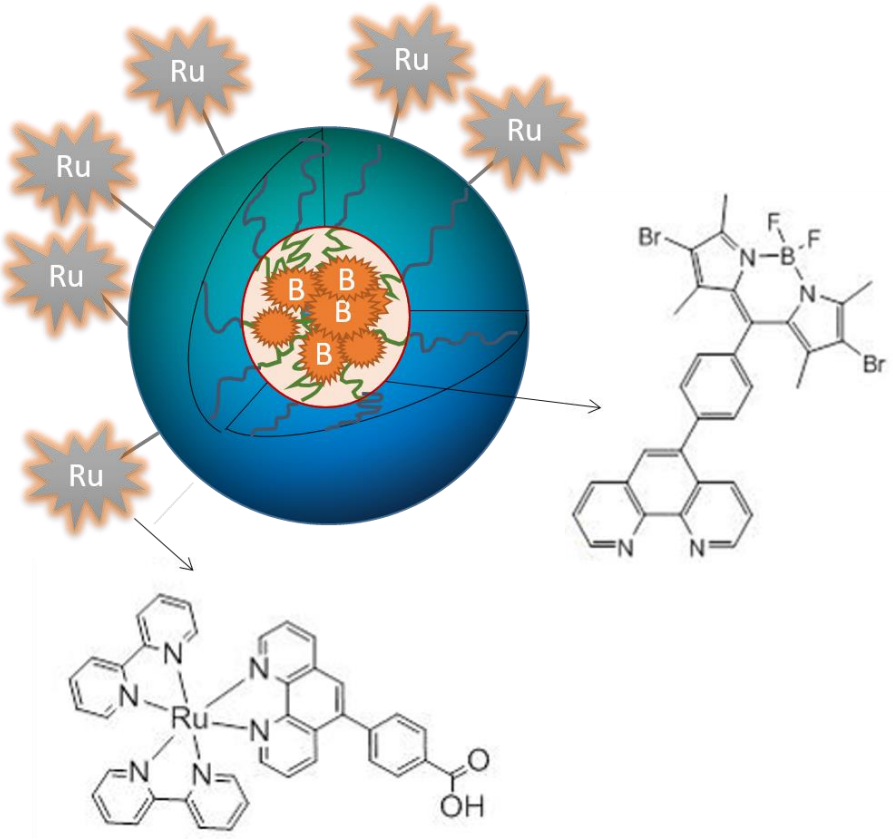


**Figure 4.15** Poly(styrene) core shell nano particle. The BODIPY moiety is encased in the poly(styrene) core while the ruthenium component [Ru-$(bpy)_2$-phen-Ar-COOH] is bound to the poly(l-lysine) shell. The particle was measured to be 105 nm in diameter with a PDI = 0.08.

The advantages of choosing poly(styrene) for the core shell particles is that they have been shown to be stable over long periods and their relatively low porosity reduces leaching of materials contained within which is idea for *in vivo* cell imaging.[37] Poly(styrene) (PS) has good optical properties, and is permeable to oxygen, allowing the probe access to dissolved oxygen.[38] Polymerization of styrene allows for the size of the particle to be adjusted during the process, and the resulting particles can be readily

prepared with high monodispersity. Surface charge and chemical modifications can be altered to improve live cell uptake.[36,39] In this case, the surface of the PS core was functionalised with a poly(L-lysine) shell. Lysine is a positively charged amino acid. As discussed in Chapter 1, peptide sequences that are rich in lysine residues are more likely to cross the cell membrane which is negatively charged. The size of the nanoparticles, the PS core and poly(L-lysine) shell, were measured by DLS to be an average of 105 nm.[40] It is hoped that the hydrophobic nature of PS nanoparticles will prevent any dye leakage. The polydispersity index (PDI) of the particles measures the width of the polymer molecular weight distribution.[41] The ideal PDI value is less than 0.2. In this case, the RuBODIPY particles have a PDI = 0.08.[40]

The core-shell particles were made by Dr. Jaco Jacobs from the group of Dr. Andreas Heise, DCU. The dyes were prepared by Christopher Burke (DCU). The encasement of the BODIPY and ruthenium conjugation, and the loading concentrations were varied in a number of particle batches in order to give optimum ratio emission intensities. The photophysical properties of these batches were then investigated, and the batch that gave optimum response to oxygen was then studied in depth described herein.

## 4.8 Photophysical properties of the RuBODIPY particles

The relative loading of the two chromophores was varied between batches by varying the amount of BODIPY in the core in order to achieve optimum relative luminescent emission intensities of probe and reference the particles chromophores. As BODIPY complexes have a much higher quantum yield than ruthenium complexes, it was important to ensure that the BODIPY emission intensity did not swamp the ruthenium emission intensity signals upon dual excitation. The emission profiles and response to oxygen concentration were analysed in PBS solution (pH 7.4) at 18 °C. Figure 4.16 shows the emission profile of the particles made in Batch 1. The PS core encapsulating the BODIPY in Batch 1 was synthesised using emulsion polymerization. The ratio of intensity between the emissions of two complexes was good. The ruthenium exhibited high emission intensity without being swamped by the high BODIPY emission signal. However, upon de-aeration with nitrogen for 15 minutes, the magnitude of the changes in intensities was comparatively small, and the BODIPY signal was found to decrease with decreasing oxygen concentration. This is not ideal as the BODPIY is the reference probe and should exhibit no emission intensity changes in response to changing oxygen.

The emission recovery over a range of oxygen concentrations shown in Figure 4.16 found that the BODIPY stabilised and the ruthenium decreased with increasing oxygen concentration. However, the oxygen stability and calibration of this batch was non-linear, so these particles could not be used as a reliable oxygen sensing probe. The reason for this behaviour is believed to be poor stability of the polystyrene core due to high porosity which lead to leaching of the reference over time.

**A**

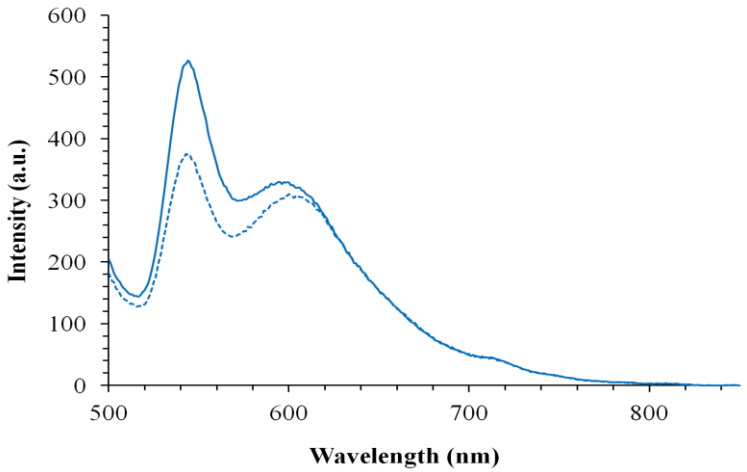


**B**

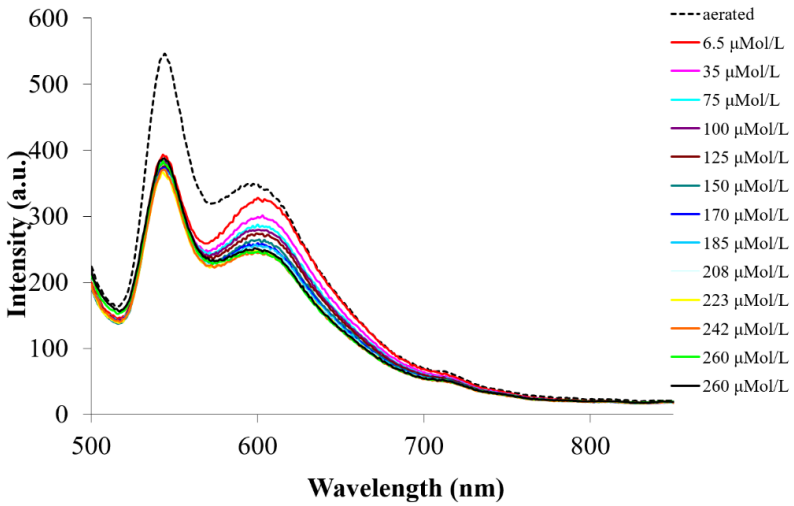


**Figure 4.16** Emission spectra of Batch 1 when excited at 458 nm in aerated (—) and deaerated (---) aqueous PBS solution. $O_2$ concentration dependent calibration data from RuBODIPY particles in PBS solution (pH 7.4). Particles were purged for with $N_2$ for 10 minutes and allowed to slowly re-aerate, measuring the emission spectra at varying oxygen concentrations (µmol/L) using a PreSens Oxygen probe.

Figure A4.2 in the appendix illustrates the oxygen dependence profile of Batch 1 after 1 month of storage in the dark. Again, the oxygen profile was found to be non-linear, and the emission profile of the BODIPY reference did not remain constant, further evidence that reference leaching had occurred over time.

The structure of the particle composition was re-examined. In this case, mini-emulsion polymerization was used, which meant that the BODIPY was encapsulated chemically during synthesis rather than diffused into the PS sphere which was the case for Batch 1. The core of the particle was reinforced for Batch 2 and 3 by increasing cross-linking in the core to ensuring no leaching of the BODIPY could occur improving stability of the dye loaded particle.[40] Figure 4.17 shows the emission profile of Batch 2 when aerated and de-aerated. In the case of Batch 2, the ruthenium emission intensity did not increase by much upon de-aeration, suggesting that this would not give a wide range of oxygen sensing. Comparing this to Batch 3 in Figure 4.18, the ruthenium gave a bigger range for oxygen sensing, while the BODIPY emission remained sufficiently intense to allow for ratiometric referencing without surpassing the ruthenium. The profiles of each batch varies due to variation in the ratio of the concentration of the chromophores in the particles. Oxygen dependence studies indicated that the ruthenium–BODIPY ratio in Batch 3 gave optimum referenced oxygen sensitivity while the BODIPY signal was highly stable. The final ratio of BODIPY: Ru of Batch 3 is 1:125. Batch 3, known as RuBODIPY particles from here on, were examined in more detail as a ratiometric oxygen sensing probe as this composition and synthetic method gave the best stability and most reproducible analytical response.

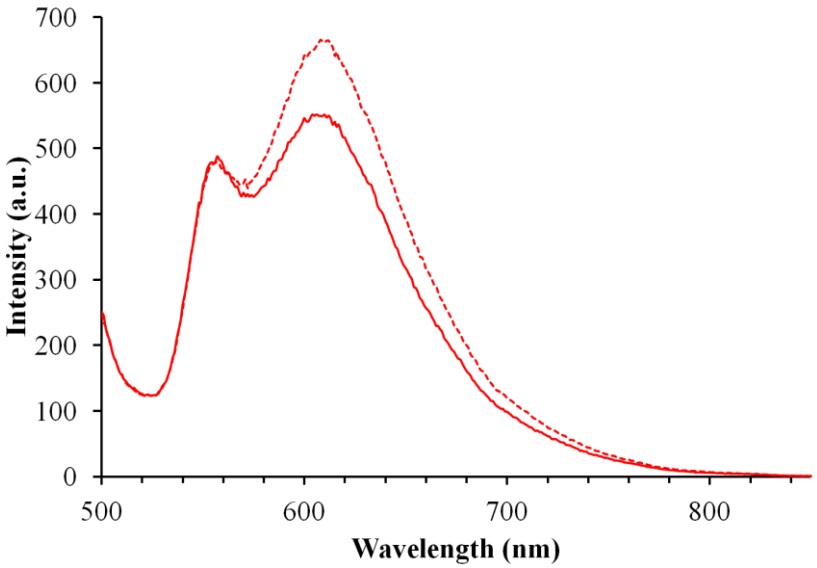


**Figure 4.17** Luminescent emission spectra of Batch 2 when excited at 458 nm in aerated (—) and deaerated (---) aqueous PBS solution. Slit width = 10 nm.

As demonstrated previously in *section 4.4*, the BODIPY reference of the dyad [Ru(bpy)$_2$-phen-BODIPY-Br$_2$] switched off in aqueous solutions and aqueous environments of the cell. Although this can be used in imaging and sensing in lipid membranes and non-aqueous environments, now as part of a core-shell it can ultimately be used as a reference probe in aqueous solutions as isolating the BODPY in the PS core prevents its quenching in aqueous media.

Figure 4.18 illustrates the excitation and emission profiles of the RuBODIPY particles in PBS solution. The excitation spectra showed two peaks at 460 nm and 510 nm, corresponding to the ruthenium and BODIPY moieties respectively. When excited at 458 nm in aqueous media the particles exhibited dual emission with peak maxima observed at 547 nm attributed to the BODIPY and at 601 nm for the ruthenium centred emission.

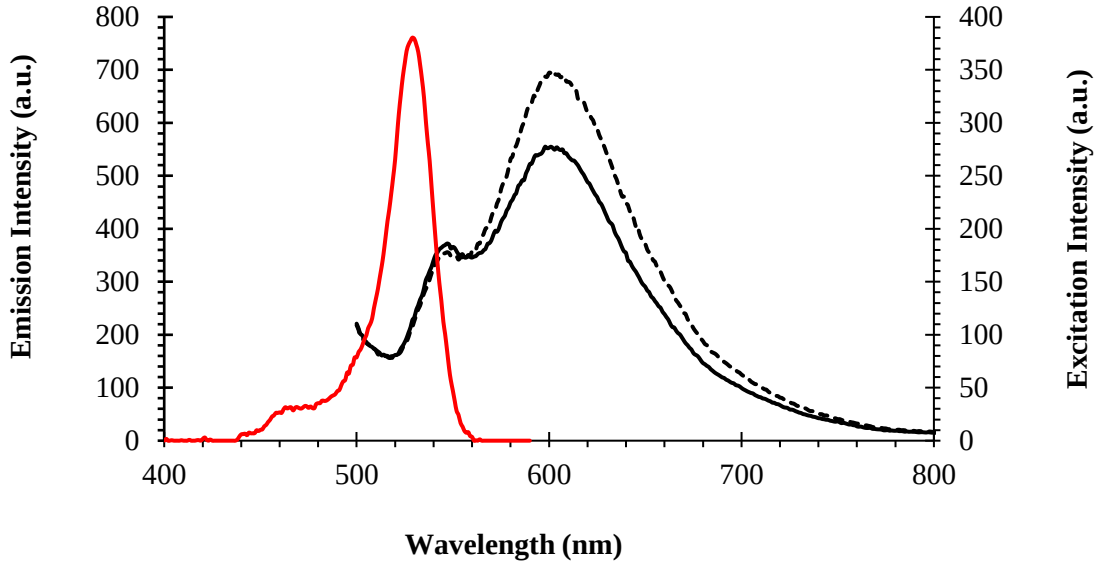


**Figure 4.18** Excitation (—) and emission spectra of RuBODIPY particles when aerated (—) and deaerated (---) in PBS solution. Solution was degassed with nitrogen for 10 minutes. The complex was excited at 458 nm at a slit width of 10 nm.

The lifetimes of the two components were measured using TCSPC in PBS solution (pH 7.4). The data was fit to a bi-exponential decay. The BODIPY lifetime was recorded to be 4.45 ± 0.3 ns (12.8 % amplitude) and the ruthenium lifetime was found to be 836 ± 12 ns (87.2 % amplitude). The lifetime for the ruthenium component is relatively higher than previously reported for the [Ru-(bpy)$_2$-phen-Ar-COOH] complex (698 ± 6 ns). This is likely attributed to the influence of the poly(L-lysine) coating to which the ruthenium is conjugated on the shell of the particle. Increased emission intensity has been reported before for ruthenium complexes on conjugation to protein for example on BSA binding reported by *Vos et al.*[42]

## 4.9 Oxygen calibration of RuBODIPY particles

The luminescent emission and lifetime of the RuBODIPY particles as a function of oxygen concentration were investigated to assess their suitability for oxygen sensing. Under air saturated conditions, the oxygen concentration in PBS solution was found to be 268 µmol/L using a PreSens fibre optic oxygen probe. The luminescent emission intensity and lifetime of the probe was measured under these conditions and the sample was de-aerated under nitrogen for 10 minutes. The emission intensity at 8 µmol/L of oxygen was recorded, and the ruthenium emission was observed to increase while the

BODIPY remained unaffected. The lifetime of the ruthenium component increased from 836 ns to 1.064 µs. The solution was gradually re-aerated over time and the spectra were measured over a range of oxygen concentrations. Figure 4.19 A illustrates the gradual decrease in emission with increasing oxygen concentration of the ruthenium centre with concomitant stability of the BODIPY emission signal. Figure 4.19 B demonstrates the luminescent lifetime plots of BODIPY and ruthenium as a function of oxygen concentration. Importantly, the BODIPY lifetime did not change while the ruthenium lifetime decreased with increasing oxygen concentration. Both the emission and lifetimes show a linear correlation with oxygen, and the response was reversible. The luminescent emission intensity in (A) returned to its original value when the oxygen concentration returned to saturation again, showing that the response to oxygen is reversible and this observation also confirms the stability of the BODOPY/PS core to leaching or other degradation.

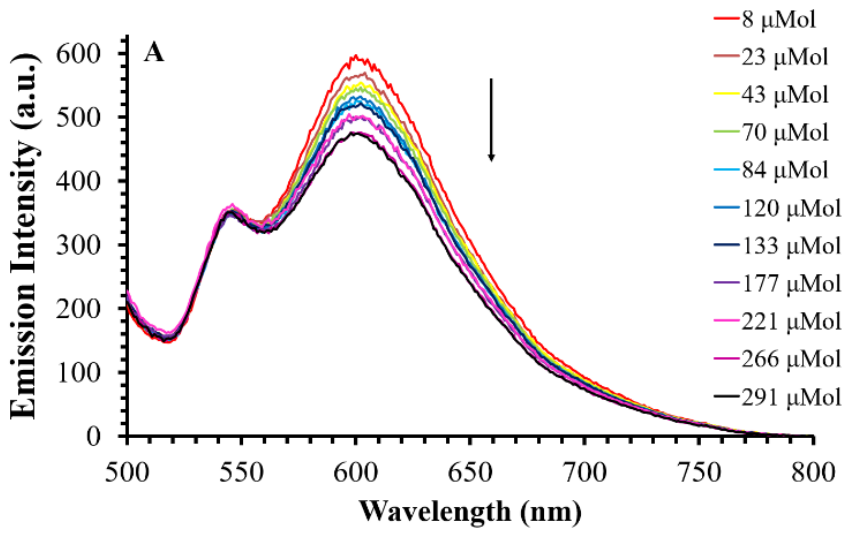

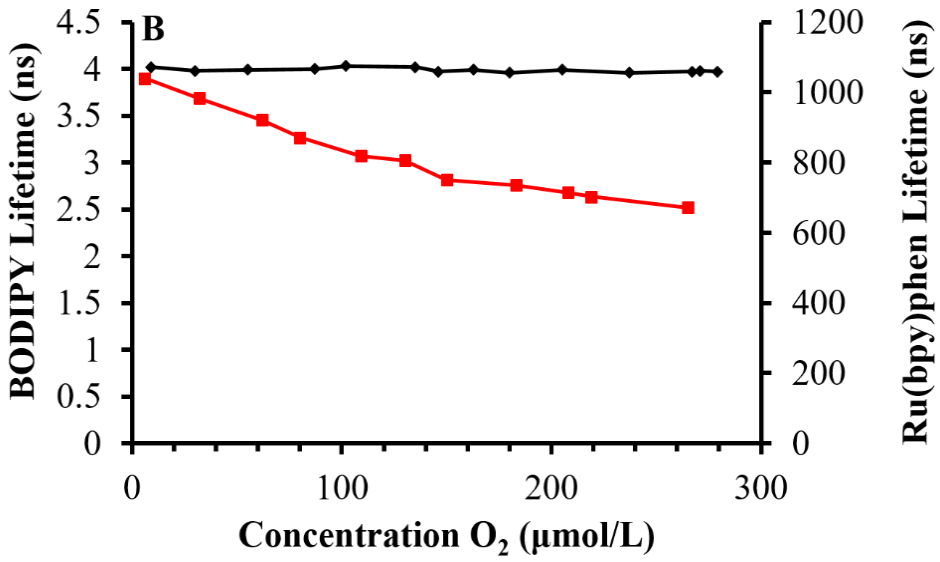


**Figure 4.19** RuBODIPY response to oxygen concentrations. Oxygen dependent emission spectra in PBS at 18 °C (A), n = 2. The ruthenium emission centre decreases with increasing [$O_2$] whilst the BODIPY is unaffected. Oxygen dependent lifetime plot under the same conditions (B) illustrates that the ruthenium lifetime (—) decreased with increasing [$O_2$] and the BODIPY lifetime (—) remained constant (n = 2).

The luminescent emission and lifetime data were plotted according to the Stern-Volmer equation (equation 4.1) to measure oxygen as a function of lifetime (τ) and emission intensity (I) described in Figure 4.20.

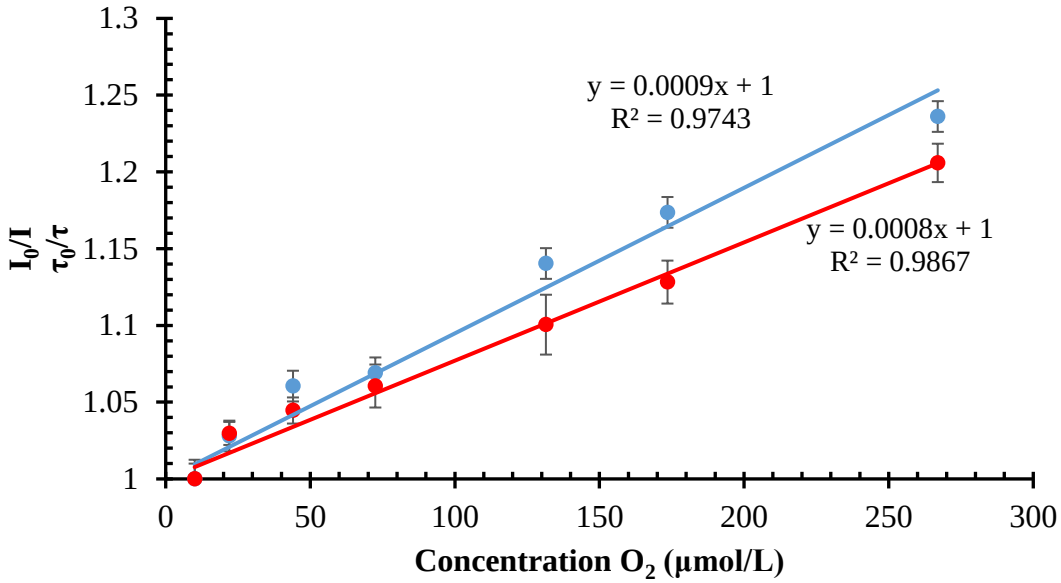


**Figure 4.20** Stern-Volmer plot of ruthenium luminescent lifetime as a function of [$O_2$] (•). Stern-Volmer plot of emission intensity as a function of [$O_2$] (•). Oxygen studies were carried out in PBS buffer solution (pH 7.4) at 18 °C. (n=2).

The Stern-Volmer constant, $K_{SV}$, can be obtained from the slope of each plot, and determines the limit of detection of a sensor. In this case, $K_{SV}$ for A and B are the same, suggesting that the oxygen response is due to dynamic quenching, which is typical for that of oxygen and transition metal complexes such as ruthenium.[15] The rate of quenching, $k_q$ can be determined from equation 4.2 in *section 4.4*. The rate of quenching by the RuBODIPY particles was found to be 7.52 x $10^8$ $M^{-1}$ $s^{-1}$. This is an order of magnitude less than the quenching rate of the [$Ru(bpy)_2$-phen-BODIPY-$Br_2$] dyad which was measured to be 9.45 x $10^9$ $M^{-1}$ $s^{-1}$ in methanol solution. This quenching rate is unexpectedly slow. Interestingly, even though the ruthenium component of the particles has a longer luminescent lifetime in aerated PBS (836 ns) compared to the molecular dyad (587 ns), the particles have a slower quenching constant. *Hartmann et al* observed similar results of their two Ru(II) complexes dissolved in polystyrene.[43] This may be due to environmental protection of the ruthenium oxygen sensor by the poly-L-lysine. Longer lifetimes of ruthenium on protein conjugation has been ascribed previously to this affect.[44] Overall, this result indicates that the RuBODIPY particles are less responsive to changing oxygen than the molecular system.

The sensitivity of both ratiometric sensors can be expressed by the overall quenching response to dissolved oxygen.[45] This can be done by obtaining a ratio of the luminescent emission intensity of the ruthenium sensor to that of the BODIPY reference. This is defined by equation 4.3:

$$Q = \frac{R(N_2) - R(O_2)}{R(N_2)} \times 100 \quad \text{…… } \mathbf{Equation\ 4.3}$$

Where Q is the quenching response, $R(N_2)$ is the ratio of the emission intensity of probe and reference in de-aerated solution, and $R(O_2)$ is the ratio of the emission intensity of the probe and reference in aerated solution. The ratiometric molecular system [$Ru(bpy)_2$-phen-BODIPY-$Br_2$] was measured to have a quenching response of 55 % in methanol solution. However, the RuBODIPY particles have a much lower quenching response of 18 %. *Philbert et al* employed Equation 4.3 to obtain a quenching response for their PEBBLEs composed of silicate, which incorporated an oxygen-sensitive Pt(II) porphyrin dye. They measured the quenching response of their polymer oxygen sensor to be 97 %.[46] They obtained a linear Stern-Volmer plot, with a $K_{SV}$ value of 0.787, indicating a faster quenching rate than our RuBODIPY particles, discussed in this section. In an earlier report, *Philbert* et al obtained a quenching response of a $[Ru(dpp)_3]^{2+}$ complex in a silica nanoparticle to be 80 %,[45] while *MacCraith et* al reported on the quenching response of the Ru(II) complex $[Ru(Ph_2phen_3]^{2+}$ in a silica film to be 30 %.[47] In order to obtain an improved quenching response from the RuBODIPY particles, the concentration of the ruthenium component on the particle surface should be increased to increase its sensitivity. As shown by the Stern Volmer plots in Figure 4.19, the particles display an excellent linear response to oxygen, however have a relatively slow quenching rate constant (kq). Therefore, increasing the concentration of ruthenium residues on the particle surface may improve the quenching rate while retaining the same linear response to oxygen.

Importantly, the luminescent intensity from the BODIPY remains constant while the emission from the ruthenium centre decreases linearly with increasing $O_2$ concentration. Figure 4.21 illustrates the ratiometric plot of the intensities, where $I_{601}/I_{547}$ ratios were

plot as a function of oxygen concentration. The data was plotted by determining the ratio between the emission intensity values at 547 nm for BODIPY and 601 nm for ruthenium, as a function of oxygen concentration.

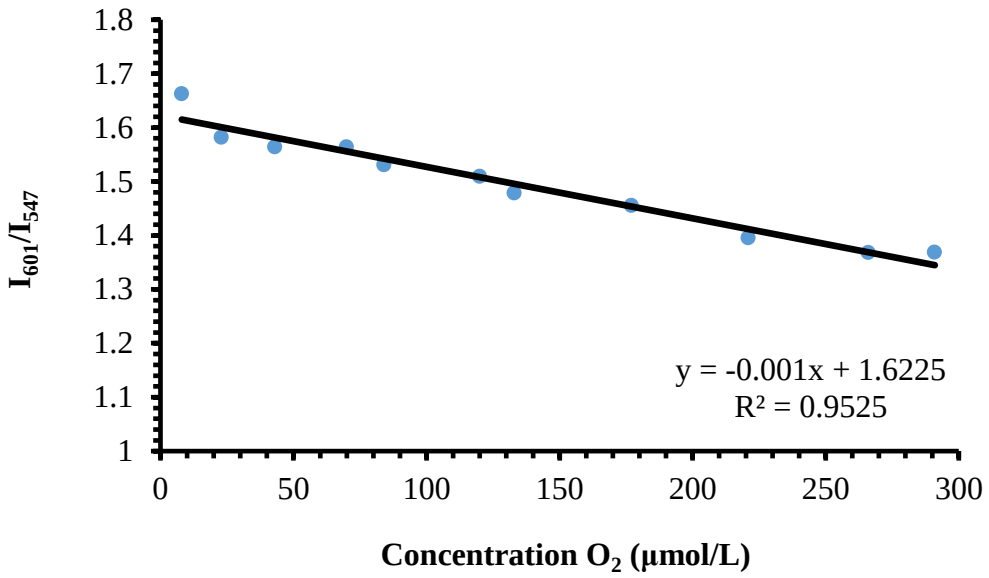


**Figure 4.21** Ratiometric plot intensities of the BODIPY centre at 547 nm and ruthenium centred emission at 601 nm as a function of [$O_2$] in PBS (18 °C). The complex was excited at 458 nm, sit width 10 nm.

## 4.10 Introduction of RuBODIPY particles to cells

The ability of the RuBODIPY particles to cross the cell membrane was assessed in CHO cells. The CHO cells were incubated with the particles in cell culture media over a range of particle concentrations of percentage of particles in the cell media (%). Confocal microscopy showed that after incubating over a range of times up to 24 h at 37 °C, the particles did not enter the cells. Surprisingly, treating the cells with 0.1 % Triton X for permeabilisation before the addition of particles did not enhance uptake, shown in Figure 4.22. After exposure to Triton X, the solution was removed and 1:10 dilution of RuBODIPY particles were added to the cells for 4 h at 37 °C, 5 % $CO_2$ in the absence of light. The particles were removed and the cells were imaged. No emission from either the ruthenium or BODIPY channel was observed.

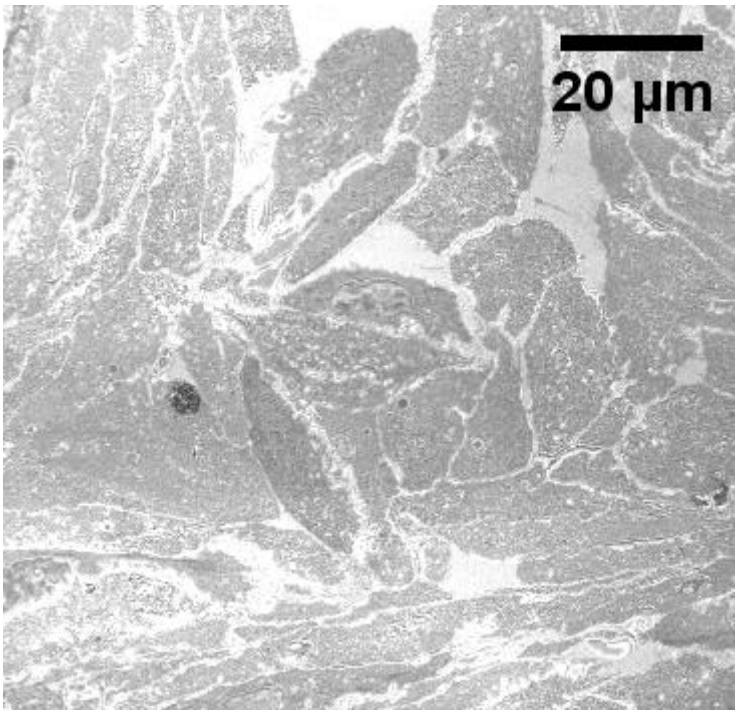


**Figure 4.22** Confocal image of CHO cells. The cells were pre-treated with 0.1 % Triton X, then incubated with 1:10 RuBODIPY particles for 4 h at 37 °C in the absence of light. The particles were excited using a 458 nm laser, and the emission was collected using a 505-550 nm band pass filter for the BODIPY emission, and a 560 nm long pass filter for the ruthenium emission. The image represents an overlay of reflectance with the ruthenium and BODIPY emission channels.

Cetyltrimethylammonium bromide (CTAB), a cationic detergent was chosen to enhance uptake. CTAB has be shown previously to be effective in coating nanoparticles and promoting their uptake.[48,49] RuBODIPY particles were sonicated overnight in 150 µM CTAB solution. The emission spectra of the particles in the 150 µM CTAB solution is presented in Figure 4.23. This demonstrates that the dual emission of the particles is unaffected by using this reagent for cell uptake.

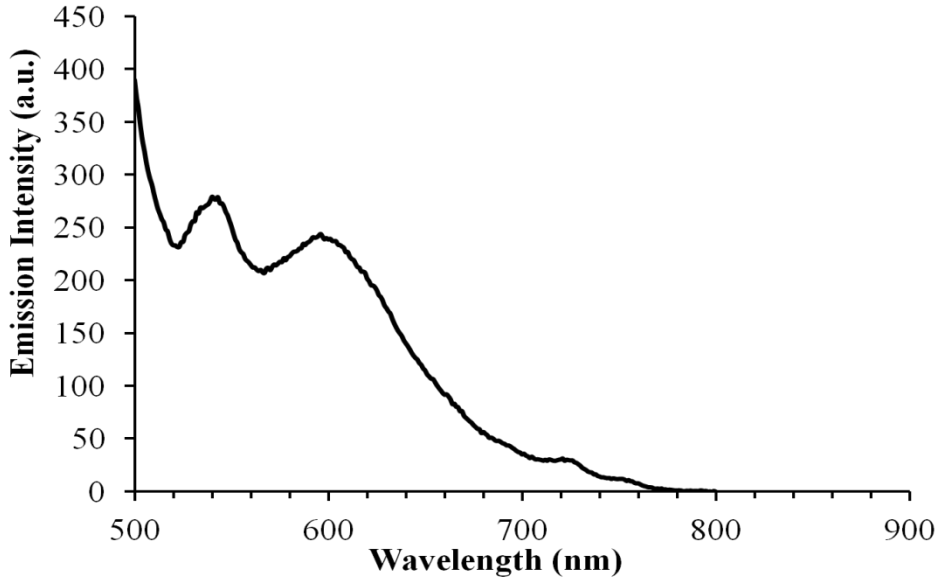


**Figure 4.23** Emission spectra of the RuBODIPY particles after sonicating with 150 μM CTAB/PBS solution overnight at 18 °C. The particles were excited at 458 nm, at a slit width of 10 nm.

The CTAB-treated RuBODIPY particles were added to CHO cells at varying concentrations to investigate their uptake. The overall total volume of CTAB added to the cells with the particles was 2 % 150 μM. Interestingly, it was found that at concentrations greater than a 1:10 dilution of particles: media added to the cells that the cells would not take up the particles. Thus, a 1:20 dilution of RuBODIPY particles in Leibovitz media were added to CHO cells. Figure 4.24 shows the live uptake of the particles using confocal microscopy.

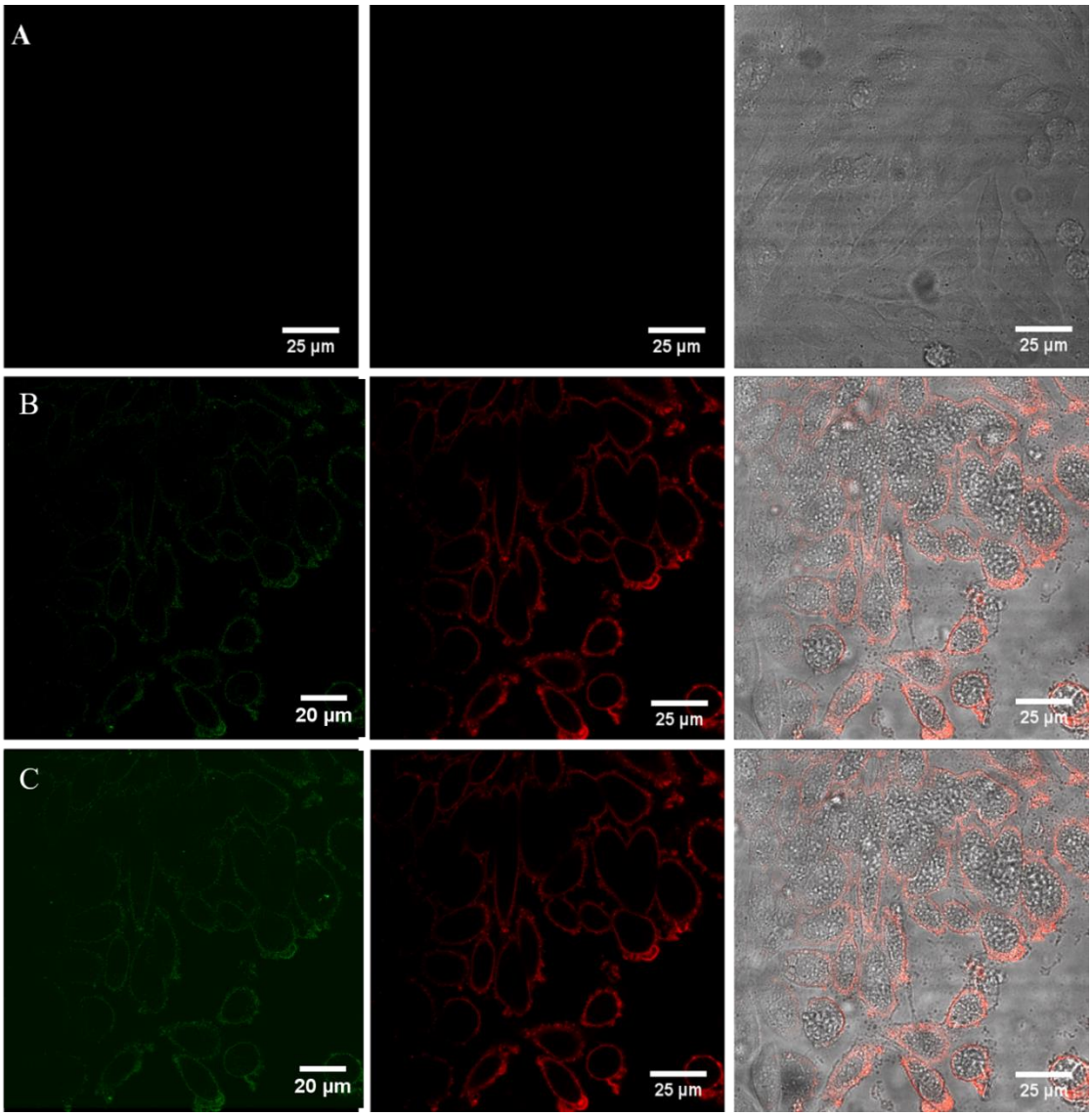


**Figure 4.24** Live uptake confocal imaging of RuBODIPY particles in CHO cells. Particles were pre-treated with 150 µM CTAB prior to exposure to CHO cell membrane. Cells were imaged before addition of particles (A). 1:20 dilution of particles/media were added to live CHO cells and imaged after 2 minutes of addition (B). Particles were removed after 5 minutes NP exposure and washed and re-introduced to fresh supplemented PBS (C). The particles were excited using a 458 nm white light laser, and the emission was collected using a long pass 520 nm filter.

The cells were imaged for emission at the probe wavelength before any particles were added (A), then after 2 minutes of addition (B). After 5 minutes of exposure to the particles, the solution was removed and the cells were washed with supplemented PBS. Figure 4.24 C shows that the particles bound to the cell membrane, and remained bound after washing. The cells were incubated for a further 2, 4, and 6 h in the absence of light at 37 °C with 5 % $CO_2$ in fresh Lebovitz media. Figure 4.25 examines the uptake,

focusing closely on a small area of cells, representative of the uptake across the sample. After 2 h, the particles appear to have crossed the cell membrane, and are distributed throughout the cytoplasm. After 4 h, the particles appear to have become more localised in specific regions, that appear to be the lysosomes and possibly endoplasmic reticulum (ER) region, but they remain nuclear excluding. After a further 6 h, the particles remain in what appears to be the lysosomes.

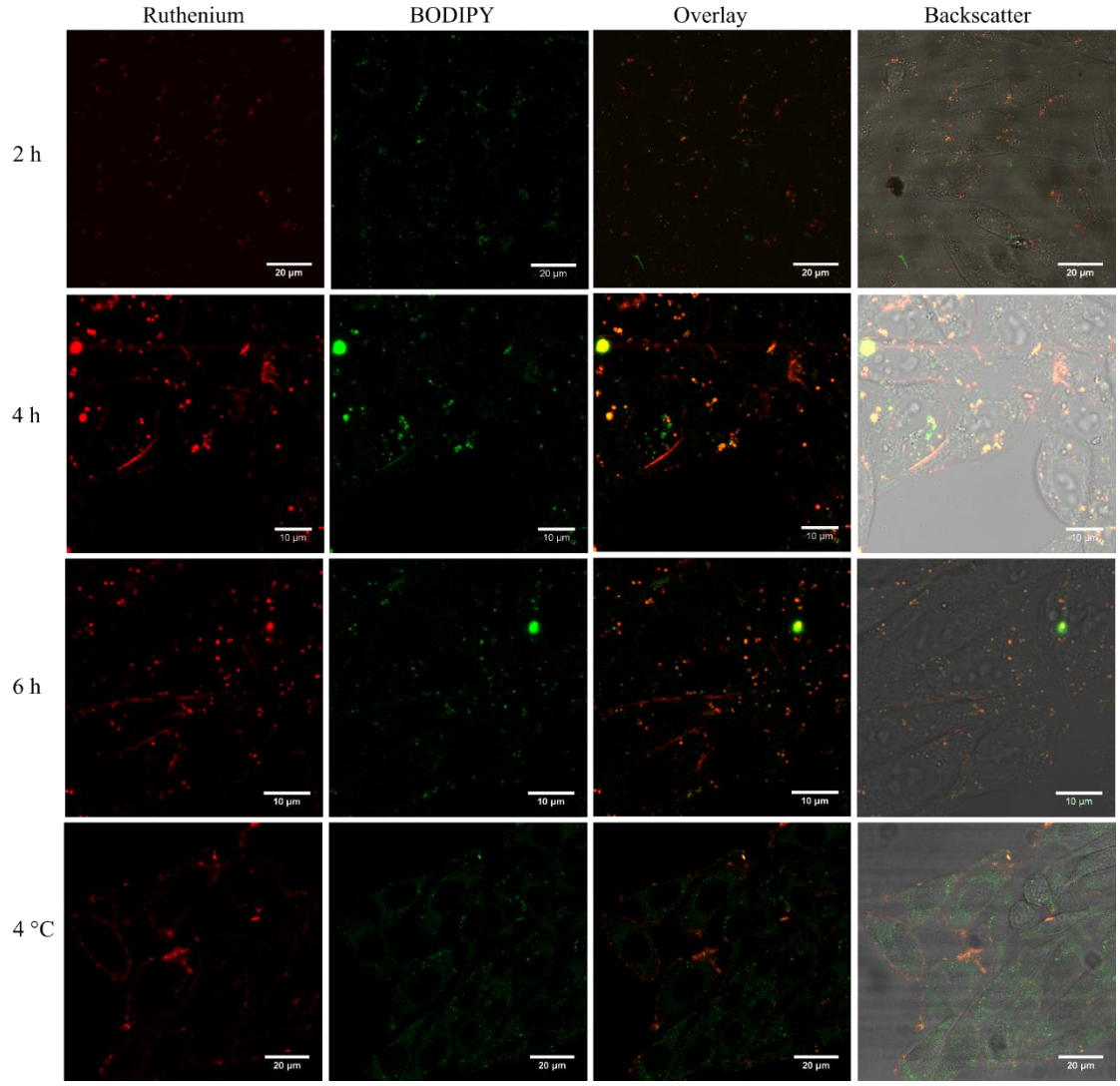


**Figure 4.25** Confocal images of live CHO cells incubated with a 1:20 dilution of RuBODIPY particles in Lebovitz media for 2 h, 4 h, and 6 h at 37 °C. CHO cells were incubated for 4 h at 4 °C to assess mode of uptake. The particles were excited using a 458 nm white light laser. The BODIPY emission was collected between 505 and 550 nm, and the ruthenium emission was collected using a long pass 605 nm filter.

From the images shown in Figure 4.25, the particles appear to localise throughout the cytoplasm and do not enter the nucleus. The luminescence from the ruthenium and the BODDIPY can be seen separately in the cells, the red channel for ruthenium (A), and the green channel for BODIPY (B). The overlap of the two channels, shown in (C), is represented in yellow. The varying intensities of the two chromophores can be seen in the images, in some cases more ruthenium than BODIPY emission coming through, and vice versa, possibly attributed to the varying oxygen concentrations throughout the cells as the particles migrate through the cytoplasm. To assess the mechanism of uptake, HeLa cells were incubated with the CTAB treated particles at 4 °C for 4 h. Figure 4.25 shows that the uptake was the same as when incubated at 37 °C. The particles were able to cross the membrane. However, their localisation appears to be more disperse in the cytoplasm as well as in the lysosomal region. This indicates that uptake occurs through passive diffusion, i.e. an energy independent mechanism. Nanoparticles of up to 200 nm in size have been reported to cross the cell membrane via endocytosis, which is an energy dependent mechanism.[50,51] In this case, passive diffusion is likely be as a result of using CTAB, permeablising the cell membrane and promoting uptake. CTAB is a cationic surfactant that dissociates aggregates and unfolds proteins. It interacts with the hydrophilic and lipophilic groups in the cell membrane, solubilising the membrane proteins. The more widely used detergent is Triton X-100, a non-ionic surfactant which is a mild detergent as it does not break protein-protein interactions, but as described this was ineffective in promoting particle uptake. CTAB is considered more toxic towards cells, however as demonstrated in this chapter, at small concentrations of 100 μM, it is not toxic towards cells while slightly permeabilizing the membrane enough for the particles to enter. Interestingly, at 37 °C, ruthenium emission intensity is 17 ± 0.1 a.u. while at 4 °C it has an emission intensity of 2.75 ± 0.3 a.u. while the BODIPY emission remains. This suggests that the particles have entered the cells and are present at both temperatures, but the ruthenium emission has decreased at 4 °C. Figure 4.26 shows a chart summarising the emission intensities of ruthenium at two regions of interest during live uptake of the particles, when incubated at 37 °C, and at 4 °C, and the corresponding images from where the ROIs were chosen.

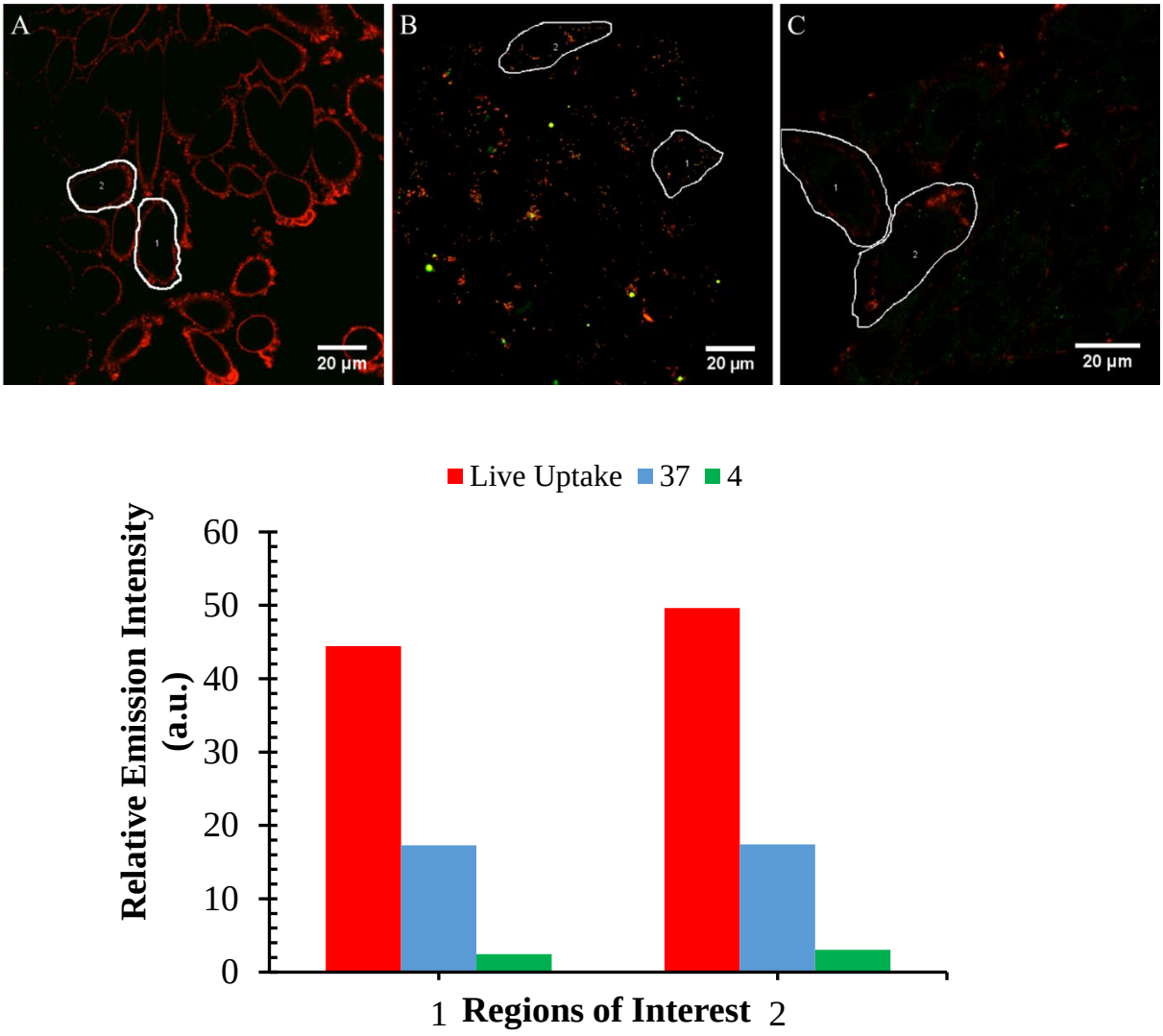


**Figure 4.26** Relative emission intensities of ruthenium during live uptake with CHO cells at (A) 37 °C (■). (B) CHO cells were incubated with 1:20 dilution RuBODIPY particles for 4 h at 37 °C (■), and (C) at 4 °C (■). The emission intensities from two regions of interest were measured using Image J.

At low temperatures, cellular metabolism slows down.[52] Therefore, oxygen consumption slows down as the cells cannot use it to produce ATP. This build-up of oxygen could be quenching the ruthenium emission, while the BODIPY remains the same as it is unaffected by oxygen concentration. As discussed in *section 4.11*, the particles have a luminescent lifetime of 603 ± 10 ns when bound to the exterior of the cell membrane which decreases to 435 ns when they localise in the lysosomes. This reduction in lifetime further suggests quenching by oxygen. Furthermore, cell membrane stability has been shown occur in an attempt to maintain homeostasis within the cell when exposed to low temperatures.[53] This could also be contributing to the build-up of

oxygen. The increased membrane stability may also confirm permeabilization caused by the CTAB as the particles are still able to cross the membrane.

Figure 4.27 shows a Z-stack of a CHO cell that was incubated with 1:20 dilution of RuBODIPY nanoparticles for 4 h. The Z-stack scanned through a single CHO cell, which was representative of the sample, starting at the top of the cell (A) to the bottom of the cell (D). B and C represent two of the slices from the scan at the centre of the cell, confirming that the particles are in fact inside the cell and not just localised at the plasma membrane, highlighted in white.

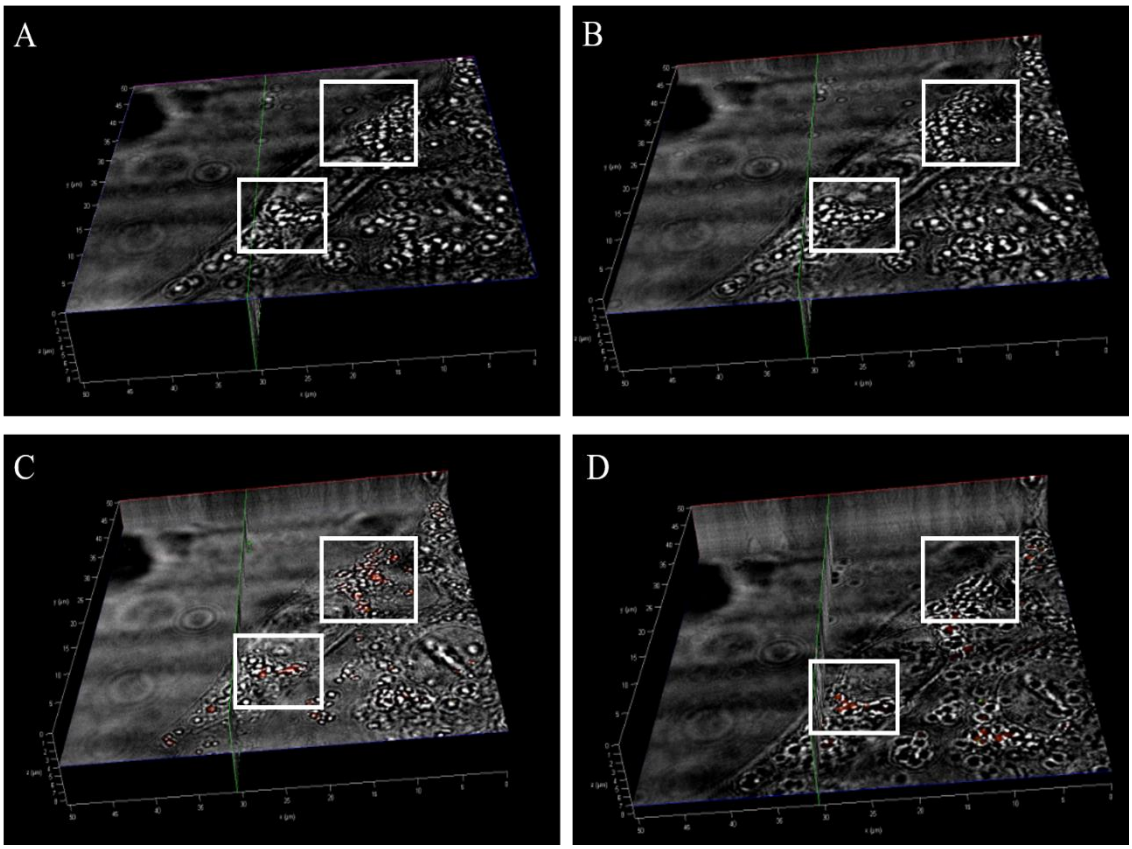


**Figure 4.27** Confocal Z-stack scan of a single CHO cell that was incubated with 1:20 dilution of RuBODIPY particles for 4 h at 37 °C in the absence of light. The sample was excited at 458 nm. The BODIPY emission was collected between 505 and 550 nm, and the ruthenium emission was collected using a long pass 605 nm filter. Each z-stack was collected every 0.2 μm. A-D represent slices at different depths through the cell.

Localisation of the particles was investigated to determine where in the cytoplasm they reside. Here, HeLa cells were incubated with the RuBODIPY particles for 4 h as described in *section 4.2.5.2.* Before imaging, cells were co-stained with commercial dyes; ER Tracker Blue (1 μM), LysoTracker Green (100 nM), and MitoTracker Deep

Red (500 nM). The commercial dyes were added to the cells for 30 minutes in PBS. Figure 4.28 shows the co-localisation of the particles with the commercial probes.

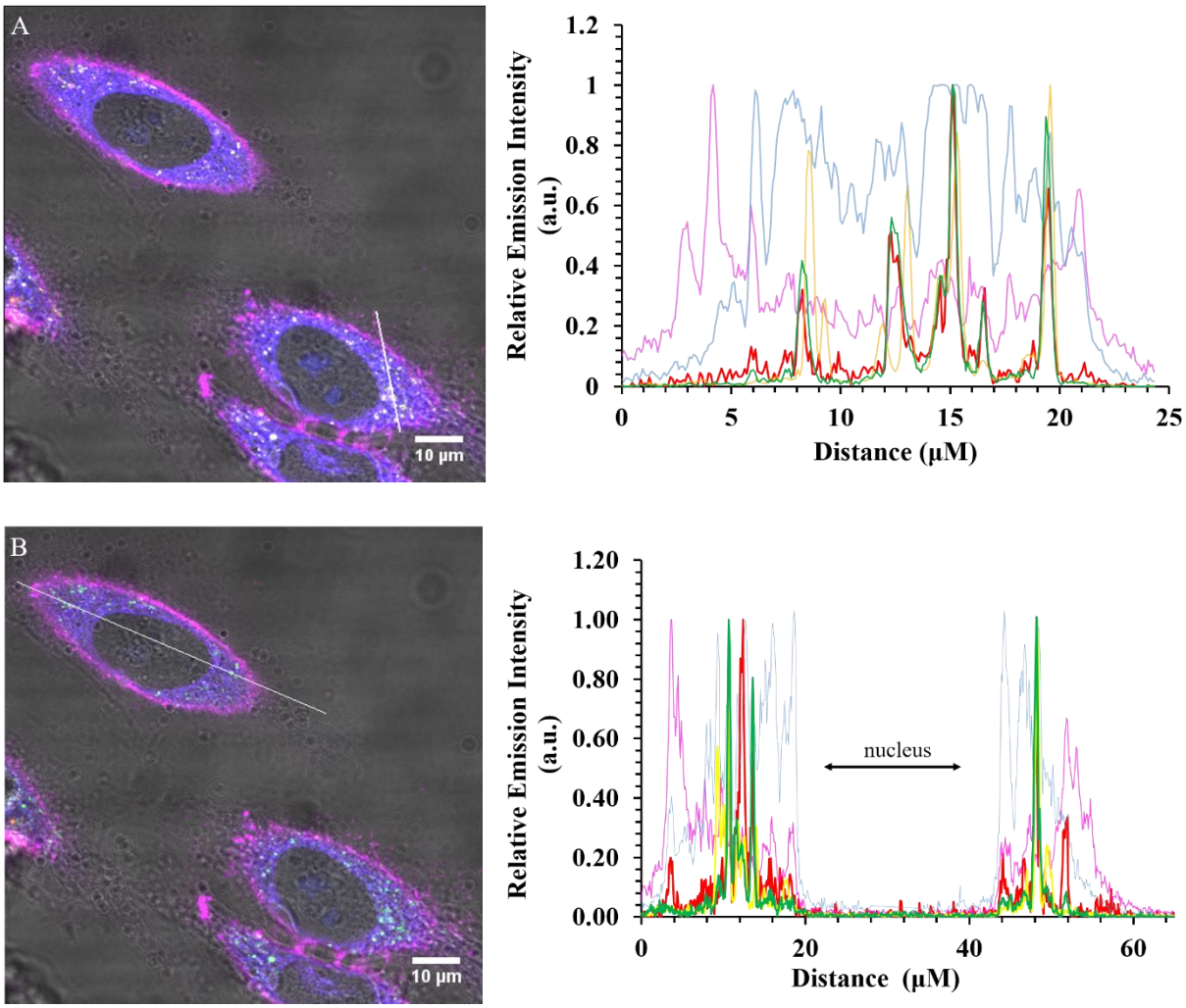


**Figure 4.28** Co-localisation of RuBODIPY particles in HeLa cells across the cytoplasm (A) and the nucleus (B). The corresponding profile demonstrates the ruthenium (—) and BODIPY (—) channels of the particles, MitoTracker Deep Red (500 nM) represented in pink (—), ER Tracker Blue (1 µM) in blue (—) and LysoTracker Green (100 nM) in yellow (—).

The ruthenium channel is represented in red, BODIPY in green, ER Tracker in blue, LysoTracker in yellow and MitoTracker Deep Red in pink. The X-Y line profile through the cytoplasm of a single HeLa cell and its corresponding plot profile describe the localisation of the complexes (A). The X-Y line profile through the nucleus of a second

HeLa cell and its corresponding plot profile confirm that the particles are nuclear excluding (B). In both cases, there is no evidence for co-localisation of particles with the mitochondria or endoplasmic reticulum (ER) localising probes. However, the plot profile of RuBODIPY particles with LystoTracker appeared to be coincident in all but one region in both A and B. Figure 4.29 examines a single HeLa cell incubated with the RuBODIPY particles and LysoTracker only.

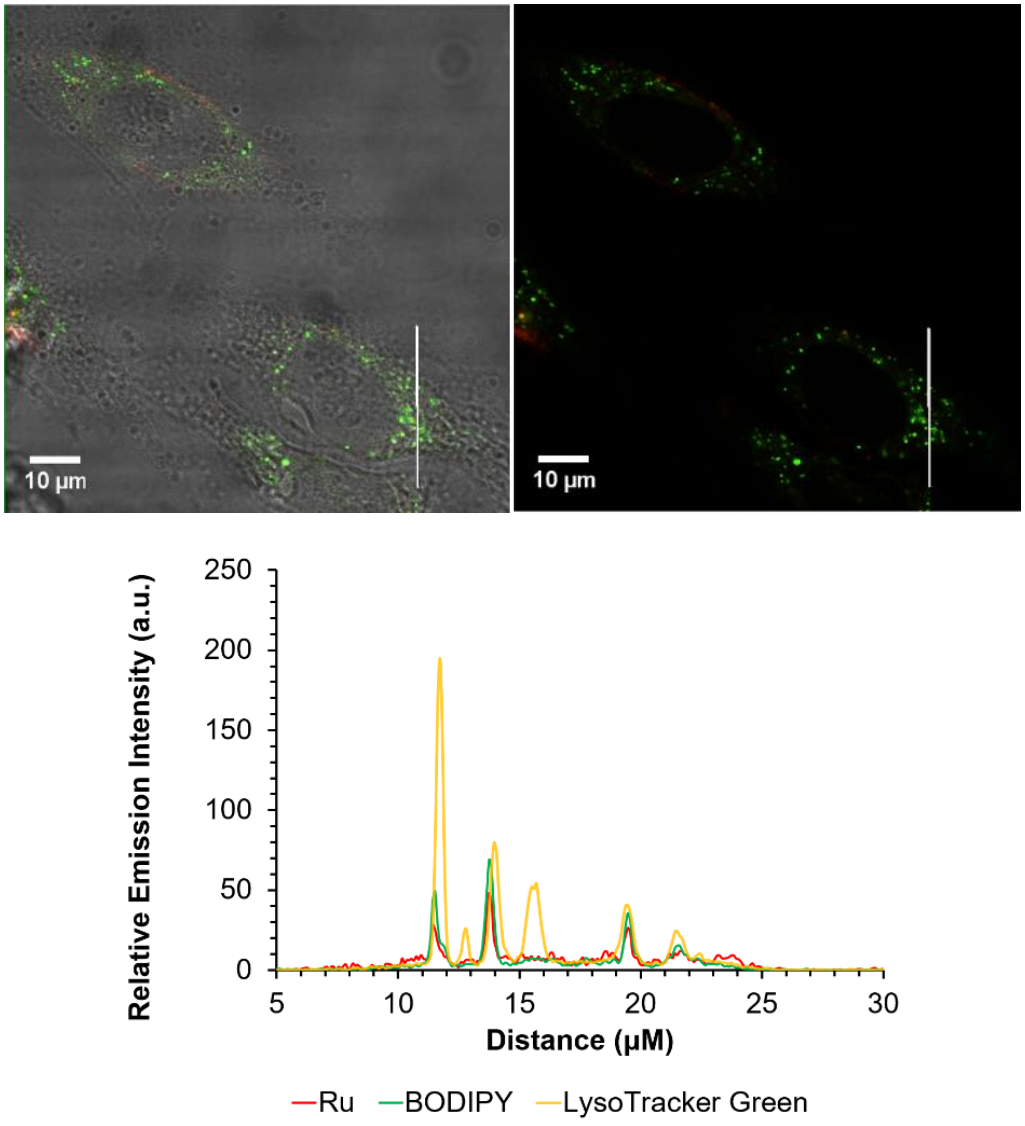


**Figure 4.29** Co-localisation studies of RuBODIPY particles in HeLa cells. Particle uptake was carried out as described previously, and cells were incubated with commercial probe LysoTracker Green (100 nM) for 20 minutes. Confocal image shows co-localisation of the particles with LysoTracker, with cross section of the cell and the corresponding distribution plot demonstrating their co-localisation.

Lysosomes are found throughout in the cytoplasm, which coincides with the confocal images. The corresponding plot profile further demonstrates that the RuBODIPY particles are localised within the lysosomes. In a similar report, *Pieber et al* demonstrated lysosomal localisation after 4 h incubation with their polystyrene nanoparticles that were also 100 nm in diameter.[54] Localisation in the lysosomes could be as a result of the mode of uptake. The role of lysosomes in the cell is to engulf/digest food and foreign objects upon entering the cell. As suggested previously, the particles cross the membrane via passive diffusion as result of permeabilisation. With no recognition peptides on the particle surface, the lysosomes may engulf the particles as a method of removing them from the cell. Similarly, cationic polystyrene particles at 100 nm in diameter have also been found to localise in the lysosomes.[55] *Xia et al* also reported on cationic polystyrene particles localising in the lysosomes, however, their particles were slightly smaller at 60 nm in diameter.[56] Entry of nanoparticles into other organelles has been shown to be size dependent. For example, *Chang et al* showed that their gold nanoparticles 13 nm in diameter localised in the endoplasmic reticulum and Golgi apparatus of murine melanoma cells.[57] In another report, *Salnikov et al* showed that gold particles that were 6 nm could not enter the mitochondria, however, 3 nm particles could enter the mitochondria intermembrane space of ventricular myocytes (cardiac cells),[58] while gold particles of 39 nm in diameter have been reported to cross the nuclear pore complex (NPC).[59] Taking all of these reports into account, it appears, for the most part, that particles with a diameter greater than 40 nm localise in the lysosomes. This suggests that particle size is just as important as surface modification for targeting cell organelles. As lysosomes have an acidic environment with a pH ranging from 3-4, [60] the emission spectra of the particles was assessed at pH 3.8. RuBODIPY particles in PBS solution (pH 7.4) were acidified using 1 mM HCl until a pH of 3.8 was obtained. Figure 4.30 compares the emission spectra at pH 7.4, and pH 3.8 which demonstrated no changes. The particles were left in the acidic solution for 1 week and the emission spectra were recorded. A slight decrease in the emission was observed, but the dual emission and ratio of the chromophores were unaffected. Likewise, the luminescent lifetime of the particles is also unaffected as the ruthenium component has a lifetime of 838 ns, and the BODIPY component is 4.45 ns, within experimental error. This result indicates that these RuBODIPY core shell particles are suitable for use as a ratiometric probe in the acidic environment of the lysosomes.

**A**

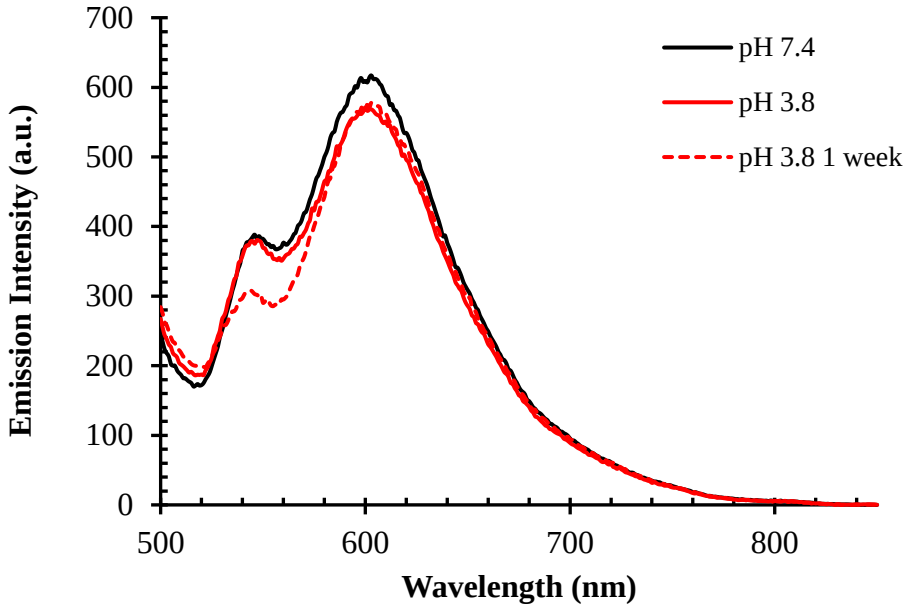


**B**

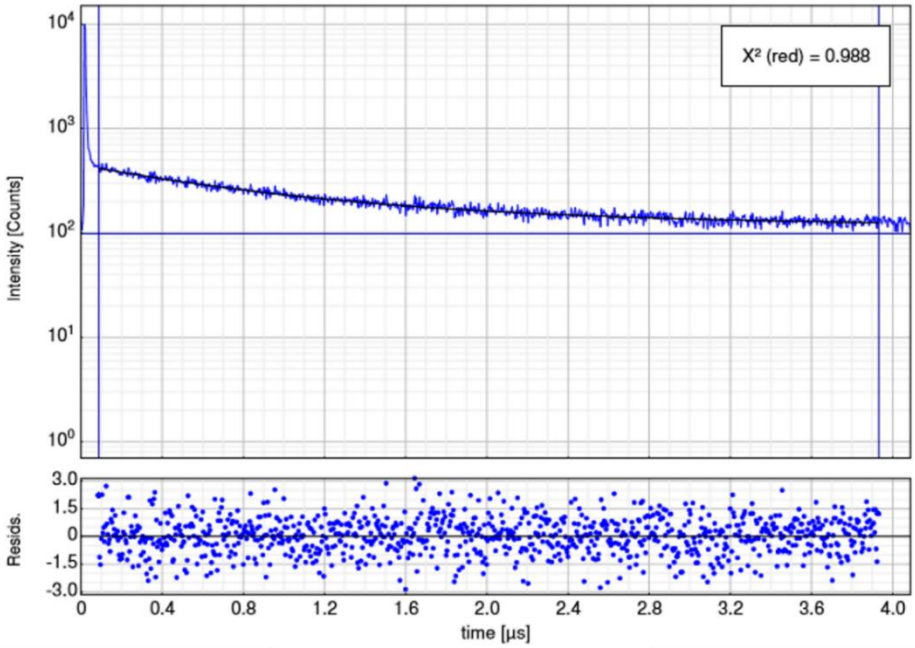


| Parameter | Value |
|---|---|
| $A_1$ [Cnts] | 260.26 |
| $\tau_1$ [µs] | 0.8382 |
| $A_2$ [Cnts] | 56.53 |
| $\tau_2$ [µs] | 4.450 |
| Bkgr. $_{Dec}$ [Cnts] | 98.94 |

**Figure 4.30** Luminescent emission spectra of RuBODIPY particles in PBS whose pH was adjusted to pH 3.8 using 0.1 M HCl, and compared to pH 7.4 (A). The particles were left at pH 3.8 for 1 week to assess any changes to the emission. They were excited at 458 nm, slit width 10 nm. The luminescent lifetime was measured using TCSPC by exciting at 405 nm (B).

## 4.11 Phosphorescent Lifetime Imaging Microscopy (PLIM) of RuBODIPY particles in cells

To assess the lifetime of the chromophores within the cells, PLIM was used. Firstly, the luminescent lifetimes of an aqueous drop containing the particles was measured in PBS/CTAB solution. 50 μL of the particle/PBS/CTAB solution was deposited on a glass slide, and the PLIM image was acquired for 20 minutes to ensure high counts were achieved. The ruthenium and BODIPY components were imaged separately. The long-lived component of the lifetime attributed to the ruthenium was determined as 628 ± 18 ns.

Next, CHO cells were prepared as described in *section 4.2.6.2*. Each short and long components were measured separately. Figure 4.31 A demonstrates the false-colour PLIM image of the lifetime distributions of the RuBODIPY particles when bound to the membrane of a single CHO cell after 5 minutes exposure. The highlighted area of the cell was examined closely to determine the luminescent lifetimes of the two components. When bound to the exterior of the cell membrane surface, the particles exhibit a lifetime of 4.49 ± 0.018 ns for the BODIPY component (B), and 603 ± 10 ns for the ruthenium component (C). The lifetime of the ruthenium decreased slightly when bound to the cell membrane, suggesting quenching is occurring. This would be expected at the cell membrane as it contains a higher concentration of dissolved oxygen due to the lipophilicity of the membrane compared to solution. [61]

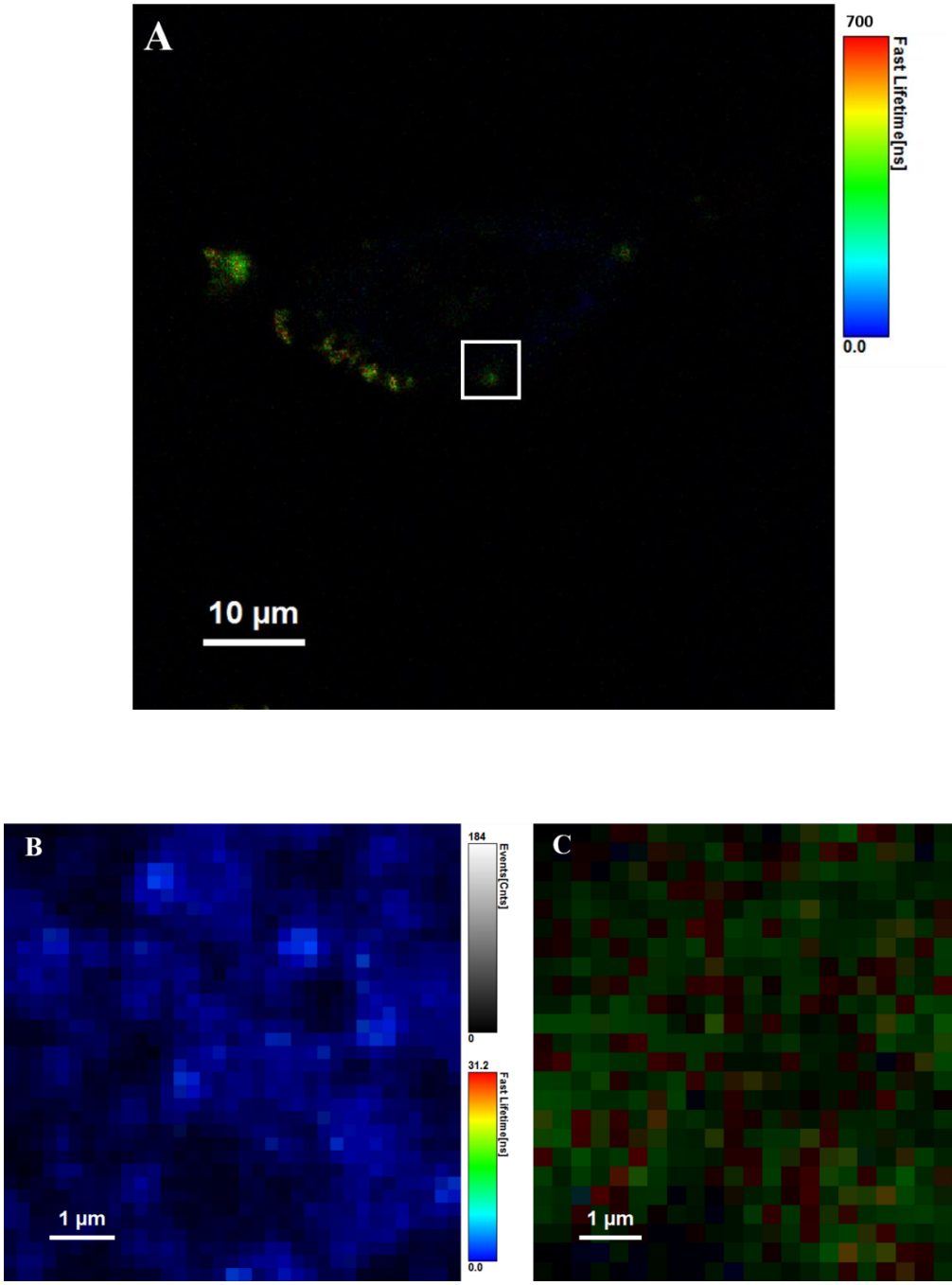


**Figure 4.31** PLIM false-colour images of the BODIPY (A), and ruthenium (B) components of the particles bound to the cell membrane. The image was acquired by focusing on a selection of particles bound to the cell membrane. Both the ruthenium and BODIPY were excited using a 405 nm laser. The BODIPY emission was collected using a 515-580 nm band pass filter at 8 ps resolution, and the $[Ru(bpy)_2\text{-Phen-Ar-COOH}]^{2+}$ was collected using a 570-700 nm band pass filter at 256 ps resolution.

Figure 4.32 illustrates the emission lifetime distributions of the particles when incubated with CHO cells for 4 h. Here, a single CHO, representative of the sample, was measured under the BODIPY settings first, then under the ruthenium settings. The lifetime of each

component was measured at the lysosomes as confirmed from co-localization studies described above.

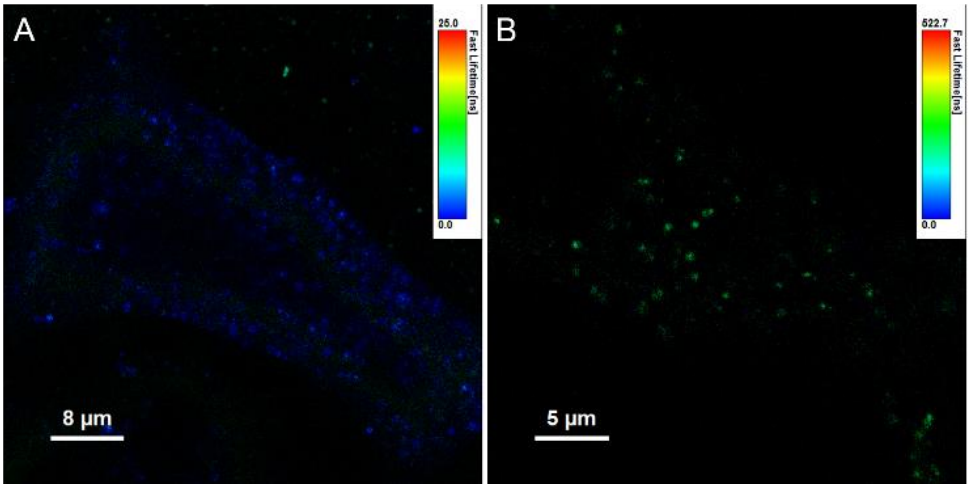


**Figure 4.32** Fluorescence lifetime images of the RuBODIPY particles in a live CHO cell. Cells were prepared as described in *section 4.2.6.2*. The false-colour images show that the BODIPY component exhibits a lifetime of 4.62 ns (A), and ruthenium has a lifetime of 435 ns (B) from within the cell. The BODIPY emission was collected using a 515-580 nm band pass filter at 8 ps resolution, and the $[Ru(bpy)_2\text{-Phen-Ar-COOH}]^{2+}$ was collected using a 570-700 nm band pass filter at 256 ps resolution.

The lifetime of the BODIPY component was found to be 4.26 ns (A). As expected, as it is isolated in the core, the luminescent lifetime did not deviate from the lifetime recorded for this component of the emission decay in solution, which was measured to be 4.45 ns. On the other hand, the lifetime of the ruthenium component for the nanoparticles localised within the lysosomes was found to be 435 ns (B). In solution, the ruthenium component of the probe decay exhibited a lifetime of 836 ns using TCSPC, and 628 ns on the PLIM. Even though the particles were prepared in the same manner at the same concentration, different luminescent lifetimes were measured. This is possibly a result of focus drift during PLIM as PLIM is acquired in conjunction with confocal, and the particles are set up on the confocal stage for imaging. Another possible reason is that during TCSPC, the sample is in a dark, sealed container. During PLIM, the particles are set up on the confocal stage. Although the experiment was carried out in a dark room, some photons may be lost during imaging. The decrease in lifetime from within the lysosomes suggests that it is being quenched. As discussed in *section 4.10*, the pH of the particles does not affect the luminescent emission or lifetime (Figure 4.30). Therefore,

the quenching of the lifetime is attributed to either oxygen or possible ROS concentration in the lysosome. By extrapolating the values from the calibration plot generated in *section 4.9* described by Figure 4.21, the oxygen concentration from within the lysosome is measured to be 600 μmol/L. This value exceeds saturation, as the concentration was measured to be 268 μmol/L in PBS solution. This suggests that the probe is being quenched further by another method.

One possible mechanism of quenching could be as a result of reactive oxygen species (ROS) production in the cell. The generation of ROS upon exposure to nanoparticles is a common observation as a reaction to the particles which are seen as a foreign object by the cell.[62] Nanoparticles can generate ROS by different mechanisms in the cell such as by their interaction with organelles like mitochondria, interaction with cell surface receptors, and interaction with redox proteins in the cell. In this case it is possibly as a result of a redox reaction in the lysosomes. Lysosomes possess a high iron pool.[63] Iron is known to play an important role as a redox-active metal producing ROS by acting as an electron donar.[64] It catalyses $H_2O_2$ to ROS species via Fenton reactions.[65] The acidic pH of the lysosomes favours ROS production via an iron redox reaction.[63] It is this redox reaction, as well as the production of ROS, that could possibly be quenching the ruthenium lifetime, as was shown in the mitochondria in *Chapter 3* that ruthenium seems to be responsive to ROS.

## 4.12 Ratiometric oxygen sensing in the cell using RuBODIPY particles

As the RuBODIPY particles demonstrated good ratiometric oxygen sensitivity *in vitro,* their ability to sense oxygen concentrations from within the cell was assessed using intensity measurements. Confocal microscopy was used to measure the emission intensities of the two chromophores in the cell, and to monitor the intensities over the course of the oxygen experiments. A range of methods to alter the oxygen concentration in the cell and in the cells environment were investigated. HeLa cells were prepared as described in *section 4.2.5.2* and after 4 h incubation, the particles were examined for oxygen sensing.

### 4.12.1 Nitrogen and argon

In order to create a hypoxic environment for the cells, nitrogen and argon were explored. *Tobita et al* reported on a ratiometric oxygen probe which consisted of an Ir(III) oxygen sensitive complex conjugated to coumarin 343 as the fluorescent reference. They introduced their probe to HeLa cells and incubated them under 20 % and 2.5 % oxygen levels. They found that at 20 % oxygen, the Ir(III) emission intensity was very low, which increased significantly at 2.5 % oxygen.[66] In an attempt to measure oxygen concentrations using the RuBODIPY particles from within the cell, de-gasses PBS was used. PBS, containing air-saturated levels of oxygen (20 %), was added to the prepared cells and left to equilibrate for 30 minutes. The cells were imaged to measure the ruthenium and BODIPY emissions separately at oxygen saturation. PBS was degassed with nitrogen for 1 h. The air-saturated PBS was removed from the cells, and was replaced with the de-aerated PBS. The cells were imaged every 2 minutes, but no change to either the BODIPY or the ruthenium emission intensities was recorded over 20 minutes.

The same process was carried out using argon. As argon is denser than oxygen it might be expected that the argon would form a layer over the cells, creating a hypoxic environment. Figure 4.33 shows a group of CHO cells that were incubated with 1:20 RuBODIPY particles for 4 h at 37 °C in the absence of light. Here, the cells were imaged with aerated PBS solution on them, representing 21 % oxygen. PBS solution was de-gassed using argon for 1 h, then added to the cells to create a hypoxic environment. The cells were imaged every 1 minute for 35 minutes, but no changes to the BODIPY or ruthenium emissions were seen.

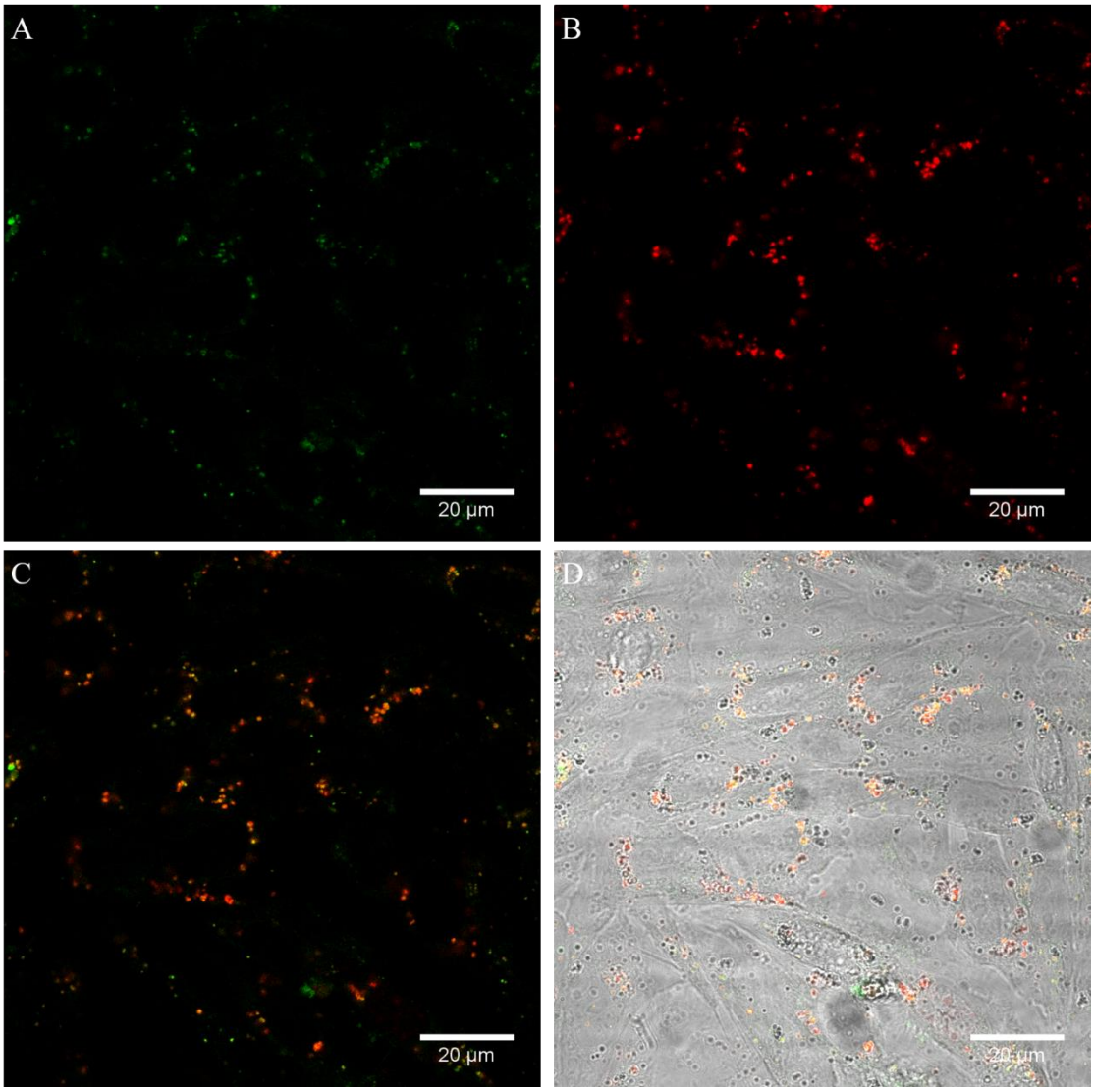


**Figure 4.33** CHO cells incubate with 1:20 RuBODIPY particles for 4 h at 37 °C in the absence of light. Aerated PBS was added to the cells to image the particles at a 21 % oxygen environment. The particles were excited at 458 nm. The BODIPY emission was collected between collected between 505 and 550 nm (A), and the ruthenium emission was collected using a long pass 605 nm filter (B). An overlay of the two channels is shown in (C), and with the background channel (D).

Figure 4.34 shows the emission of the BODIPY and ruthenium channels before the de-aerated PBS was added (A), after 10 minute's addition of the argon/PBS solution, and after 35 minutes. Four regions of interest (ROIs) were selected to measure any changes in emission intensities over the course of the experiment. However, no changes were seen at the ROIs. A possibility for this may be that this method is not suitable for altering the cells environment enough for the RuBODIPY particles to measure any changes.

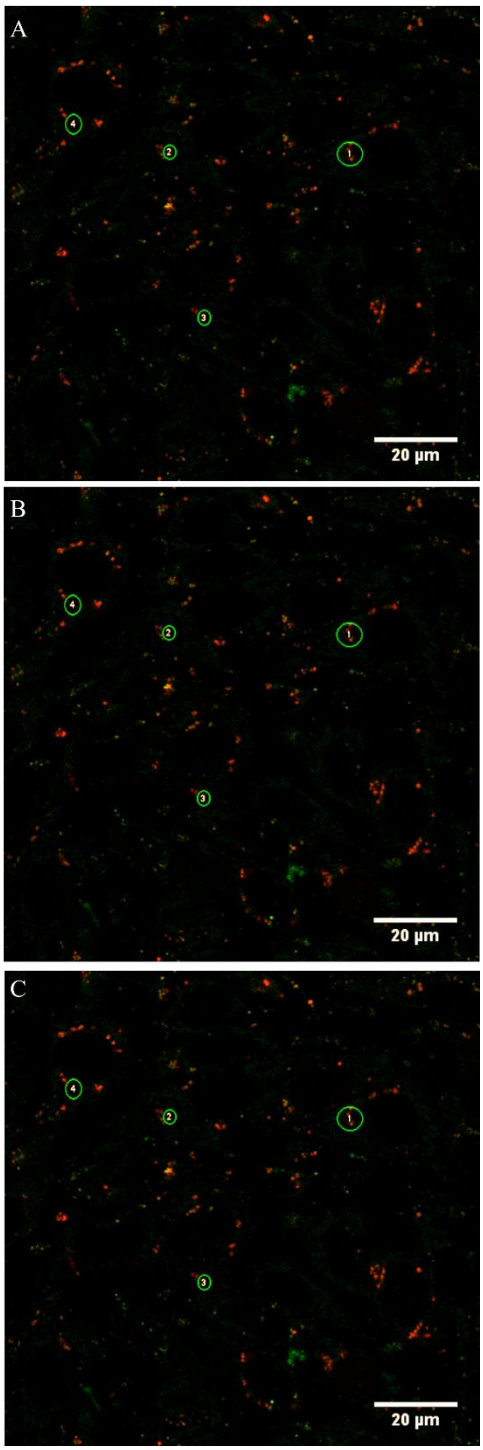


**Figure 4.34** RuBODIPY particles (1:20 dilution) in CHO cells when fully aerated in aerated PBS (A). PBS purged with argon gas for 1 h was added to the cells, and the emission intensity was recorded at 10 minutes (B), and at 35 minutes (C). The images show both the ruthenium and BODIPY channels overlayed, with the regions of interest highlighted for monitoring the emission changes. The particles were excited at 458 nm. The BODIPY emission was collected between collected between 505 and 550 nm (A), and the ruthenium emission was collected using a long pass 605 nm filter.

### 4.12.2 Chemical method

Instead of changing the cell's external environment, the cells internal oxygen concentrations were altered by stimulating with chemicals. There have been many reports of oxygen sensing using valinomycin[23] and Antimycin A.[6,13] Antimycin and $H_2O_2$ were used to alter the internal environment of the cell. Antimycin A is an inhibitor of electron transfer at complex III in mitochondria. It blocks the mitochondria from consuming oxygen in the cell. Therefore, there is a build up of oxygen in the cell, altering the natural concentration.[67] 100 mg/mL Antimycin A in PBS was added to the cells. Over 2 h, the ruthenium emission was monitored *via* confocal imaging. Figure 4.35 shows a CHO cell, representative of the sample, before Antimycin A was added (A) and after 2 h exposure (B). The cell was imaged very 1 minute to measure any changes in the particles emission intensity. The average intensity of ruthenium remained at 87.23 a.u. over the course of the experiment, suggesting that Antimycin A did not affect the oxygen concentration of the cells. However, we know from experiments in Chapter 4 that Antimycin effectively alters $O_2$ conc.

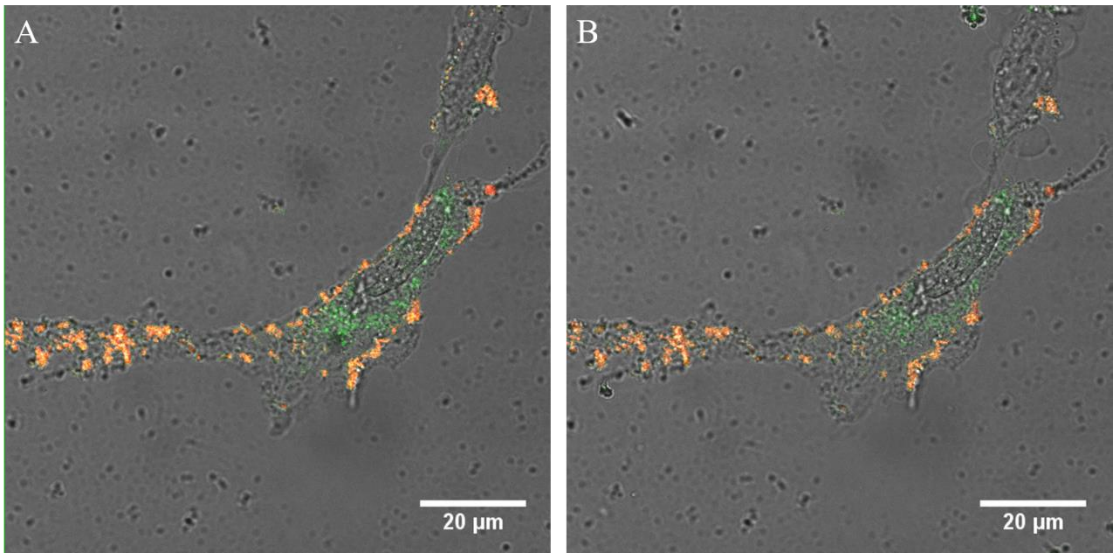


**Figure 4.35** A single CHO cell before the addition of Antimycin A (A) and after 2 h exposure to 100 µg/mL Antimycin A in PBS. CHO cells were incubated with 1:20 RuBODIPY particles for 4 h at 37 °C in the absence of light prior to imaging. The particles were excited at 458 nm. The BODIPY emission was collected between collected between 505 and 550 nm (A), and the ruthenium emission was collected using a long pass 605 nm filter.

Likewise, in a separate experiment, $H_2O_2$ was added to cells to introduce oxidative stress. 30 μM $H_2O_2$ in PBS solution to yield a final volume of 1 mL was added to the cells. The cells were imaged every 2 minutes and the emission was monitored. After 30 minutes, the concentration was increased to give a final concentration of 60 μM. After 1 h, no change to the ruthenium emission was seen across a number of cells.

After investigating a multiple of methods to alter the cell's external and internal oxygen concentration, and therefore measure the oxygen concentration using the ratiometric RuBODIPY particles, it was found to be unsuccessful. Although the particles showed excellent and reproducible oxygen sensitivity in PBS solution, their location within the lysosomes may be preventing the change in emission to be recorded. Alternatively, the particles are measuring changing oxygen but the method of detection *via* confocal microscopy may not be sensitive enough to monitor the changes to these particles.

## 4.13 Cytotoxicity

The effect of the RuBODIPY particles on the viability of the cells was examined using CHO cells. Cells were prepared as described in *section 4.2.7*. CTAB treated particles were added to CHO cells to yield final dilutions of 1:5, 1:10, 1:20, 1:50, and 1:100 particles: media in each well. The cells were incubated for 5 minutes to allow the particles to bind to the cell membrane. The solution was removed and the cells were washed with supplemented PBS. The cells were replaced with fresh cell culture media and incubated for 24 h at 37 °C with 5 % $CO_2$. Resazurin (Alamar Blue) Reagent was added to the cells for 7 hand the viability was measured.

Figure 4.36 describes the results of the assay. It was found that the particles were moderately toxic towards CHO cells. At concentrations as high as 1:5, 50 % of cells remained viable (as a percentage of cells with no particles added).

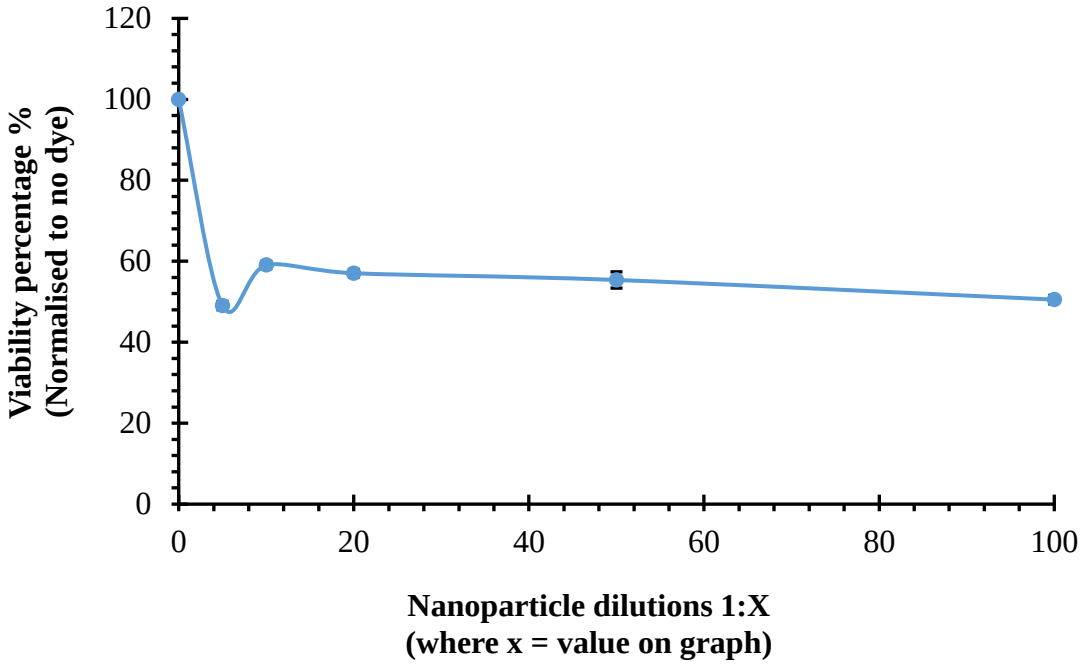


**Figure 4.36** Cytotoxicity of RuBODIPY nanoparticles. Particles were added to CHO cells to yield final dilution concentrations of particles to media and incubated for 24 h in the dark at 37 ºC at 5 % $CO_2$. CHO viability was assessed using the Resazurin (Alamar Blue) assay (n=3).

From this result, we reason that the particles remain in the lysosomes and do not affect cell viability. Images taken after incubation with the particles for 24 h demonstrate that the particles are still in the cells, ruling out removal or degradation by the acidic environment of the lysosome. Another suggestion for the viability could be that only a certain number of particles can bind to the cell membrane, irrespective of the concentration added to begin with. Therefore, the same amount of particles are crossing the membrane and localising in the cell, and the same number of cells remain viable after 24 h. PS particles are, generally, not cytotoxic towards cells. Pieber and co-workers reported on PS particles 100 nm in diameter, which after 24 h incubation localised in the lysosomes of endothelial cells and were non-toxic. [68] The group of *Fecondo et al* reported on 13 nm gold nanoparticles conjugated to a lysosomal CPP sequence. Similarly, their particles localised in the lysosomes and did not induce any toxic effects on CHO cells.[69] *Weiss et al* reported on a series of $SiO_2$ particles which were labelled with FITC, and monitored three different sizes in HeLa cells; 70 nm, 200 nm, and 500 nm. They found that all sizes localised in lysosomal compartments of the cells following 24 h incubation, and induced no toxic effects.[70]

However, the toxicity induced in the 50 % of cells that do not survive the incubation may be due to ROS production in the lysosomes as discussed previously in *section 4.11*, where the cells undergo apoptosis as a result. Strongly cationic PS particles can induce oxidative stress. *Simmet et al* demonstrated that PS-NH(2) particles of ~100 nm in diameter induced proton accumulation in the lysosomes of macrophages which is associated with lysosomal destabilisation. This destabilisation, in turn, caused damage to the mitochondrial membrane, triggering ROS.[71] Similarly, *Wang et al* showed that their cationic $NH_2$-PS particles (61 nm) generated ROS and induced ER stress after 6 h of treatment. The ROS production increased with increasing particle concentration in macrophages and human bronchial epithelial cells.[72] Another possibility is that the particles localising in the lysosomes are affecting the acidifying proton pump, effecting homeostasis. In this case, it is thought that the cationic charge of the particles neutralises the lysosomes, causing osmotic swelling and resulting in the lysosomes rupturing. Such outcomes was reported by *Xia et al*. Their cationic $NH_2$-PS particles (~60 nm) induced cytotoxic effects on macrophages. They attribute the toxicity to lysosomal degradation by a loss of proton pump activity, and thus osmotic swelling and rupture of the lysosomes occurred. [56] Lysosomal rupture releases lysosomal enzymes which can trigger pro-apoptotic signals such as Bid and Bax. The enzymes can also interfere with the mitochondrial, causing an increase in ROS productions.

The specific cause or source of the particle toxicity is unknown. One possible reason is that the $[Ru(bpy)_2\text{-phen-COOH}]^{+2}$ complex located on the particle surface may be inducing toxic effects on the cells. This complex was shown in Chapter 3 to be toxic when it localised in the mitochondria and throughout the cytoplasm. The cationic nature of the CTAB may be another cause of the toxicity of the RuBODIPY particles. The final concentration of CTAB (150 μM) was the same for each concentration of particles added to the cells during the assay. The fact that the percentage of cells remained the same over the range of particle concentrations strongly does it suggest it is CTAB rather than the particles which is inducing toxicity. In order to assess the true cause of toxicity, another method of encouraging cell uptake would have to be explored rather than using a detergent like CTAB such as functionalising the surface with polyethylene glycol residues (PEG),[73-75] or a poly-arginine peptide sequence. Using PEG as a cross-linking system during the preparation of the particles may also help to maintain particle stability and protect from enzymatic degradation once inside the cells.[76]

## 4.14 Conclusions

Chapter 4 examined two approaches to ratiometric sensing of $O_2$ in the cellular environment. One probe was [Ru(bpy)$_2$-phen-BODIPY-Br$_2$], a molecular dyad, and the other consisted of a core-shell poly(styrene) nanoparticle with BODIPY at the core and [Ru(bpy)$_2$-phen-COOH]$^{+2}$ on the particle surface. Both probes contained the same molecular components, the non-oxygen sensitive reference complex consisted of a BODIPY complex. BODIPYs are not environmentally sensitive because of their short fluorescent lifetimes. The oxygen-sensitive complex was a Ru(II) polypyridyl complex, whose long luminescent lifetime renders it sensitive to oxygen concentration. A key reason for choosing these components for dyad and particle is that their emission spectra do not overlap so they could be ratio metrically assessed and monitored based on the relative emission intensities.

For the molecule dyad, [Ru(bpy)$_2$-phen-BODIPY-Br$_2$] challenges associated with such probes is that there can be cross-talk and self-quenching between the two moieties. In this case, the probe was excited at a single wavelength, 458 nm, which resulted in dual-emission without any crosstalk. The BODIPY emission centred around 552 nm, while the ruthenium emission centred at 607 nm. However, it was found that the BODOPY component of the dyad was sensitive to aqueous media wherein, the BODIPY emission switched off in PBS solution, leaving just the ruthenium emission present. Applying the same material to a nanoparticle core-shell probe, 100 nm in diameter. The BODIPY probe was located in a poly(styrene) core to avoid contact with aqueous solutions. The oxygen sensitive ruthenium was located on the poly(L-lysine) coating on the outside off the shell, to allow it to come in contact with oxygen. The RuBODIPY particles exhibited dual-emitting properties in aqueous PBS solution when excited at 458 nm, with the BODIPY emission centred at 547 nm and the ruthenium emission centred at 601 nm.

The photophysical properties of both probes were examined in aqueous and non-aqueous solutions. Their oxygen sensing abilities were assessed by de-aerating with nitrogen, and measuring the luminescent emission intensity and lifetime as a function of oxygen concentration. The ruthenium exhibited excellent oxygen sensitivity, while the BODIPY reference remained unaffected.

Both probes were introduced to CHO cells. Confocal microscopy showed that [Ru(bpy)$_2$-phen-BODIPY-Br$_2$] entered the cytoplasm and nucleoli of the cells following 24 h incubation. On the other hand, the RuBODIPY particles localised in the lysosomes,

which is typical of particles of ~100 nm in diameter. The ruthenium luminescent lifetime was quenched beyond the lifetime of oxygen quenching. The reason for this is possibly due to ROS production as a result of lysosomal degradation, but this requires further exploration.

Cytotoxicity studies found that [$Ru(bpy)_2$-phen-BODIPY-$Br_2$] was highly toxic towards CHO cells following 24 h incubation, with concentrations above 15 μM killing all the cells. In contrast, 50 % of cells remained viable after exposure to high concentrations of RuBODIPY particles. The difference in toxic effects was attributed to where the probes localise in the cell. [$Ru(bpy)_2$-phen-BODIPY-$Br_2$] resided in the cytoplasm and nucleoli. As it enters the nucleus, it was expected to be toxic when coming in contact with nuclear DNA. As RuBODIPY particles located in the lysosomes, it may require longer exposure times to see the same level of toxicity. This is something that would need to be explored further.

Finally, RuBODIPY particles ability to report on oxygen concentrations from within the cell was explored in PBS solution which was de-gassed with nitrogen and argon, separately, and was added to live cells. The emission intensities were measured over time as a result of the changing oxygen concentration in the cells environment. However, no changes were observed. Chemical methods were also assessed. Rotenone and $H_2O_2$ were added to live cells in order to alter the oxygen levels from within the cells. Again, no changes in emission intensity was observed. It was thought that this was as a result of the RuBODIPY particles residing in the lysosomes as the lysosomes may not respond to changing oxygen levels in the same manner in which other cellular organelles such as the mitochondria would respond.

Both ratiometric methods showed excellent oxygen sensing abilities in vitro, but were unable to transfer to live cells. One possible use for [$Ru(bpy)_2$-phen-BODIPY-$Br_2$] would be to introduce it to liposomes to see how the BODIPY moiety behaves in the lipid bilayer. As for the RuBODIPY particles, future work may include conjugating or functionalising the ruthenium complex on the particle shell in order to direct the particles away from the lysosomes to assess if they are capable of measuring oxygen *in vivo*. Functionalising the surface with polyethylene glycol residues or poly-peptide sequences would also ensure the particles are membrane permeable, and therefore, CTAB would not need to be used to assist in the particles crossing the cell membrane.

## *References*


1. Sedlmeier A, Achatz DE, Fischer LH, Gorris HH, Wolfbeis OS. Photon upconverting nanoparticles for luminescent sensing of temperature. *Nanoscale*. 2012;4:7090.

2. Schäferling M. Nanoparticle-based luminescent probes for intracellular sensing and imaging of pH. *WIREs Nanomed Nanobiotechnol*. 2015.

3. Korzeniowska B, Schulz A, Wencel D, McDonagh C. Luminescent nanoparticle-based intracellular sensing. *IEEE Sensors*. 2011:1709-1711.

4. Morris KJ, Roach MS, Xu W, Demas JN, DeGraff BA. Extracellular oxygen concentration mapping with a confocal multiphoton laser scanning microscope and TCSPC card. *Anal Chem*. 2007;79:9310-9314.

5. Fercher A, Borisov SM, Zhdanov AV, Klimant I, Papkovsky DB. Intracellular O2 sensing probe based on cell-penetrating phosphorescent nanoparticles. *ACS Nano*. 2011;5:5499-5508.

6. Martin A, Byrne A, Burke CS, Forster RJ, Keyes TE. Peptide-bridged dinuclear ru(II) complex for mitochondrial targeted monitoring of dynamic changes to oxygen concentration and ROS generation in live mammalian cells. *J Am Chem Soc*. 2014;136:15300-15309.

7. Mills A. Oxygen indicators and intelligent inks for packaging food *Chem Soc Rev*. 2005;34:1003-1001.

8. O'Mahony FC, O'Riordan TC, Papkovskaia N, Kerry JP, Papkovsky DB. Non-destructive assessment of oxygen levels in industrial modified atmosphere packaged cheddar cheese. *Food Control*. 2006;17(4):286-292.

9. Hansen S, Kensy F, Käser A, Büchs J. Potential errors in conventional DOT measurement techniques in shake flasks and verification using a rotating flexitube optical sensor. *BMC Biotechnology*. 2011;49.

10. Jin P, Chu J, Miao Y, Tan J, Zhang S, Zhu W. A NIR luminescent copolymer based on platinum porphyrin as high permeable dissolved oxygen sensor for microbioreactors. *AIChE*. 2013;59:2743-2752.

11. Dmitriev RI, Ropiak HM, Ponomarev GV, Yashunsky DV, Papkovsky DB. Cell-penetrating conjugates of coproporphyrins with oligoarginine peptides: Rational design and application for sensing intracellular O2. *Bioconj Chem*. 2011;22:2507-2518.

12. Sud D, Mycek MA. Calibration and validation of an optical sensor for intracellular oxygen measurements. *J Biomed Opt*. 2009;12:20506.

13. Fercher A, Borisov SM, Zhdanov AV, Klimant I, Papkovsky DB. Intracellular O2 Sensing probe based on cell-penetrating phosphorescent nanoparticles. *ACS Nano*. 2011;5:5499-5508.

14. Dmitriev RI, and Papkovsky DB. Optical probes and techniques for O2 measurement in live cells and tissue. *Cell Mol Life Sci*. 2012;69(12):2025-2039.

15. Wanga X, Wolfbeis OS. Optical methods for sensing and imaging oxygen: Materials, spectroscopies and applications *Chem Soc Rev*. 2014;43:3666-3761.

16. Wang X, Gorris HH, Stolwijk JA, et al. Self-referenced RGB colour imaging of intracellular oxygen. *Chem. Sci.* 2011(2):901.

17. Cao Y, Koo YL, Kopelman R. Poly(decyl methacrylate)-based fluorescent PEBBLE swarm nanosensors for measuring dissolved oxygen in biosamples. *Analyst*. 2004;129:745-750.

18. Napp J, Behnke T, Fischer L, et al. Targeted luminescent near-infrared polymer-nanoprobes for in vivo imaging of tumor hypoxia. *Anal Chem*. 2011;83:9039-9046.

19. Choi JY, Kim JS, Ingale SL, et al. Effect of potential multimicrobe probiotic product processed by high drying temperature and antibiotic on performance of weanling pigs. *J Anim Sci*. 2011;89(6):1795-1804.

20. Kondrashina AV, Dmitriev RI, Borisov SM, et al. A phosphorescent nanoparticle-based probe for sensing and imaging of (intra)cellular oxygen in multiple detection modalities. *Adv Funct Mater 2012, 22, 4931–4939*. 2012;22:4931-4939.

21. Dmitriev RI, Borisov SM, Kondrashina AV, et al. Imaging oxygen in neural cell and tissue models by means of anionic cell-permeable phosphorescent nanoparticles. *Cell Mol Life Sci*. 2015;72:367-381.

22. Dmitriev RI, Zhdanov AV, Nolan YM, Papkovsky DB. Imaging of neurosphere oxygenation with phosphorescent probes. *Biomaterials*. 2013;34(37):9307-9317.

23. Hara D, Komatsu H, Son A, Nishimoto S, Tanabe K. Water-soluble phosphorescent ruthenium complex with a fluorescent coumarin unit for ratiometric sensing of oxygen levels in living cells. *Bioconjugate Chem*. 2015;26:645-649.

24. Feng Y, Cheng J, Zhou L, Zhou X, and Xiang H. Ratiometric optical oxygen sensing: A review in respect of material design. *Analyst*. 2012;137:4885.

25. Yoshihara T, Murayama S, Tobita S. Ratiometric molecular probes based on dual emission of a blue fluorescent coumarin and a red phosphorescent cationic iridium(III) complex for intracellular oxygen sensing. *Sensors*. 2015;15:13503-13521.

26. Martin A, Byrne A, Dolan C, Forster RJ, Keyes TE. Solvent switchable dual emission from a bichromophoric ruthenium–BODIPY complex. *Chem Commun*. 2015;51:15839-15841.

27. Demas JN, DeGraff BA. Applications of luminescent transition platinum group metal complexes to sensor technology and molecular probes. *Coord Chem Rev*. 2001;211(1):317-351.

28. Galangau O, Dumas-Verdes C, M ´ eallet-Renault R, Clavier G. Rational design of visible and NIR distyryl-BODIPY dyes from a novel fluorinated platform. *Org Biomol Chem*. 2010;8:4546-4553.

29. Pellegrin Y, Forster RJ, Keyes TE. pH dependent photophysics and role of medium on photoinduced electron transfer between ruthenium polypyridyl complex and anthraquinone. *Inorg Chim Acta*. 2009;362(6):1715-1722.

30. Demas JN, Adamson AW. Tris (2,2'-bipyridine)ruthenium(II) sensitized reactions of some oxalato complexes. *J Am Chem Soc*. 1973;95:5159-5168.

31. Puckett CA, Barton JK. Fluorescein redirects a ruthenium-octaarginine conjugate to the nucleus. *J Am Chem Soc*. 2009;131:8738-8739.

32. Fercher A, Ponomarev GV, Yashunski D, Papkovsky DB. Evaluation of the derivates of phosphorescent pt-coproporphyrin as intracellular oxygen-sensitive probes. *Anal Bioanal Chem*. 2010;396:1793-1803.

33. Zhang H, Chen J, Guo X, Wang H, Zhang H. Highly sensitive low-background fluorescent probes for imaging of nitric oxide in cells and tissues. *Anal Chem*. 2014;86:3115.

34. Jiang X, Gao R, Yue Y, Sun G, Zhao W. A NIR BODIPY dye bearing 3,4,4*a*-trihydroxanthene moieties. *Org Biomol Chem*. 2012;10:6861.

35. Chen J, Zhang H, Guo X, Wang H, Zhan H. Off–on" red-emitting fluorescent probes with large stokes shifts for nitric oxide imaging in living cells. *Anal Bioanal Chem*. 2013;405:7447-7456.

36. Jacobs J, Byrne A, Gathergood N, Keyes TE, Heuts JPA, Heise A. Facile synthesis of fluorescent latex nanoparticles with selective binding properties using amphiphilic glycosylated polypeptide surfactants. *Macromolecules*. 2014;47:7303-7310.

37. Holzapfel V, Musyanovych A, Landfester K, Lorenz MR, Maila¨nder V. Preparation of fluorescent carboxyl and amino functionalized polystyrene particles by miniemulsion polymerization as markers for cells. *Macromol Chem Phys*. 2005;206:2440-2449.

38. Im SH, Khalil GE, Callis J, Ahn BH, Gouterman M, Xia Y. Synthesis of polystyrene beads loaded with dual luminophors for self-referenced oxygen sensing. *Talanta*. 2005;67(3):492-497.

39. Cywinski PJ, Moro AJ, Stanca SE, Biskup C, Mohr GJ. Ratiometric porphyrin-based layers and nanoparticles for measuring oxygen in biosamples. *Sensors Actuators B: Chem*. 2009;135(2):472-477.

40. Jacobs J. Towards polypeptide based nanoparticles. *Dublin City University*; 2015.

41. Sheu W. Molecular weight averages and polydispersity of polymers. *Journal of Chemical Education*. 2001;78:554-555.

42. Ryan EM, O'Kennedy R, Feeney MM, Kelly JM, Vos JG. Covalent linkage of ruthenium polypyridyl compounds to poly(L-lysine), albumins, and immunoglobulin G. *Bioconjugate Chem*. 1992;3:285-290.

43. Hartmann P, Leiner MJP. Luminescence quenching behavior of an oxygen sensor based on a ru(l1) complex dissolved in polystyrene. *Anal Chem*. 1995;67:88-93.

44. Ryan EM, O'Kennedy R, Feeney MM, Kelly JM, Vos JG. Covalent linkage of ruthenium polypyridyl compounds to poly(L-lysine), albumins, and immunoglobulin G. *Bioconjugate Chem*. 1992;3:285-290.

45. Xu H, Aylott JW, Kopelman R, Miller TJ, Philbert MA. A real-time ratiometric method for the determination of molecular oxygen inside living cells using Sol−Gel-based spherical optical nanosensors with applications to rat C6 glioma *Anal Chem*. 2001;73:4124-4133.

46. Koo YL, Cao Y, Kopelman R, Koo SM, Brasuel M, Philbert MA. Real-time measurements of dissolved oxygen inside live cells by organically modified silicate fluorescent nanosensors *Anal Chem*. 2004;76:2498-2505.

47. Lavin P, McDonagh CM, MacCraith BD. Optimization of ormosil films for optical sensor applications. *Journal of Sol-Gel Science and Technology*. 1998;13:641-645.

48. Rajagopal K, Kumar Singh P, Kumar R, Siddiquia KF. CTAB-mediated, single-step preparation of competent *Escherichia coli*,*Bifidobacterium* sp. and *Kluyveromyces lactis* cells. *Meta Gene*. 2014;2:807-818.

49. Berry V, Gole A, Kundu S, Murphy CJ, Saraf RF. Deposition of CTAB-terminated nanorods on bacteria to form highly conducting hybrid systems. *J Am Chem Soc*. 2005;127:17600-17601.

50. Rejman J, Oberle V, Zuhorn IS, Hoekstra D. Size-dependent internalization of particles via the pathways of clathrin- and caveolae-mediated endocytosis. *Biochem J*. 2004;377:159-169.

51. Geiser M, Rothen-Rutishauser B, Kapp N, et al. Ultrafine particles cross cellular membranes by nonphagocytic mechanisms in lungs and in cultured cells. . *Environ Health Perspect*. 2005;113:1555-1560.

52. Kammersgaard LP, Jørgensen HS, Rungby JA, et al. Admission body temperature predicts long-term mortality after acute stroke: The copenhagen stroke study. *Stroke*. 2002;33:1759-1762.

53. Polderman KH. Application of therapeutic hypothermia in the ICU: Opportunities and pitfalls of a promising treatment modality. *2004*. Intensive Care Medicine;30:556-575.

54. Fröhlich E, Meindl C, Roblegg E, Ebner B, Absenger M, Piebe TR. Action of polystyrene nanoparticles of different sizes on lysosomal function and integrity. *Particle and Fibre Toxicology*. 2012;9:26.

55. Liu Y, Li W, Lao F, et al. Intracellular dynamics of cationic and anionic polystyrene nanoparticles without direct interaction with mitotic spindle and chromosomes. *Biomaterials*. 2011;32(32):8291-8303.

56. Xia T, Kovochich M, Liong M, Zink JI, Nel AE. Cationic polystyrene nanosphere toxicity depends on cell-specific endocytic and mitochondrial injury pathways. *ACS Nano*. 2008;2:85-96.

57. Chang M, Shiau A, Chen Y, Chang C, Chen HHW, Wu C. Increased apoptotic potential and dose-enhancing effect of gold nanoparticles in combination with single-dose clinical electron beams on tumor-bearing mice. *Cancer Sci*. 2008;99:1479-1484.

58. Salnikov V, Lukyánenko YO, Frederick CA, Lederer WJ, Lukyánenko V. Probing the outer mitochondrial membrane in cardiac mitochondria with nanoparticles. *Biophys J*. 2007;92(3):1058-1071.

59. Panté N, Kann M. Nuclear pore complex is able to transport macromolecules with diameters of ~39 nm. *Mol Biol Cell*. 2002;13:425-443.

60. Boya P, Kroemer G. Lysosomal membrane permeabilization in cell death. *Oncogene*. 2008;27:6434-6451.

61. Neugebauer U, Pellegrin Y, Devocelle M, et al. Ruthenium polypyridyl peptide conjugates: Membrane permeable probes for cellular imaging. *Chem Commun. 2008, 5307–5309*. 2008;42:5307-5309.

62. Soenen SJ, Rivera-Gil P, Montenegro J, Parak WJ, De Smedt SC, Braeckmans K. Cellular toxicity of inorganic nanoparticles: Common aspects and guidelines for improved nanotoxicity evaluation. *Nano Today*. 2011;6(5):446-465.

63. Denamur S, Tyteca D, Marchand-Brynaert J, et al. Role of oxidative stress in lysosomal membrane permeabilization and apoptosis induced by gentamicin, an aminoglycoside antibiotic . *Free Radical Biology & Medicine*. 2011;51:1656-1665.

64. Nohl H, Gille L. Lysosomal ROS formation. *Redox Report*. 2005;10:199-205.

65. Fu J, Shao Y, Wang L, Zhu Y. Lysosome-controlled efficient ROS overproduction against cancer cells with a high pH-responsive catalytic nanosystem. *Nanoscale*. 2015;7:7275.

66. Yoshihara T, Yamaguchi Y, Hosaka M, Takeuchi T, Tobita S. Ratiometric molecular sensor for monitoring oxygen levels in living cells. *Angew Chem Int Ed*. 2012;51:4148-4151.

67. Park W, Han Y, Kim S, Kim S. *J Cellular BioChem*. 2007;102:98-109.

68. Fröhlich E, Meindl C, Roblegg E, Ebner B, Absenger M, Pieber TR. Action of polystyrene nanoparticles of different sizes on lysosomal function and integrity. *Particle and Fibre Toxicology*. 2012;9:1-13.

69. Dekiwadia CD, Lawrie AC, Fecondo JV. Peptide-mediated cell penetration and targeted delivery of gold nanoparticles into lysosomes. *J Pept Sci*. 2012;18:527-534.

70. Al-Rawi M, Diabate S, Weiss C. Uptake and intracellular localization of submicron and nano-sized SiO2 particles in HeLa cells. *Arch Toxicol*. 2011;85:813-826.

71. Lunov O, Syrovets T, Loos C, et al. Amino-functionalized polystyrene nanoparticles activate the NLRP3 inflammasome in human macrophages. *ACS Nano*. 2011;5:9648-57.

72. Chiu H, Xia T, Lee Y, Chen C, Tsai J, Wang Y. Cationic polystyrene nanospheres induce autophagic cell death through the induction of endoplasmic reticulum stress. *Nanoscale*. 2015;7:736.

73. Suh J, Choy K, Lai SK, et al. PEGylation of nanoparticles improves their cytoplasmic transport *Int J Nanomedicine*. 2007;2:735-741.

74. Cruz LJ, Tacken PJ, Fokkink R, Figdor CG. The influence of PEG chain length and targeting moiety on antibody-mediated delivery of nanoparticle vaccines to human dendritic cells. . *Biomaterials 2011*. 2011;32:6791-6803.

75. Karakoti AS, Das S, Thevuthasan S, Seal S. PEGylated inorganic nanoparticles. *Angew Chem Int Ed Engl*. 2011;50:1980-1994.

76. Isa ILM, Srivastava A, Tiernan D, et al. Hyaluronic acid based hydrogels attenuate inflammatory receptors and neurotrophins in interleukin-1β induced inflammation model of nucleus pulposus cells. *Biomacromolecules*. 2015;16:1714-1725.

# Chapter 5: Application of Ru(II) probes to Stimulated Emission Depletion (STED) microscopy

## 5.1 Introduction

Optical microscopy has played a crucial role in developments in cell biology permitting imaging of live cells, tissues and other biological structures.[1-5] However, the spatial resolution of classical microscopes is limited due to the diffraction limit, which hinders the imaging of more detailed biological performances. STimulated Emission Depletion (STED) microscopy has been shown to greatly increase the resolving power of light microscopes and so is an attractive proposition for imaging live cell organelles which are often smaller than 1 μm. For example, the mitochondria in mammalian cells, such as HeLa and CHO cells, range from 1 – 2 μM long and 0.2 – 0.7 μM wide. While the lowest resolution achievable using confocal microscopy is 150 – 200 nm, detail in their structure such as the mitochondrial cristae cannot be imaged in high resolution. Likewise, the nucleus is ~10 μm in diameter. While the nucleus is visible using confocal microscopy, structural detail such as nuclear pores cannot be resolved as they are ~ 80 nm long. The development of STED makes it possible to non-invasively image and resolve organelle structures and molecular dynamics at the nano-scale.[6] There have been many reports of STED imaging of cellular processes using fluorescent-based probes for example in non-invasively imaging nerve and synaptic tissues in neuronal cultures [7] and dendritic spine synaptic signals.[8] As discussed in *section 1.12* in Chapter 1, STED microscopy uses separate laser beams for fluorescence excitation and quenching the fluorophore. It works by depleting a zone around the edge of the focal region of emitting fluorophore which is achieved by switching the fluorophore in the depletion zone to a dark state by stimulating its emission with a high intensity laser that matches the emission wavelength (usually the red edge of the emission) of the fluorophore. This effectively reduces the spot size of the incident laser to below the diffraction limit. The greater the intensity of the STED depletion laser, the more efficient the depletion process and the better the resolution.[9] As a result, the fluorophore must be stable under continuous irradiation. All of these conditions put significant demands on the stability and photophysics of the STED fluorophore. Therefore, there is a need for much improved imaging probes to meet these demands.

The ideal properties of a good STED probe include 1) a high quantum yield, 2) good photostability, 3) possess a long lived emissive state, and 4) their emission spectrum must overlap with the STED depletion laser. The probe should also permeate the cell membrane and target with high precision for specific and detailed imaging. Many fluorescent dyes used for labelling STED samples are organic dyes which have short-

lived emissive states, are prone to quenching at high concentrations, and tend to easily photo-bleach.[10] Photo-stable dyes typically used for STED imaging such as Alexa Fluor, Atto and Chromeo exhibit good stability and quantum yields but show modest permeability and no selectivity in their distribution in cells so stain non-specifically leading to large backgrounds .[11-14]

The photophysical properties associated with transition metal complex luminophores such as a large stokes shift, long lived emission states, excellent photostability and high quantum yields makes them potentially ideal candidates as STED imaging probes. To date, the properties of Ru(II) have been exploited in conventional imaging and as sensor probes.[15-17] With its unique optical properties and proven cell compatibility, Ru(II) complexes are explored here as probes for STED microscopy.[14,18] As discussed in Chapter 1, cell penetrating peptides (CPPs) have been used in recent years to direct such complexes to image and sense at the organelle level.[19-22] By combining transition metal complexes with CPP or signal peptides, super resolution imaging enabled by the localisation of the probe at specific sub-cellular sites can be achieved to yield high contrast images compared to conventional imaging

The aim of this chapter is to explore the application of Ru(II) polypyridyl complexes as imaging probes in STED microscopy as potential STED. As shown previously in Chapter 3, cell penetrating and signal peptides (CPPs) have outstanding targeting abilities, capable of directing peptide conjugate probes to specific cell organelles. This chapter exploits the power of signal peptides by using two novel organelle targeted ruthenium polypyridyl complex peptide conjugates that target the endoplasmic reticulum (ER), and the nucleus, in order to achieve high-resolution STED images of these organelles. The endoplasmic reticulum (ER) plays a key role in the cell in protein assembly, lipid biosynthesis, and vesicular trafficking.[23] There are four separate sub-compartments in the ER; rough ER, smooth ER, transitional ER, and nuclear envelope, making it a complicating organelle.[24] The ER has recently become implicated as a key determinant in many disease states such as cancer, diabetes, neurodegeneration, and heart disease.[25-27] Therefore, optical imaging protocols which enable the details of the ER specifically to be examine e.g. in diseased states is becoming important in the field of diagnostics. The ER is a complicated organelle, and so the size varies. ER tubules can range from 30 to 100 nm in diameter, and the cisternae can be as tightly packed as 16 nm.[23,28] Therefore confocal microscopy cannot achieve such resolutions needed to image the structure of the ER in great detail. The ER-directing peptide

RQIKIWFQNRRMKWKK will be examined in directing $[Ru(bpy)_2phen\text{-}Ar\text{-}COOH]^{2+}$ complex to the ER.

Likewise, developing DNA-targeted probes for imaging in live cells is of great importance in theranostis given the significant role DNA has and its role in diseases. A key focus of targeted metal luminophore DNA probes is to intercalate with the DNA either in order to kill the cell. Whereas there has been extensive research on solution phase studies between the metal complexes particular of ruthenium and DNA, to date, there have been very few applied to targeting DNA in vivo and particularly for the purpose of imaging.[29-32] *Puckett et al* successfully directed $[Ru(phen)(bpy')(dppz)]^{2+}$ complex conjugated to the nuclear targeting signal RrRk to the nucleus of HeLa cells.[33] *Gottschaldt et al* used D-glucose sugar moiety conjugated to a ruthenium polypyridyl complex to direct the complex to the nucleus of HepG2 cells.[34] In both cases, the groups directed ruthenium to the nucleus, but showed no DNA binding. *Gill et al* are one of the few groups who have successfully shown nuclear localisation of a dinuclear Ru(II) probe.[15,35] Here they demonstrated cell uptake and DNA staining in MCF-7 cells, and captured four phases of chromosomal aggregation in mitosis, the process of cell division. Combining Ru(II) complexes with a nuclear localising sequence to target the nucleus can only enhance the precision of complex localising there. The NLS sequence VQRKRQKLMP, known as NF-κB originates from the NF-κB transcription factor. Nuclear factor-κB (NF-κB) is a family of transcription factors that plays a role in the transcription of DNA, as well as inflammation and cell proliferation.[36] This sequence will be explored further in directing Ru(II) complex to the nucleus.

This chapter details the ER targeting complex $[(Ru(bpy)_2phen\text{-}Ar)_2\text{-}ER]^{9+}$, and $[Ru(dppz)(bpy)(bpy\text{-}Ar\text{-}NFkB)]^{6+}$ nuclear targeting complex as novel STED imaging probes**.** Detailed cell studies were carried out including uptake and localisation of the complexes in HeLa cells, as well as cytotoxicity studies. $[(Ru(bpy)_2phen\text{-}Ar)_2\text{-}ER]^{9+}$ , $[(Ru(bpy)_2phen\text{-}Ar)_2\text{-}Arg_8]^{7+}$ and $[Ru(dppz)(bpy)(bpy\text{-}Ar\text{-}NFkB)]^{6+}$ were investigated as STED imaging probes, and were compared to the commercial dye Alexa Fluor Phalloidin 532. Results from confocal fluorescence and STED imaging studies were compared out to assess the performance of Ru(II) polypyridyl complexes as a STED probes. Complex stability under the 660 nm STED depletion was also assessed and compared to the highly stable Alexa probe. STED images of the endoplasmic reticulum (ER) in HeLa cells were collected, which demonstrated a much improved resolution

compared to the confocal equivalent. Finally, images of nuclear DNA chromosomes at the different stages of mitosis were captured using STED microscopy.

## 5.2 Materials and Methods

### 5.2.1 Materials

$[Ru(bpy)_2phen\text{-}Ar\text{-}COOH]^{2+}$ parent complex was synthesised by Christopher S. Burke (DCU).[37] $[Ru(dppz)(bpy)(bpyArCOOH)](PF_6)_2$ parent complex and its NLS conjugate $[Ru(dppz)(bpy)(bpy\text{-}Ar\text{-}NFkB)]^{6+}$ (Scheme 5.2) were synthesised by Christopher S. Burke (DCU). Polypeptides (> 95 %) were purchased from Celtek Peptides (TN, USA) and used without further purification. All chemicals and solvents used in experimental procedures were purchased from Sigma Aldrich (Ireland). All solutions were made using deionised water, which was purified by a Milli-Q plus 18.5 Millipore purifying system.

HeLa cells were purchase from ATCC Cell Biology Collecetion (UK). Resazurin reagents were acquired from Promokine. Cell culture media, serum and penicillin / streptomycin were purchased from Sigma Aldrich. Cell culture flasks were purchased from Corning Incorporated and VWR. Alexa Fluor Phalloidin 532 and ProLong Gold Antifade Mountant were purchased from Life Technologies.

### 5.2.2 Synthesis of the $[Ru(bpy)_2\text{-}Phen\text{-}Ar\text{-}COOH]^{2+}$ conjugate

A solution of $[Ru(bpy)_2\text{-}Phen\text{-}Ar\text{-}COOH]^{2+}$ (8 mg, 0.009 mmol) in DMF (1 ml) with (2-(1H-benzotriazol-1-yl)-1,1,3,3-tetramethyluronium hexafluorophosphate, HBTU (13.0 mg, 0.039 mmol) was stirred for 10 min at room temperature. Added to this was the peptide (sequence RQIKIWFQNRRMKWKK) (10 mg) in DMF (0.5 ml) with DIPEA (15 μL) and stirred for 21 h. The solution was placed on ice and a saturated aqueous solution of potassium hexafluorophosphate was added to induce precipitation. After stirring for 10 min, the orange suspension was then filtered using 0.5 μm filter paper and the product was washed with diethylether. The product was dissolved in minimum acetone, and DCM was added dropwise to the product/acetone solution to induce

precipitation. The suspension was filtered and left under $N_2$ for 24 h to yield pure conjugate, $[(Ru(bpy)_2phen\text{-}Ar)_2\text{-}ER]^{9+}$ (Scheme 5.1). An indication of reaction progress and purity was easily followed by TLC.

### 5.2.3 Spectroscopic Measurements

The UV/Vis spectra were recorded on a Jasco V-679 UV/Vis/NIR spectrometer. Fluorescence emission and excitation were measured using a Cary Eclipse Fluorescence Spectrometer, both at a slit width of 5 nm. Solution measurements were carried out in 1% DMSO with PBS, and neat PBS in a Hellma quartz cuvette of 1 cm optical path length.

### 5.2.4 Luminescent Lifetime Measurements

The lifetimes were collected using a FluoTime 100 Time-Correlated Single Photon Counting (TCSPC) instrument. The 405 nm laser was used for parent and conjugate complexes, provided from a Picoquant 'PDL 800B' pulsed diode laser. 10,000 counts were collected for each lifetime measurement. The measurements were carried out using Nanoharp software. The luminescent lifetimes were calculated using the PicoQuant FluoFit software by fitting an exponential decay function to each plot. The data was then fitted to a mono-exponential decay to the background decay curve, using a tail fit with a $\chi^2$ value between 0.9-1.1.

### 5.2.5 Real-time confocal luminescent imaging

HeLa cells were seeded at 1.5 x $10^5$ cells in 2 mL media on 35 mm glass-bottom culture dishes. Cells were grown for 48 h at 37 ºC at 5 % $CO_2$. The growth medium was removed and 70 μM of $[Ru(bpy)_2\text{-}Phen\text{-}Ar\text{-}Arg_8]^{10+}$ or $[(Ru(bpy)_2phen\text{-}Ar)_2\text{-}ER]^{9+}$ in phenol red-free media was added and left to incubate for 4 h at 37 ºC at 5 % $CO_2$ in the dark. In the case of $[Ru(dppz)(bpy)(bpy\text{-}Ar\text{-}NFkB)]^{6+}$, 40 μM was added to the cells for 24 h. The dye/media solution was removed and cells were washed with PBS supplemented with 1.1 mM $MgCl_2$ and 0.9 mM $CaCl_2$. For live cell imaging, cells were imaged immediately

using a Leica TSP DMi8 confocal microscope using a 100X oil immersion objective lens. A 488 nm white light laser was used to excite $[(Ru(bpy)_2phen\text{-}Ar)_2\text{-}ER]^{9+}$, and its emission was collected using a band pass 590-700 nm filter set. [Ru(dppz)(bpy)(bpy-Ar-NFkB)]$^{6+}$ was excited using a 470 nm white light laser and the emission was collected using a band pass filter 565 – 700 nm. Nuclear stain DAPI was added to the cells (300 nM) for 1 h prior to imaging. DAPI was excited using a 633 nm laser and the emission was collected between 637 – 730 nm.

### 5.2.6 Cytotoxicity

HeLa cells were seeded in a 96-well plate in 100 µL of media at 1 x $10^4$ cells per well for 24 h at 37 ºC with 5 % $CO_2$. $[(Ru(bpy)_2\text{-}phen\text{-}Ar)\text{-}ER]^{9+}$ or [Ru(dppz)(bpy)(bpy-Ar-NFkB)]$^{6+}$ was added to give final concentrations of 200, 150, 100, 50, 20, 10, 1, 0.1 µM of the complex. The cells were incubated with the complex for 24 h at 37 ºC at 5 % $CO_2$. 10 µL of Resazurin (Alamar Blue) reagent was added to each well, and incubated for a further 7 h in the dark at 37 ºC. The resazurin was converted to resorufin in viable cells and its absorbance was measured at 570 nm, with background measured at 600 nm using a Tecan 96-well plate reader.

### 5.2.7 Phosphorescent lifetime imaging microscopy

HeLa cells were seeded on a 35 mm glass bottom dish at 1.5 x $10^5$ in 2 mL for 24 h at 37 °C at 5 % $CO_2$. [Ru(dppz)(bpy)(bpy-Ar-NFkB)]$^{6+}$ (40 µM) was added to the cells and incubated for 24 h in the absence of light. The complex was removed and the cells were washed twice with supplemented PBS. Live PLIM images were acquired usung MicroTime 200, PicoQuant, attached to a Zeiss LSM510 confocal microscope using a 63 x oil immersion objective. Each PLIM image was acquired for 5 minutes with 256×256 resolution. 405 nm laser was used to excite the sample, and emission collected using a long pass 530 nm filter. The data was analysed using PicoQuant Symphotime software. Lifetimes were fit to a mono-exponential decay until a $\chi^2$ value of 0.9 - 1.1 was achieved. The average lifetime was taken from 2 separate experiments (n = 2).

### 5.2.8 STED microscopy of fixed cells

For fixed samples, HeLa cells were seeded at 1.5 x $10^5$ cells on 35 mm glass slides treated with poly-L-lysine for 30 minutes. 70 μM of $[Ru(bpy)_2\text{-Phen-Ar-Arg}_8]^{10+}$ or $[(Ru(bpy)_2phen\text{-Ar})_2\text{-ER}]^{9+}$ for 4 h, or 40 μM of $[Ru(dppz)(bpy)(bpy\text{-Ar-NFkB})]^{6+}$ for 24 h was added in cell media and left to incubate at 37 ºC at 5 % $CO_2$ in the dark. The dye/media solution was removed and cells were washed with PBS supplemented with 1.1 mM $MgCl_2$ and 0.9 mM $CaCl_2$. HeLa cells were fixed using 3.8 % paraformaldehyde after washing with supplemented PBS for 15 minutes in the dark. The solution was removed and slides were washed twice with PBS. For Alexa 532 staining, 1:40 dilution of Alexa Fluor 532 with PBS was added to fixed HeLa cells for 30 minutes, removed, and washed three times with PBS. Fixed cells were mounted using Prolong Gold Antifade Mountant (ThermoFisher Scientific). To acquire STED images, a Leica DMI8 confocal system with STED lasers was used. For $[(Ru(bpy)_2phen\text{-Ar})_2\text{-ER}]^{9+}$, a 488 nm white light laser was used to excite the complex collecting the emission between 590 - 700 nm, and a 528 nm white light laser was used to excite Alexa 532 collecting the emission between 534 – 675 nm with a 100X oil immersion objective. For $[Ru(dppz)(bpy)(bpy\text{-Ar-NFkB})]^{6+}$ the 470 nm confocal laser line and a 660 nm STED depletion laser. Images were scanned at 1024 x 1024 resolutions using a scan speed of 0.01/s. A line accumulation of 6x was used, where the laser scanned each line 6 times to collect enough photons. A frame accumulation of 2x was used to eliminate as much background as possible and to collect a high number of photons. A time gating system was used to separate the two complexes. Alexa 532 was set to 0 - 3.5 ns, and ruthenium set to 5 – 12 ns. A 660 nm depletion laser was used to acquire the STED images, and images were accumulated twice for best signal. Images were deconvolved using Huygens Professional software. All data and FWHM analysis were carried out on raw images before deconvolution process using OriginPro.

### 5.2.9 Photostability Studies

HeLa cells were seeded on poly-L-lysine coated 35 mm glass slides at $1.5 \times 10^5$ for 48 h. $[(Ru(bpy)_2phen\text{-}Ar)_2\text{-}ER]^{9+}$ (70 μM) was added to the cells for 4 h at 37 °C and 5 % $CO_2$ in the absence of light. The cells were washed twice with supplemented PBS. The cells were fixed with 3.8 % paraformaldehyde for 15 minutes and washed with PBS. For Alexa 532 staining, 1:40 dilution of Alexa Fluor 532 with PBS was added to fixed HeLa cells for 30 minutes, removed and washed three times with PBS. Fixed cells were mounted using Prolong Gold. The samples were imaged using the optimised STED settings described in *section 5.2.7*. A 488 nm white light laser was used to excite $[(Ru(bpy)_2phen\text{-}Ar)_2\text{-}ER]^{9+}$ , collecting the emission between 590 -700 nm, and a 528 nm white light laser was used to excite Alexa 532 collecting the emission between 534 – 675 nm with a 100X oil immersion objective. The STED depletion line at 660 nm at 0.05 W was used for both samples. The images were acquired at 1024 x 1024 resolution every 1 minutes over a 30 minute window at a pixel dwell time of 2.43 μs. The emission intensity of a selected area in both samples was measured at each time interval over the 30 minutes and the intensity data was plotted to show stability over time.

## 5.3 Photophysical properties and Characterisation

### 5.3.1 $[(Ru(bpy)_2\text{-}phen\text{-}Ar)\text{-}ER]^{9+}$

Scheme 5.1 illustrates the structure of $[(Ru(bpy)_2phen\text{-}Ar\text{-}COOH)]$, in this instance, conjugated to endoplasmic reticulum directing peptide sequence RQIKIWFQNRRMKWKK, described in *section 5.2.2*, to yield $[(Ru(bpy)_2phen\text{-}Ar)_2\text{-}ER]^{9+}$. The sequence comes from the *Drosophila* transcription factor Antennepedia, which is made up of 60 amino acids.[38] It is this particular 16 amino acid peptide sequence, also known as Penetratin [39] that is responsible for internalisation by all cells.[40,41] The sequence corresponds to the 3rd helix of the DNA binding domain of Antennepedia. Although the sequence is long, it is rich in arginine (R) and lysine (K) residues, which are well known to promote cell uptake due to their positive charge.[42,43]

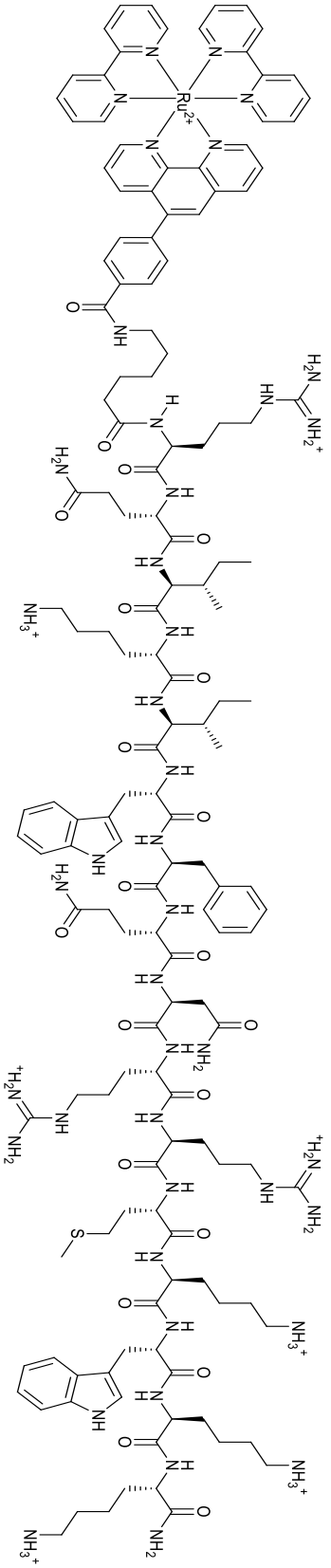

**Scheme 5.1** Chemical structure of $[(Ru(bpy)_2\text{-phen-Ar})\text{-ER}]^{9+}$

Figure 5.1 shows the spectroscopic properties of $[(Ru(bpy)_2phen\text{-}Ar)_2\text{-}ER]^{9+}$ in aqueous solution. The parent complex $[Ru(bpy)_2phen\text{-}Ar\text{-}COOH]^{2+}$, which was discussed in Chapter 3, exhibits an electronic absorption maximum at 460 nm. Upon conjugation to the endoplasmic reticulum (ER) directing peptide sequence RQIKIWFQNRRMKWKK, the absorption shows a slight blue shift in peak maximum to 454 nm, which is assigned to the metal dπ to ligand π* charge transfer (MLCT) transition. The strong absorbance band observed at 284 nm arises from a π-π* transition of the polypyridyl ligands.

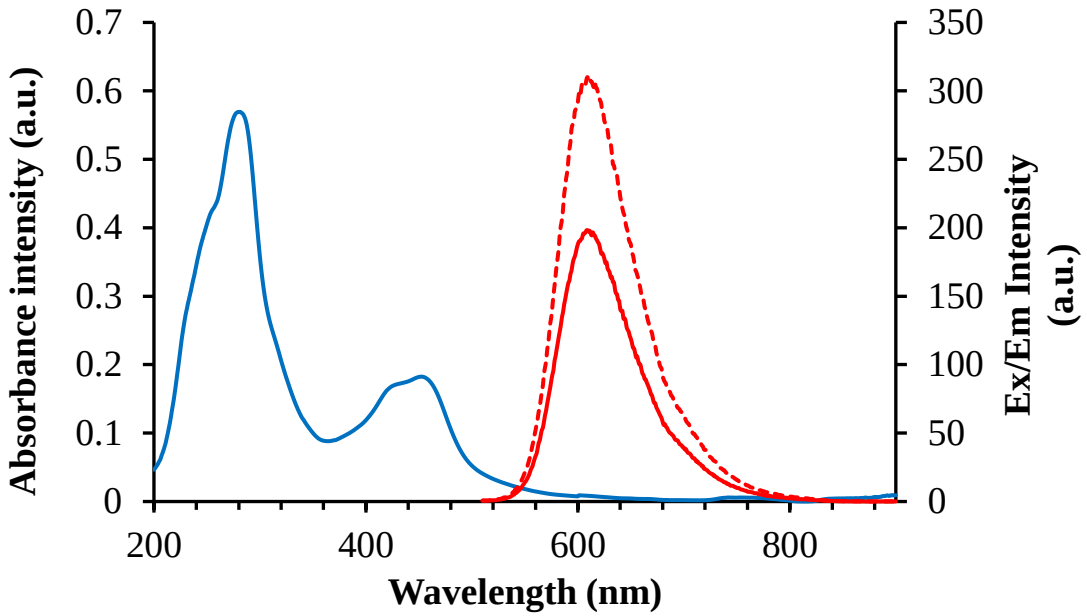


**Figure 5.1** Spectroscopic data of $[(Ru(bpy)_2\text{-}phen\text{-}Ar)\text{-}ER]^{9+}$ in PBS (50 μM). The absorbance **(—)**, and the emission under aerated **(—)** and de-aerated **(- - -)** conditions when excited at 454 nm. Slit width = 5 nm.

When excited into the MLCT transition at 454 nm, an intense emission peak is observed, which is centred at $\lambda_{max}$ 602 nm. When de-aerated with nitrogen for 15 minutes, $[(Ru(bpy)_2\text{-}phen\text{-}Ar)\text{-}ER]^{9+}$ emission intensity increases as expected, as oxygen quenching is reduced. The lifetime of $[(Ru(bpy)_2\text{-}phen\text{-}Ar)\text{-}ER]^{9+}$ was measured using TCSPC, and was found to be 683 ± 8 ns in aerated PBS solution (pH 7.4). Upon de-aeration with nitrogen, the lifetime increased from 683 ± 8 ns to 1.064 μs ± 14 ns. This is considerably higher than the parent complex, but similar to pervious peptide conjugates discussed in Chapter 3. $[Ru(bpy)_2phen\text{-}Ar\text{-}COOH]^{2+}$, the parent complex has a quantum yield (φ) of 0.046 ± 0.003. Upon conjugation to the ER peptide sequence,

surprisingly, the quantum yield decreases to 0.032 ± 0.0015, possibly as a result of the large peptide sequence.

### 5.3.2 [Ru(dppz)(bpy)(bpy-Ar-NFkB)]$^{6+}$

Scheme 5.2 describes the structure of [Ru(dppz)(bpy)(bpyArCOOH)]$^{2+}$ parent complex conjugated to the nuclear localising sequence (NLS) VQRKRQKLMP–$NH_2$, to yield the complex [Ru(dppz)(bpy)(bpy-Ar-NFkB)]$^{6+}$, where dppz = dipyrido[3,2–a:2',3'-]phenazine). The peptide sequence VQRKRQKLMP is known as NF-κB. The sequence originates from the NF-κB transcription factor. Its function is to internalise NF-κB to the nucleus.[44,45]

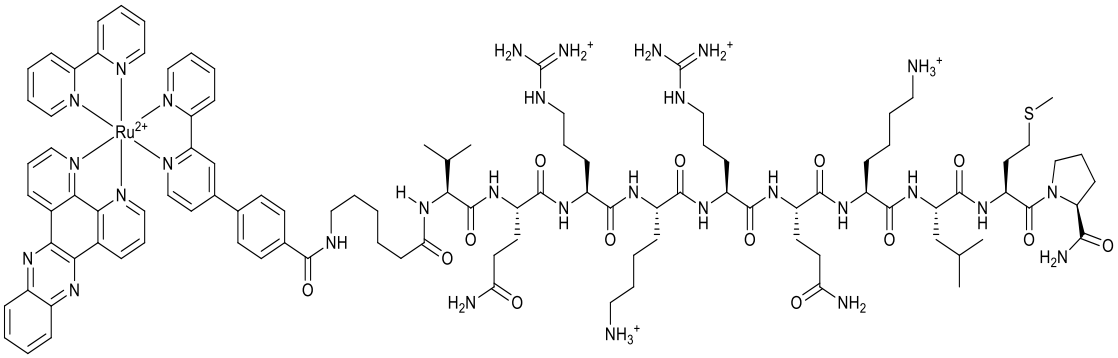

**Scheme 5.2** Chemical structure of [Ru(dppz)(bpy)(bpy-Ar-NFkB)]$^{6+}$

Figure 5.2 shows the spectroscopic properties of [Ru(dppz)(bpy)(bpy-Ar-NFkB)]$^{6+}$. In both acetonitrile and water, the absorbance exhibits similar peak features. The band at 282 nm is assigned to the bpy-centered π-π* transitions, in comparison with [Ru(bpy)$_3$]$^{2+}$. The band at 354 nm can be ascribed to the dppz intraligand π-π* transitions.[46] A peak maximum at 454 nm is assigned to the metal centre π to the phenazine ligand π* charge transfer (MLCT) transition.[47] In non-aqueous media, when excited into the MLCT at 454 nm, a strong emission peak is observed, centred at 620 nm. However, in aqueous solution, [Ru(dppz)(bpy)(bpy-Ar-NFkB)]$^{6+}$ does not emit. This confirms that [Ru(dppz)(bpy)(bpy-Ar-NFkB)]$^{6+}$ behaves, as described for related DPPZ containing complexes as a 'light switch'. The 'light switch' effect is as a result of the phenazine moiety coming in contact with the nitrogen atoms in water.[31]

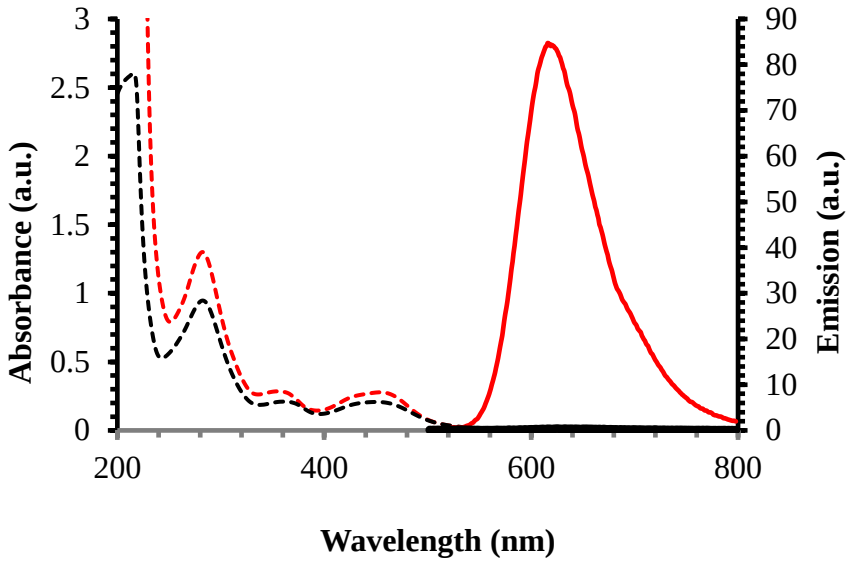


**Figure 5.2** Absorbance and emission spectra of [Ru(dppz)(bpy)(bpy-Ar-NFkB)]$^{6+}$ in MeCN (—) and water (—) at 10 μM. Slit width 5 nm.

The luminescent lifetime of [Ru(dppz)(bpy)(bpy-Ar-NFkB)]$^{6+}$ was found to be 241 ± 1 ns in aerated acetonitrile solution, which increased to 408 ± 20 ns when de-aerated with nitrogen. There was no luminescent lifetime in aqueous PBS solution as [Ru(dppz)(bpy)(bpy-Ar-NFkB)]$^{6+}$ does not emit in water. Table 5.1 summarises the photophysical data of [Ru(dppz)(bpy)(bpy-Ar-NFkB)]$^{6+}$and [(Ru(bpy)$_2$-phen-Ar)-ER]$^{9+}$ for comparison.

**Table 5.1** Photophysical properties of the $[Ru(bpy)_2phen\text{-}Ar\text{-}COOH]^{2+}$ parent complex and $[(Ru(bpy)_2\text{-}phen\text{-}Ar)\text{-}ER]^{9+}$ in PBS solution, and $[Ru(dppz)(bpy)(bpy\text{-}Ar\text{-}NFkB)]^{6+}$ in MeCN.

* ER = peptide sequence RQIKIWFQNRRMKWKK

§ NFκB = peptide sequence VQRKRQKLMP

| **Complex** | **Φ (%)** | **UV-Vis $Abs_{max}$ (nm)** | **$Em\lambda_{max}$ (nm)** | **τ (ns) aerated (18 °C)** | **τ (ns) deaerated (18 °C)** |
|---|---|---|---|---|---|
| **$[Ru(bpy)_2phen\text{-}Ar\text{-}COOH]^{2+}$** | 0.046 ± 0.003 | 460 | 604 | 455 ± 11 | 780 ± 9 |
| **$[(Ru(bpy)_2phen\text{-}Ar)_2\text{-}ER]^{9+}$ *** | 0.032 ± 0.0015 | 454 | 602 | 683 ± 8 | 1.064 μs ± 14 ns |
| **$[Ru(dppz)(bpy)(bpy\text{-}Ar\text{-}NFkB)]^{6+}$ §** | | 454 | 620 | 241 ± 1 | 408 ± 20 |

## 5.4 Cell uptake and Endoplasmic reticulum co-localisation of $[(Ru(bpy)_2\text{-}phen\text{-}Ar)\text{-}ER]^{9+}$

In order to assess the ability of $[(Ru(bpy)_2\text{-}phen\text{-}Ar)\text{-}ER]^{9+}$ to cross the cell membrane and localise in the endoplasmic reticulum (ER), HeLa cells were used. HeLa cells were prepared as described in *section 5.2.5*. All images were acquired using a Leica TSP DMi8 confocal microscope with a 100X oil immersion objective lens. Ru(II) was excited using a 488 nm white light laser line and its emission was collected between 590 – 700 nm.

### 5.4.1 Cell uptake studies of [(Ru(bpy)$_2$-phen-Ar)-ER]$^{9+}$

Uptake studies of [(Ru(bpy)$_2$-phen-Ar)-ER]$^{9+}$ were carried out in live HeLa cells. In Chapter 3, it was demonstrated that [Ru(bpy)$_2$phen-Ar-COOH]$^{2+}$ parent complex did not cross the cell membrane. [(Ru(bpy)$_2$-phen-Ar)-ER]$^{9+}$ (70 μM) was incubated with HeLa cells at 37 °C in the absence of light and its uptake was assessed.

Uptake was found to be instantaneous using confocal microscopy upon incubation with [(Ru(bpy)$_2$-phen-Ar)-ER]$^{9+}$ in phenol red-free media. After 2 hr, the complex was found to distribute throughout the cytoplasm, localising around but not entering, the nuclear envelope, as illustrated in Figure 5.3. A and B expand a selection of HeLa cells, demonstrating that the uptake is the same throughout the sample. C and D focus on a single HeLa cell for a more detailed view on the uptake.

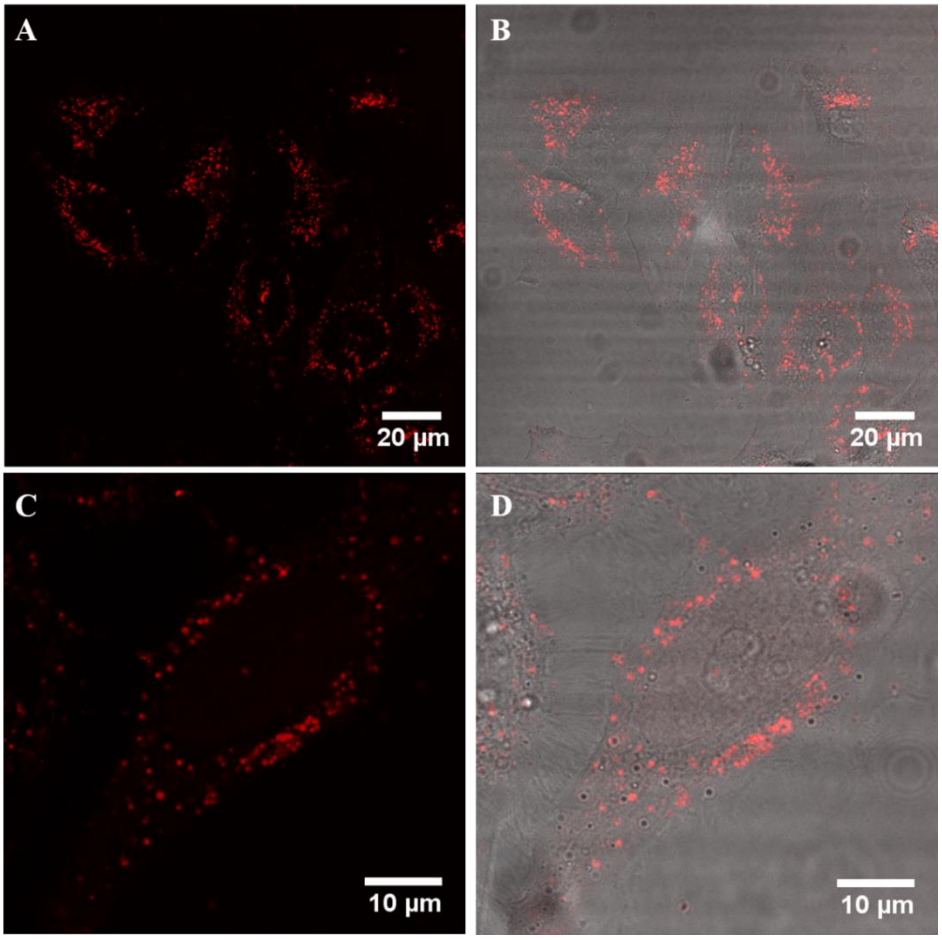


**Figure 5.3** Confocal microscopy of HeLa cells incubated with [(Ru(bpy)$_2$-phen-Ar)-ER]$^{9+}$ (70 μm) in phenol red-free media for 2 h at 37 °C in the absence of light. A and C show [(Ru(bpy)$_2$-phen-Ar)-ER]$^{9+}$ emission channel, and B and D show the overlay with the background channel. The complex was excited using a 488 nm white light laser, and its emission was collected between 590 - 700 nm.

After 4 hr, [(Ru(bpy)$_2$-phen-Ar)-ER]$^{9+}$ appeared to have become selectively localised in the cell. Figure 5.4 illustrates the uptake in HeLa cells after 4 hr exposure. A and B describe a selected area of HeLa cells, are representative of the broader sample. The distribution within the cells was consistent throughout the selected area, and the whole sample. [(Ru(bpy)$_2$-phen-Ar)-ER]$^{9+}$ appeared to have localised in a punctate manner in the cells, around the nuclear envelope.

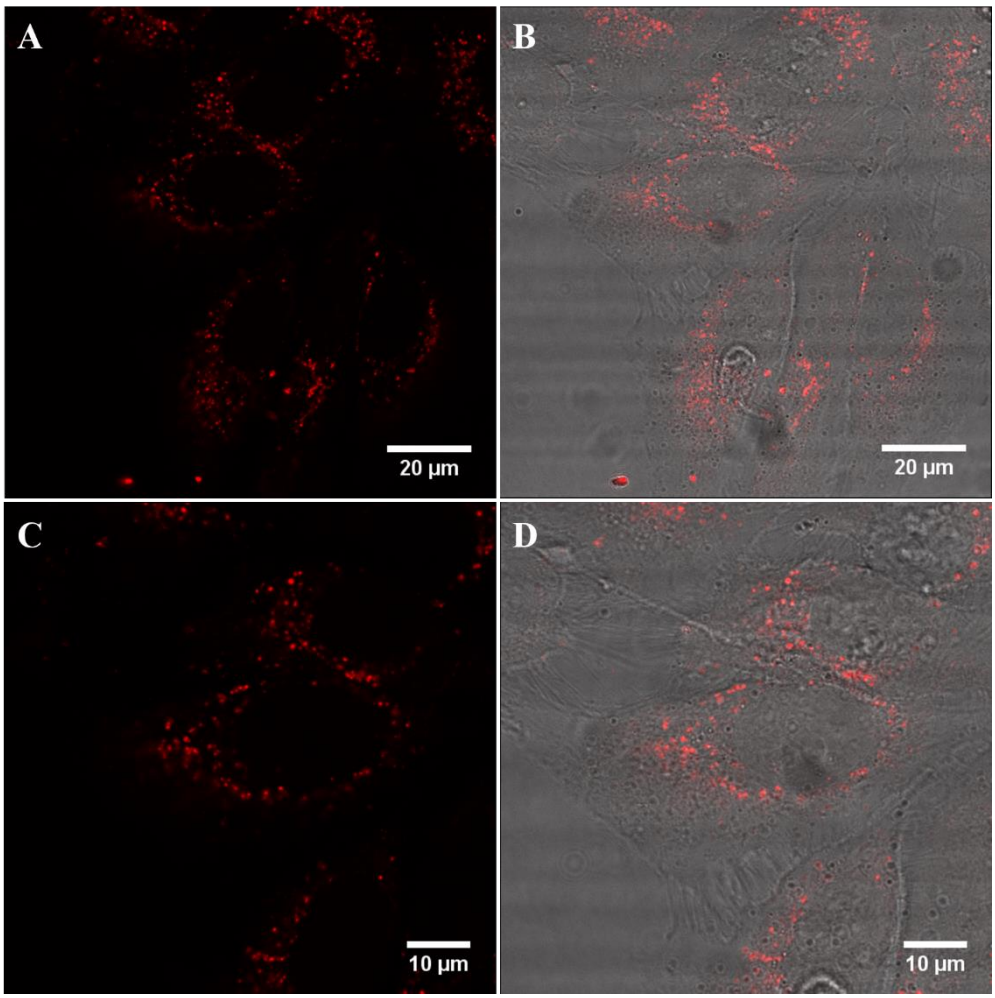


**Figure 5.4** Confocal microscopy of [(Ru(bpy)$_2$-phen-Ar)-ER]$^{9+}$ HeLa cells. The cells were incubated with 70 µM of [(Ru(bpy)$_2$-phen-Ar)-ER]$^{9+}$ in phenol red-free media for 4 h at 37 °C. [(Ru(bpy)$_2$-phen-Ar)-ER]$^{9+}$ was excited at 488 nm and its emission collected between 590 - 700 nm.

Figure 5.4 C and D describes a single HeLa cell, illustrating that [(Ru(bpy)$_2$-phen-Ar)-ER]$^{9+}$ is nuclear excluding. Its localisation around the nuclear envelope suggests that it could be residing in the endoplasmic reticulum (ER). The peptide sequence RQIKIWFQNRRMKWKK has been shown previously to be taken up by

endocytosis.[48,49] The punctate manner may suggest that the complex was taken up by endocytosis, and resides in tiny vesicles in the ER.

### 5.4.2 Endoplasmic reticulum localisation studies

To assess if the ER peptide sequence RQIKIWFQNRRMKWKK was successful in directing a ruthenium polypyridyl complex to the ER, co-localisation studies were carried out. HeLa ells were prepared as described in *section 5.2.5.* After 4 hr incubation with $[(Ru(bpy)_2\text{-phen-Ar})\text{-ER}]^{9+}$ (70 μM), HeLa cells were dual-stained with the commercial probe ER-Tracker Blue (1 μM) for a further 30 minutes before imaging. Figure 5.5 shows the accumulation of the complexes in HeLa cells, where $[(Ru(bpy)_2\text{-phen-Ar})\text{-ER}]^{9+}$ is represented in red, ER-Tracker Blue in blue, and their co-localisation in purple. To confirm that $[(Ru(bpy)_2\text{-phen-Ar})\text{-ER}]^{9+}$ and ER-Tracker Blue were coincident in the ER, a line section across a random location on a HeLa cell was selected and its corresponding fluorescent intensity profile was plot. The distribution intensities coincide exactly, confirming that the two complexes reside in the ER, and both probes are nuclear excluding.

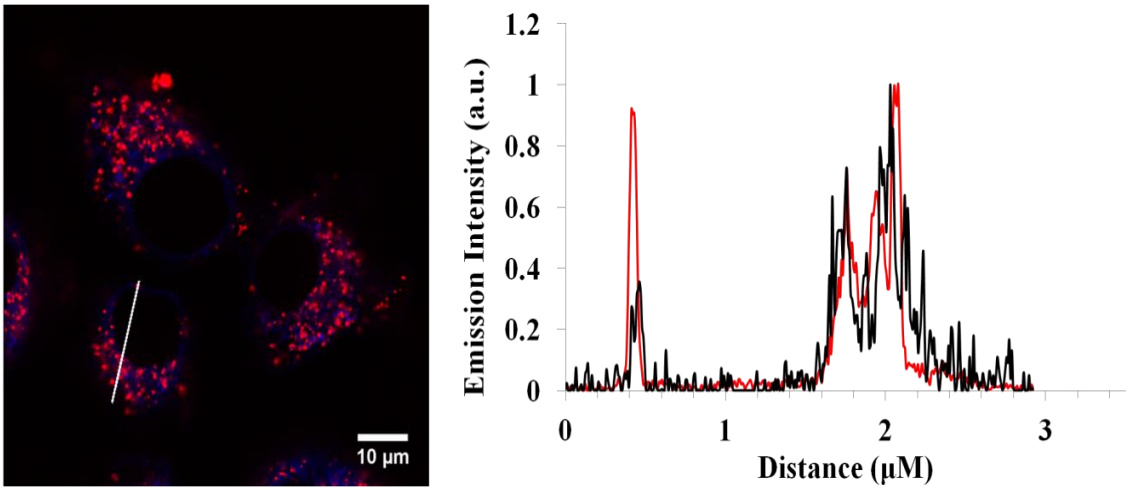


**Figure 5.5** Co-localisation of $[(Ru(bpy)_2\text{-phen-Ar})\text{-ER}]^{9+}$ (red) and ER-Tracker Blue (blue) in HeLa cells. The corresponding intensity distribution plot confirms that $[(Ru(bpy)_2\text{-phen-Ar})\text{-ER}]^{9+}$ (red) and ER-Tracker Blue (black) are coincident in the ER. $[(Ru(bpy)_2\text{-phen-Ar})\text{-ER}]^{9+}$ was excited at 488 nm and its emission was collected at 590 – 700 nm. ER-Tracker Blue was excited at 405 nm and its emission was collected at 450 – 550 nm.

Upon closer examination of the STED image, discussed later in *section 5.10* the mosaic manner in which [(Ru(bpy)$_2$-phen-Ar)-ER]$^{9+}$ is localising in the ER could suggest the complex is within the smooth ER of the cell. The smooth ER consists of a double membrane that makes up sacs called cisternae. Compared to the rough ER, the smooth ER has no ribosomes attached to it, and appears more dilated and convoluted. [50]

This result demonstrates that the peptide sequence RQIKIWFQNRRMKWKK is highly effective in directing ruthenium complexes across the cell membrane and selectively to the ER of a cell.

## 5.5 Cell uptake and nuclear localisation of [Ru(dppz)(bpy)(bpy-Ar-NFkB)]$^{6+}$

In order to assess the ability of [Ru(dppz)(bpy)(bpy-Ar-NFkB)]$^{6+}$ to cross the cell membrane and nuclear envelope to localise in the nucleus, HeLa cells were again used. Cells were prepared as described in *section 6.2.5*. All images were acquired using a Leica TSP DMi8 confocal microscope with a 100X oil immersion objective lens. Ru(II) was excited using a 470 nm white light laser line and its emission was collected between 570 – 700 nm.

### 5.5.1 Live uptake of [Ru(dppz)(bpy)(bpy-Ar-NFkB)]$^{6+}$

Live uptake studies were carried out to assess the efficiency of uptake. [Ru(dppz)(bpy)(bpy-Ar-NFkB)]$^{6+}$ (40 μM) was added to the cells in HeLa media, and the uptake was monitored every 3 minutes by confocal microscopy. Figure 5.6 describes the uptake every 15 minutes over a 60 minute time period. As expected, no emission is observed in the aqueous media. After 45 minutes, a slight emission can be observed from the cell membrane, which reflects the less aqueous conditions found in a lipid membrane. No emission wold be expected from the cytoplasm of the cell due to the aqueous environment.

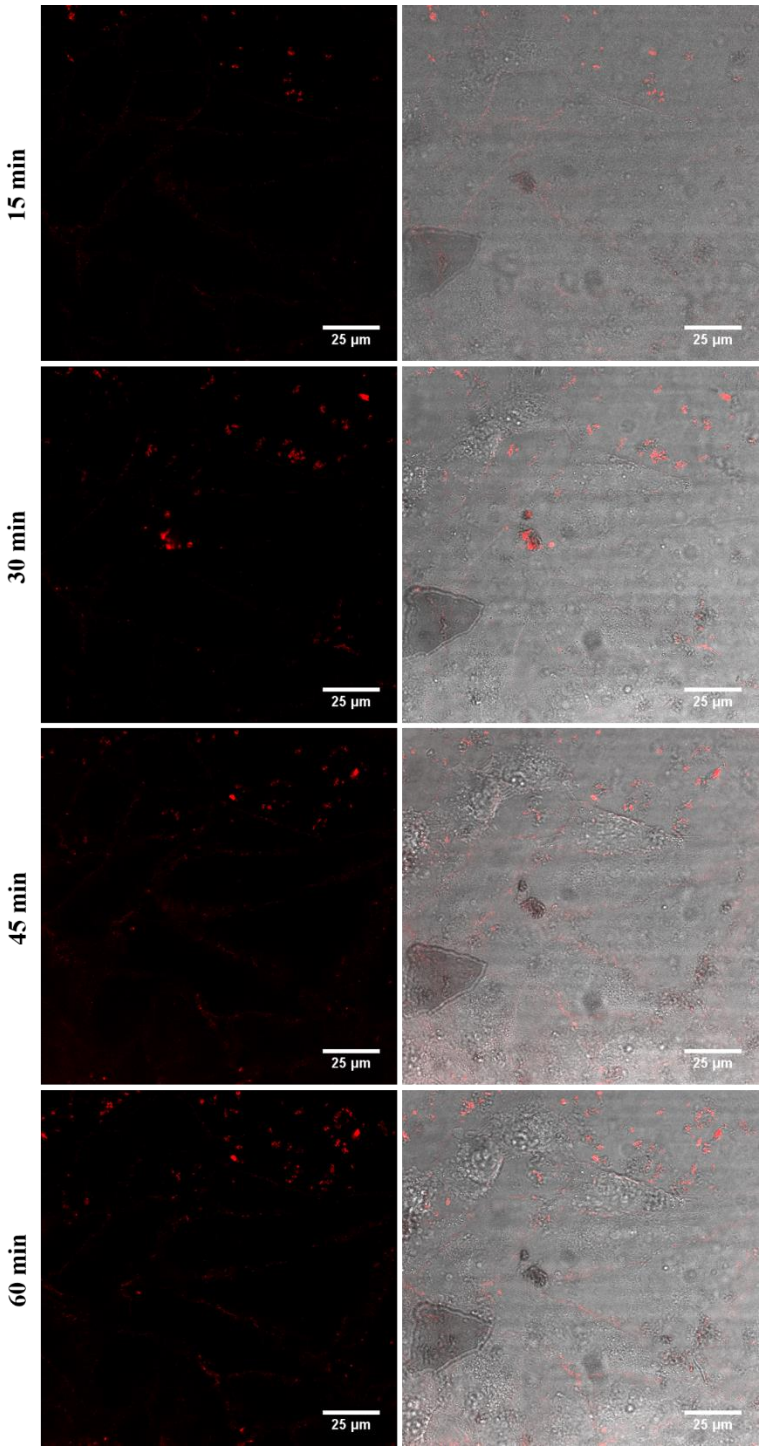


**Figure 5.6** Live uptake of [Ru(dppz)(bpy)(bpy-Ar-NFkB)]$^{6+}$ in HeLa cells. Uptake was monitored and confocal image was collected every 15 minutes. [Ru(dppz)(bpy)(bpy-Ar-NLS)]$^{6+}$ was excited using a 470 nm white light laser and the emission was collected between 565-700 nm.

The cells were incubated with [Ru(dppz)(bpy)(bpy-Ar-NFkB)]$^{6+}$ over 24 h and imaged to monitor uptake. Figure 5.7 describes a group of HeLa cells after 6 h incubation with the complex. Emission can be observed from the cell membrane, and now from the cytoplasm.

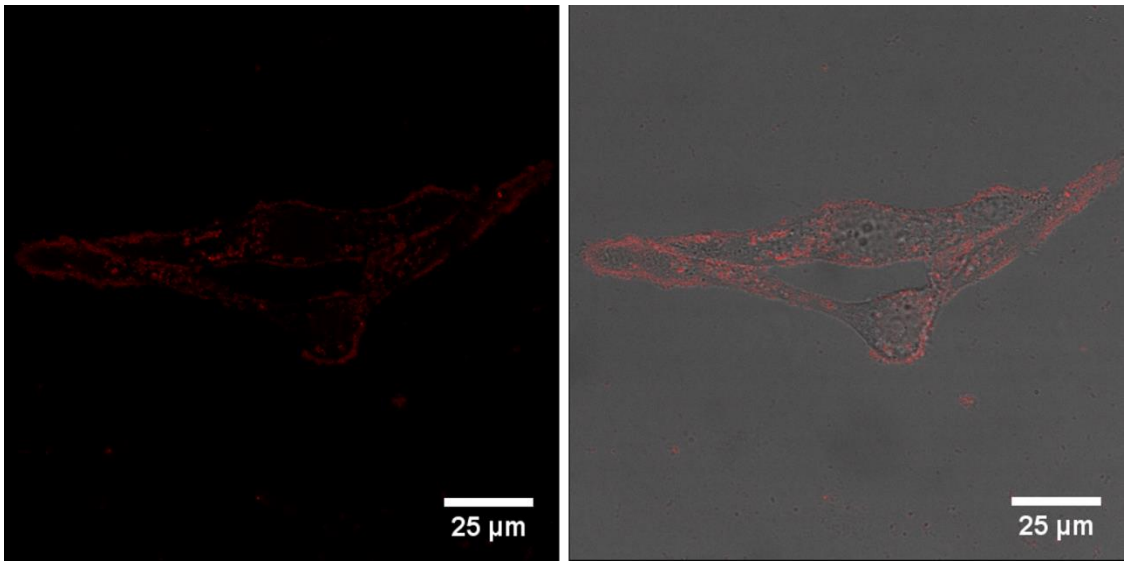


**Figure 5.7** Confocal microscopy of live HeLa cells incubated with [Ru(dppz)(bpy)(bpy-Ar-NFkB)]$^{6+}$ for 6 h in cell media at 37 °C in the absence of light. [Ru(dppz)(bpy)(bpy-Ar-NLS)]$^{6+}$ was excited using a 470 nm white light laser and the emission was collected between 565-700 nm.

It is possible that [Ru(dppz)(bpy)(bpy-Ar-NFkB)]$^{6+}$ is binding to RNA that is present in the cytoplasm. *Ragin et al* have previously demonstrated that the NLS sequence NF-κB locates in the cytosol and nucleus.[44] When bound to RNA, [Ru(bpy)$_2$(dppz)]$^{2+}$ has been shown to luminesce, although not as brightly as when bound to nuclear DNA.[51] As no luminescence was observed in the nucleus, the cells were left to incubate further.

Figure 5.8 shows confocal fluorescence images of HeLa cells following their incubation with [Ru(dppz)(bpy)(bpy-Ar-NFkB)]$^{6+}$ for 24 h, focusing on three different HeLa cells in the sample where the complex has not bound to nuclear DNA (A), and when it has bound (B and C). The uptake across the sample varied. No luminescence in the nucleus was observed in some cells, represented in (A). However, [Ru(dppz)(bpy)(bpy-Ar-NFkB)]$^{6+}$ did enter and bind to nuclear DNA in the majority of cells. The luminescence in (B) confirms that the complex has been 'switched on' as a result of binding. Under the same imaging conditions, the luminescence in (C) is brighter than that of (B)

suggesting that intercalation with the DNA has occurred. The $[Ru(bpy)_2(dppz)]^{2+}$ complex has been demonstrated to bind to DNA, displaying intense luminescence, but can also intercalate with the double helix, further enhancing the luminescence.[47] The uptake and binding in the nucleus does not appear to be uniform across all the cells in the sample – this may be a consequence of the different stages in the cell life cycle, or due to variation in the rate at which binding is occurring.

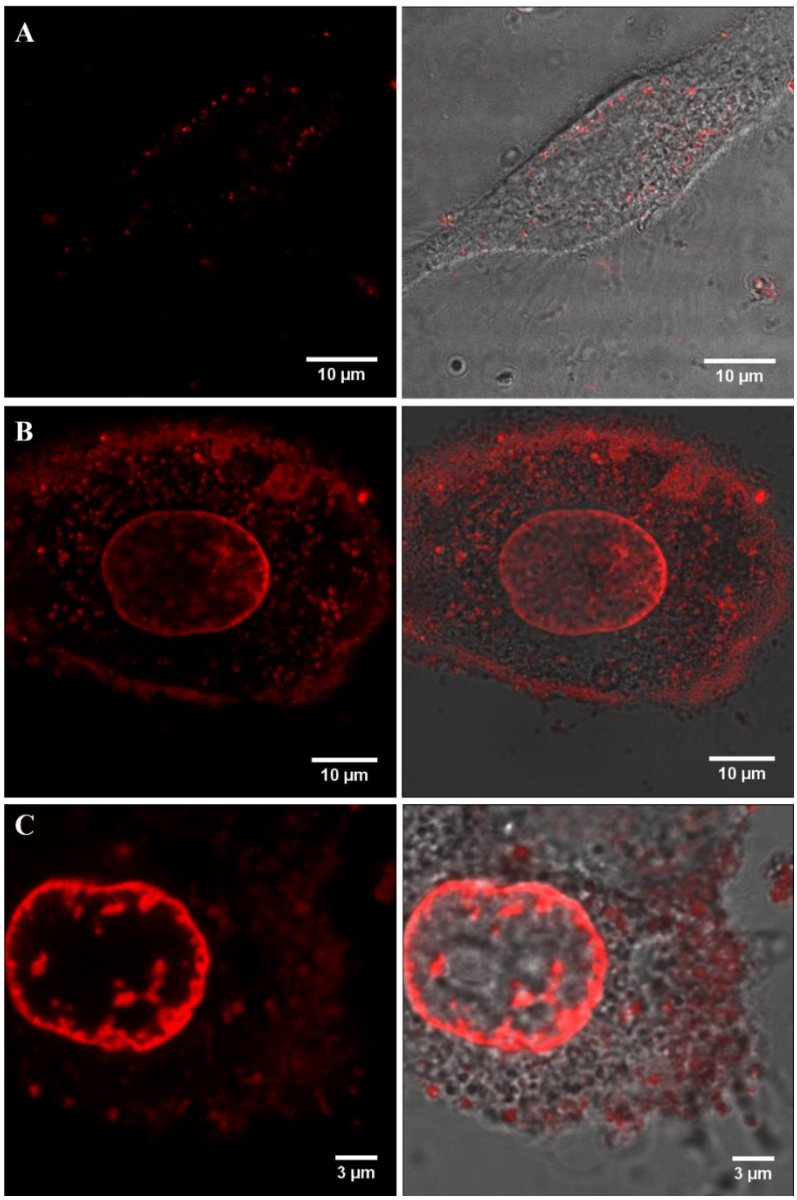


**Figure 5.8** HeLa cells incubated with 40 µM $[Ru(dppz)(bpy)(bpy\text{-}Ar\text{-}NFkB)]^{6+}$ for 24 h. No luminescence was observed in the nucleus in a couple of cells across the sample (A). When bound, $[Ru(dppz)(bpy)(bpy\text{-}Ar\text{-}NFkB)]^{6+}$ luminescence is observed (B), and emits more intensely wen intercalated with the DNA (C). $[Ru(dppz)(bpy)(bpy\text{-}Ar\text{-}NLS)]^{6+}$ was excited using a 470 nm white light laser and the emission was collected between 565-700 nm.

### 5.5.2 Nuclear localisation of [Ru(dppz)(bpy)(bpy-Ar-NFkB)]$^{6+}$

To confirm that [Ru(dppz)(bpy)(bpy-Ar-NFkB)]$^{6+}$ had entered the nuclear envelope, HeLa cells were incubated with the commercial probe DAPI (300 nM). HeLa cells were prepared as described in *section 5.2.5*. Prior to imaging, DAPI was introduced to the cells for 1 h at 37 °C in the absence of light. The cells were washed and imaged. Figure 5.9 describes the nucleus of a HeLa cell, dual stained with [Ru(dppz)(bpy)(bpy-Ar-NFkB)]$^{6+}$ represented in red, DAPI in blue, and their co-localisation in pink/purple. From the image, both complexes appear to reside in the nucleus in a similar manner.

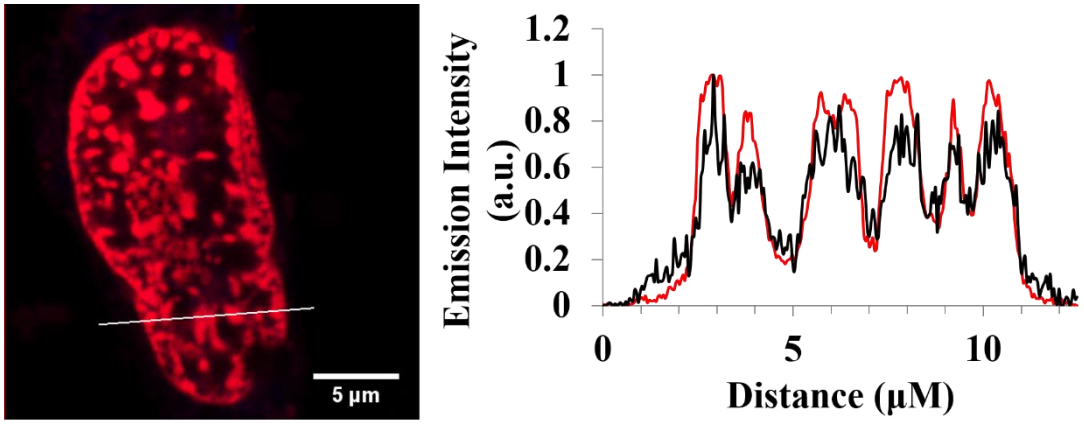


**Figure 5.9** Co-localisation of [Ru(dppz)(bpy)(bpy-Ar-NFkB)]$^{6+}$ (40 µM) (red) and DAPI (300 nM) (blue) in the nucleus of a single HeLa cell. [Ru(dppz)(bpy)(bpy-Ar-NLS)]$^{6+}$ was excited using a 470 nm white light laser and the emission was collected between 565-700 nm. DAPI was excited at 633 nm and the emission was collected between 637-730 nm. The corresponding plot profile indicating both compounds co-localize within the nucleus, where (—) represents [Ru(dppz)(bpy)(bpy-Ar-NLS)]$^{6+}$ and (—) DAPI.

To prove that the two complexes were coincident in the nucleus, a line section across the sample was selected and its corresponding fluorescent intensity profile was plotted, show in in Figure 5.9. The distribution plot confirms that the two complexes both reside in the nucleus. Similar results have been reported from *Blackmore et al* using the NF-κB sequence.[45] They successfully directed two Ru(II) complexes, [Ru(bpy)$_2$PIC-βAla-NFkB]$^{6+}$ and [Ru(dpp)$_2$PIC-βAla-NFkB]$^{6+}$ to the nucleus of CHO cells. This result indicates the high selectivity of the NF-κB peptide sequence in directing transition metal complexes, of different ligand compositions, to the nucleus.

## 5.6 Phosphorescent lifetime imaging (PLIM) of [Ru(dppz)(bpy)(bpy-Ar-NFkB)]$^{6+}$ in the nucleus

As discussed earlier in *section 5.3.2*, there is no luminescence observed from [Ru(dppz)(bpy)(bpy-Ar-NFkB)]$^{6+}$ in aqueous solution, but is switched on when in a non-aqueous environment, such as when it is bound to DNA. PLIM can be applied to measure the luminescent lifetime of the complex when it begins to bind with nuclear, and monitor the intercalation process with DNA from within the nucleus.

As illustrated by Figure 5.8 A, [Ru(dppz)(bpy)(bpy-Ar-NFkB)]$^{6+}$ luminescence was not observed in the nucleus of all cells in the sample when they had been incubated with the complex for 24 h at 37 °C in the absence of light. However, absence of luminescence does not necessarily mean the complex has not entered the nucleus as it may be present but not bound to DNA, and therefore is incapable of emitting. Phosphorescence lifetime imaging microscopy (PLIM) was carried out to assess if the complex had entered the nucleus but had not yet intercalated with DNA. Figure 5.10 shows the confocal imaging and the corresponding false-colour PLIM image of the lifetime distributions in the cell. The cells were prepared as described in *section 5.2.7*. Figure 5.10 (A) shows a live single HeLa cell incubated with [Ru(dppz)(bpy)(bpy-Ar-NFkB)]$^{6+}$ for 24 h. A slight emission from [Ru(dppz)(bpy)(bpy-Ar-NFkB)]$^{6+}$ can be observed around the nuclear envelope, but there is no indication it has intercalated with DNA. The PLIM image shows that the ruthenium complex localised in the nucleus, which exhibits a different luminescent lifetime distribution than the dye in the cytoplasm. Using SymphoTime Software it was found that the lifetime of [Ru(dppz)(bpy)(bpy-Ar-NFkB)]$^{6+}$ in the nucleus was 189 ns, compared to 398 ns when bound to membrane structures in the nucleus (B), further protecting [Ru(dppz)(bpy)(bpy-Ar-NFkB)]$^{6+}$ from an aqueous environment. This is a significant increase from the lifetime in non-aqueous solution, which was found to be 241 ns. As there is no emission when [Ru(dppz)(bpy)(bpy-Ar-NFkB)]$^{6+}$ is in an aqueous environment, the emission lifetime from (A) suggests that [Ru(dppz)(bpy)(bpy-Ar-NFkB)]$^{6+}$ has entered the nucleus and has bound to some DNA proteins present, but has not yet intercalated with the DNA.

On the other hand, the complex emission from the cytoplasmic region exhibited a shorter luminescent lifetime than the lifetime when in the nucleus, ranging between 36 and 67 ns compared to 398 ns, indicating that the complex is not bound to DNA but is shielded from the water molecules. Examining the structural distribution of the dye in the cell,

indicates that the emission is coming from the membrane structures in the nucleus of the cell. Such emission on DPPZ binding to lipid membrane structures has been reported before and is attributed to weak intercalation of this ligand into the membrane. *Cosgrave et al* observed similar binding membrane structures with $[Ru(dppz)_2PIC\text{-}Arg_8]^{10+}$ complex in Sp2 mouse myeloma cells. [52] The longer nuclear lifetimes compared to the cytoplasm indicates that protection from the surrounding water molecules is more effective when $[Ru(dppz)(bpy)(bpy\text{-}Ar\text{-}NFkB)]^{6+}$ is bound to DNA compared to membrane structures. Similar results were reported by *Baggaley et al*. They reported on a dinuclear ruthenium polypyridyl complex that when bound to nuclear DNA, and demonstrated a decrease in luminescent lifetime in the cytoplasm (124 ns) compared to the nucleus (200 ns) using PLIM.[35]

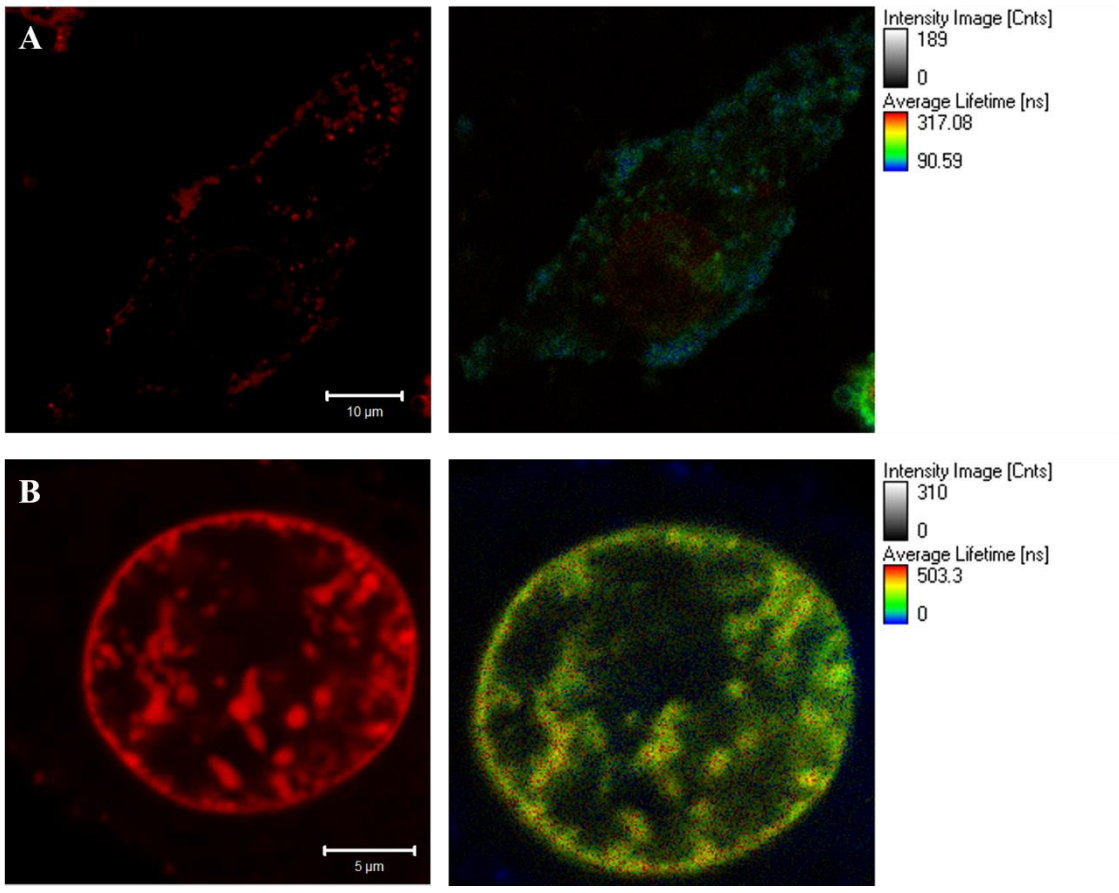


**Figure 5.10** Confocal and luminescent lifetime images of $[Ru(dppz)(bpy)(bpy\text{-}Ar\text{-}NFkB)]^{6+}$ (40 µM) in the nucleus of HeLa cells comparing when unbound (A) and bound (B) to nuclear proteins and membrane structures. $[Ru(dppz)(bpy)(bpy\text{-}Ar\text{-}NFkB)]^{6+}$ was excited at 488 nm and the emission was collected using a long pass 560 nm filter. The PLIM image was acquired by exciting at 405 nm, and emission was collected using a long pass 530 nm filter.

## 5.7 Cytotoxicity

The toxicity of $[(Ru(bpy)_2\text{-phen-Ar})\text{-ER}]^{9+}$ was evaluated in HeLa cells, as described in *section 5.2.6*, and compared to the toxicity of $[(Ru(bpy)_2\text{phen-Ar})_2\text{-Arg}_8]^{10+}$. As discussed in Chapter 3, it was found that $[(Ru(bpy)_2\text{phen-Ar})_2\text{-Arg}_8]^{10+}$ was highly toxic towards HeLa cells, where only 40 % of cells remained viable at 50 μM after 24 h exposure to the complex. Figure 5.11 demonstrates that, in contrast to $[(Ru(bpy)_2\text{phen-Ar})_2\text{-Arg}_8]^{10+}$, $[(Ru(bpy)_2\text{-phen-Ar})\text{-ER}]^{9+}$ displayed little to no toxicity towards HeLa cells over 24 hours incubation.

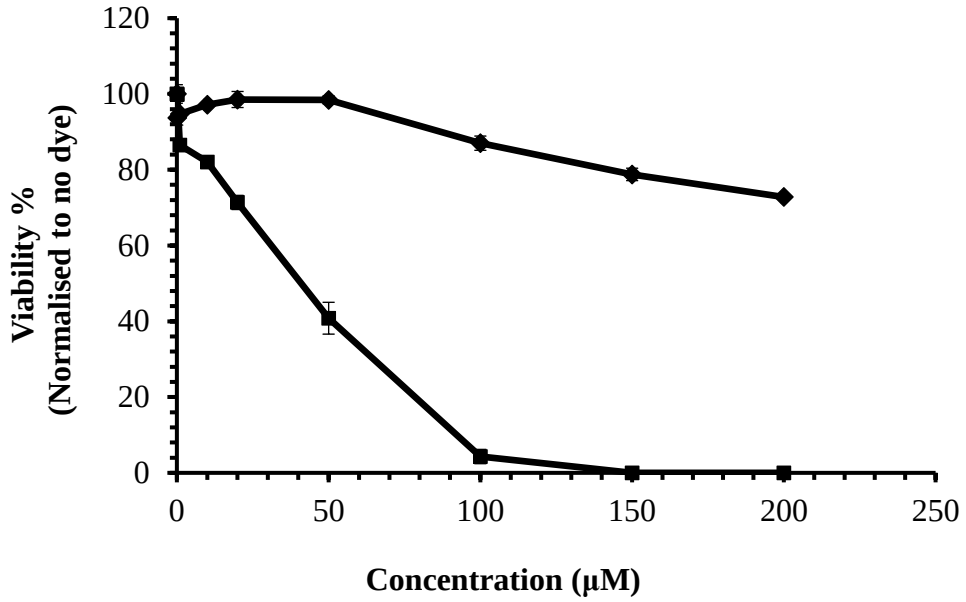


**Figure 5.11** Cytotoxicity studies of $[(Ru(bpy)_2\text{-phen-Ar})\text{-ER}]^{9+}$ **(♦)** and **(■)** $[(Ru(bpy)_2\text{phen-Ar})_2\text{-Arg}_8]^{10+}$ in HeLa cells over 24 h at 37 °C in the absence of light. The Resazurin (Alamar Blue) assay was used to determine the percentage (%) of viable cells remaining. (n = 3)

After 24 h exposure, it was found that 72 % of cells were still viable at high concentrations of 200 μM $[(Ru(bpy)_2\text{-phen-Ar})\text{-ER}]^{9+}$, where 0 % were viable at 200 μM $[(Ru(bpy)_2\text{phen-Ar})_2\text{-Arg}_8]^{10+}$. As the metal complex in each probe is identical the distinction in terms of toxicity must be attributable to the identity of the peptide. This may be because the octa-arginine is fundamentally cytotoxic which we can exclude on the basis that other Ru(II) complexes bound to this peptide (e.g. Chapter 2) were not cytotoxic or it may be a result of the variation in location of the metal complex as a consequence of peptide targeting. The octa-arginine peptide sequence distributes the complex throughout the entire cell, with no organelle specificity, whereas the ER peptide

leads to precise targeting and localisation of the metal complex to within the smooth ER. The smooth ER is involved in the production and storage of lipids, regulation of intracellular $Ca^{2+}$, and detoxification.[53] Whereas on the other hand, $[(Ru(bpy)_2phen\text{-}Ar)_2\text{-}Arg_8]^{10+}$ enters many cellular organelles including the mitochondria. As the mitochondria are involved in the production of the cell energy in the form of ATP, and in respiration, any interference here would expect to have toxic effects towards the cell. Therefore, the $[(Ru(bpy)_2\text{-phen-Ar})\text{-ER}]^{9+}$ complex localising in the smooth ER alone may prevent toxic effects on the cell over the 24 h exposure period of this experiment.

Similarly, the toxicity of $[Ru(dppz)(bpy)(bpy\text{-Ar-NFkB})]^{6+}$ was evaluated in HeLa cells as described previously in *section 5.2.6*. It was compared to the parent complex $[Ru(dppz)(bpy)(bpyArCOOH)]^{2+}$, and to the octa-arginine conjugate, $[Ru(dppz)(bpy)(bpy\text{-Ar-}Arg_8]^{10+}$, to assess if location was a factor in the toxicity of the complex. Figure 5.12 shows the results. As expected, the parent complex did not induce toxicity as it is not taken up by the cells.

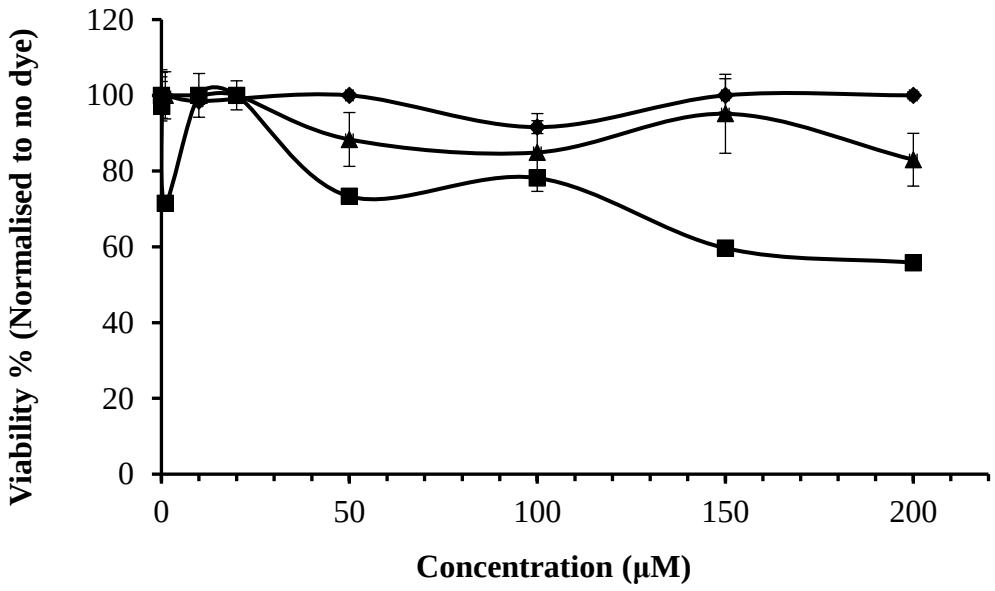


**Figure 5.12** Cell viability studies in HeLa cells. $[Ru(dppz)(bpy)(bpyArCOOH)]^{2+}$ parent complex (•), $[Ru(dppz)(bpy)(bpy\text{-Ar-NFkB})]^{6+}$ (■), and $[Ru(dppz)(bpy)(bpy\text{-Ar-}Arg_8]^{10+}$ (▲) were added to HeLa cells at various concentrations and left to incubate for 24 h at 37 °C in the absence of light. The resazurin (Alamar Blue) assay was used to determine the percentage (%) of viable cells remaining. (n = 2).

Whereas [Ru(dppz)(bpy)(bpy-Ar-NFkB)]$^{6+}$ was found to be moderately toxic towards the cells, with 55 % still viable after exposure to 200 μM for 24 h. At 50 μM, 73 % remained viable. This reflects the results from the uptake studies, where the cells were still viable after incubation with 40 μM for 24 h. This result is somewhat surprising as the complex is localised in the nucleus and intercalating with the nuclear DNA, where it might be expected to impeded cell division. Interestingly in contrast to the very high toxicity of [(Ru(bpy)$_2$phen-Ar)$_2$-Arg$_8$]$^{10+}$ when incubated with [Ru(dppz)(bpy)(bpy-Ar-Arg$_8$]$^{10+}$ , 83 % of cells were still viable at 200 μM and 88 % and 50 μM. This result indicates that, as indicated in Chapter 3, it is indeed the [(Ru(bpy)$_2$phen-Ar)]$^{2+}$ complex that is toxic, but that its ability to exert a toxic effect depends on its location, it would appear to be toxic when it enters the mitochondria. Many reported metal complexes used as a DNA stain possess anti-proliferative effects on the cells over long exposure times as a result of localising in the nucleus, interfering with processes involving DNA. For example, *Gill et al* reported on [Ru(phen)$_2$(tpphz)]$^{2+}$ metallo-intercalator, which exhibited high toxic effects towards human cancer cells.[54] In other work, *Barton et al* reported on a highly toxic rhodium complex, whose toxicity was a result of it binding to DNA.[55] Following 24 h exposure to the complex, less than 10 % of cells remained viable at low concentrations of 25 μM. Such complexes are useful as anti-proliferative, anti-cancer drugs. However, their high toxicity is not ideal for cell imaging of nuclear DNA. On the other hand, the low toxicity of [Ru(dppz)(bpy)(bpy-Ar-NFkB)]$^{6+}$ allows for the complex to be applied as a DNA imaging agent to image chromosomal DNA in live cells. However, photocytotoxicity may become an issue over extended imaging windows.

## 5.8 Application of Ru(II) complexes to super resolution microscopy

As discussed previously, ruthenium complexes possess the properties for stimulated emission depletion (STED) microscopy. Their large Stokes shift, high quantum yields, long lived emissive state are among the desired properties of a STED imaging probe. Both [(Ru(bpy)$_2$-phen-Ar)-ER]$^{9+}$ and [Ru(dppz)(bpy)(bpy-Ar-NFkB)]$^{6+}$ displayed many of these important properties, when evaluated in *section 5.3*.

Alexa Fluor Phalloidin 532 is a commercial prove that stains the actin filaments in a cell. Alexa Fluor dyes are known for their high quantum yields and photostability, which have been applied to super resolution microscopy.[14,18,56]

Figure 5.13 shows the fluorescence spectra of [(Ru(bpy)$_2$-phen-Ar)-ER]$^{9+}$ excited at 470 nm and emission detection at 611 nm, and Alexa 532 excited at 528 nm and emission detected at 552 nm. The excitation and emission of [(Ru(bpy)$_2$-phen-Ar)-ER]$^{9+}$ (red) demonstrate its large Stokes shift. The absorbance and emission spectra of Alexa 532 confirms that there is no spectral overlap with [(Ru(bpy)$_2$-phen-Ar)-ER]$^{9+}$. Therefore, they can be introduced into a single sample for comparison to asses if they are suitable for STED imaging of cells.

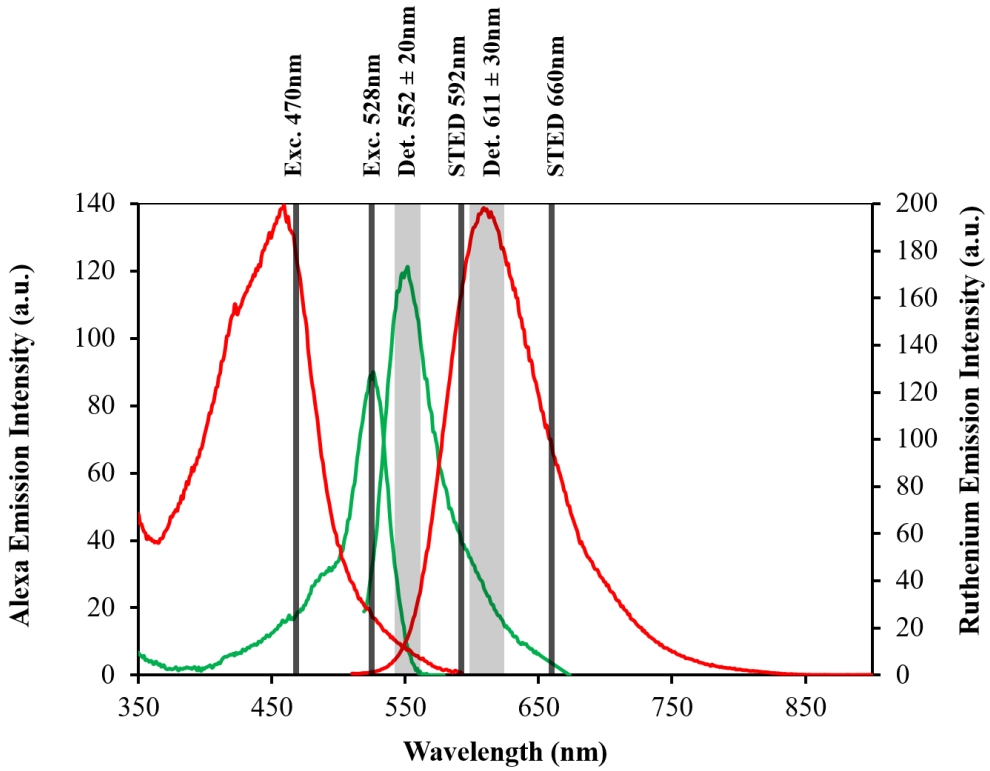


**Figure 5.13** Spectral rationale of confocal and STED setup. Ruthenium excitation and emission (—), and Alexa Fluor 532 excitation and emission spectra (—), in aerated PBS solution.

Figure 5.13 also shows the STED depletion laser at 660 nm. Both [(Ru(bpy)$_2$-phen-Ar)-ER]$^{9+}$ and Alexa 532 emission profiles overlap with the 660 nm depletion laser, indicating that they are well suited for this laser line without re-absorption by the ground state of the dye.

In order to achieve emission depletion through STED and avoid re-excitation, the STED laser line must overlap with the tail of the emission spectra. In the case of [(Ru(bpy)$_2$-phen-Ar)-ER]$^{9+}$ , it has an Em$\lambda_{max}$ at 611 nm. Therefore, the 660 nm STED depletion

laser coincides with the red tail of the emission spectra, to give sufficient depletion without re-excitation. In the case of Alexa 532, it has an $Em\lambda_{max}$ at 552 nm. From Figure 5.13, the 660 nm STED depletion laser overlaps slightly with the tail of the emission spectra. As it only slightly overlaps, it might be expected that the 592 nm STED depletion laser would result in better emission depletion than the 660 nm laser as 592 nm overlaps more with the emission tail. Therefore, the performance of the complex was assessed comparing depletion separately by both 592 nm and 660 nm depletion laser lines. HeLa cells were prepared as described in *section 5.2.8*. HeLa cells were fixed with 3.8 % paraformaldehyde, then stained with Alexa 532 (1: 40) for 30 minutes, and washed three times with PBS. Cells were mounted using ProLong Gold Antifade Mountant for 24 h. This ensures the sample has a refractive index (RI) = 1.47, which is closely matched to the index of the immersion oil used (1.518). Figure 5.14 shows STED images of a single HeLa cell. The images were acquired using the 592 nm (A) and 660 nm (B) depletion lasers. It might be expected that the 592 nm laser would be better suited to Alexa 532 depletion due to closer overlap of with its emission spectrum. However, it is evident from the images that the overall resolution and clarity is much improved following excitation with the 660 nm laser.

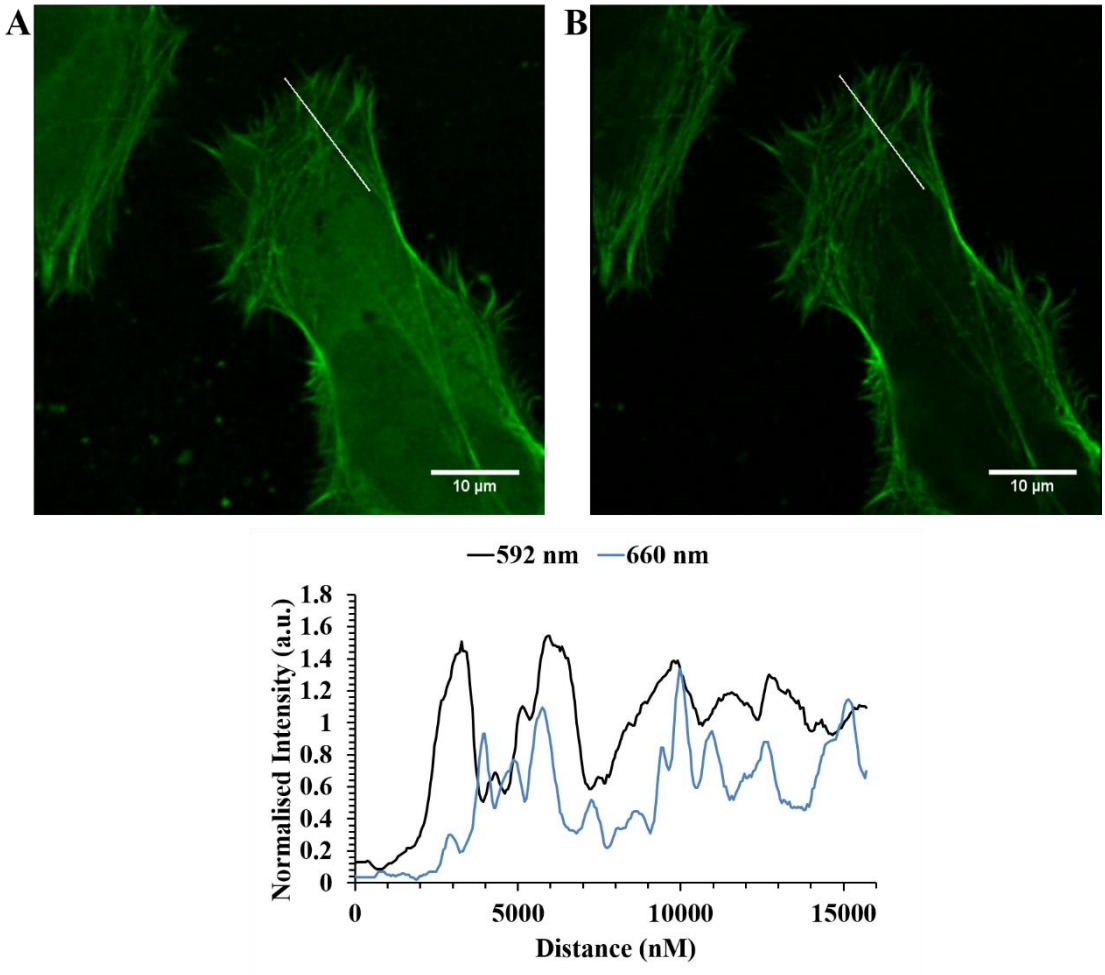


**Figure 5.14** STED imaging of Alexa Fluor Phalloidin 532 in HeLa cells fixed with 3.8 % paraformaldehyde and mounted with Prolong Gold. The STED images were collected following excitation with the 592 nm (A) and 660 nm (B) depletion lasers. The following X-Y plot confirms the improved resolution and elimination of background noise upon exciting with the 660 nm laser (—) compared to the 592 nm laser (—).

This is confirmed by the X-Y plot of the selected line profile through the region of interest. The plot from the 660 nm image (—) displays much improved resolution compared to the plot at 592 nm (—). For example, between 1000 nm and 1500 nm across the X-Y profile in Figure 5.14, the actin filaments are resolved when excited with the 660 nm depletion laser, resulting in more detail observed in the peaks in the X-Y plot compared to the wider, more intense peaks when the 592 nm laser was used. An improvement in structural detail of the actin filaments is obtained exciting at 660 nm, because it reduces the background noise which was observed when the 592 nm laser which is attributed to re-excitation of the Alexa under this wavelength. This results in an overall sharper, clearer image. This confirms that the 660 nm depletion laser is best

suited towards Alexa 532, and can be used as a comparison to assess the performance of $[(Ru(bpy)_2\text{-phen-Ar})\text{-ER}]^{9+}$ as a STED imaging probe.

## 5.9 Confocal microscopy versus STED microscopy of dual-stained HeLa cells

Single-colour staining means that only one molecular species can be observed in a cell at a given time. Dual-staining allows for multiple organelles to be imaged during the course of a single experiment. Such experiments can enable one to study and monitor multiple sites, particularly dynamics at multiple sites within a single cell at once. For dual colour experiments the chosen luminophores must not spectrally overlap, but at the same time must be depletable using a single STED depletion laser. As discussed in *section 5.6*, the ruthenium (II) poplypyridyl complex and Alexa 532 emission spectra do not overlap but both species emission can be stimulated for each with the 660 nm STED depletion laser. To evaluate $[(Ru(bpy)_2\text{-phen-Ar})\text{-ER}]^{9+}$ and $[(Ru(bpy)_2\text{phen-Ar})_2\text{-Arg}_8]^{10+}$ as STED probes, HeLa cells were prepared with either $[(Ru(bpy)_2\text{-phen-Ar})\text{-ER}]^{9+}$ or $[(Ru(bpy)_2\text{phen-Ar})_2\text{-Arg}_8]^{10+}$ (70uM) as described in *section 5.2.8* and were dual-stained with Alexa 532. Samples were mounted with ProLong Gold Antifade Mountant for 24 h, and were imaged by both confocal and STED microscopy using a Leica TSP DMi8 instrument.

Figure 5.15 shows a single HeLa cell using a 100X objective lens, where the image was collected from the edge of the cell, showing the actin filaments in the cell. Here, the confocal image was compared to the super-resolution image. Figure 5.15 A compares a confocal and continuous wave STED (CW-STED) image at the region of interest. The confocal image was obtained by exciting at 528 nm and collecting the emission between 534 – 675 nm. Figure 5.15 B shows $[(Ru(bpy)_2\text{phen-Ar})_2\text{-Arg}_8]^{10+}$, which was excited at 488 nm, and the emission was collected between 590 – 700 nm.

Upon dual staining, it is evident that Alexa 532 has forced some $[Ru(bpy)_2\text{phen-Ar})_2\text{-Arg}_8]^{10+}$ complex to enter the actin filaments. Alexa 532 has an overall negative charge, and the phalloidin has a very strong affinity for the actin filaments in a cell. As the cells require fixing with 3.8 % paraformaldehyde in order to stain with Alexa 532, the negative charge of the probe may cause association of the positively charged $[Ru(bpy)_2\text{phen-Ar})_2\text{-Arg}_8]^{10+}$ drawing it with it as it stains the actin filaments. As will be discussed in *section 5.10*, when stained and fixed by itself, $[Ru(bpy)_2\text{phen-Ar})_2$-

$Arg_8]^{10+}$ does not stain the actin filaments, indicating it is phalloidin that drives $[Ru(bpy)_2phen\text{-}Ar)_2\text{-}Arg_8]^{10+}$ to the actin filaments on fixing. The overall resolution of the CW-STED images has improved compared to the confocal images. To further evaluate the improvement of using CW-STED versus confocal imaging, the full width half maxima (FWHM) of a selected filament of each complex was assessed. The full width half maxima of the point spread function is used to evaluate the relative quality of the confocal and CW-STED images. The fluorescence intensity of the X-Y plots are fitted to a Gaussian distribution in order to measure the FWHM. In the case of $[(Ru(bpy)_2phen\text{-}Ar)_2\text{-}Arg_8]^{10+}$, the FWHM was greatly improved from 226.66 nm in the confocal image, to 86.8 nm after acquiring a CW-STED image. In comparison, the FWHM of Alexa 532 reduced just slightly from 363.8 nm to 315.4 nm. After using CW-STED, $[(Ru(bpy)_2phen\text{-}Ar)_2\text{-}Arg_8]^{10+}$ exhibited more than a 60 % improvement compared to only 10 % for Alexa 532. *Urban et al* reported on STED imaging of the actin filaments in a neuronal cell[57] where they used Lifeact YFP to label the actin of the live cells. They excited the sample at 490 nm and used a 595 nm STED depletion laser to image to actin filaments inside synapses of up to 120 μm below the tissue surface. They were able to achieve spatial resolutions of between 60 to 80 nm of the actin filaments. These results are similar to the resolution achieved using $[(Ru(bpy)_2phen\text{-}Ar)_2\text{-}Arg_8]^{10+}$ to inadvertently image the actin of HeLa cells.

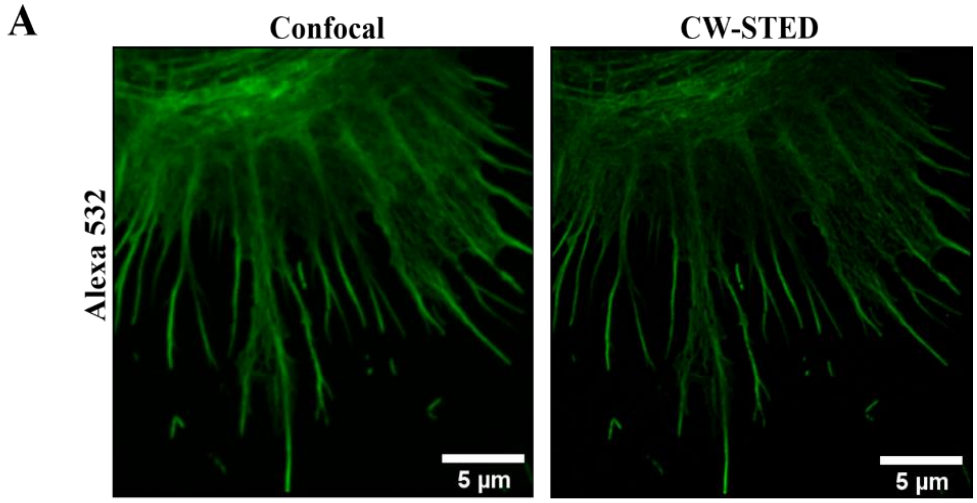

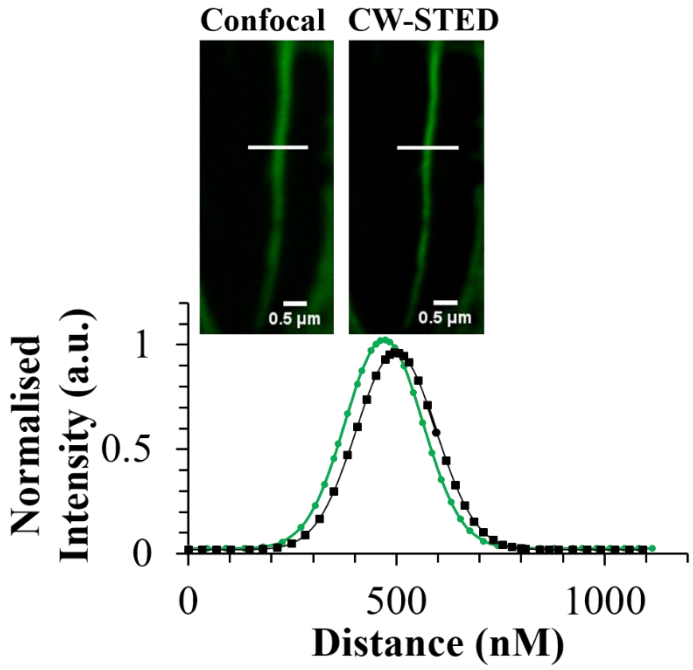
Confocal
CW-STED
0.5 µm
0.5 µm
Normalised Intensity (a.u.)
1
0.5
0
0
500
1000
Distance (nM)

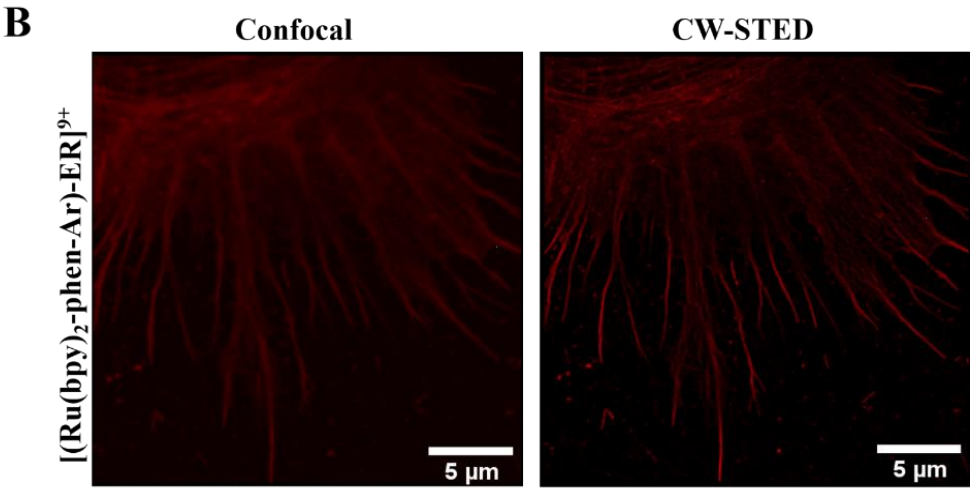
B
Confocal
CW-STED
[(Ru(bpy)2-phen-Ar)-ER]9+
5 µm
5 µm

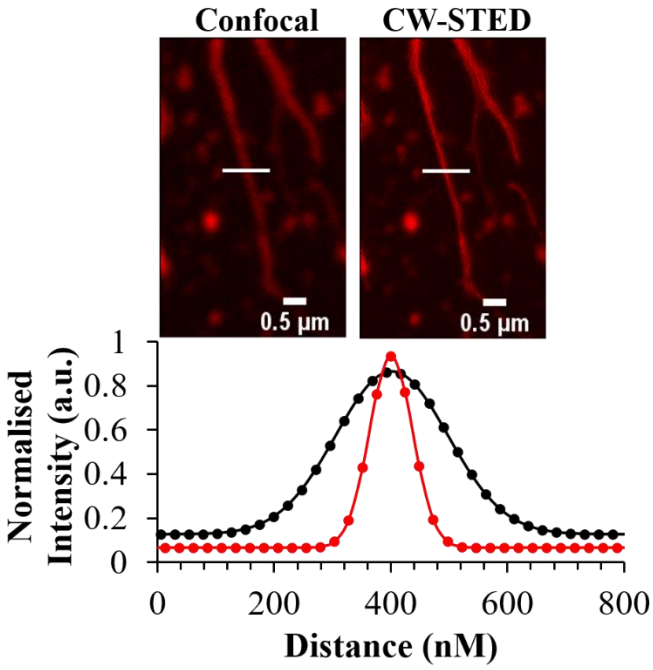


**Figure 5.15** Alexa 532 (A) and $[(Ru(bpy)_2phen\text{-}Ar)_2\text{-}Arg_8]^{10+}$ (B) in a fixed single HeLa cell. The confocal image and CW-STED image of each complex is compared, with their corresponding intensity plot profiles describing the full width half maxima (FWHM) improvements in resolution. The FWHM was obtained by fitting fluorescence-intensity to Gaussian distributions (OriginPro). Alexa 532 was excited at 528 nm and the emission was collected between 534 and 675 nm. $[Ru(bpy)_2phen\text{-}Ar)_2\text{-}ER]^{9+}$ was excited using a 488 nm white light laser and 660 nm depletion laser. The 660 nm STED depletion laser was used for both probes.

## 5.10 Evaluation of time-gated STED microscopy

Up until now, all of the STED images acquired in this chapter were carried out using continuous wave STED (CW-STED). Time-gated detection in super resolution serves as a spatial filter that reduces background noise and any auto-fluorescence from the sample, improving the resolution of the image quality.[58,59] Time-gated STED is also very useful in resolving two dyes with different excited emissive lifetimes.[60,61] Time-gate detection is used in fluorescence microscopy to suppress background from an image such as auto-fluorescence. Time-gate imaging exploits the luminescent lifetime of the probe by eliminating the detection of arriving excited photons based on their arrival times. Auto-fluorescence and background noise typically have fluorescent lifetimes of ~3 ns. Using time-gate imaging can eliminate such interferences based on the lifetime of the detected photons to improve spatial resolution. For this reason, probes that possess

long luminescent lifetimes are ideal for imaging using this technique. Time-gate detection limits the detected fluorescence of each channel and suppresses the detection signals in the first nanosecond after the excitation pulse, which results in a reduced detected fluorescence signal. The loss of signal, however, is compensated by the increased resolution achieved.[62] Using continuous-wave (CW) laser in STED reduces the complexity and increases the versatility of the system. However, CW lasers result in a lower peak intensity compared to a pulsed laser, which reduces the overall resolution of CW-STED system as it continuously excites the fluorophores all at the same time. Therefore, using time-gating detection improves on the resolution by discarding the early photons and recording the photons located at the donut centre of the STED beam where the higher effective spatial resolution is.[63]

To evaluate the power of using time-gated STED (gCW-STED) over no gating applied (CW-STED), HeLa cells were prepared as described in *section 2.5.8*. Figure 5.16 compares gCW-STED and CW-STED of a single HeLa cell dual-stained with Alexa 532 (A) and $[(Ru(bpy)_2phen\text{-}Ar)_2\text{-}ER]^{9+}$ (B). In *section 5.3*, is was found that $[(Ru(bpy)_2phen\text{-}Ar)_2\text{-}ER]^{9+}$ has a luminescent lifetime of 683 ± 8 ns in aqueous media. Therefore, the two complexes can be readily resolved by exploiting the large difference in their luminescent lifetimes using the time-gating system. The time-gating system allows for time windows, $T_g$, to be selected. In this case, Alexa 532 was imaged at time window $T_g$ between 0 – 3.5 ns, and the window for $[(Ru(bpy)_2phen\text{-}Ar)_2\text{-}ER]^{9+}$ was set to $T_g$ between 3.5 – 12 ns.

Alexa Fluor Phalloidin 532 showed no improvement in image resolution or quality as a result of using gCW-STED (A). This was further demonstrated by the X-Y distribution plot, where no change in the resolution was seen. This was reflected in the FWHM values, where it actually increased from 218.9 nm at CW-STED to 225.5 nm when the gating system was applied. This is possibly as a result of a reduction in the signal to noise ratio at the shorter lifetimes as some of the emission intensity is gated out for the short lived probe as some emission intensity is excluded from the image. On the other hand, $[(Ru(bpy)_2phen\text{-}Ar)_2\text{-}ER]^{9+}$ exhibited a much improved image resolution upon imaging with gCW-STED. From Figure 5.16 (B) it is evident that the overall resolution of the gCW-STED image is much clearer than with CW-STED, which is reflected in the resolution of the three spots compared with CW STED.

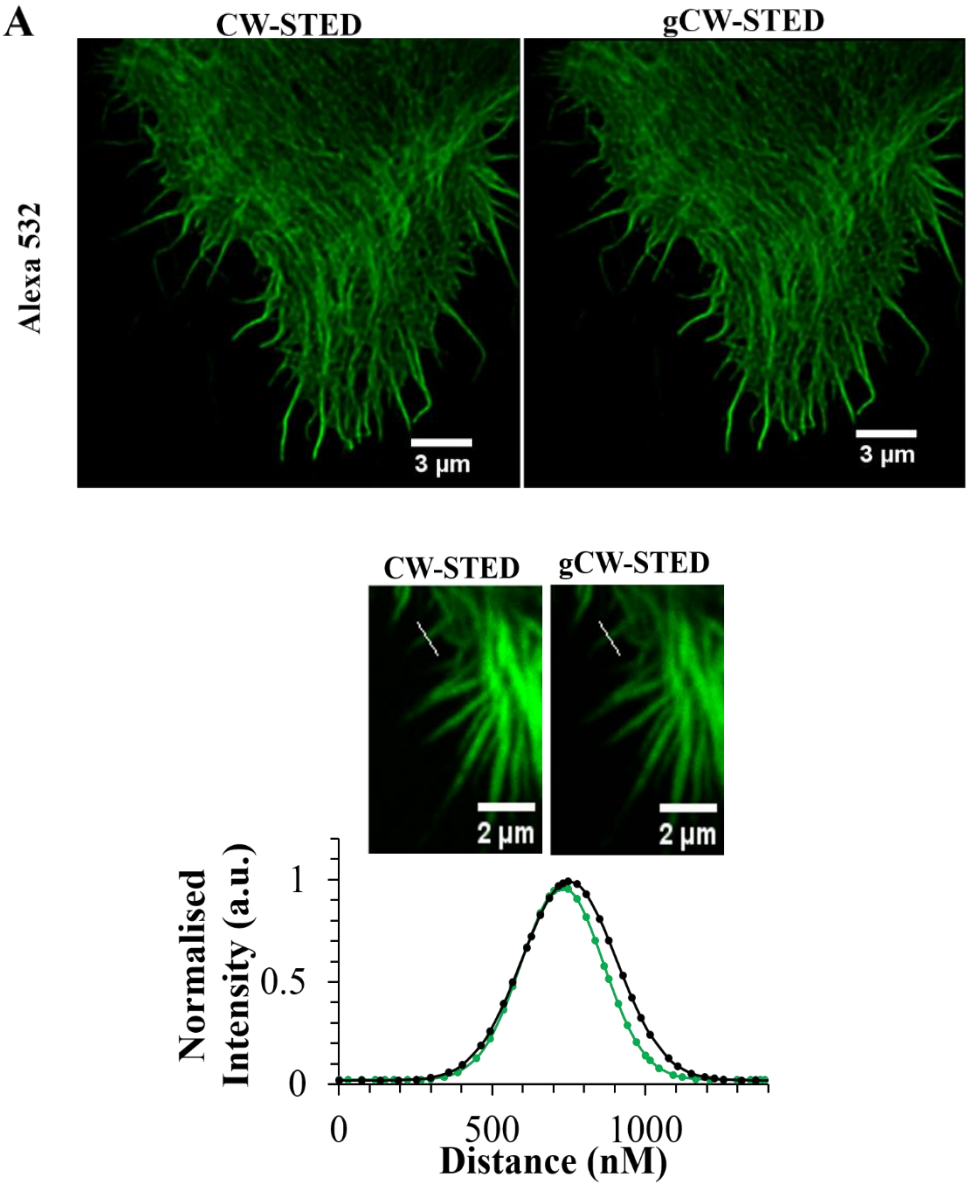
A
CW-STED
gCW-STED
Alexa 532
3 µm
3 µm
CW-STED
gCW-STED
2 µm
2 µm
Normalised Intensity (a.u.)
1
0.5
0
0
500
1000
Distance (nM)
B
CW-STED
gCW-STED
[(Ru(bpy)2-phen-Ar)-ER]9+
3 µm
3 µm

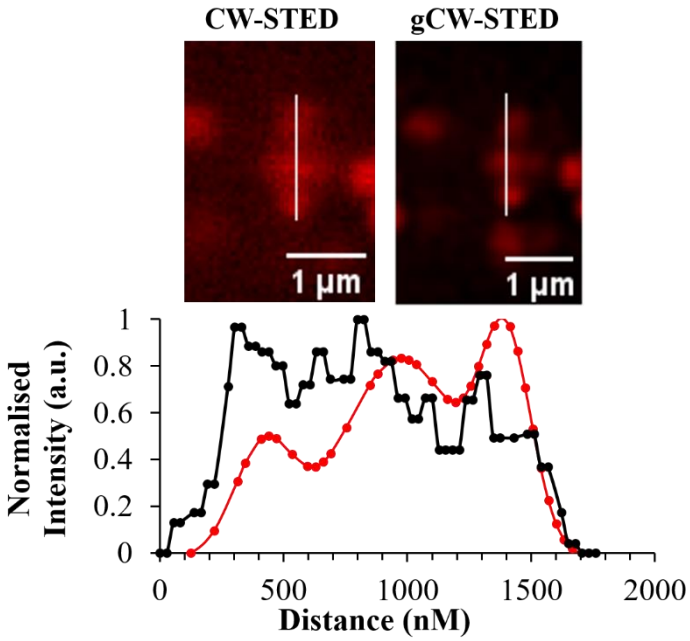


**Figure 5.16** CW-STED and gCW-STED images of a fixed HeLa cell dual stained with Alexa 532 (A) and [(Ru(bpy)$_2$-phen-Ar)-ER]$^9$ (B). The X-Y line traces through a fixed HeLa cell highlighting the improvement of using gating (—) and (—) versus no gating (—) shown by the line traces and plot profiles. Alexa 532 was excited at 528 nm and the emission was collected between 534 and 675 nm. [Ru(bpy)$_2$phen-Ar)$_2$-ER]$^{9+}$ was excited using a 488 nm white light laser and 660 nm depletion laser. The 660 nm STED depletion laser was used for both probes. The time-gating system was set to a window of $T_g$ = 0 – 3 ns for Alexa 532, and a window of $T_g$ = 3.5 -12 ns for [Ru(bpy)$_2$phen-Ar)$_2$-ER]$^{9+}$.

Even though gCW-STED is a relatively new concept, there have been a few reports on the improvements in resolution using this technique.[58,61] *Vicidomini et al* have reported on high spatial resolution images using a time-gated system with a continuous wave STED laser.[59] Figure 5.17 shows an example from their work. They used Atto647N to immuno-stain the microtubules of fixed PtK2 mammalian cells. Here they compare the confocal image in the inset of (A), with the CW-STED (A), and the resolved image following gCW-STED (B). The corresponding intensity plot reflects the improvements in the resolving power of using time-gated detection systems. They were able to resolve single microtubules to a resolution of 89 nm. Interestingly, they also compared time-gated windows, varying the size of the window used. In Figure 5.17 B, the window was set to $T_g$ = 1.5 ns, while in Figure 5.17 D the window was set to $T_g$ = 6 ns. The fluorescent lifetime of Atto647 is ~ 3 ns. The dis-improvement in using a larger time window is due to the uncorrelated background induced by the scattering of the STED beam which

dominates over the shorter lifetime signal. These results demonstrate that the long-lived lifetimes of transition metals are highly suited to the gCW-STED system to improve image resolution.

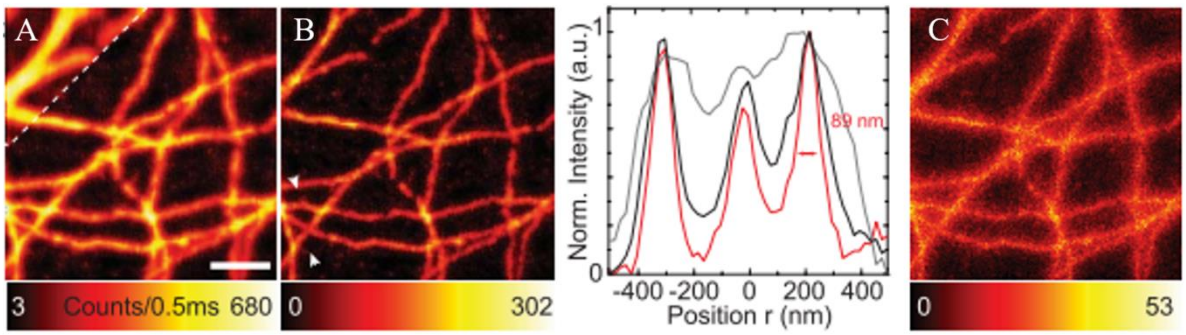


**Figure 5.16** Comparison of using CW-STED (A) with tCW-STED (B) of Atto647N stained microtubules of fixed PtK2 cells. The corresponding intensity plot if the arrows in (B) demonstrates the resolution following confocal (—), CW-STED (—), and gCW-STED (—). The time-gated window for (B) was set to $T_g$ = 1.5 ns. The time-gated window for (C) was set to $T_g$ = 6 ns.[59]

The only practical limitation of using gCW-STED is the loss of some 'good' signal that is lost as it is gated out, depending on the luminescent lifetime of the luminophore. Applying the gate acts as a spatial frequency filter, and therefore a decrease in signal can occur. However, time-gated detection greatly improves the resolution in CW-STED, and the chosen imaging parameters can help overcome the loss in signal.

## 5.11 Photostability of $[(Ru(bpy)_2phen\text{-}Ar)_2\text{-}ER]^{9+}$ under gCW-STED imaging

Photostability is one of the key issues for new STED imaging probe. Alexa probes, in general, are highly photostable, which is one of the reasons why they are so widely used in STED microscopy in spite of their poor Stokes shift. We were interested in evaluating the relative photostability of the Alexa probe with the ruthenium complexes used here. The photostability of $[(Ru(bpy)_2phen\text{-}Ar)_2\text{-}ER]^{9+}$ was assessed in fixed HeLa cells and compared to Alexa 532 under the same conditions. Samples were prepared and mounted as described in *section 5.2.9*. The samples were imaged continuously for 30 minutes (every 60 seconds) at a STED laser power of 0.5 W. Each frame was acquired at 1024 x 1024 resolution to mimic imaging conditions for each complex.

Figure 5.17 shows the photobleaching of Alexa 532 (top row) and $[(Ru(bpy)_2phen\text{-}Ar)_2\text{-}ER]^{9+}$ (bottom row) in a HeLa cell (A) following 1 minute, 15 minutes, and 30 minutes of continuous STED imaging. Figure 5.10 (B) is the corresponding plot of the emission intensities over time. Their values were taken from a selected area at each frame for $[(Ru(bpy)_2phen\text{-}Ar)_2\text{-}ER]^{9+}$ and Alexa 532. As expected, the emission intensity of each probe decreased over time with each frame accumulation using the 660 nm depletion laser. From the plots in Figure 5.17 B, the decay rate of $[(Ru(bpy)_2phen\text{-}Ar)_2\text{-}ER]^{9+}$ was measured to be $7.66 \times 10^{-4}$ $s^{-1}$, while Alexa 532 has a decay rate of $5.27 \times 10^{-4}$ $s^{-1}$ under the same STED imaging conditions. Therefore two complexes both exhibit emission intensity decays at very similar rates of the order of $10^{-4}$ $s^{-1}$. Although the decay rate for of $[(Ru(bpy)_2phen\text{-}Ar)_2\text{-}ER]^{9+}$ is very slightly faster, under the conditions used here it is important to remember that the STED source is a much closer match to the $[(Ru(bpy)_2phen\text{-}Ar)_2\text{-}ER]^{9+}$ emission indicating that the photostability is at least as good as that of the highly photostable Alexa 532.

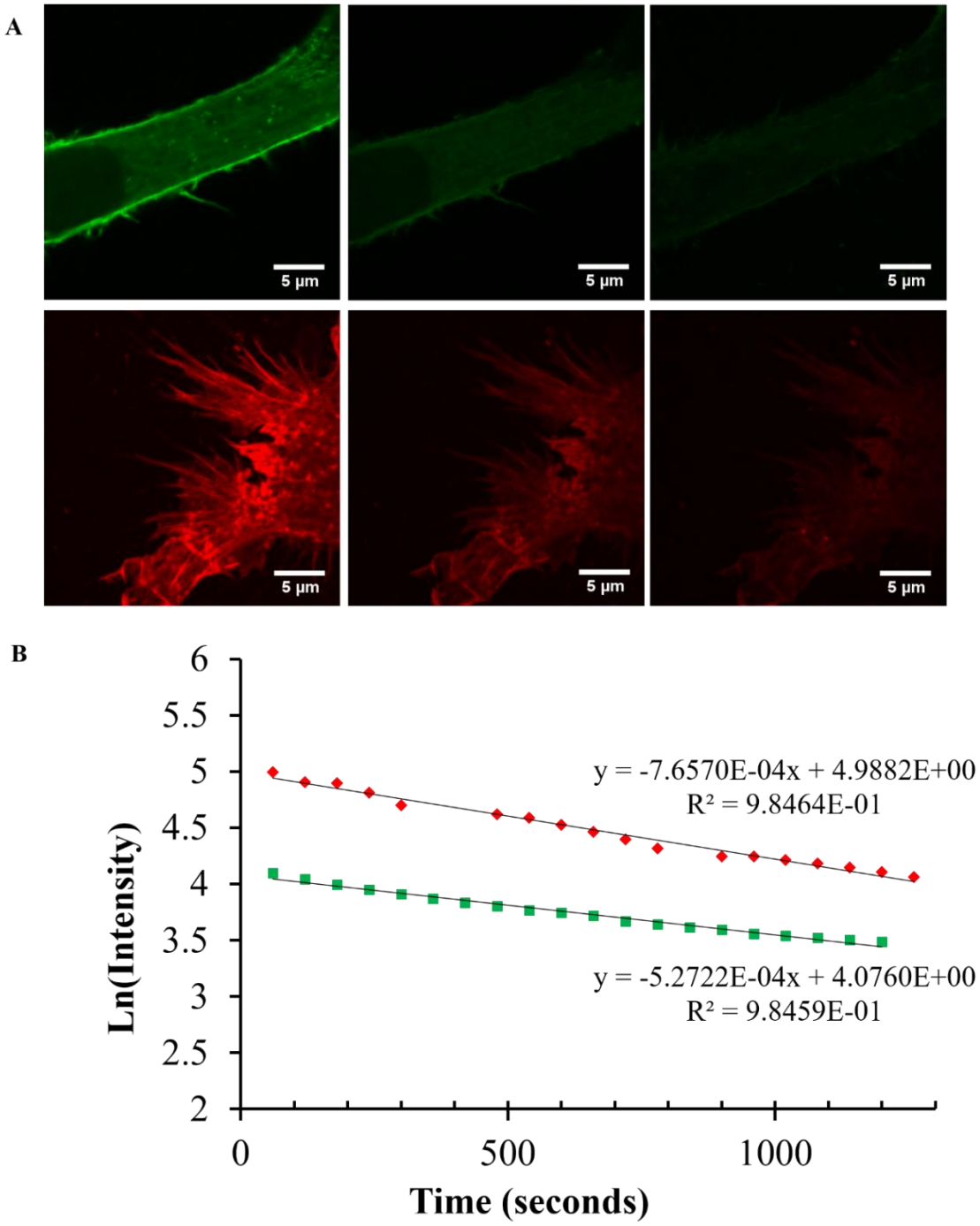


**Figure 5.17** Photostability of Alexa 532 (top) and $[(Ru(bpy)_2phen\text{-}Ar)_2\text{-}ER]^{9+}$ (bottom) in a fixed HeLa cell at 1, 15, and 30 minutes of continuous imaging (A). A plot of the emission intensities over time shows the gradual decrease in emission over time for Alexa 532 (—) and $[(Ru(bpy)_2phen\text{-}Ar)_2\text{-}ER]^{9+}$ (—). The 660 nm laser (0.5 W) was used to collect the images of each probe.

## 5.12 STED imaging of the endoplasmic reticulum

In *section 5.4.2*, $[(Ru(bpy)_2phen\text{-}Ar)_2\text{-}ER]^{9+}$ was shown to localise within the endoplasmic reticulum (ER) of HeLa cells. In order to improve the image resolution of the ER, STED microscopy was applied, but without the dual-staining with Alexa 532.

HeLa cells were prepared as described in *section 5.2.8*, without the addition of Alexa 532. The cells were stained with $[(Ru(bpy)_2phen\text{-}Ar)_2\text{-}ER]^{9+}$ for 4 h, fixed, and mounted. Figure 5.18 shows the confocal image of $[(Ru(bpy)_2phen\text{-}Ar)_2\text{-}ER]^{9+}$ in the ER of a HeLa cell. The inset image shows the corresponding STED image. In Figure 5.18 (A), the confocal image shows $[(Ru(bpy)_2phen\text{-}Ar)_2\text{-}ER]^{9+}$ in the ER, and appears to be distributed in a punctate manner. A gCW-STED image was acquired using the 660 nm STED depletion laser, and the image was deconvolved using Huygens Professional software. The result shows that the spatial resolution of the selected area has been greatly improved. The detailed structure of the ER can be clearly seen on $[(Ru(bpy)_2phen\text{-}Ar)_2\text{-}ER]^{9+}$ labelling where it has a tube-like structure. Figure 5.18 (B) shows a different HeLa cell of the same sample. Similarly, the gCW-STED image shows the same well-resolved structure of the ER with tubular structures compared to the confocal image which indicates only that whole spots with no evidence for the central hole in the ER tubing. The precise labelling of the ER combined with gCW-STED results in background free images, with no auto-fluorescence from the surrounding cell.

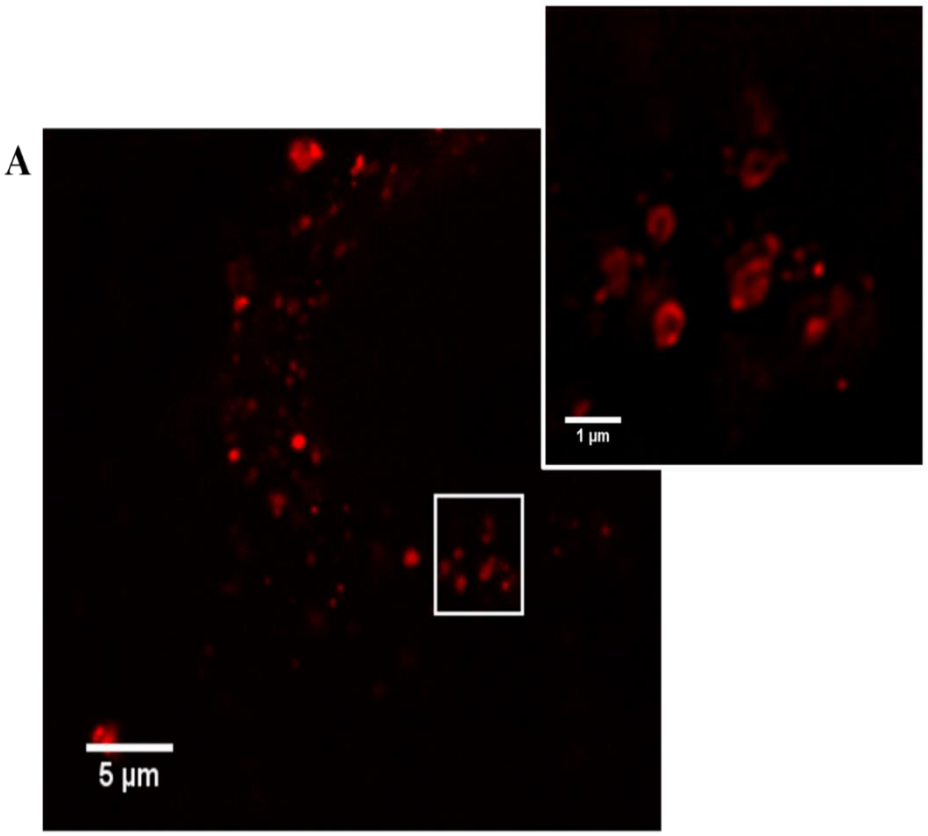
A
1 µm
5 µm

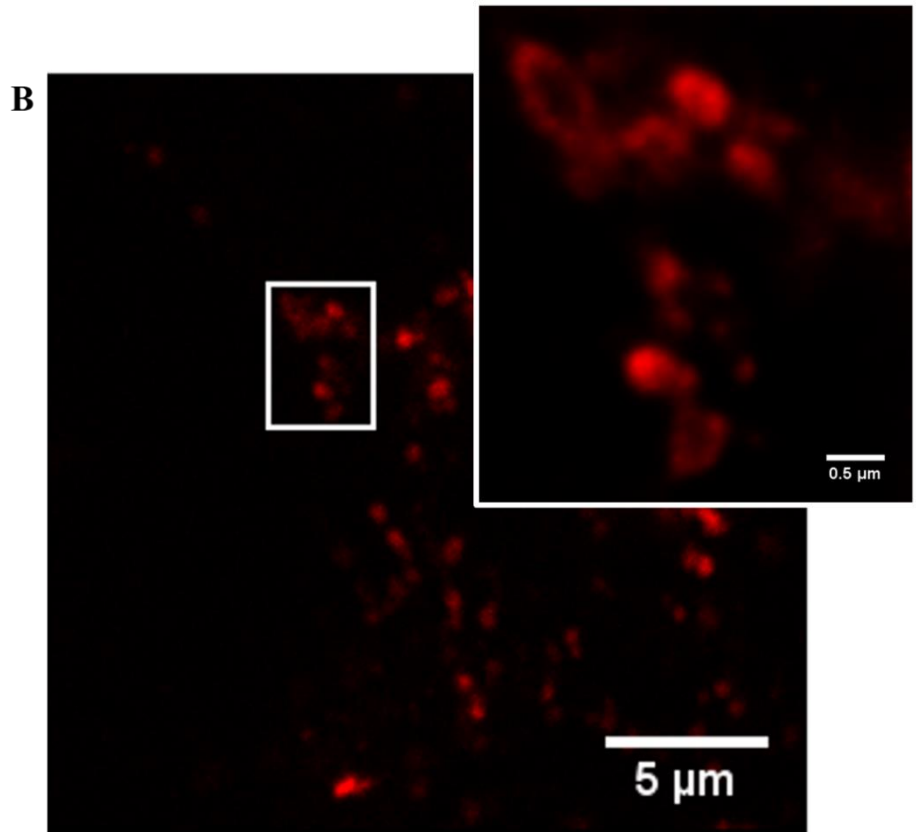
B
0.5 µm
5 µm

**Figure 5.18** gCW-STED image of $[(Ru(bpy)_2phen\text{-}Ar)_2\text{-}ER]^{9+}$ in the endoplasmic reticulum of fixed HeLa cells mounted with ProLong Gold (A and B). $[(Ru(bpy)_2phen\text{-}Ar)_2\text{-}ER]^{9+}$ was excited using a 488 nm white light laser and the emission was collected between 590 and 700 nm. The 660 nm STED depletion laser was used to acquire a STED image. The time-gating system was set to $T_g$ = 3.5 -12 ns.

Water-soluble proteins found in the cytosol of the cell are captured by the ER, and they are released into the lumen of the ER.[64] These STED images appear to capture $[(Ru(bpy)_2phen\text{-}Ar)_2\text{-}ER]^{9+}$ in the lumen of the smooth ER, evident, as mentioned as tubular like structures. Figure 5.19 shows an electron micrograph image of the smooth ER of a hormone-secreting leydig cell. The shape and structure of these features is similar to that of the STED images presented in Figure 5.18.

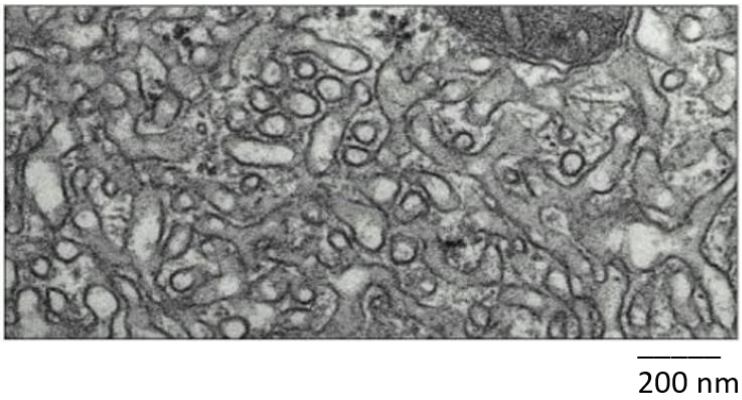


**Figure 5.19** Electron micrograph of the smooth ER of a hormone-secreting leydig cell.[64]

*Schneider et al* reported on the 3D structure of the ER, and other cellular organelles, of mouse adenocarcinoma cells using an X-ray microscope developed by their group. [65] Figure 5.20 illustrates the 3D data complied together from a series of X-ray tomograms taken through a cell. The 3D image of the ER, represented in green, exhibits small, tubular like structures, which are quite similar to the structures of $[(Ru(bpy)_2phen\text{-}Ar)_2\text{-}ER]^{9+}$ imaged using STED.

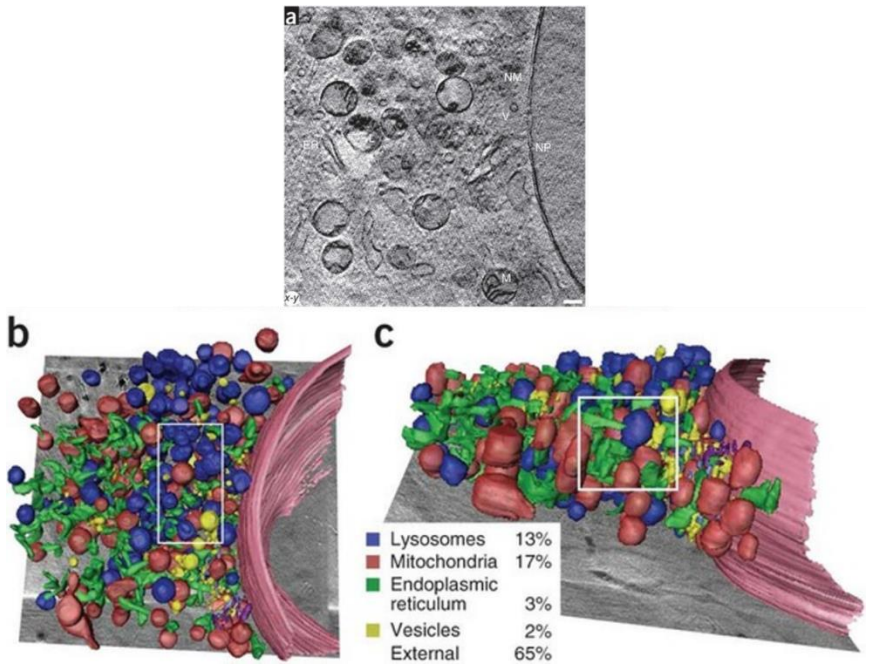


**Figure 5.20** 3D imaging of cellular organelles. X-ray tomograms of the cytosol of a mouse adenocarcinoma cell (A). The 3D compilation data of a series of x-ray images to give a representative image of the organelles in the cytosol (B and C). Image taken from reference [65]

Moreover, many studies have examined the changing shape of the ER structure during mitosis. [66,67] The group of *Lu et al* have shown, using conventional fluorescence microscopy, that the ER structure is mostly tubular during metaphase of the cell cycle, which from Figure 5.18 the cell appears to be at, further confirming the tubular structure of the ER via STED microscopy. Figure 5.21 shows Z-stack images of the organisation of the ER in a HeLa cell. The 3D reconstruction images of the tubules of the ER highly resemble the tubule structures captured during STED in Figure 5.18.

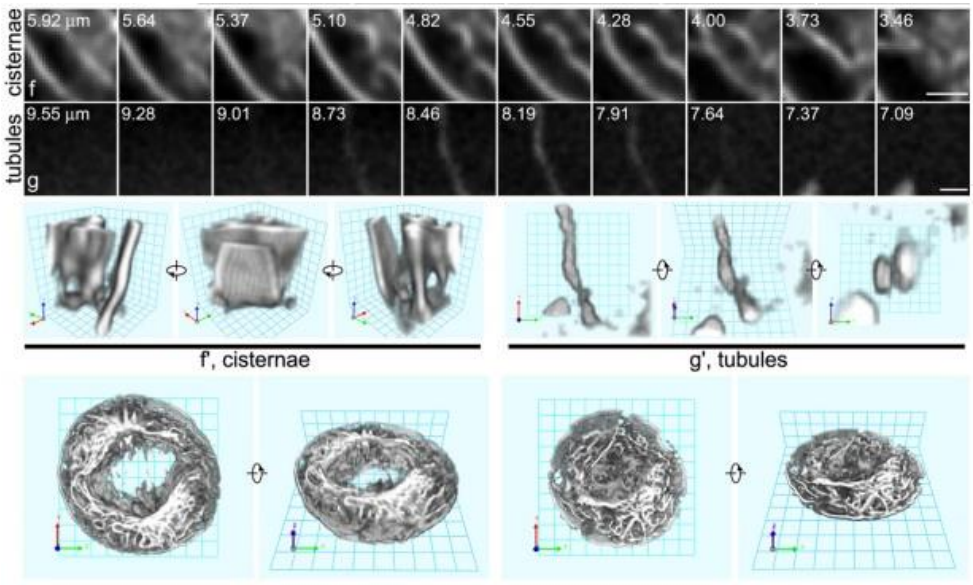


**Figure 5.21** Confocal Z-stack of the tubules and cisternae of the ER of a HeLa cell during metaphase. The Z-stack images were compiled to give 3D images of the ER structures.[67]

Upon closer inspection of Figure 5.18 A, an X-Y line trace through the ER was plot to evaluate the improvement in resolution between the confocal and STED images, shown in Figure 5.22. Under confocal imaging each tubule is resolved as a single spherical point, which was fitted to a Gaussian plot. The FWHM of the two spots was found to 532.4 nm and 527.6 nm. On the other hand, the X-Y plot of the STED image reveals the walls of the tubules, and the hollow nature of the tubule, possibly the lumen, which is clearly resolved in the Gaussian distribution plot. The FWHM of the first spot was found to be 309.3 nm and 183.25 nm across the now resolved ER. The second spot was found to be 279 nm and 388.18 nm.

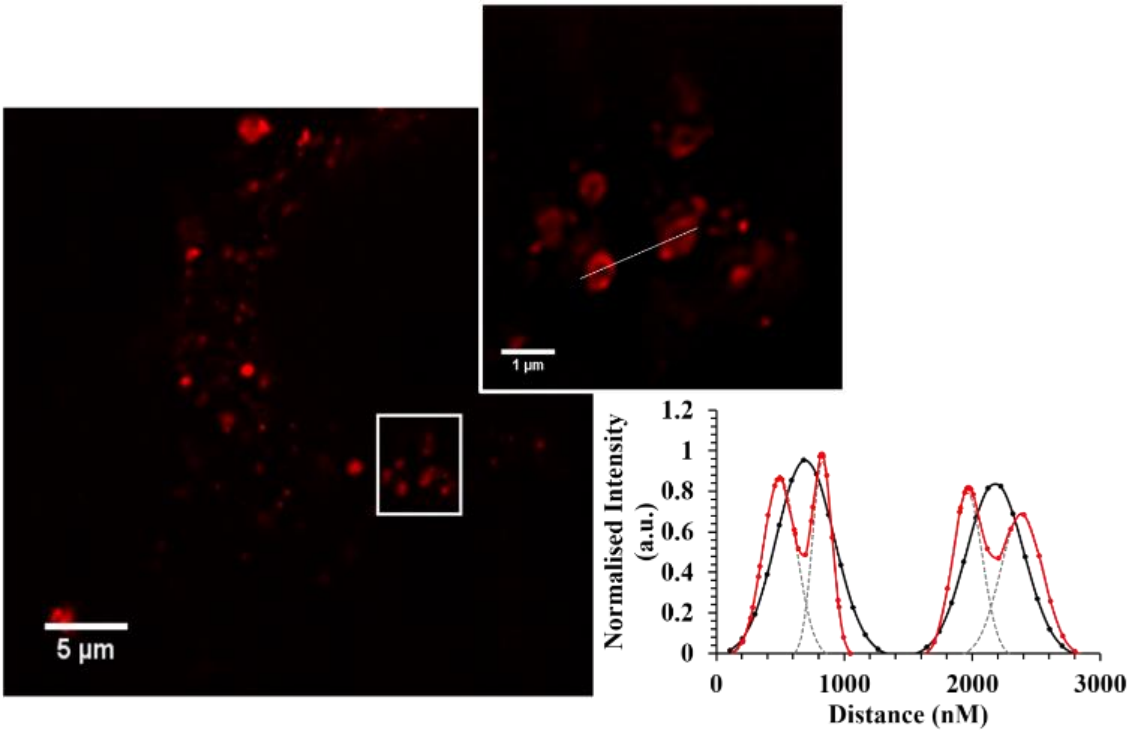


**Figure 5.22** gCW-STED image of $[(Ru(bpy)_2phen\text{-}Ar)_2\text{-}ER]^{9+}$ in the endoplasmic reticulum of fixed HeLa cells mounted with ProLong Gold. $[(Ru(bpy)_2phen\text{-}Ar)_2\text{-}ER]^{9+}$ was excited using a 488 nm white light laser and 660 nm depletion laser. The time-gating system was set to $T_g$ = 3.5 -12 ns. The x-y line trace through a selected area of the ER stained with $[(Ru(bpy)_2phen\text{-}Ar)_2\text{-}ER]^{9+}$. The corresponding plot profile compares confocal (—) with STED (—). The fluorescence-intensity was fit to a Gaussian distribution (OriginPro) to obtain the separated distributions for the STED profile fitting, indicated by grey dashed lines.

*Hell et al* reported on resolutions of 65 nm of the ER of live PtK2 cells, expressing fluorescent protein Citrine.[14] The most recent report of super resolution imaging of the ER employed dual-staining of the organelle to carry out two-photon STED microscopy. *Bottanelli et al* were able to achieve 50 nm resolutions of the ER.[68] Figure 5.23 A shows the ER dual-stained, and the close up in B. Here they used SNAP-KDEL590 to stain the lumen, and Halo-S-C61β to stain the ER membrane. Although the two dual-stained structures can be seen in Figure 5.23 B, the image quality and structure detail is not clear.

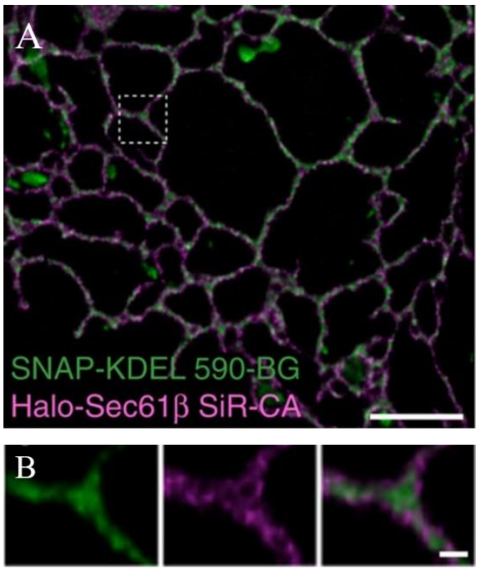


**Figure 5.23** Two-photon STED images of the ER of COS-7 cells (A) and the magnified region from the white box shown in (B). The ER were dual-stained with SNAP-KDEL590 to stain the lumen (green), and Halo-S-C61β to stain the ER membrane (pink). Scale bar A = 2 μM. Scale bar B = 200 nm.[68]

In both cases, they appear to be measuring across the tubules of the ER, while in our images $[(Ru(bpy)_2phen\text{-}Ar)_2\text{-}ER]^{9+}$ appears to be localising in the lumen which may account for the difference in resolution achieved. Furthermore, in the reports from *Hell et al* and *Bottanelli et al* the ER was stained with fluorescent organic dyes. To our knowledge, there has been no reports of STED imaging of the ER using transition metal complexes, nor using signal peptides for targeted staining and imaging. The improvement in image resolution achieved using $[(Ru(bpy)_2phen\text{-}Ar)_2\text{-}ER]^{9+}$ allows the ER to be imaged in great detail. Using such optical methods in live cells may offer opportunity to monitor changes to the ER in real time. It also demonstrates the power of using ruthenium polypyridyl complexes with site-targeted peptide sequences to image specific organelles in great detail.

## 5.13 Stimulated emission depletion (STED) microscopy of nuclear DNA

As $[Ru(dppz)(bpy)(bpy\text{-}Ar\text{-}NFkB)]^{6+}$ has been successfully directed to the nucleus and shown to bind to DNA given the 'switching on' of the luminescence, time-gated, continuous wave STED (gCW-STED) was employed in an attempt to image the chromosomes when $[Ru(dppz)(bpy)(bpy\text{-}Ar\text{-}NFkB)]^{6+}$ has bound. To date, to our

knowledge, there have been no reports on STED images of nuclear DNA in the cell. HeLa cells were prepared as described in *section 5.2.8*. The cells were fixed and mounted prior to imaging.

Figure 5.24 describes the confocal image of $[Ru(dppz)(bpy)(bpy\text{-}Ar\text{-}NFkB)]^{6+}$ bound to chromosomal DNA in the nucleus of a HeLa cell. The chromosomes appear to be aligning down the middle of the nucleus preparing for cell division. This stage in mitosis is called Metaphase. Figure 5.24 compares the confocal image with the gCW-STED image. The images were acquired sequentially using a Leica TSP DMi8 system. The gCW-STED image was acquired using the 660 nm depletion laser. It is evident from the tow images that applying gCW-STED has greatly improved the resolution of the image. Chromosomes are made up of two chromatin, and are joined in the middle at the centromere, giving the chromosomes their well-known shape. The chromosome shape can be observed in greater detail as they align along the metaplate after employing gCW-STED imaging.

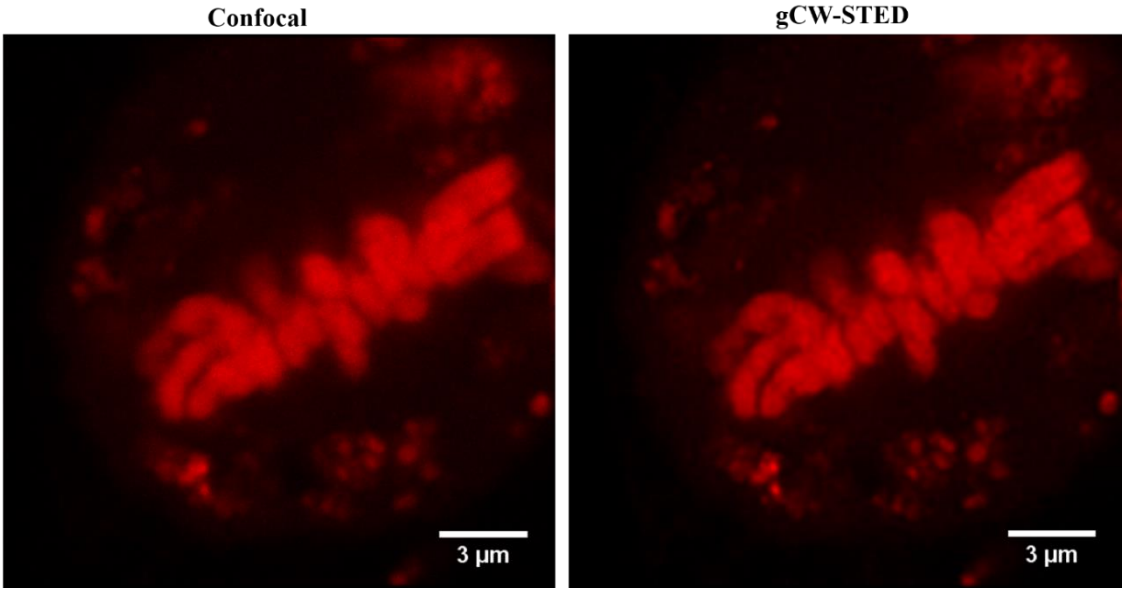


**Figure 5.24** Confocal and gCW-STED images of $[Ru(dppz)(bpy)(bpy\text{-}Ar\text{-}NFkB)]^{6+}$ bound to the chromosomes in the nucleus of a HeLa cell. Cells were incubated with 40 µM complex for 24 h at 37 °C in the absence of light. The cells were fixed and mounted using ProLong Gold prior to imaging. $[Ru(dppz)(bpy)(bpy\text{-}Ar\text{-}NFkB)]^{6+}$ was excited using a 470 nm white light laser and the emission was collected using a band pass filter 565 – 700 nm. STED was acquired using the 660 nm depletion laser.

Figure 5.25 shows a new HeLa cell in the same sample. Again, the chromosomes have aligned along the metaplate, preparing for cell division. In this case, it is evident from the gCW-STED acquired image that the chromosomes are still in their pairs, suggesting that the cell is in early metaphase. Individual sister chromatids are distinguishable, as are the grooves in the chromosome structures where the chromatids join at the centromere sites. The improvement in the resolution is reflected in the X-Y line profile through a single chromosome. The Gaussian distribution of the STED image can clearly resolve and distinguish the chromatids of the chromosome, which is not seen in the confocal image.

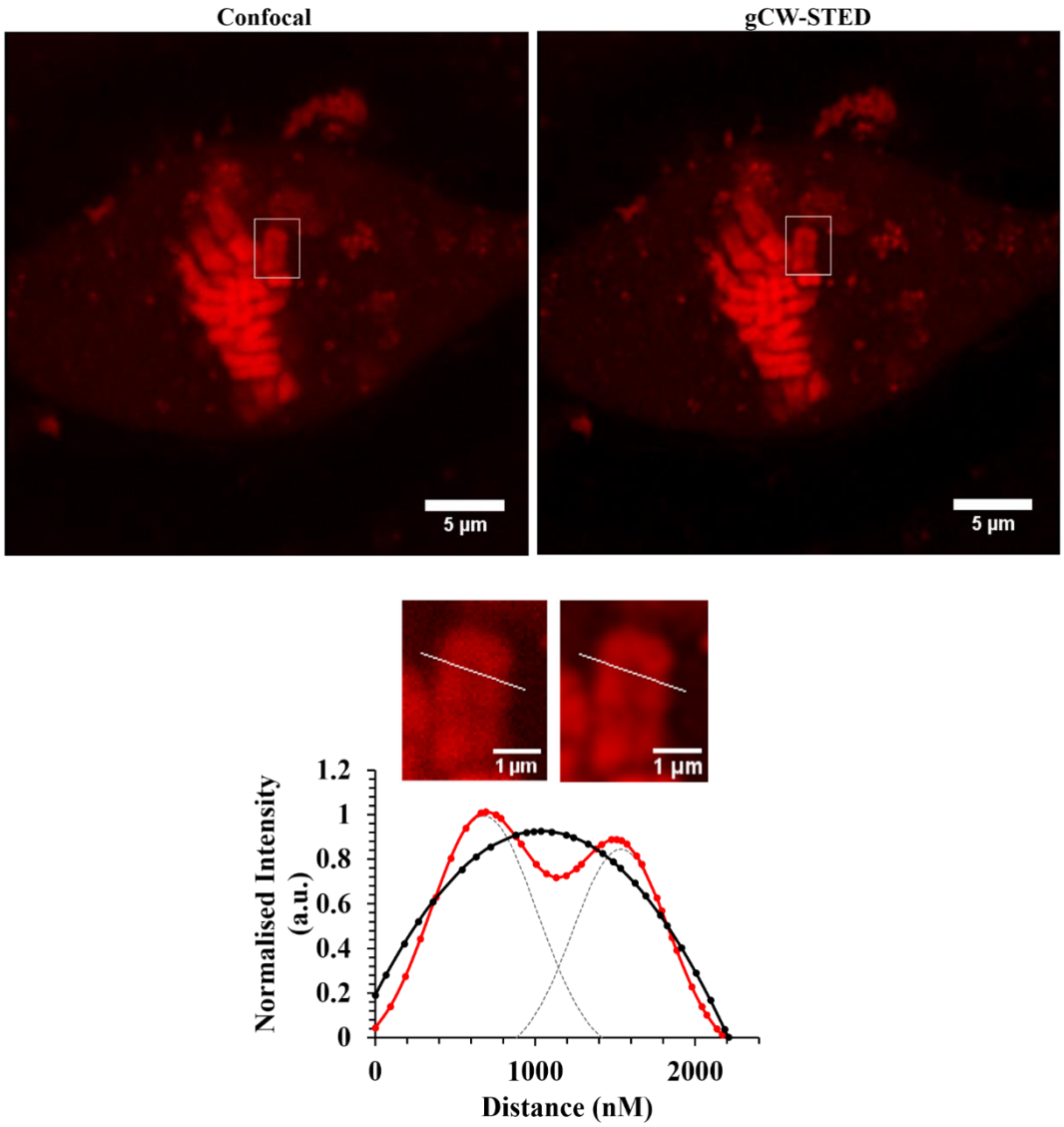


**Figure 5.25** Confocal and gCW-STED images of [Ru(dppz)(bpy)(bpy-Ar-NFkB)]$^{6+}$ in a fixed HeLa cell. The line plot of a single chromosome and its corresponding distribution confirms an improvement in using STED (—) compared to confocal (—).The fluorescence-intensity was fit to a Gaussian distribution (OriginPro) to obtain the separated distributions for the STED profile fitting, indicated by grey dashed lines. [Ru(dppz)(bpy)(bpy-Ar-NFkB)]$^{6+}$ was excited using a 470 nm white light laser and the emission was collected using a band pass filter 565 – 700 nm. STED was acquired using the 660 nm depletion laser.

Figure 5.26 illustrates the different stages in mitosis using [Ru(dppz)(bpy)(bpy-Ar-NFkB)]$^{6+}$ as an imaging agent. When bound to nuclear DNA, mitosis, the process of cell division, can be observed. Figure 5.24 describes HeLa cells at the different stages of mitosis. During interphase the chromatin are dividing, and are in a relaxed state in the nucleus, shown in A. The fibres then begin to condense into chromosomes in Prophase

(B), where each chromosome containing two chromatin. From B the chromosomes are migrating towards the centre of the nucleus. The micro tubules, which are responsible for eventually pulling the chromosomes apart, begin to bind to the chromosomes in Prometaphase, shown in C. From C the chromosomes are now in the centre of the nucleus, ready to align for the next phase. The chromosomes then align along the middle of the nucleus in Metaphase, along the metaplate, shown in D. From this image, the shape of the sister chromatids of some of the chromosomes can be resolved. Figure E shows the single sister chromatids of the chromosomes being pulled apart in Anaphase, and the shape of the nucleus elongates to get ready for separation. Finally, in telophase, the new nuclear envelopes form around the daughter chromosomes, forming two new cells, shown in F. Here, the chromosomes become relaxed in the cell again as the two new cells are formed. These stages can all be clearly seen from DNA staining with $[Ru(dppz)(bpy)(bpy\text{-}Ar\text{-}NFkB)]^{6+}$.

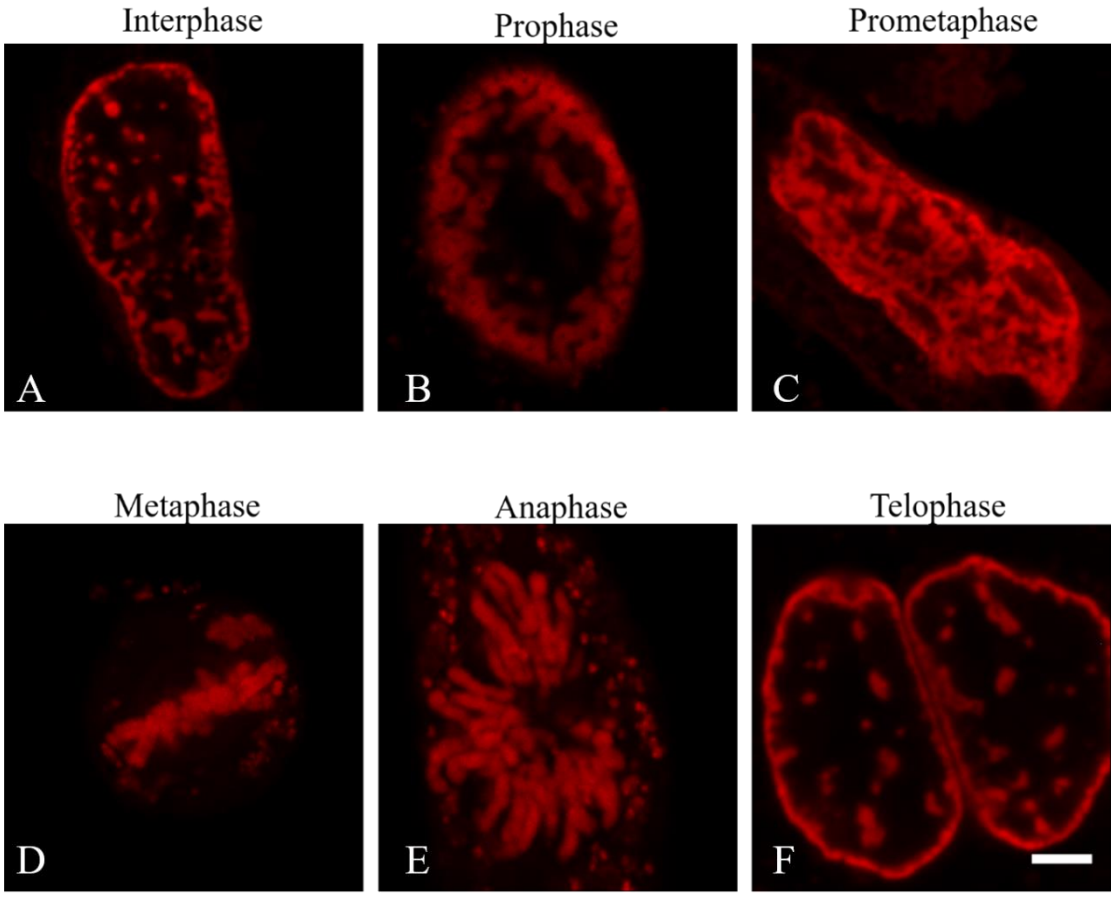


**Figure 5.26** gCW-STED imaging of the stages in mitosis using 40 μM $[Ru(dppz)(bpy)(bpy\text{-}Ar\text{-}NFkB)]^{6+}$ to stain the nuclear DNA of HeLa cells. $[Ru(dppz)(bpy)(bpy\text{-}Ar\text{-}NFkB)]^{6+}$ was excited using a 470 nm white light laser and the emission was collected using a band pass filter 565 – 700 nm. STED was acquired using the 660 nm depletion laser.

As discussed previously in Chapter 5, there have been few reports of nuclear localising complexes for the purpose of imaging. Those that have directed such complexes to the nucleus did not target or bind to DNA. However, *Gill et al* managed to inadvertently direct a ruthenium complex to the nucleus of MCF-7 cells without the use of CPP sequences or sugar moieties.[15] They successfully imaged the chromosomes in the nucleus at the different stages of mitosis, shown in Figure 5.27.

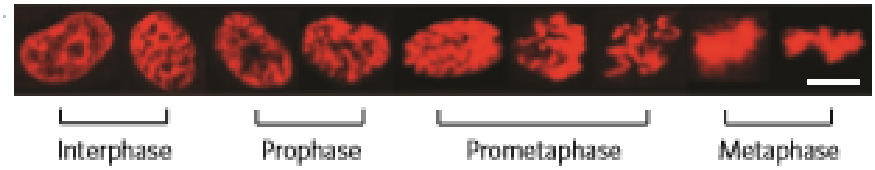


**Figure 5.27** Confocal images of $[(phen)_2Ru(tpphz)Ru(phen)_2]^{4+}$ in the nucleus of MCF-7 cells. The complex bound to nuclear DNA and the stages in cell division were captured.[15]

While the chromosomal DNA can be made out in the phases of mitosis in Figure 5.27, the gCW-STED images acquired in this work, shown in Figure 5.26 show a dramatic improvement in resolution in comparison, where much more detail in the structure of individual sister chromatids can be resolved, as well as where they join at the centromeres. These improvements highlight the improvement in spatial resolution in the focal plane of STED over diffraction-limited approaches like confocal microscopy.

## 5.14 Conclusions

Chapter 5 discussed the application of Ru(II) complexes to STED microscopy. Cell-penetrating peptide sequences were used to specifically target the endoplasmic reticulum using the sequence RQIKIWFQNRRMKWKK, and the nucleus using the sequence VQRKRQKLMP, for more precise imaging using STED microscopy, and compared to a commercial probe.

The photophysical properties of both $[(Ru(bpy)_2phen\text{-}Ar)_2\text{-}ER]^{9+}$ and $[Ru(dppz)(bpy)(bpy\text{-}Ar\text{-}NFkB)]^{6+}$ were examined. $[(Ru(bpy)_2phen\text{-}Ar)_2\text{-}ER]^{9+}$ exhibited a strong absorbance band at 454 nm and an emission maximum of 602 nm. Its

long lived emissive lifetime of 683 ns in aerated aqueous solution showed excellent oxygen sensitivity, increasing dramatically to 1.064 μs when de-aerated. On the other hand, the properties of $[Ru(dppz)(bpy)(bpy\text{-}Ar\text{-}NFkB)]^{6+}$ were investigated in both aqueous and non-aqueous solutions. In PBS solution the complex exhibited no emission, while an intense luminescent emission was observed in acetonitrile, successfully demonstrating the 'light switch' effect when in non-aqueous acetonitrile solution. In acetonitrile it exhibited a luminescent lifetime of 241 ± 1 ns. These photophysical properties- large Stokes shift, long lived emissive state, and high quantum yield suggested that these Ru(II) complexes would be well suited for super resolution microscopy.

Confocal microscopy demonstrated that $[(Ru(bpy)_2phen\text{-}Ar)_2\text{-}ER]^{9+}$ (75 μM) exhibited efficient uptake in HeLa cells, distributing throughout the cytoplasm after 2 h, and finally localising within the ER after 4 h. Co-localisation studies confirmed that the complex was in the ER, illustrating the high selectivity of the chosen CPP sequence RQIKIWFQNRRMKWKK. On the other hand, $[Ru(dppz)(bpy)(bpy\text{-}Ar\text{-}NFkB)]^{6+}$ exhibited no luminescence in HeLa cells after 1 h exposure to the complex. After 4 h, a slight luminescence was seen in the cytoplasm, possibly as a result of the complex binding to RNA or proteins there. After 24 h, the complex was found to localise in the nucleus, confirmed by dual-staining with DAPI nuclear localising dye. The emission intensity of $[Ru(dppz)(bpy)(bpy\text{-}Ar\text{-}NFkB)]^{6+}$ varied in the nucleus compared to when bound and intercalated with nuclear DNA.

As a result of the promising photophysical properties of $[(Ru(bpy)_2phen\text{-}Ar)_2\text{-}ER]^{9+}$, it was compared to Alexa Fluor Phalloidin 532 in HeLa cells for continuous wave STED (CW-STED) microscopy. It was found that the resolution using CW-STED was greatly improved when the 660 nm depletion laser was applied. The full width half maxima values confirmed that $[(Ru(bpy)_2phen\text{-}Ar)_2\text{-}ER]^{9+}$ resolution improved more so than that of Alex 532. Time-gating was employed as a method to resolve the two complexes in a dual-stained sample based on their emission lifetimes. Due to its long lifetime, using time-gating CW-STED (gCW-STED) with $[(Ru(bpy)_2phen\text{-}Ar)_2\text{-}ER]^{9+}$ improved the resolution further compared to using CW-STED, as any background noise or auto-fluorescence was eliminated at the shorter lifetimes. $[(Ru(bpy)_2phen\text{-}Ar)_2\text{-}ER]^{9+}$ also demonstrated excellent photostability over a time course experiment, and diminished at a similar rate to that of the highly photostable Alexa 532.

gCW-STED was carried out to acquire high resolution images of the ER stained solely with $[(Ru(bpy)_2phen\text{-}Ar)_2\text{-}ER]^{9+}$ and of the nucleus stained with [Ru(dppz)(bpy)(bpy-Ar-NFkB)]$^{6+}$ . The resolution of the acquired images were greatly enhanced compare to the confocal images. Detailed structural resolution of the ER was seen, where they were observed as tubular-like structures. The same structures appeared as closed spots in confocal fluorescence the cell without resolution of the open porous nature of the ER. Likewise, the resolution was improved and the background noise was reduced upon applying gCW-STED to image the chromosomal aggregation in six phases in cell division in fixed HeLa cells stained with [Ru(dppz)(bpy)(bpy-Ar-NFkB)]$^{6+}$ using gCW-STED microscopy.

Finally, the long luminescent lifetimes of [Ru(dppz)(bpy)(bpy-Ar-NFkB)]$^{6+}$ in non-aqueous solution meant [Ru(dppz)(bpy)(bpy-Ar-NFkB)]$^{6+}$ was well suited to PLIM imaging. It was found that the lifetime of [Ru(dppz)(bpy)(bpy-Ar-NFkB)]$^{6+}$ increased significantly when bound to DNA (398 ns) compared to when in solution (241 ns). The cytoplasmic region gave a shorter lifetime, indicating its presence there. As [Ru(dppz)(bpy)(bpy-Ar-NFkB)]$^{6+}$ does not luminescence in aqueous environments, the luminescent lifetimes were attributed to it binding to membrane structures in the cytoplasm.

Ruthenium polypyridyl complexes demonstrated excellent suitability and compatibility with both CW- and gCW-STED. Their large Stokes shift, long lifetimes, and impeccable photostability gave an improvement in image resolution compared to the conventional confocal images. Furthermore, they have proven to be reliable in reporting from various cell organelles when combined with CPPs. The ability of [Ru(dppz)(bpy)(bpy-Ar-NFkB)]$^{6+}$ to report on lifetime differences between the different phases in mitosis will allow for further investigation of the chromatin environment under a variety of physiological changes, for example, proliferation. Combining this lifetime data with gCW-STED microscopy may give a correlation between changes in lifetime and the visualisation of the DNA environment for in-depth monitoring on structural changes to DNA in different states. This means Ru(II) complexes are a valuable new class of imaging probes for super resolution microscopy.

## *References*


1. Rankin B, Moneron G, Wurm C, et al. Nanoscopy in a living multicellular organism expressing GFP. *Biophys J*. 2011;100(12):L63-L65.

2. Schmidt R, Wurm CA, Punge A, Egner A, Jakobs S, Hell SW. Mitochondrial cristae revealed with focused light. *Nano Lett*. 2009;9:2508-2510.

3. Schmidt R, Wurm CA, Jakobs S, Engelhardt J, Egner A, Hell SW. Spherical nanosized focal spot unravels the interior of cells. *Nature Methods*. 2008;5:539.

4. Mishina NM, Mishin AS, Belyaev Y, et al. Live-cell STED microscopy with genetically encoded biosensor. *Nano Lett*. 2015;15:2928-2932.

5. Wurm CA, Kolmakov K, Göttfert F, et al. Novel red fluorophores with superior performance in STED microscopy. *Optical Nanoscopy 2012, 1:7*. 2012;1:1-7.

6. Chéreau R, Tønnesen J, Nägerl UV. STED microscopy for nanoscale imaging in living brain slices. *Methods*. 2015;88:57-66.

7. D'Este E, Kamin D, Göttfert F, El-Hady A, Hell S. STED nanoscopy reveals the ubiquity of subcortical cytoskeleton periodicity in living neurons. *Cell Reports*. 2015;10(8):1246-1251.

8. Tønnesen J, Katona G, Rózsa B, Nägerl UV. Spine neck plasticity regulates compartmentalization of synapses. *Nature Neuroscience*. 2014;17:678-685.

9. Fernández-Suárez M, Ting AY. Fluorescent probes for superresolution imaging in living cell. *Nature Reviews Molecular Cell Biology*. 2008;9:929.

10. Kasper R, Harke B, Forthmann C, Tinnefeld P, Hell SW, Sauer M. Single-molecule STED microscopy with photostable organic fluorophores. *Small*. 2010;6:1379-1384.

11. Kolmakov K, Wurm CA, Meineke DNH, et al. Polar red-emitting rhodamine dyes with reactive groups:Synthesis, photophysical properties, and two-color STED Nanoscopy applications. *Chem Eur J*. 2014;20:146-157.

12. Wildanger D, Medda R, Kastrup K, Hell SW. A compact STED microscope providing 3D nanoscale resolution. *Journal of Microscopy*. 2009;236:35-43.

13. Meyer L, Wildanger D, Medda R, et al. Dual-color STED microscopy at 30-nm focal-plane resolution. *Small*. 2008;4:1095-1100.

14. Moneron G, Medda R, Hein B, Giske A, Westphal V, Hell SW. Fast STED microscopy with continuous wave fiber lasers. *Optics Express*. 2010;18:1302-1309.

15. Gill MR, Garcia-Lara J, Foster SJ, Smythe C, Battaglia G, Thomas JA. A ruthenium(II) polypyridyl complex for direct imaging of DNA structure in living cells. *Nature Chemistry*. 2009;1:662-667.

16. Puckett CA, Barton JK. Mechanism of cellular uptake of a ruthenium polypyridyl complex. *Biochemistry*. 2008;47:11711-11716.

17. Neugebauer U, Pellegrin Y, Devocelle M, et al. Ruthenium polypyridyl peptide conjugates: Membrane permeable probes for cellular imaging. *Chem Commun*. 2008;42:5307-5309.

18. Beater S, Holzmeister P, Pibiri E, Lalkens B, Tinnefeld P. Choosing dyes for cw-STED nanoscopy using self-assembled nanorulers. *Phys Chem Chem Phys*. 2014;16:6990-6996.

19. Adamson K, Dolan C, Moran N, Forster RJ, Keyes TE. RGD labelled ru(II) polypyridyl conjugates for platelet integrin Î±IIbÎ²3 recognition and as reporters of integrin conformation. *Bioconjugate Chem*. 2014;25:928-944.

20. Horton KL, Stewart KM, Fonseca SB, Guo G, O. Kelley S. Mitochondria-penetrating peptides. *Chemistry & Biology*. 2008;15:375-382.

21. Yousif LF, Stewart KM, Horton KL, O. Kelley S. Mitochondria-penetrating peptides: Sequence effects and model cargo transport. *ChemBioChem*. 2009;10:2081-2088.

22. Puckett CA, Barton JK. Fluorescein redirects a ruthenium-octaarginine conjugate to the nucleus. *J Am Chem Soc*. 2009;131:8738-8739.

23. Voeltz GK, Rolls MM, Rapoport TA. Structural organization of the endoplasmic reticulum. *EMBO Rep*. 2002;3:944-950.

24. Lavoie C, Roy L, Lanoix J, et al. Taking organelles apart, putting them back together and creating new ones: Lessons from the endoplasmic reticulum. *Prog Histochem Cytochem*. 2011;46(1):1-48.

25. Matus S, Glimcher LH, Hetz C. Protein folding stress in neurodegenerative diseases: A glimpse into the ER. *Curr Opin Cell Biol*. 2011.

26. Fonseca SG, Urano F, Burcin M, Gromada J. Stress hypERactivation in the β-cell. *Islets*. 2010;2:1-9.

27. Prins D, Michalak M. Endoplasmic reticulum proteins in cardiac development and dysfunction. *Can J Physiol Pharmacol*. 2009;87:419-425.

28. Bernales S, McDonald KL, Walter P. Autophagy counterbalances endoplasmic reticulum expansion during the unfolded protein response. *PLoS Biol*. 206;4:423.

29. Blasius R, Nierengarten H, Luhmer M, et al. Photoreaction of [ru(hat)2phen]2+ with guanosine-5'-monophosphate and DNA: Formation of new types of photoadducts. *Chem Eur*. 2005;11:1507-1517.

30. Moucheron C, Kirsch-De Mesmaeker A, Kelly JM. Photoreactions of ruthenium (II) and osmium (II) complexes with deoxyribonucleic acid (DNA). *Journal of Photochemistry and Photobiology B: Biology*. 1997;40(2):91-106.

31. Delaney S, Pascaly M, Bhattacharya PK, Han K, Barton JK. Oxidative damage by ruthenium complexes containing the dipyridophenazine ligand or its derivatives: A focus on intercalation. *Inorganic Chemistry*. 2002;41:1966-1974.

32. Shi S, Liu J, Li J, et al. Synthesis, characterization and DNA-binding of novel chiral complexes Δ- and Λ-[ru(bpy)2L]2+ (l = o-mopip and p-mopip). *J Inorg Biochem*. 2006;100(3):385-395.

33. Puckett CA, Barton JK. Targeting a ruthenium complex to the nucleus with short peptides. *Bioorg Med Chem*. 2010;18(10):3564-3569.

34. Gottschaldt M, Schubert US, Rau S, et al. Sugar-selective enrichment of a D-glucose-substituted ruthenium bipyridyl complex inside HepG2 cancer cells. *ChemBioChem*. 2010;11:649-652.

35. Baggaley E, Gill MR, Green NH, et al. Dinuclear ruthenium(II) complexes as two-photon, time-resolved emission microscopy probes for cellular DNA. *Angew Chem Int Ed*. 2014;53:3367-3371.

36. Oeckinghaus A, Ghosh S. The NF-κB family of transcription factors and its regulation. *Cold Spring Harb Perspect Biol*. 2009;4:1-14.

37. Martin A, Byrne A, Burke CS, Forster RJ, Keyes TE. Peptide-bridged dinuclear ru(II) complex for mitochondrial targeted monitoring of dynamic changes to oxygen concentration and ROS generation in live mammalian cells. *J Am Chem Soc*. 2014;136:15300-15309.

38. Pietersz GA, Li W, Apostolopoulos V. A 16-mer peptide (RQIKIWFQNRRMKWKK) from antennapedia preferentially targets the class I pathway. *Vaccine*. 2001;19(11–12):1397-1405.

39. Liu C, Tai L, Zhang W, Wei G, Pan W, Lu W. Penetratin, a potentially powerful absorption enhancer for noninvasive intraocular drug delivery. *Mol Pharmaceutics*. 2014;11:1218-1227.

40. Derossi D, Calvet S, Trembleau A, Brunissen A, Chassaing G, Prochiantz A. Cell internalization of the third helix of the antennapedia homeodomain is receptor-independent. *The Journal of Biological Chemistry*. 1996;271:18188-18193.

41. Derossi D, Joliot AH, Chassaing G, Prochiantz A. The third helix of the antennapedia homeodornain translocates through biological membranes. *The Journal of Biological Chemistry*. 1994;269:10444-10450.

42. Lindgren M, Langel U. Classes and prediction of cell-penetrating peptides. *Methods Mol Biol*. 2011;683:3-19.

43. Jafari S, Dizaj SM, Adibkia K. Cell-penetrating peptides and their analogues as novel nanocarriers for drug delivery. *Bioimpacts*. 2015;5:103-111.

44. Ragin AD, Morgan RA, Chmielewski J. Cellular import mediated by nuclear localization signal peptide sequences. *Chem Biol*. 2002;9(8):943-948.

45. Blackmore L, Moriarty R, Dolan C, et al. Peptide directed transmembrane transport and nuclear localization of ru(II) polypyridyl complexes in mammalian cells. *Chem Commun*. 2013;49:2658.

46. Liu X, Shen Y, Shu J, Xiao Y, Zhang S, Lu J. DNA interaction, photocleavage and topoisomerase I inhibition by ru(II) complex with a new ligand possessing phenazine unit. *J Fluoresc*. 2015;25:1527-1535.

47. Friedman AE, Chambron J, Sauvage J, Turro NJ, Barton JK. Molecular ‘‘Light switch” for DNA: Ru(bpy)2(dppz)$^{2+}$. *J Am Chem Soc*. 1990;112:4960-4962.

48. Pujals S, Fernández-Carneado J, López-Iglesias C, Kogan MJ, Giralt E. Mechanistic aspects of CPP-mediated intracellular drug delivery: Relevance of CPP self-assembly. *Biochimica et Biophysica Acta (BBA) - Biomembranes*. 2006;1758(3):264-279.

49. Thorén PEG, Persson D, Isakson P, Goksör M, Önfelt A, Nordén B. Uptake of analogs of penetratin, tat(48–60) and oligoarginine in live cells. *Biochem Biophys Res Commun*. 2003;307(1):100-107.

50. Estrada de Martin P, Novick P, Ferro-Novick S. The organization, structure, and inheritance of the ER in higher and lower eukaryotes. *Biochem Cell Biol*. 2005;83:752-761.

51. McConnell AJ, Song H, Barton JK. Luminescence of [ru(bpy)2(dppz)]2+ bound to RNA mismatches. *Inorg Chem*. 2013;52:10131-10136.

52. Cosgrave L, Devocelle M, Forster RJ, Keyes TE. Multimodal cell imaging by ruthenium polypyridyl labelled cell penetrating peptides. *Chem Commun*. 2010;46:103-105.

53. Porth C. *Essentials of pathophysiology: Concepts of altered health states.* Lippincott Williams & Wilkins; 2011.

54. Gill MR, Derrat H, Smythe CGW, Battaglia G, Thomas JA. Ruthenium(II) metallo-intercalators: DNA imaging and cytotoxicity. *ChemBioChem*. 2011;12:877.

55. Ernst RJ, Song H, Barton JK. DNA mismatch binding and antiproliferative activity of rhodium metalloinsertors. *J Am Chem Soc*. 2009;131:2359-2366.

56. Klar TA, Jakobs S, Dyba M, Egner A, Hell SW. Fluorescence microscopy with diffraction resolution barrier broken by stimulated emission. *Proc Natl Acad Sci USA*. 2000;97:8206-8210.

57. Urban N, Willig K, Hell S, Nägerl U . STED nanoscopy of actin dynamics in synapses deep inside living brain slices. *Biophys J*. 2011;101(5):1277-1284.

58. Vicidomini G, Moneron G, Han KY, et al. Sharper low-power STED nanoscopy by time gating. *Nature Methods*. 2011;8:571-573.

59. Vicidomini G, Schönle A, Ta H, et al. STED nanoscopy with time-gated detection: Theoretical and experimental aspects *PLOS ONE*. 2013;8:e54421.

60. Testa I, Wurm CA, Medda R, et al. Multicolor fluorescence nanoscopy in fixed and living cells by exciting conventional fluorophores with a single wavelength. *Biophys J*. 2010;99:2686-2694.

61. Bückers J, Wildanger D, Vicidomini G, Kastrup L, Hell SW. Simultaneous multi-lifetime multi-color STED imaging for colocalization analyses. *Optics Express*. 2011;19:3130-3143.

62. Göttfert F, Wurm C, Mueller V, et al. Coaligned dual-channel STED nanoscopy and molecular diffusion analysis at 20 nm resolution. *Biophys J*. 2013;105(1):L01-L03.

63. Bianchini P, Peres C, Oneto M, Galiani S, Vicidomini G, Diaspro A. STED nanoscopy: A glimpse into the future. *Cell Tissue Res*. 2015;360:143-150.

64. Alberts B, Johnson A, Lewis J, Raff M, Roberts K, Walter P, eds. *Molecular biology of the cell. the endoplasmic reticulum.*. New York: Garland Science; 2002; No. 4.

65. Schneider G, Guttmann P, Heim S, et al. Three-dimensional cellular ultrastructure resolved by X-ray microscopy. *Nature Methods*. 2010;7:985-987.

66. McCullough S, Lucocq J. Endoplasmic reticulum positioning and partitioning in mitotic HeLa cells. . *J Anat*. 2005;206:415-425.

67. Lu L, Ladinsky MS, Kirchhausen T. Cisternal organization of the endoplasmic reticulum during mitosis. *Mol Biol Cell*. 2009;20:3471-3480.

68. Bottanelli F, Kromann EB, Allgeyer ES, et al. Two-colour live-cell nanoscale imaging of intracellular targets. *Nat Commun*. 2016;7:10778.

# Chapter 6: Conclusions and Future Work

This thesis focused on the application of novel Ruthenium and Osmium (II) polypyridyl complexes as contrast agents and sensing probes in live cell imaging applications. There has been a dramatic upsurge in interest in metal complexes as imaging agents over the past decade, driven in part by increased understanding of targeting and cell permeation of molecules which has come from developments in pharmaceutical and therapeutic sciences. And, also in part by increased acceptance that metal complexes with the right ligand combinations can be rendered very stable and thus have low toxicity toward cells.

The work presented here advances our understanding of both the cytotoxicity of Ru and Os complexes, indeed Chapter 2 detailed the first example of an Os (II) complex applied to cell imaging and explored the high precision with which peptides can target such metal complexes within the cell. We also explored the applications of these luminescent probes in quantitatively measuring oxygen concentrations *in vivo* and their performance in the latest development in super resolution microscopy, STimulated Emission Depletion (STED).

Chapter 2 detailed the first application of an Os(II) polypyridyl complex conjugated to an octa-arginine peptide sequence for cell imaging. Up until now, Os(II) had only been employed in therapeutic applications as anti-cancer agents because of their high cytotoxicity when coordination to arene or similar ligands. Here we demonstrated that Os(II) is a suitable probe for cell imaging, with an $Em_{max}$ of 710 nm. Uptake studies in live CHO cells showed that Os(II) gave bright, high contrast images at low concentrations. It was also found to be non-toxic towards both CHO and Sp2 cells, a perhaps surprising attribute which is important for a cell imaging probe. Its outstanding photostability even compared to its Ru(II) analogue means it can undergo long exposures under confocal laser scanning without photobleaching during imaging experiments. The only drawback of the Os(II) explored noted is it relatively short luminescent lifetime, which rendered it insensitive to oxygen. However, this could possibly be used to study reactive oxygen species (ROS) in live cells, as Os(II) luminescent lifetime can be quenched in the presence of ROS. This is something that will be explored in the future.

Chapter 3 focused on a dinuclear Ru(II) probe conjugated to the MPP sequence FrFKFrFK to not only direct the probe to the mitochondria of live cells, but to also quantitatively measure oxygen and ROS from within the mitochondria. This was successfully demonstrated phosphorescent lifetime imaging microscopy (PLIM) which

allowed us to draw dynamic maps of the metabolic response of live cells to Antymycin A.

Chapter 4 examined the use of ratiometric probes for oxygen sensing *in vivo*, which consisted of the oxygen-sensitive Ru(II) complex and the oxygen-insensitive BODIPY reference probe. A single molecule ratiometric probe proved unsuccessful as when in aqueous solution the BODIPY reference switched off, meaning quantitative ratiometric oxygen sensing in cells could not be done. A core-shell ratiometric probe consisting of the BODIPY reference in a poly(styrene) core and the Ru(II) probe located on the outside of a poly-L-lysine shell overcame this problem as the BODIPY was now protected from aqueous solutions. At 100 nm in diameter, the particles crossed the cell membrane via passive diffusion with the help of the detergent CTAB, and localised in the lysosomes. However, ratiometric sensing from within the cells was unsuccessful. It was concluded that this was as a result of the particles locating in the lysosomes and the confocal was unable to successfully detect any changes in the luminescent emission intensity. One approach to try overcome this is to functionalise the outside of the particles in order to direct them away from the lysosomes when inside the cell. Increasing the concentrations of the probes used in the particles is also another factor that will be investigated to improve the particles.

Finally, Chapter 5 explored the application of Ru(II) polypyridyl probes to STED microscopy, where the high precision targeting, large Stokes shifts and ability to switch on/off upon binding to DNA might offer key advantages over conventional and rather limited range of probes applied to these methods. Targeting specific organelles is challenging, but is potentially very useful as it allows for precise imaging and sensing at these sites. Using signal peptide sequences enable the complex to be recognised by the cells for uptake, and once inside the cell to be directed to their target organelle. In this case, two Ru(II) complexes were used, both conjugated to two different signal peptides. The peptide sequence RQIKIWFQNRRMKWKK from the *Drosophila* transcription factor Antennepedia was used to target the endoplasmic reticulum (ER). On the other hand, VQRKRQKLMP peptide sequence, known as NF-κB, a nuclear transcription factor, was used to target the nucleus. The probes were directed to the endoplasmic reticulum and nucleus of live HeLa cells, confirmed using confocal microscopy. The Ru(II) complexes proved to highly photostable when compared to Alexa Fluor 532commercial probe which is widely used as a STED probe because of its photostability. Combining precise targeting probes with super resolution STED

microscopy allows for detailed, high resolution imaging specific organelles. Upon applying STED, high spatial resolution images of the ER were achieved, resolving single spots in the confocal image to the tube-like structure of the ER in the equivalent STED images. The 'light switch' effect of $[Ru(dppz)]^{2+}$ complex was successful, as the complex emitted when bound to nuclear DNA, brought to the nucleus by the targeting peptide sequence. STED images of nuclear DNA during the different stages of cell division were captured, with very little background noise. Resolution as low as 86 nm were achieved.

The future work to emerge from this thesis will focus on new transition metal complexes as suitable STED probes for live STED imaging. Os(II) complexes would make excellent STED probes because of their incredible photostability. There is currently a huge interest in the use of live STED imaging at the moment because of the improved resolutions as low as 20 nm. Dual-staining of samples also allows for live multi-photon STED images to capture interactions and complex dynamics between the different cellular organelles in real time. However, the increased resolutions achieved using STED needs to be exploited to capture live biological occurrences in order to study and understand at a sub-cellular level, something which is missing from the field at the moment. As demonstrated in this thesis, transition metal complexes are nearly ideal as STED imaging probes. Their multi-modal uses can combine STED imaging with intracellular sensing which is why the focus of future STED probes should be centred in developing transition metal complexes as suitable STED probes.

## Appendix

# Chapter 4 Dual-emission Ruthenium-BODIPY ratiometric complex for Oxygen Sensing

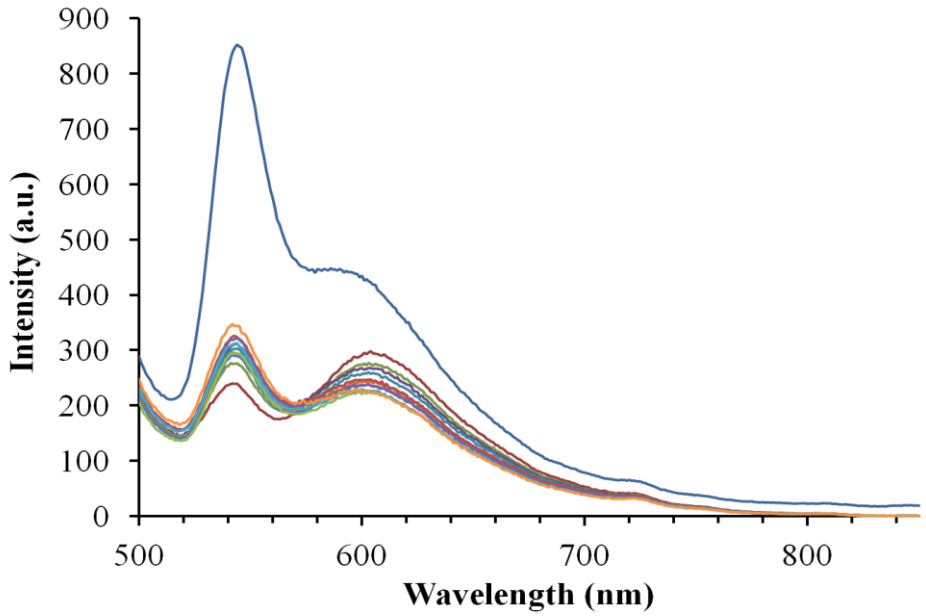


**Figure A4.1** $O_2$ calibration repeat of Compound 376 in PBS solution (pH 7.4) one month after Figure A1. Particles were stored in the dark before being used again. Particles were purged for with $N_2$ for 10 minutes and allowed to slowly re-aerate, measuring the emission spectra at varying oxygen concentrations (μmol/L) using a PreSens Oxygen probe.

**Publications**

1. Peptide-Bridged Dinuclear Ru(II) Complex for Mitochondrial Targeted Monitoring of Dynamic Changes to Oxygen Concentration and ROS Generation in Live Mammalian Cells. A Martin, A Byrne, CS Burke, RJ Forster, TE Keyes. *J.Am.Chem.Soc*. 2014; 136:15300-15309.

2. Facile Synthesis of Fluorescent Latex Nanoparticles with Selective Binding Properties Using Amphiphilic Glycosylated Polypeptide Surfactants. J Jacobs, A Byrne, N Gathergood, TE Keyes, JPA Heuts, A Heise. *BioMacromolecules*. 2014;47:7303-7310.

3. An Osmium (II) Polypyridyl Polyarginine Conjugate as a Probe for Live Cell Imaging; A Comparison of Uptake, Localization and Cytotoxicity with its Ru(II) Analogue. A Byrne, C Dolan, RD Moriarty, A Martin,U Neugebauer, RJ Forster, A Davies, Y Volkov, TE Keyes. *DaltonTrans*. 2015;44:14323–14332.

4. Solvent switchable dual emission from a bichromophoric ruthenium–BODIPY complex. A Martin, A Byrne, C Dolan, RJ Forster, TE Keyes. *Chem.Commun*. 2015;51:15839—1584.

5. Peptide Targeted Ruthenium (II) Luminophores for Stimulated Emission Depletion (STED) Microscope. A Byrne, CS Burke, TE Keyes. *Submitted to J.Am.Chem.Soc.*

6. Transition metal luminophores for cell imaging. CS Burke, A Byrne, TE Keyes. *Advances in Imaging and Sensing*. Submitted Book Chapter.